

Theory of Multidimensional Spectroscopy and Excitation Transfer Processes in Nanostructures

vorgelegt von
Master of Science
Judith Felicitas Specht
geb. in Tett nang

von der Fakultät II – Mathematik und Naturwissenschaften
der Technischen Universität Berlin
zur Erlangung des akademischen Grades

Doktor der Naturwissenschaften
– Dr. rer. nat. –

genehmigte Dissertation

Promotionsausschuss:

- Vorsitzende: Prof. Dr. rer. nat. Birgit Kanngießer
1. Gutachter: Prof. Dr. rer. nat. Andreas Knorr
2. Gutachterin: Priv.-Doz. Dr. rer. nat. Sylke Blumstengel
3. Gutachter: Dr. rer. nat. Marten Richter

Tag der wissenschaftlichen Aussprache: 9. März 2018

Berlin 2018

Abstract

Advances in the manufacturing of semiconductor-based hybrid nanostructures draws attention towards possible optoelectronic and quantum computational applications. The present work develops theoretical models to study the coherent couplings and excitation transfer mechanisms in nanostructures and aims at a microscopic understanding of the underlying Coulomb-mediated processes, thus, laying the foundation to access the full functionality of the studied quantum systems. A rich and versatile theoretical toolbox is developed capable of describing a variety of semiconductor nanostructures.

Nonlinear four-wave mixing spectroscopy in its various realizations depending on the specific temporal and spatial configuration and polarization of the pulse sequence is a valuable tool to infer the excitonic structure and dynamics of different kinds of quantum systems. In particular, the combination of polarization-resolved nanooptical excitation with two-dimensional double quantum coherence spectroscopy is employed to derive a quantum state tomography protocol for Förster coupled, spin-degenerate two-level quantum emitters (e.g., quantum dots). The here suggested reconstruction scheme makes it possible to resolve the internal structure of the probed quantum system by decomposing the collective optical response into the contributions from the single quantum emitters.

Photon echo spectroscopy, a different four-wave mixing technique, is simulated to evidence coherent couplings in monolayer transition-metal dichalcogenides and, thus, the formation of strongly correlated higher-order states without direct analogue in conventional semiconductors. A thorough implementation of the valley- and spin-dependent optical selection rules and separation of the involved quantum pathways in the presented calculations allows to identify different types of intervalley biexcitons in measured two-dimensional spectra.

A theoretical treatment including electrostatic Coulomb couplings and fine-structure splitting is developed to analyze the two-dimensional spectra measured in a two-beam four-wave mixing experiment of individual quantum dots and quantum dot molecules in rephasing and double-quantum pulse configurations. The spectral signatures can be traced back to the underlying coupling mechanisms and strengths that determine the single- and double-excitonic resonances, yielding a good agreement between theory and experiment.

Using a density-matrix equation technique, the geometry-dependent excitation transfer across a semiconductor/molecule hybrid interface is studied within physically reasonable parameter ranges. For this purpose, Förster-type non-radiative coupling is modeled microscopically using a partial charge technique, and the case of creating excitons in an optically active, highly ordered layer of organic molecules by strong electrical pumping of the semiconductor substrate is considered. It is found that the interlayer coupling efficiency is highly sensitive to changes in the resonance energy detuning, the molecular coverage, the charge carrier temperature and concentration in the semiconductor quantum well, the interlayer separation, and the spatial orientation of the flat-lying molecules on top of the substrate.

Finally, the theoretical framework for these hybrid inorganic/organic systems is extended to treat the Coulomb coupling between Wannier excitons in the semiconductor substrate including interface roughness, acoustic phonon scattering, and radiative recombination, and Frenkel excitons in the disordered organic film including intermolecular Coulomb interaction and the coupling to vibrational modes. For this purpose, a perturbative approach is chosen to derive the transition amplitudes between exciton densities in the hybrid system, and a cumulant expansion technique is used to describe the coupling to vibrational modes in the organic layer, which constitutes the main dephasing mechanism in such systems.

Kurzfassung

Fortschritte in der Herstellung von Halbleiter-basierten Hybrid-Nanostrukturen rücken mögliche Anwendungen im Bereich der Optoelektronik und des Quantencomputings in den Fokus. Die vorliegende Arbeit entwickelt theoretische Modelle, um kohärente Kopplungen und Mechanismen des Anregungstransfers in Nanostrukturen zu untersuchen, und zielt auf ein mikroskopisches Verständnis der zugrundeliegenden Coulomb-induzierten Prozesse. Damit legt sie die Grundlage, um auf die volle Funktionalität der untersuchten Quantensysteme zuzugreifen.

Nichtlineare Vier-Wellen-Mischungs-Spektroskopie in ihren verschiedenen von der zeitlichen und räumlichen Konfiguration und der Polarisierung der Pulssequenz abhängigen Realisierungen ist eine wertvolle Methode, um die exzitonische Struktur und Dynamik unterschiedlicher Quantensysteme zu erschließen. Insbesondere wird eine Kombination aus polarisationsaufgelöster nanooptischer Anregung und zweidimensionaler Zwei-Quanten-Kohärenz-Spektroskopie angewandt, um ein Quantentomographie-Protokoll für Förster-gekoppelte, spinentartete Zwei-niveau-Quantenemitter (z.B. Quantenpunkte) herzuleiten. Das vorgestellte Rekonstruktionschema ermöglicht es, die innere Struktur des untersuchten Quantensystems aufzulösen, indem die kollektive optische Antwort in die Beiträge der einzelnen Quantenemitter zerlegt wird.

Photon-Echo-Spektroskopie, eine weitere Vier-Wellen-Mischungs-Technik, wird simuliert, um kohärente Kopplungen in Monolagen von Übergangsmetall-Dichalkogeniden und somit die Bildung von stark korrelierten Zuständen höherer Ordnung ohne direktes Analogon in herkömmlichen Halbleitern nachzuweisen. Eine gründliche Implementierung der valley- und spinabhängigen optischen Auswahlregeln und eine Trennung der beteiligten Quantenpfade erlauben es, verschiedene Arten von Intervalley-Biexzitonen in den gemessenen zweidimensionalen Spektren zu identifizieren.

Eine theoretische Beschreibung unter Einbeziehung von elektrostatischen Coulombkopplungen und Feinstrukturaufspaltung wird entwickelt, um zweidimensionale Spektren von einzelnen Quantenpunkten und Quantenpunktmolekülen zu analysieren, welche mittels Vier-Wellen-Mischung in Form von Zwei-Strahl-Experimenten in Photon-Echo- und Zwei-Quanten-Kohärenz-Pulskonfigurationen gemessen wurden. Die spektralen Signaturen erlauben Rückschlüsse auf die zugrundeliegenden Kopplungsmechanismen und -stärken, welche die einzel- und doppelexzitonischen Resonanzen bestimmen, und zeigen eine gute Übereinstimmung zwischen Theorie und Experiment.

Mit Hilfe einer Dichtematrix-Technik wird der von der Geometrie abhängige Anregungstransfer an der Grenzfläche einer Halbleiter-Molekül-Hybridstruktur innerhalb physikalisch sinnvoller Parameterbereiche untersucht. Zu diesem Zweck wird mittels einer Partialladungsmethode Förster-Kopplung mikroskopisch modelliert und es wird der Fall betrachtet, dass Exzitonen in einer optisch aktiven, geordneten organischen Molekülschicht durch starkes elektrisches Pumpen des Halbleitersubstrats generiert werden. Die Kopplungseffizienz zwischen den beiden Schichten erweist sich als hochempfindlich gegenüber Änderungen in der Verstimmung zwischen den Resonanzenergien, der molekularen Bedeckungsdichte, der Ladungsträgertemperatur und -konzentration im Halbleiter-Quantenfilm, dem Schichtabstand und der räumlichen Orientierung der flachen Moleküle auf dem Substrat.

Abschließend wird das theoretische Modell zur Beschreibung dieser hybriden inorganisch-organischen Systeme erweitert, um den Einfluss von Oberflächenrauigkeit, Streuung an akustischen Phononen und radiativer Rekombination im Halbleitersubstrat sowie intermolekularer Coulombwechselwirkung und Kopplung an Vibrationsmoden im ungeordneten organischen Film auf die Coulombkopplung zwischen Wannier- und Frenkel-Exzitonen zu berücksichtigen. Zu diesem Zweck wird ein störungstheoretischer Ansatz gewählt, um die Übergangsamplituden zwischen Exzitonichten im Hybridsystem herzuleiten, und eine Kumulantenentwicklung wird benutzt, um die Kopplung an Vibrationsmoden in der organischen Schicht zu beschreiben, welche hauptsächlich für die Dephasierung solcher Systeme verantwortlich ist.

Contents

Abstract	iii
Kurzfassung	v
Acronyms	xi
1 Introduction	1
1.1 Motivation	1
1.2 Structure of the thesis	2

PART I: THEORETICAL BACKGROUND

2 Fundamental theoretical concepts	5
2.1 Density-matrix theory in Liouville space	5
2.1.1 Time evolution of the density operator	5
2.1.2 Interaction expansion of the coupling to an external optical field	6
2.1.3 Quantum master equations in open quantum systems	7
2.2 Solid-state Hamilton operator	8
2.2.1 Electronic and free radiation part and electron-photon interaction	9
2.2.2 Ionic part and electron-phonon interaction	10
2.3 Factorization schemes	12
2.4 Markov approximation	12
2.5 Feynman disentanglement theorem for time-ordered operators	13
3 Coherent multidimensional spectroscopy	15
3.1 Introduction	15
3.2 Four-wave mixing spectroscopy	16
3.2.1 Experimental setup	16
3.2.2 Heterodyne detection	16
3.3 Calculation of heterodyne-detected coherent signals	17
3.3.1 Third-order polarization and response function	17
3.3.2 Liouville space pathways and double-sided Feynman diagrams	18
3.3.3 Double quantum coherence signal	19
3.3.4 Phase cycling	20

PART II: MULTIDIMENSIONAL SPECTROSCOPY OF SEMICONDUCTOR NANOSTRUCTURES

4 Probing spin-dependent exciton wave functions with localized 2D spectra	23
4.1 Introduction	23
4.2 Coupled quantum dots	24
4.2.1 Model system	24
4.2.2 Local states and dipole selection rules	25
4.2.3 Hamilton operator	26
4.2.4 Delocalized exciton basis	27

4.3	Linear and nonlinear far-field spectroscopy	28
4.3.1	Linear absorption	28
4.3.2	Two-dimensional DQC spectroscopy	28
4.3.3	Evaluation of the linear and 2D far-field spectra	29
4.4	Localized DQC spectroscopy	31
4.4.1	Spatiotemporal pulse control	31
4.4.2	Modification of the electron-light coupling for localized excitation	31
4.4.3	Localization of the first pulse	32
4.4.4	Localization of the second pulse	34
4.5	Reconstruction schemes	34
4.5.1	Extraction of the single-exciton coefficients	35
4.5.2	Extraction of the two-exciton coefficients	37
4.6	Summary	42
5	Coherent coupling of excitons and trions in monolayer transition metal dichalcogenides	45
5.1	Introduction	45
5.2	Coherent photon echo spectroscopy	46
5.2.1	Calculation of the rephasing one-quantum signal	46
5.2.2	Off-diagonal peaks as indicators of coherent couplings	47
5.2.3	Elimination of inhomogeneous broadening along the cross-diagonal	49
5.3	Spin- and valley-selective optical transitions in monolayer MoSe ₂	50
5.4	Experimental setup and numerical implementation	52
5.5	Evaluation of the spectra	53
5.5.1	Comparison between experiment and theory	53
5.5.2	Discussion of the calculated spectra	56
5.6	Conclusion	60
6	2D rephasing and double-quantum spectroscopy of single QDs and QD molecules	63
6.1	Introduction	63
6.2	Two-beam four-wave mixing spectroscopy	64
6.3	Calculation of the four-wave mixing signals	65
6.3.1	Rephasing photon echo signal	65
6.3.2	Double quantum coherence signal	66
6.4	Quantum dot model system	67
6.4.1	Individual QD exciton-biexciton system with fine-structure splitting	67
6.4.2	Quantum dot molecule	67
6.4.3	Hamiltonian and model parameters	68
6.5	Discussion of the spectral signatures	69
6.6	Comparison to a Förster-coupled quantum dot molecule	73
6.7	Summary	74
PART III: EXCITATION TRANSFER IN HYBRID INORGANIC/ORGANIC SYSTEMS		
7	Excitation transfer from semiconductor continuum states into a molecular layer	77
7.1	Introduction	77
7.2	Modeling the hybrid inorganic/organic system	78
7.2.1	Model system	78
7.2.2	Hamilton operator	79

7.3	Partial charge approximation of the Coulomb matrix elements	81
7.3.1	Partial charge technique for the intermolecular Coulomb coupling	82
7.3.2	Partial charge technique for the interlayer Coulomb coupling	83
7.4	Transformation of the molecular orbitals into a Bloch basis	85
7.5	Molecular exciton basis	87
7.6	Equations of motion of the hybrid system	91
7.7	Calculation of the interlayer transfer rate	94
7.8	Evaluation of the numerical results	95
7.8.1	Variation of the resonance energy detuning	95
7.8.2	Variation of the molecular coverage	96
7.8.3	Tuning the electrical driving	98
7.8.4	Variation of the orientation and distance of the molecular film	100
7.9	Summary	101
8	Coupling of Wannier and Frenkel excitons in a hybrid inorganic/organic system	103
8.1	Introduction	103
8.2	Inorganic part: Wannier excitons	104
8.2.1	Exciton states in disordered quantum wells	104
8.2.2	Electron–phonon interaction	107
8.2.3	Electron–photon interaction	108
8.2.4	Total Hamiltonian for disordered quantum wells in exciton basis	109
8.2.5	Equations of motion in density matrix formalism	109
8.2.6	Phenomenological Lindblad approach	110
8.3	Organic part: Frenkel excitons	112
8.3.1	Local molecular basis states	112
8.3.2	Diagonalization of the electronic Hamiltonian	112
8.3.3	Electron–phonon interaction	114
8.4	Exciton dynamics in the hybrid system	117
8.4.1	Molecule–semiconductor Coulomb coupling	117
8.4.2	Hamiltonian and Liouville propagator	118
8.4.3	Transition amplitudes	120
8.4.4	Cumulant expansion	121
8.4.5	Transition rates	126
8.4.6	System of equations for the population dynamics	128
8.5	Summary and outlook	128
9	Conclusion and outlook	131

APPENDICES

A	Calculation of the rephasing photon echo signal	135
B	Details on the derivation and implementation of the HIOS transfer rates	139
B.1	Dielectric screening at the hybrid interface	139
B.2	Quaternions	140
B.3	Transformation to momentum representation	141
B.4	Discrete Fourier transform	143
B.5	Derivation of the eigenproblem of the molecular excitons	145
B.5.1	Calculation of the matrix elements in the exciton basis	145
B.5.2	Normalization of the molecular exciton states in the discrete basis	146

B.6 Derivation of the equations of motion for the hybrid system	147
B.6.1 Homogeneous exciton density of the molecular system	147
B.6.2 Molecule–semiconductor coherence	148
B.7 Numerical implementation of the in-scattering rate	150
B.8 Reciprocal space analysis of the transfer rates for varying detunings	152
C Details on the derivation of the Wannier-Frenkel excitation transfer dynamics	155
C.1 Equations of motion of the exciton densities and polarizations	155
C.1.1 Radiative and phonon scattering rates	158
C.2 Calculation of the semiconductor–molecule transition amplitude	159
C.3 Calculation of the intermolecular transition amplitude	161
Publications	163
Proceedings	163
Selbständigkeitserklärung	165
Danksagung	167
Bibliography	169

Acronyms

1D	one-dimensional
2D	two-dimensional
2D-DFT	two-dimensional discrete Fourier transform
BZ	Brillouin zone
CBM	conduction band minimum
COM	center-of-mass
DFT	density-functional theory
DQC	double quantum coherence
EOM	equation of motion
ESA	excited state absorption
ESE	excited state emission
FSS	fine-structure splitting
FWM	four-wave mixing
GSB	ground state bleaching
HIOS	hybrid inorganic/organic systems
HOMO	highest occupied molecular orbital
L4P	ladder-type quarterphenyl
LA	longitudinal-acoustic
LUMO	lowest unoccupied molecular orbital
PE	photon echo
PES	potential energy surface
PL	photoluminescence
QD	quantum dot
QW	quantum well
TMD	transition-metal dichalcogenide
UC	unit cell
VBM	valence band maximum
vdW	van der Waals

1

Introduction

1.1 Motivation

Excitons, i.e., Coulomb bound correlated electron-hole pair states, dominate the optoelectronic properties of many dielectric solids and are particularly pronounced in the case of confined quantum systems such as semiconductor nanostructures [Bas88, Hau04]. Therefore, an in-depth insight into the structural and dynamical properties of excitonic complexes, their binding energies and couplings, and coherent light-matter interactions is of outstanding importance regarding possible solid-state realizations of coupled quantum emitters for optoelectronic and quantum informational platforms [Bio00, Bay01, Mic03, Lov03, Bes05].

However, complex nanostructured materials often exhibit highly congested levels and couplings that are challenging to resolve experimentally. Especially the nature of the coupling (e.g., electrostatic or non-radiative Förster-type) plays a decisive role in the design of devices. In this context, multidimensional nonlinear spectroscopy [Muk95] comes into play as powerful instrument to disentangle the complex optical response of various kinds of quantum systems. It overcomes many of the limitations of conventional one-dimensional techniques since it has the ability to isolate distinct quantum pathways, to unfold the third-order excitonic response across different frequency axes, and to separate homogeneous broadening of the individual emitters from inhomogeneity of the transition energies [Muk00, Tia03, Jon03, Axt04, Lan07, Yan08, Cho08, Kar10, Sie10, Lan10, Fin12, Nar15]. The application of a sequence of ultrafast laser pulses with defined polarizations creates coherent superpositions of distinct excitonic states and reveals many-particle correlations between them. This is exploited in this work to examine higher-order correlated states in coupled quantum dots and monolayer transition-metal dichalcogenides by calculating four-wave mixing signals and comparing them to experimental data. This way, two-dimensional spectroscopy provides unique access to fundamental structural properties such as the nature of coupling, binding energies, optical selection rules, and excited state configurations.

Dipole-dipole Förster-type excitation transfer can couple distant physical subsystems leading to the formation of collective resonances that are potentially delocalized over the whole structure described by a hybridization of the local basis states [Gue02, Lov03, Ger05, Chr10]. Using conventional far-field spectroscopy techniques, these couplings can be inspected. However, it is difficult to quantify to which extent an observed delocalized excitonic resonance contains contributions from the different single emitters. To tackle this shortcoming, one can combine temporal with spatial pulse control by using localized excitation of the single quantum emitters with nano-optical fields [Zha09, Kin09, Hua09, Mer08, Nov11, Gue02, Bri05, vFr98, Pet04, Web11].

Over the last two decades, hybrid inorganic/organic systems have emerged as promising new material class capable of combining the optoelectronic properties of their constituents to form novel, tailorable device functionality [Bas99, Blu06, Its07, Nev08, Blu10, Vay12,

[Lia13, Qia15, Fri15, Sch15, Lju17]. Hybrid inorganic/organic systems are composed of two complementary material components that differ fundamentally in their optoelectronic properties: On the one hand, organic materials such as organic dye molecules usually exhibit a strong light-matter coupling, thus enhancing the radiative emission yield. Moreover, the thermal stability, the absorption and fluorescence efficiency and linewidth, the geometry, spatial arrangement, orientation, and ordering of molecules in thin films can be manipulated by the specific chemical synthesis and deposition technique [Kob12, Blu10], hence, making molecules extremely versatile building blocks in terms of their optical and electrochemical properties. On the other hand, inorganic semiconductor nanostructures such as ZnO quantum wells have multiple advantageous features such as extended band states, atomically smooth interfaces, high charge carrier mobilities, and efficient electrical carrier injection. Combining these different material classes leads to the formation of novel types of excitations, e.g., Frenkel-Wannier excitons [Agr98, Blu06] and hybrid charge transfer excitons (i.e., bound excitons with the electron and hole located at different sites of the hybrid interface) [Vay12, Pie15, Eye15]. Having in mind the use of hybrid inorganic/organic systems as light-emitting devices, this work develops a theoretical framework based on a density-matrix equation technique to describe Förster-type non-radiative energy transfer across the inorganic/organic interface.

1.2 Structure of the thesis

This thesis is composed of three main parts:

The first part comprises the most important theoretical foundations of this work, including some basic concepts of solid-state quantum mechanics and density-matrix theory in Chap. 2, as well as an introduction into the theoretical toolbox to calculate coherent multidimensional spectroscopy signals in Chap. 3.

In the second part, several third-order techniques are presented to resolve the internal structure of different nanostructures. Chapter 4 treats a quantum state tomography protocol to retrieve the excitonic wave functions of coupled quantum dots. In Chap. 5, photon echo spectroscopy of atomically thin transition-metal dichalcogenides is investigated and a comparison with experimental data allows to identify multiple higher-order correlated states. As a last example for the implementation of two-dimensional polarization-resolved four-wave mixing spectroscopy, the experimentally observed signatures of individual quantum dots are simulated including optical selection rules, Coulomb coupling, and fine-structure splitting in Chap. 6 to illustrate the formation of a quantum dot molecule composed of two electrostatically coupled quantum dots.

The third part of this thesis is dedicated to the theoretical description of the excitation transfer efficiency and dynamics in hybrid inorganic/organic systems. Therefore, as a first step, in Chap. 7 a density-matrix technique in momentum representation is developed to describe the excitation transfer coupling between the Markovian electron-hole continuum in an electrically driven idealized semiconductor quantum well and a highly ordered molecular adlayer. This framework is in the following Chap. 8 extended to treat disorder, radiative dephasing, and exciton-phonon scattering processes in both the organic and inorganic constituent using a perturbative approach and a cumulant expansion technique.

Finally, a brief conclusion summarizes the main results and gives an outlook for future investigations.

Part I

Theoretical background

2

Fundamental theoretical concepts

2.1 Density-matrix theory in Liouville space

2.1.1 Time evolution of the density operator

If the state of a quantum mechanical system is characterized by a single state vector $|\psi(t)\rangle$ in Hilbert space, this state is called a *pure state* with wave function ψ . Its temporal evolution is described by the Schrödinger equation $\frac{\partial|\psi\rangle}{\partial t} = -\frac{i}{\hbar}\hat{H}|\psi\rangle$. The expectation value of an arbitrary operator \hat{A} is then given by $\langle\hat{A}\rangle = \langle\psi(t)|\hat{A}|\psi(t)\rangle$. However, in many experimental setups only a statistical ensemble of pure states is accessible. Therefore, a *mixed state* description is introduced, where p_i denotes the probability for the system to be in state $|\psi_i(t)\rangle$. The density operator

$$\hat{\rho}(t) \equiv \sum_i p_i |\psi_i(t)\rangle\langle\psi_i(t)| \quad (2.1)$$

can be assigned to this mixed state. The density matrix elements with respect to an arbitrary basis set $\{|n\rangle\}$ have the form

$$\rho_{nm}(t) = \sum_i p_i \langle n|\psi_i\rangle\langle\psi_i|m\rangle. \quad (2.2)$$

The density matrix is Hermitian, its diagonal elements are non-negative and its trace (i.e., the sum over all diagonal elements) is 1. The diagonal elements of the density matrix $\hat{\rho}(t)$ represent the population of the specific state, whereas the non-diagonal elements describe transition amplitudes between two states and are referred to as coherences or polarizations. An observable $\langle\hat{A}\rangle$ is calculated according to

$$\langle\hat{A}\rangle = \sum_i p_i \langle\psi_i(t)|\hat{A}|\psi_i(t)\rangle = \text{tr} [\hat{A}\hat{\rho}(t)]. \quad (2.3)$$

Based on the Schrödinger equation, the dynamics of the density matrix can be derived yielding the Liouville–von Neumann equation:

$$\frac{\partial\hat{\rho}}{\partial t} = -\frac{i}{\hbar} [\hat{H}, \hat{\rho}]_- \equiv -\frac{i}{\hbar} \mathcal{L}\hat{\rho}, \quad (2.4)$$

where the Liouville operator \mathcal{L} has been introduced. It is called *superoperator*, since it does not act on state vectors but on operators of the Hilbert space. The new space where the density operator is considered a vector and the operators are represented by superoperators is called *Liouville space*. The Liouville–von Neumann equation describing the temporal evolution of the density operator in Liouville space is the formal analogon of the Schrödinger equation in

Hilbert space. Analogous to the time evolution operator in Hilbert space, the Liouville space propagator $\mathcal{U}(t, t_0)$ is introduced with $\hat{\rho}(t) = \mathcal{U}(t, t_0)\hat{\rho}(t_0)$, yielding the Liouville equation

$$\frac{\partial \mathcal{U}(t, t_0)}{\partial t} = -\frac{i}{\hbar} \mathcal{L}(t) \mathcal{U}(t, t_0) \quad (2.5)$$

with initial condition $\mathcal{U}(t_0, t_0) = 1$. The formal solution of this differential equation yields

$$\mathcal{U}(t, t_0) = \exp_{\leftarrow} \left(-\frac{i}{\hbar} \int_{t_0}^t d\tau \mathcal{L}(\tau) \right). \quad (2.6)$$

The expression $\exp_{\leftarrow}(\dots)$ represents the time-ordered expansion

$$\mathcal{U}(t, t_0) = 1 + \sum_{n=1}^{\infty} \left(-\frac{i}{\hbar} \right)^n \int_{t_0}^t d\tau_n \int_{t_0}^{\tau_n} d\tau_{n-1} \cdots \int_{t_0}^{\tau_2} d\tau_1 \mathcal{L}(\tau_n) \mathcal{L}(\tau_{n-1}) \cdots \mathcal{L}(\tau_1) \quad (2.7)$$

with $t \geq \tau_n \geq \cdots \geq \tau_1 \geq t_0$.

2.1.2 Interaction expansion of the coupling to an external optical field

The Hamilton operator of the considered quantum system is assumed to be composed of an electronic part representing the closed system and a semiclassical interaction with the external light field $\mathbf{E}(t)$: $\hat{H}(t) = \hat{H}_e(t) + \hat{H}_{\text{el-L}}(t)$ with $\hat{H}_{\text{el-L}} = -\mathbf{E}(\mathbf{r}, t) \cdot \hat{\mathbf{d}}$. $\hat{\mathbf{d}}$ denotes the dipole operator, cf. Eq. (2.41). Accordingly, also the Liouville operator is split into $\mathcal{L}(t) = \mathcal{L}_e(t) + \mathcal{L}_{\text{el-L}}(t)$ [Muk95, Abr09], and an interaction picture with respect to \mathcal{L}_e can be introduced, where the propagator of Eq. (2.6) becomes:

$$\mathcal{U}(t, t_0) = \mathcal{U}_0(t, t_0) \mathcal{U}_1(t, t_0) \quad (2.8)$$

with

$$\mathcal{U}_0(t, t_0) = \exp_{\leftarrow} \left(-\frac{i}{\hbar} \int_{t_0}^t d\tau \mathcal{L}_e(\tau) \right) \quad (2.9)$$

and

$$\mathcal{U}_1(t, t_0) = \exp_{\leftarrow} \left(-\frac{i}{\hbar} \int_{t_0}^t d\tau \mathcal{U}_0(t_0, \tau) \mathcal{L}_{\text{el-L}}(\tau) \mathcal{U}_0(\tau, t_0) \right). \quad (2.10)$$

$\mathcal{G}(t - t_0) \equiv \Theta(t - t_0) \mathcal{U}_0(t, t_0)$ is the retarded Green's function describing the free evolution of the density matrix between two interaction events [Abr09]. With that, the time evolution superoperator becomes

$$\mathcal{U}(t, t_0) = \mathcal{U}_0(t, t_0) \exp_{\leftarrow} \left(-\frac{i}{\hbar} \int_{t_0}^t d\tau \mathcal{U}_0(t_0, \tau) \mathcal{L}_{\text{el-L}}(\tau) \mathcal{U}_0(\tau, t_0) \right). \quad (2.11)$$

The initial time t_0 can be chosen as an arbitrary time before the onset of the external electric field, e.g., $t_0 \rightarrow -\infty$.

Also the density operator $\hat{\rho}(t)$ can be expanded in orders of $\mathbf{E}(t)$:

$$\hat{\rho}(t) = \hat{\rho}^{(0)}(t) + \hat{\rho}^{(1)}(t) + \hat{\rho}^{(2)}(t) + \dots \quad (2.12)$$

The contribution in n -th order of the electric field is expressed using the retarded Green's function \mathcal{G} [Muk95]

$$\begin{aligned} \hat{\rho}^{(n)}(t) = & \left(-\frac{i}{\hbar} \right)^n \int_{t_0}^t d\tau_n \int_{t_0}^{\tau_n} d\tau_{n-1} \cdots \int_{t_0}^{\tau_2} d\tau_1 \mathcal{G}(t - \tau_n) \mathcal{L}_{\text{el-L}}(\tau_n) \\ & \times \mathcal{G}(\tau_n - \tau_{n-1}) \mathcal{L}_{\text{el-L}}(\tau_{n-1}) \cdots \mathcal{G}(\tau_2 - \tau_1) \mathcal{L}_{\text{el-L}}(\tau_1) \mathcal{G}(\tau_1 - t_0) \hat{\rho}(t_0). \end{aligned} \quad (2.13)$$

The Green's functions ensure that $t_0 \leq \tau_1 \leq \tau_2 \leq \dots \leq \tau_n \leq t$. The τ_i represent the interaction times with the external light fields. Introducing the dipole superoperator $\mathcal{D}\hat{A} \equiv [\hat{\mathbf{d}}, \hat{A}]$, the Liouville operator of the electron-light interaction takes the form $\mathcal{L}_{\text{el-L}}(t) = -\mathbf{E}(\mathbf{r}, t) \cdot \mathcal{D}$. Plugging this expression into Eq. (2.13), one obtains

$$\begin{aligned} \hat{\rho}^{(n)}(t) = & \left(-\frac{i}{\hbar}\right)^n \int_{t_0}^t d\tau_n \int_{t_0}^{\tau_n} d\tau_{n-1} \dots \int_{t_0}^{\tau_2} d\tau_1 \mathcal{G}(t - \tau_n) \mathbf{E}(\mathbf{r}, \tau_n) \cdot \mathcal{D} \\ & \times \mathcal{G}(\tau_n - \tau_{n-1}) \mathbf{E}(\mathbf{r}, \tau_{n-1}) \cdot \mathcal{D} \dots \mathcal{G}(\tau_2 - \tau_1) \mathbf{E}(\mathbf{r}, \tau_1) \cdot \mathcal{D} \hat{\rho}(t_0), \end{aligned} \quad (2.14)$$

where $\mathcal{G}(\tau_1 - t_0)\hat{\rho}(t_0) = \hat{\rho}(t_0)$ was used. Substituting the interaction times τ_i by the time intervals t_i between two subsequent interactions according to

$$t_1 \equiv \tau_2 - \tau_1, \quad t_2 \equiv \tau_3 - \tau_2, \quad \dots, \quad t_n \equiv t - \tau_n \quad (2.15)$$

and sending $t_0 \rightarrow -\infty$ yields [Muk95]

$$\begin{aligned} \hat{\rho}^{(n)}(t) = & \left(\frac{i}{\hbar}\right)^n \int_0^\infty dt_n \int_0^\infty dt_{n-1} \dots \int_0^\infty dt_1 \mathcal{G}(t_n) \mathbf{E}(\mathbf{r}, t - t_n) \cdot \mathcal{D} \\ & \times \mathcal{G}(t_{n-1}) \mathbf{E}(\mathbf{r}, t - t_n - t_{n-1}) \cdot \mathcal{D} \dots \mathcal{G}(t_1) \mathbf{E}(\mathbf{r}, t - t_n - \dots - t_1) \cdot \mathcal{D} \hat{\rho}(-\infty). \end{aligned} \quad (2.16)$$

For calculating spectroscopic signals, typically the quantity of interest is the n -th order of the induced polarization $\mathbf{P}(t)$. It is given as the expectation value of the density operator:

$$\mathbf{P}^{(n)}(t) = \langle \hat{\mathbf{d}} \rangle^{(n)} = \text{tr} \left[\hat{\mathbf{d}} \hat{\rho}^{(n)}(t) \right]. \quad (2.17)$$

2.1.3 Quantum master equations in open quantum systems

In Sec. 2.1.1 it was shown that in the Schrödinger picture the time evolution of the density matrix is given by the Liouville–von Neumann equation. However, in situations where the relevant quantum mechanical system S is weakly coupled to a reservoir R (i.e., an environment with continuous modes), it is more convenient to treat the problem in the interaction picture [Bre02, May00, Car99]. Let us assume that the full system Hamiltonian is given by

$$\hat{H}(t) = \hat{H}_0 + \hat{H}_{\text{S-B}}(t), \quad (2.18)$$

where the time-independent part \hat{H}_0 subsumes the free Hamilton operators of the system and the reservoir and $\hat{H}_{\text{S-B}}(t)$ describes the interaction between the system and the reservoir. Keeping in mind that observables must not be affected by the choice of the physical picture, i.e.,

$$\langle \hat{A}(t) \rangle = \text{tr} \left[\hat{A}(t) \hat{\rho}(t) \right] \stackrel{!}{=} \text{tr} \left[\hat{A}_{\text{I}}(t) \hat{\rho}_{\text{I}}(t) \right], \quad (2.19)$$

the interaction-picture operator

$$\hat{A}_{\text{I}}(t) \equiv U_0^\dagger(t, t_0) \hat{A}(t) U_0(t, t_0) \quad (2.20)$$

and the interaction-picture density matrix

$$\hat{\rho}_{\text{I}}(t) \equiv U_{\text{I}}(t, t_0) \hat{\rho}(t_0) U_{\text{I}}^\dagger(t, t_0) \quad (2.21)$$

can be introduced. Here, the Schrödinger operator $\hat{A}(t)$ of Eq. (2.3) is allowed to depend explicitly on time. The interaction-picture time evolution operator $U_{\text{I}}(t, t_0) \equiv U_0^\dagger(t, t_0) U(t, t_0)$ is a product of

$$U_0(t, t_0) = e^{-\frac{i}{\hbar} \hat{H}_0(t-t_0)} \quad \text{and} \quad U(t, t_0) = \exp_{\leftarrow} \left[\int_{t_0}^t d\tau \hat{H}(\tau) \right]. \quad (2.22)$$

The Liouville–von Neumann equation is accordingly translated into the interaction picture:

$$\frac{\partial}{\partial t} \hat{\rho}_I(t) = -\frac{i}{\hbar} \left[\hat{H}_I(t), \hat{\rho}_I(t) \right]_- \quad (2.23)$$

with the interaction-picture system-reservoir coupling Hamiltonian

$$\hat{H}_I(t) \equiv U_0^\dagger(t, t_0) \hat{H}_{S-B}(t) U_0(t, t_0). \quad (2.24)$$

Integrating Eq. (2.23) yields

$$\hat{\rho}_I(t) = \hat{\rho}_I(0) - \frac{i}{\hbar} \int_0^t ds \left[\hat{H}_I(s), \hat{\rho}_I(s) \right]_- . \quad (2.25)$$

The initial time t_0 has been arbitrarily set to 0. Inserting this back into Eq. (2.23) and taking the partial trace over the reservoir degrees of freedom leads to the integro-differential equation

$$\frac{\partial}{\partial t} \hat{\rho}_S(t) = -\frac{1}{\hbar^2} \int_0^t ds \operatorname{tr}_B \left[\hat{H}_I(t), \left[\hat{H}_I(s), \hat{\rho}_I(s) \right]_- \right]_- , \quad (2.26)$$

where the reduced system density matrix $\hat{\rho}_S \equiv \operatorname{tr}_B [\hat{\rho}_I]$ has been introduced and it was assumed $\operatorname{tr}_B \left[\hat{H}_I(t), \hat{\rho}_I(t_0) \right]_- = 0$ [Bre02].

As a next step, a Born approximation is performed where the reservoir-system coupling is assumed to be weak, such that the full system density matrix is approximated by a tensor product $\hat{\rho}_I(s) \approx \hat{\rho}_S(s) \otimes \hat{\rho}_B$ with a time-independent reservoir density matrix $\hat{\rho}_B$.

According to Eq. (2.26), the system state at time t depends on all previous times. Within the Markov approximation, $\hat{\rho}_S(s)$ is replaced by $\hat{\rho}_S(t)$, leading to the time-local Redfield master equation [Red57, Bre02]

$$\frac{\partial}{\partial t} \hat{\rho}_S(t) = -\frac{1}{\hbar^2} \int_0^t ds \operatorname{tr}_B \left[\hat{H}_I(t), \left[\hat{H}_I(s), \hat{\rho}_S(t) \otimes \hat{\rho}_B \right]_- \right]_- . \quad (2.27)$$

To obtain a Markovian master equation, the integration variable s is substituted by $t-s$, leaving the integration boundaries unchanged. s then parametrizes how far back in time memory effects are accounted for. Let τ_B be a characteristic timescale for the decay of bath correlations. In Markov approximation, this timescale is very small (and not resolved), such that the integrand vanishes very quickly for $s \gg \tau_B$ and the upper integration boundary can be sent to infinity:

$$\frac{\partial}{\partial t} \hat{\rho}_S(t) = -\frac{1}{\hbar^2} \int_0^\infty ds \operatorname{tr}_B \left[\hat{H}_I(t), \left[\hat{H}_I(t-s), \hat{\rho}_S(t) \otimes \hat{\rho}_B \right]_- \right]_- . \quad (2.28)$$

This is the quantum master equation in Born-Markov approximation.

2.2 Solid-state Hamilton operator

The many-particle solid-state Hamilton operator \hat{H}^s is derived using an adiabatic (or Born-Oppenheimer) approximation, where the lattice dynamics is separated from the electron dynamics [Hak73, Czy04]. The electronic system is assumed to follow the motion of the cores instantaneously, since the latter takes place on a much slower time scale due to the large core masses. The Hamiltonian in first quantization contains electronic (e) and ionic (i) parts and their interaction correcting for the Born-Oppenheimer approximation:

$$\hat{H}^s = \hat{H}_e + \hat{H}_i + \hat{H}_{e-i}. \quad (2.29)$$

2.2.1 Electronic and free radiation part and electron-photon interaction

The electronic part \hat{H}_e incorporates the interaction with an electromagnetic field assuming minimal coupling. Within the effective mass approximation, a modified electron mass m_e is introduced to account for the interaction of the electrons with the static field of the ions [Coh92]:

$$\hat{H}_e = \sum_{j=1}^{N_e} \frac{(\mathbf{p}_j - e\mathbf{A}_\perp(\mathbf{r}_j, t))^2}{2m_e} + \frac{e^2}{4\pi\epsilon_0\epsilon_r} \sum_{i<j} \frac{1}{|\mathbf{r}_i - \mathbf{r}_j|} + \frac{1}{2} \int d^3r \left\{ \epsilon_0 \mathbf{E}_\perp^2(\mathbf{r}, t) + \frac{1}{\mu_0} \mathbf{B}^2(\mathbf{r}, t) \right\}. \quad (2.30)$$

The electromagnetic field in Coulomb gauge is quantized according to [Coh92, Hak73]:

$$\mathbf{A}_\perp(\mathbf{r}, t) = \sum_{l, \mathbf{q}} \sqrt{\frac{\hbar}{2\epsilon_0\omega_q V}} \left(\mathbf{e}_{l, \mathbf{q}} e^{i\mathbf{q} \cdot \mathbf{r}} \hat{c}_{l, \mathbf{q}}(t) + \mathbf{e}_{l, \mathbf{q}} e^{-i\mathbf{q} \cdot \mathbf{r}} \hat{c}_{l, \mathbf{q}}^\dagger(t) \right) \quad (2.31)$$

with wave vector \mathbf{q} , frequency $\omega_q = cq$, quantization volume V , polarization vector $\mathbf{e}_{l, \mathbf{q}}$, and photon mode l . The photonic creation ($\hat{c}_{l, \mathbf{q}}^\dagger$) and annihilation ($\hat{c}_{l, \mathbf{q}}$) operators satisfy the bosonic commutation relations:

$$[\hat{c}_{l, \mathbf{q}}, \hat{c}_{l', \mathbf{q}'}^\dagger]_- = \delta_{\mathbf{q}, \mathbf{q}'} \delta_{l, l'}, \quad [\hat{c}_{l, \mathbf{q}}, \hat{c}_{l', \mathbf{q}'}^\dagger]_- = 0. \quad (2.32)$$

The nanostructures considered in this work are small compared to the wavelength of the radiation field, such that the vector potential is assumed to be spatially invariant over the sample size: $\mathbf{A}_\perp(\mathbf{r}, t) \approx \mathbf{A}_\perp(\mathbf{0}, t)$ (long-wavelength approximation). In order to express the atom-field interaction in terms of an electric dipole coupling between the radiation field and the atomic dipole moment $\mathbf{d} = \sum_j e\mathbf{r}_j$, a unitary transformation (Göppert-Mayer transformation [Göp31])

$$\hat{T} = \exp\left[-\frac{i}{\hbar} \mathbf{d} \cdot \mathbf{A}_\perp(\mathbf{0}, t)\right] \quad (2.33)$$

is applied to the full Hamiltonian according to $\hat{H}'_e = \hat{T} \hat{H}_e \hat{T}^\dagger$, yielding [Coh92]

$$\hat{H}'_e = \sum_{j=1}^{N_e} \frac{\mathbf{p}_j^2}{2m_e} - \mathbf{d} \cdot \sum_{l, \mathbf{q}} (\mathcal{E}_{l, \mathbf{q}} \hat{c}_{l, \mathbf{q}} - \mathcal{E}_{l, \mathbf{q}}^* \hat{c}_{l, \mathbf{q}}^\dagger) + \frac{e^2}{4\pi\epsilon_0\epsilon_r} \sum_{i<j} \frac{1}{|\mathbf{r}_i - \mathbf{r}_j|} + \sum_{l, \mathbf{q}} \hbar\omega_q \hat{c}_{l, \mathbf{q}}^\dagger \hat{c}_{l, \mathbf{q}} \quad (2.34)$$

with

$$\mathcal{E}_{l, \mathbf{q}} \equiv i \sqrt{\frac{\hbar\omega_q}{2\epsilon_0 V}} \mathbf{e}_{l, \mathbf{q}}. \quad (2.35)$$

The electronic system is also quantized by introducing Heisenberg field operators for electrons with wave vector \mathbf{k} in band $\lambda \in \{c, v\}$

$$\hat{\Psi}_s^{(\dagger)}(\mathbf{r}) = \sum_{\lambda, \mathbf{k}} \psi_{\lambda, \mathbf{k}}^{(*)}(\mathbf{r}) \hat{a}_{\lambda, \mathbf{k}}^{(\dagger)}. \quad (2.36)$$

The electronic annihilation (creation) operators $\hat{a}_{\lambda, \mathbf{k}}^{(\dagger)}$ fulfill the fermionic commutation relations:

$$[\hat{a}_{\lambda, \mathbf{k}}, \hat{a}_{\lambda', \mathbf{k}'}^\dagger]_+ = \delta_{\mathbf{k}, \mathbf{k}'} \delta_{\lambda, \lambda'}, \quad [\hat{a}_{\lambda, \mathbf{k}}, \hat{a}_{\lambda', \mathbf{k}'}^\dagger]_+ = 0. \quad (2.37)$$

This leads to the Hamiltonian in second quantization consisting of a interaction-free electron part \hat{H}_{el}^s , a free radiation part \hat{H}_{pt}^s , a Coulomb part \hat{H}_C^s , and an electron-photon interaction Hamiltonian $\hat{H}_{\text{el-pt}}^s$:

$$\hat{H}_e = \int d^3r \hat{\Psi}_s^\dagger(\mathbf{r}) \hat{H}'_e \hat{\Psi}_s(\mathbf{r}) = \hat{H}_{\text{el}}^s + \hat{H}_{\text{pt}}^s + \hat{H}_C^s + \hat{H}_{\text{el-pt}}^s \quad (2.38)$$

$$\begin{aligned}
&= \sum_{\lambda, \mathbf{k}} \varepsilon_{\lambda, \mathbf{k}} \hat{a}_{\lambda, \mathbf{k}}^\dagger \hat{a}_{\lambda, \mathbf{k}} + \sum_{l, \mathbf{q}} \hbar \omega_{\mathbf{q}} \hat{c}_{l, \mathbf{q}}^\dagger \hat{c}_{l, \mathbf{q}} + \frac{e^2}{4\pi\epsilon_0\epsilon_r} \sum_{i < j} \frac{1}{|\mathbf{r}_i - \mathbf{r}_j|} \\
&+ \sum_{l, \mathbf{q}} \sum_{\lambda, \lambda', \mathbf{k}, \mathbf{k}'} (M_{l, \mathbf{q}}^{\lambda\lambda', \mathbf{k}\mathbf{k}'} \hat{c}_{l, \mathbf{q}} \hat{a}_{\lambda, \mathbf{k}}^\dagger \hat{a}_{\lambda', \mathbf{k}'} + M_{l, \mathbf{q}}^{\lambda\lambda', \mathbf{k}\mathbf{k}'*} \hat{c}_{l, \mathbf{q}}^\dagger \hat{a}_{\lambda', \mathbf{k}'}^\dagger \hat{a}_{\lambda, \mathbf{k}})
\end{aligned} \tag{2.39}$$

The electron-photon coupling matrix element is given as

$$M_{l, \mathbf{q}}^{\lambda\lambda', \mathbf{k}\mathbf{k}'} \equiv \int d^3r \psi_{\lambda, \mathbf{k}}^*(\mathbf{r}) e \mathbf{r} \cdot \boldsymbol{\mathcal{E}}_{l, \mathbf{q}} \psi_{\lambda', \mathbf{k}'}(\mathbf{r}). \tag{2.40}$$

The treatment is usually restricted to interband processes with $\lambda \neq \lambda'$ neglecting intraband processes with $\lambda = \lambda'$.

The external light field applied in typical optical experiments (such as photoluminescence (PL) measurements) can usually be described using a semiclassical approach, where the incoming laser light is treated as classical electromagnetic field $\mathbf{E}(t)$ and only the Schrödinger field of the electrons is quantized. The Hamiltonian in dipole approximation takes the form:

$$\hat{H}_{\text{el-L}} = - \sum_{\mathbf{k}, \mathbf{k}'} \mathbf{d}_{\text{cv}}^{\mathbf{k}\mathbf{k}'} \cdot \mathbf{E}(t) \hat{a}_{\text{c}, \mathbf{k}}^\dagger \hat{a}_{\text{v}, \mathbf{k}'} + h.c. \tag{2.41}$$

For semiconductor nanostructures where the electronic wave function $\psi_{\lambda, \mathbf{k}}(\mathbf{r}) = \xi_{\lambda, \mathbf{k}}(\mathbf{r}) u_{\lambda, \mathbf{k}}(\mathbf{r})$ can be factorized into an envelope part $\xi_{\lambda, \mathbf{k}}$ and a Bloch part $u_{\lambda, \mathbf{k}}$, the transition matrix element $\mathbf{d}_{\text{cv}}^{\mathbf{k}\mathbf{k}'}$ is given as product of the microscopic interband dipole moment $\mathbf{d}_{\lambda\lambda'} \equiv \int_{\text{uc}} d^3\tilde{r} u_{\lambda, \mathbf{k}\approx\mathbf{0}}^*(\tilde{\mathbf{r}}) e \tilde{\mathbf{r}} u_{\lambda', \mathbf{k}\approx\mathbf{0}}(\tilde{\mathbf{r}})$ and the overlap integral of the envelope functions for the valence and conduction bands, $\chi_{\lambda\lambda'}^{\mathbf{k}, \mathbf{k}'} = \int d^3r \xi_{\lambda, \mathbf{k}}^*(\mathbf{r}) \xi_{\lambda', \mathbf{k}'}(\mathbf{r})$.

2.2.2 Ionic part and electron–phonon interaction

The ionic Hamiltonian \hat{H}_i comprises the kinetic energy of the ions (usually treated perturbatively) and the effective interaction between the ions, described as screened Coulomb potential between the ions (i.e., cores plus inner shells) and the outer electrons including the time-averaged adiabatic electronic potentials [Czy04, Yu05]:

$$\hat{H}_i = \sum_{n=1}^{N_{\text{uc}}} \frac{\mathbf{P}_n^2}{2M} + V_i(\{\mathbf{R}_n\}). \tag{2.42}$$

Here, \mathbf{P}_n denotes the momentum, M the mass, and \mathbf{R}_n the position of the ion in the n -th unit cell (UC). Since the treatment is restricted to acoustic phonons (as discussed later), only one basis atom per UC is considered. Assuming that the ions vibrate around their equilibrium positions $\mathbf{R}_n^{(0)} \equiv \{\mathbf{R}_n^{(0)}\}$, the positions $\mathbf{R} \equiv \{\mathbf{R}_n\}$ are expressed by $\mathbf{R}_n = \mathbf{R}_n^{(0)} + \mathbf{u}_n$, where \mathbf{u}_n describes the displacement of the ion in the n -th unit cell with respect to its equilibrium position $\mathbf{R}_n^{(0)}$. In the harmonic approximation, the potential is expanded in a Taylor series around the equilibrium positions to second order in the displacement [Mad72, Czy04, Mah00]:

$$\begin{aligned}
V_i(\mathbf{R}) \approx V_i(\mathbf{R}^{(0)}) + \sum_{n=1}^{N_{\text{uc}}} \sum_{\mu=1}^3 \underbrace{\frac{\partial V_i(\mathbf{R})}{\partial R_{n\mu}} \Big|_{\mathbf{R}^{(0)}}}_{=0} u_{n\mu} + \frac{1}{2} \sum_{n, n'=1}^{N_{\text{uc}}} \sum_{\mu, \mu'=1}^3 \underbrace{\frac{\partial^2 V_i(\mathbf{R})}{\partial R_{n\mu} \partial R_{n'\mu'}} \Big|_{\mathbf{R}^{(0)}}}_{\equiv \Phi_{n\mu}^{n'\mu'}} u_{n\mu} u_{n'\mu'}.
\end{aligned} \tag{2.43}$$

By introducing normal coordinates and diagonalizing the dynamical matrix $D_{n\mu}^{n'\mu'} \equiv \Phi_{n\mu}^{n'\mu'} / M$, the ionic motion can be expressed by a set of uncoupled harmonic oscillators representing

collective vibrations. Applying the usual quantization procedure yields quantized displacement operators

$$\hat{\mathbf{u}}_n = i \sum_{j,\mathbf{q}} \sqrt{\frac{\hbar}{2MN_{\text{uc}}\omega_{j,\mathbf{q}}}} \mathbf{e}_{j,\mathbf{q}} e^{i\mathbf{q}\cdot\mathbf{R}_n^{(0)}} (\hat{b}_{j,\mathbf{q}} + \hat{b}_{j,-\mathbf{q}}^\dagger). \quad (2.44)$$

The quantized free phonon Hamiltonian is given by

$$\hat{H}_i = \sum_{j,\mathbf{q}} \hbar\omega_{j,\mathbf{q}} \left(\hat{b}_{j,\mathbf{q}}^\dagger \hat{b}_{j,\mathbf{q}} + \frac{1}{2} \right) \quad (2.45)$$

with the bosonic annihilation (creation) operators $\hat{b}_{j,\mathbf{q}}^{(\dagger)}$ for phonon mode j with wave vector \mathbf{q} . They fulfill the commutator relations $[\hat{b}_{j,\mathbf{q}}, \hat{b}_{j',\mathbf{q}'}^\dagger]_- = \delta_{j,j'} \delta_{\mathbf{q},\mathbf{q}'}$. The free phonon Hamiltonian Eq. (2.45) is supposed to be identical for all electronic states in the semiconductor, since the vibrational modes are highly delocalized over the crystal lattice due to the translational invariance. Also, the electronic state density is usually high, such that the nuclear vibrations are hardly affected by changes in the electronic states. This changes in the case of molecules, where the concept of potential energy surfaces (PESs) is introduced in order to account for the different equilibrium positions (cf. Sec. 8.3.3).

The electron–phonon interaction Hamiltonian reads:

$$\hat{H}_{\text{e-i}} = \sum_{i=1}^{N_{\text{e}}} V_{\text{el-ph}}(\mathbf{r}_i) = \sum_{i=1}^{N_{\text{e}}} \sum_{n=1}^{N_{\text{uc}}} V_{\text{e-i}}(\mathbf{r}_i - \mathbf{R}_n). \quad (2.46)$$

Again, the interaction potential is expanded in powers of the displacements and terms in $\mathcal{O}(u^2)$ are neglected:

$$V_{\text{el-ph}}(\mathbf{r}_i) \approx \underbrace{\sum_{n=1}^{N_{\text{uc}}} V_{\text{e-i}}(\mathbf{r}_i - \mathbf{R}_n^{(0)})}_{\text{Bloch part}} - \underbrace{\sum_{n=1}^{N_{\text{uc}}} \nabla V_{\text{e-i}}(\mathbf{r}_i - \mathbf{R}_n^{(0)}) \cdot \mathbf{u}_n}_{\equiv \tilde{V}_{\text{el-ph}}(\mathbf{r}_i)} \quad (2.47)$$

The first part gives rise to Bloch states for the electronic motion in the periodic potential of the (fixed) ions. The second term describes the electron–phonon interaction. Fourier transforming the potential according to $V_{\text{e-i}}(\mathbf{r}) = 1/N_{\text{uc}} \sum_{\mathbf{Q}} V_{\text{e-i}}(\mathbf{Q}) e^{i\mathbf{Q}\cdot\mathbf{r}}$, plugging in the quantized displacement operator Eq. (2.44), and using $1/N_{\text{uc}} \sum_n e^{i(\mathbf{q}-\mathbf{Q})\cdot\mathbf{R}_n} \approx \sum_{\mathbf{G}_s} \delta_{\mathbf{q}-\mathbf{Q},\mathbf{G}_s}$ yields:

$$\tilde{V}_{\text{el-ph}}(\mathbf{r}_i) = \sum_{j,\mathbf{q},\mathbf{G}_s} \sqrt{\frac{\hbar}{2\rho V \omega_{j,\mathbf{q}}}} V_{\text{e-i}}(\mathbf{q} + \mathbf{G}_s) (\mathbf{q} + \mathbf{G}_s) \cdot \mathbf{e}_{j,\mathbf{q}} e^{i(\mathbf{q}+\mathbf{G}_s)\cdot\mathbf{r}_i} (\hat{b}_{j,\mathbf{q}} + \hat{b}_{j,-\mathbf{q}}^\dagger). \quad (2.48)$$

\mathbf{G}_s denotes a reciprocal lattice vector of the semiconductor quantum well (QW), ρ is the mass density of the solid and V the sample volume. The Schrödinger field is also quantized and the particle density operator is introduced:

$$\hat{\rho}(\mathbf{r}) = \hat{\Psi}_s^\dagger(\mathbf{r}) \hat{\Psi}_s(\mathbf{r}) = \sum_{\lambda,\lambda'} \sum_{\mathbf{k},\mathbf{k}'} \psi_{\lambda,\mathbf{k}}^*(\mathbf{r}) \psi_{\lambda',\mathbf{k}'}(\mathbf{r}) \hat{a}_{\lambda,\mathbf{k}}^\dagger \hat{a}_{\lambda',\mathbf{k}'}. \quad (2.49)$$

Note that the spin index σ is not mentioned explicitly here, since an interaction with the lattice vibrations does not affect the spin state of the electrons. The electron–phonon interaction Hamiltonian in second quantization is given by [Czy04, Mah00]:

$$\begin{aligned} \hat{H}_{\text{el-ph}}^{\text{s}} &= \int d^3r \hat{\Psi}_s^\dagger(\mathbf{r}) \tilde{V}_{\text{el-ph}}(\mathbf{r}) \hat{\Psi}_s(\mathbf{r}) \\ &= \sum_{j,\mathbf{q},\mathbf{G}_s} \sqrt{\frac{\hbar}{2\rho V \omega_{j,\mathbf{q}}}} V_{\text{e-i}}(\mathbf{q} + \mathbf{G}_s) (\mathbf{q} + \mathbf{G}_s) \cdot \mathbf{e}_{j,\mathbf{q}} \hat{\rho}(\mathbf{q} + \mathbf{G}_s) (\hat{b}_{j,\mathbf{q}} + \hat{b}_{j,-\mathbf{q}}^\dagger) \end{aligned} \quad (2.50)$$

with form factor $\hat{\rho}(\mathbf{q} + \mathbf{G}_s) = \int d^3r e^{i(\mathbf{q}+\mathbf{G}_s)\cdot\mathbf{r}} \hat{\rho}(\mathbf{r})$.

2.3 Factorization schemes

When evaluating equations of motion (EOM) of single-particle observables given as correlations of the form $\langle \hat{a}_i^\dagger \hat{a}_j \rangle$, one often faces the problem that they couple to higher order quantities, e.g., two-particle correlations $\langle \hat{a}_i^\dagger \hat{a}_j^\dagger \hat{a}_k \hat{a}_l \rangle$. To close the system of differential equations, various factorization schemes are used depending on the character of the involved operators and the expansion level. A Hartree-Fock factorization of fermionic two-particle correlations is given by [Fic90]

$$\langle \hat{a}_i^\dagger \hat{a}_j^\dagger \hat{a}_k \hat{a}_l \rangle \approx \langle \hat{a}_i^\dagger \hat{a}_l \rangle \langle \hat{a}_j^\dagger \hat{a}_k \rangle - \langle \hat{a}_i^\dagger \hat{a}_k \rangle \langle \hat{a}_j^\dagger \hat{a}_l \rangle, \quad (2.51)$$

where two-particle correlations are neglected. The bosonic analogon reads

$$\langle \hat{b}_i^\dagger \hat{b}_j^\dagger \hat{b}_k \hat{b}_l \rangle \approx \langle \hat{b}_i^\dagger \hat{b}_l \rangle \langle \hat{b}_j^\dagger \hat{b}_k \rangle + \langle \hat{b}_i^\dagger \hat{b}_k \rangle \langle \hat{b}_j^\dagger \hat{b}_l \rangle. \quad (2.52)$$

If electron-photon or electron-phonon interaction is present, also mixed (or assisted) expectation values containing both fermionic and bosonic operators such as $\langle \hat{b}_i^\dagger \hat{b}_j^\dagger \hat{A} \rangle$ can occur, where \hat{A} denotes an arbitrary combination of fermionic creation and annihilation operators. On the second-order Born level, they are factorized according to [Fic90, Sch94, Axt94, Bre02, Wal04]

$$\langle \hat{b}_i^\dagger \hat{b}_j^\dagger \hat{A} \rangle \approx \langle \hat{b}_i^\dagger \hat{b}_j^\dagger \rangle \langle \hat{A} \rangle. \quad (2.53)$$

Note that a factorization on a lower level, $\langle \hat{b}_i^{(\dagger)} \hat{A} \rangle \approx \langle \hat{b}_i^{(\dagger)} \rangle \langle \hat{A} \rangle$ is not considered here since expectation values of the form $\langle \hat{b}_i^{(\dagger)} \rangle$ vanish in the case of phonons treated as a bath in thermal equilibrium or in the case of photons in the absence of coherent electromagnetic fields.

2.4 Markov approximation

A Markov approximation is frequently used to solve linear, inhomogeneous differential equations of the form

$$i\hbar \frac{d}{dt} \langle O \rangle(t) = \hbar\omega \langle O \rangle(t) + P(t) \quad (2.54)$$

by neglecting quantum-mechanical memory effects. The formal solution of this problem is found by variation of constants:

$$\langle O \rangle(t) - \underbrace{\langle O \rangle(-\infty)}_{=0} = -\frac{i}{\hbar} \int_{-\infty}^t dt' P(t') e^{i\omega(t'-t)}. \quad (2.55)$$

The above Eq. (2.55) shows that a solution for a particular time t depends on all previous times t' and therefore has a memory.

Substituting $s = t - t'$ leads to

$$\langle O \rangle(t) = \frac{i}{\hbar} \int_{-\infty}^0 ds P(t-s) e^{-i\omega s} = -\frac{i}{\hbar} \int_0^{\infty} ds P(t-s) e^{-i\omega s}. \quad (2.56)$$

Provided that the inhomogeneity (function with time argument $(t-s)$) temporally varies much slower than the oscillation resulting from the exponential function determined by the free

energy of the considered quantity, it is valid to neglect the memory kernel by approximating $P(t-s) \approx P(t)$ and move $P(t)$ outside the integral:

$$\langle O \rangle(t) = -\frac{i}{\hbar} P(t) \underbrace{\int_0^{\infty} ds e^{-i\omega s}}_{=\zeta(\omega)}. \quad (2.57)$$

$\zeta(\omega)$ is the generalized δ function (Heitler Zeta function) [Cho12]. It is evaluated by introducing a convergence factor γ :

$$\zeta(\omega) = \lim_{\gamma \rightarrow 0} \int_0^{\infty} ds e^{-(i\omega + \gamma)s} = \lim_{\gamma \rightarrow 0} \frac{1}{i\omega + \gamma} = \pi\delta(\omega) - i\mathcal{P}\left(\frac{1}{\omega}\right), \quad (2.58)$$

where \mathcal{P} denotes the Cauchy principal value and the δ function ensures energy conservation. Usually, the principal value is neglected and only the delta function for the free energy is taken into account, such that the differential equation is solved in Markov approximation according to:

$$\langle O \rangle(t) = -\frac{i}{\hbar} \pi\delta(\omega) P(t). \quad (2.59)$$

In many physical contexts, the inhomogeneity $P(t-s)$ contains fast oscillations, e.g., stemming from the free energy of polarizations of the form $\langle \hat{a}_i^\dagger \hat{a}_j \rangle$. Consequently, the Markov approximation introduced above is not directly applicable. In these cases, a rotating frame is introduced by separating the fast oscillating part from the slowly varying function $\tilde{P}(t-s)$:

$$P(t-s) = \tilde{P}(t-s) e^{-i\omega_P(t-s)}. \quad (2.60)$$

The memory of $\tilde{P}(t-s)$ is neglected setting $P(t-s) \approx \tilde{P}(t) e^{-i\omega_P(t-s)}$. Plugging this into Eq. (2.56) yields

$$\langle O \rangle(t) = -\frac{i}{\hbar} \underbrace{\tilde{P}(t) e^{-i\omega_P t}}_{=P(t)} \int_0^{\infty} ds e^{-i\omega s} e^{i\omega_P s} = -\frac{i}{\hbar} P(t) \int_0^{\infty} ds e^{-i(\omega - \omega_P)s} \quad (2.61)$$

The solution in Markov approximation is then given by:

$$\langle O \rangle(t) = -\frac{i}{\hbar} \pi\delta(\omega - \omega_P) P(t). \quad (2.62)$$

2.5 Feynman disentanglement theorem for time-ordered operators

Let an operator $\hat{U}(t, t_0)$ be given by a time-ordered exponential of the form

$$\hat{U}(t, t_0) = \exp_{\leftarrow} \left[\int_{t_0}^t d\tau (\hat{A}_1(\tau) + \hat{A}_2(\tau)) \right] \quad (2.63)$$

with arbitrary operators $\hat{A}_1(\tau)$ and $\hat{A}_2(\tau)$. According to the Feynman disentanglement theorem [Fey51], this operator can be decomposed into

$$\hat{U}(t, t_0) = \hat{U}_1(t, t_0) \hat{U}_2(t, t_0) \quad (2.64)$$

with

$$\hat{U}_1(t, t_0) = \exp_{\leftarrow} \left[\int_{t_0}^t d\tau \hat{A}_1(\tau) \right], \quad (2.65)$$

$$\hat{U}_2(t, t_0) = \exp_{\leftarrow} \left[\int_{t_0}^t d\tau \hat{U}_1(t_0, \tau) \hat{A}_2(\tau) \hat{U}_1(\tau, t_0) \right]. \quad (2.66)$$

3

Coherent multidimensional spectroscopy

3.1 Introduction

Nonlinear optical spectroscopy in its various experimental realizations is a powerful tool to study the dynamics, energies, and microscopic couplings of higher excitonic states in semiconductor nanostructures. In nuclear magnetic resonance experiments, multidimensional frequency space spectra are acquired by Fourier transforming temporal sequences of radio frequency pulses [Wüt03, Van05]. The remarkable technical progress in femtosecond pulse-shaping allows to extend multidimensional spectroscopy techniques to optical frequencies: Ultrafast sequences of short pulses with precisely tuned durations and time intervals as well as defined frequencies, wave vectors, phases, envelopes, and polarizations are applied to the sample [Gal98, Muk00, Wei09]. This work focuses on four-wave mixing (FWM) spectroscopy probing the optical response of a system in third order of the electric field, the so-called $\chi^{(3)}$ regime. In particular, multidimensional coherent spectroscopy techniques allow a detailed insight into the dynamical and structural properties by spreading the spectroscopic signal into (at least) two dimensions [Muk95, Muk00, Gal98, Tia03, Jon03, Axt04, Lan07, Yan08, Cho08, Kar10, Lan10, Fin12, Nar15, Kre15].

One-dimensional (1D) spectroscopy techniques such as linear absorption, photoluminescence, and Raman, probe the energies and oscillator strengths of the system resonances. However, complex nanostructured materials exhibit highly interlaced levels and couplings which often remain unresolved in standard 1D optical experiments. Also, inhomogeneous broadening can mask detailed spectral features in the optical response if the signal is projected onto a single frequency axis. Coherent two-dimensional (2D) spectroscopy offers an additional degree of freedom in terms of the additional frequency axis in order to disentangle the complex optical signal [Muk00]. Moreover, a specific excitation configuration can be selected, thus reducing the number of quantum pathways contributing to the signal, which can be used, e.g., to eliminate inhomogeneous broadening [Kuz07, Sie10], cf. Chap. 5. Also, while 1D spectra show the energetic positions of the system resonances, only two-dimensional spectroscopy techniques allow to determine whether two specific transitions are fully independent or coupled [Lan07, Moo13a, Moo14, Fin13, Spe15, Del17]. This way, 2D spectroscopy is a powerful technique to study many-body effects in quantum systems such as semiconductor quantum wells (QWs) [Sto09, Kar10, Tur10, Moo14] as well as ensembles of quantum dots (QDs) [Moo13a, Moo13b] and nanocrystals [Cas16].

In this chapter, the theoretical treatment of heterodyne-detected coherent multidimensional spectroscopy is demonstrated. First, the setup of a typical FWM experiment with heterodyne detection is briefly illustrated in Sec. 3.2. Then, in Sec. 3.3.1, the third-order polarization and response function are derived based on the density matrix formalism introduced in Sec. 2.1. Two different signals are discussed in the later chapters of this work, namely the double quantum coherence (DQC) and the photon echo (PE) signal, corresponding to different Liouville space

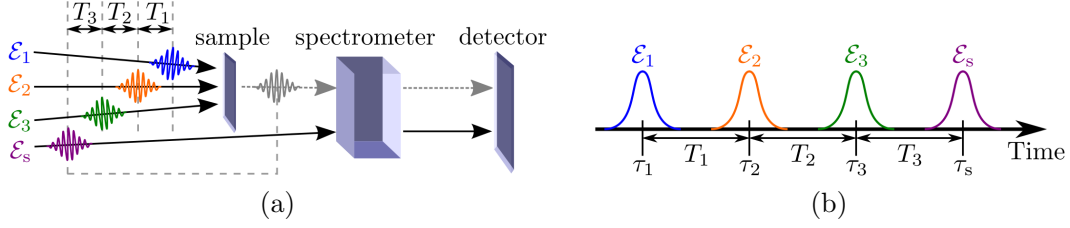


Figure 3.1: (a) Sketch of a typical FWM experiment with three incoming laser pulses \mathcal{E}_1 , \mathcal{E}_2 , and \mathcal{E}_3 and a local oscillator field \mathcal{E}_s that mixes with the signal field for heterodyne detection. (b) Timeline for the pulse sequence applied in a heterodyne-detected FWM experiment.

pathways. They are visualized using the so-called double-sided Feynman diagrams representing the evolution of the density matrix illustrated in Sec. 3.3.2 for the DQC case. Finally, the DQC signal function is derived in Sec. 3.3.3 and the phase cycling technique is briefly discussed in Sec. 3.3.4.

3.2 Four-wave mixing spectroscopy

3.2.1 Experimental setup

In a FWM experiment, a sequence of three temporally separated pulses centered at times τ_1 , τ_2 , and τ_3 is applied to the sample, cf. Fig. 3.1 (b). The interaction-free time intervals between two subsequent pulses are denoted T_1 and T_2 , as illustrated in Fig. 3.1 (b). The time ordering of the pulses can be controlled by varying the delay times between them.¹

The total optical field applied to the system is therefore composed of three pulses

$$\mathbf{E}(\mathbf{r}, t) = \sum_{j=1}^3 \sum_{u_j=\pm 1} \mathcal{E}_j^{u_j}(\mathbf{r}, t - \tau_j) e^{iu_j(\mathbf{k}_j \cdot \mathbf{r} - \omega_j(t - \tau_j))} \quad (3.1)$$

and $\mathcal{E}_j^{u_j}(t - \tau_j)$ denotes the envelope of the j -th pulse with wave vector \mathbf{k}_j and laser frequency ω_j . The factors u_j can take the values $+1$ or -1 with $\mathcal{E}_j^{-1} = (\mathcal{E}_j^{+1})^*$. The total wave vector of a specific signal \mathbf{k}_s is then given by a linear combination of the wave vectors of the incident pulses: $\mathbf{k}_s = u_1\mathbf{k}_1 + u_2\mathbf{k}_2 + u_3\mathbf{k}_3$. This way, different signals can be separated by directional selection (induced grating). These different so-called Liouville space pathways are discussed in more detail in Sec. 3.3.2. Note that a conventional pump-probe experiment is a special case of FWM with $T_1 = 0$ and $\mathbf{k}_1 = \mathbf{k}_2$.

3.2.2 Heterodyne detection

Early nonlinear optical spectroscopy experiments were restricted to large ensemble measurements due to the bad signal-to-noise ratio that worsens with increasing order in the electric field. However, heterodyne spectral interferometry enables to measure high signal strengths even when probing single quantum systems and allows to retrieve both the amplitude and the phase of the measured signal [Muk95, Gal98, Lan05, Yan08, Abr09]. For heterodyne detection, an additional phase-locked laser pulse, the so-called local oscillator with envelope \mathcal{E}_s , is applied at time τ_s in signal field direction (cf. Fig. 3.1). It interferes with the emitted signal, and

¹ To exclude time-reverse ordered interactions with the incoming pulses and higher orders of electron-light interactions, it is assumed that the pulses have no temporal overlap and each pulse interacts once with the sample.

the resulting field is then detected. This way, real and imaginary part of the signal can be resolved. The intensity of the heterodyne pulse is much higher than the induced signal field, thus enhancing the heterodyne detected signal. It is given by a convolution of the induced polarization $\mathbf{P}_{\mathbf{k}_s}^{(3)}$ in direction \mathbf{k}_s (cf. Eq. (3.9)) with the local oscillator field (after subtracting the well-known intensity of the heterodyne field, cf. [Abr09]):

$$S_{\mathbf{k}_s}^{(3)}(T_3, T_2, T_1) = \int_{-\infty}^{+\infty} dt \mathbf{P}_{\mathbf{k}_s}^{(3)}(t) \cdot \mathcal{E}_s^*(t - \tau_s) e^{i\omega_s(t - \tau_s)}. \quad (3.2)$$

Note that the signal depends on the variable delay times T_j between the four laser pulses.

3.3 Calculation of heterodyne-detected coherent signals

3.3.1 Third-order polarization and response function

The observable of interest in non-linear optical $\chi^{(3)}$ experiments is the induced polarization in third order of the electric field. As shown in Sec. 2.1, it is given by $\mathbf{P}^{(n)}(t) = \text{tr} [\hat{\mathbf{d}} \hat{\rho}^{(n)}(t)]$. Inserting the expansion of the n -th order density operator of Eq. (2.16) yields:

$$P_{\alpha}^{(3)}(\mathbf{r}, t) = \int_0^{\infty} dt_3 \int_0^{\infty} dt_2 \int_0^{\infty} dt_1 \sum_{\beta, \gamma, \delta=1}^3 R_{\alpha\beta\gamma\delta}^{(3)}(t_3, t_2, t_1) \times E_{\beta}(\mathbf{r}, t - t_3) E_{\gamma}(\mathbf{r}, t - t_3 - t_2) E_{\delta}(\mathbf{r}, t - t_3 - t_2 - t_1) \quad (3.3)$$

with the third order response function

$$R_{\alpha\beta\gamma\delta}^{(3)}(t_3, t_2, t_1) = \left(\frac{i}{\hbar}\right)^3 \text{tr} \left[\hat{\mathbf{d}}_{\alpha} \mathcal{G}(t_3) \mathcal{D}_{\beta} \mathcal{G}(t_2) \mathcal{D}_{\gamma} \mathcal{G}(t_1) \mathcal{D}_{\delta} \hat{\rho}(-\infty) \right]. \quad (3.4)$$

Eq. (3.4) contains the three subsequent interactions of the system with the incoming fields. t_1 , t_2 , and t_3 denote the intervals between the interaction processes that are described by the dipole superoperators \mathcal{D} with $\mathcal{D} \equiv [\hat{\mathbf{d}}, \cdot]$. During the time intervals t_j , the system density matrix experiences a free propagation represented by the Green's operators $\mathcal{G}(t_j)$. The time ordering of the interactions is depicted in Fig. 3.2 (a).

Note that the optical response of Eq. (3.3) contains in principle $3^3 = 27$ contributions stemming from the three interactions with the light field composed of three pulses. However, assuming a temporal separation of the pulses, one is left with four independent wave vector combinations contributing to the response function in third order of the electric field:

$$\mathbf{k}_I = -\mathbf{k}_1 + \mathbf{k}_2 + \mathbf{k}_3, \quad (3.5)$$

$$\mathbf{k}_{II} = +\mathbf{k}_1 - \mathbf{k}_2 + \mathbf{k}_3, \quad (3.6)$$

$$\mathbf{k}_{III} = +\mathbf{k}_1 + \mathbf{k}_2 - \mathbf{k}_3, \quad (3.7)$$

$$\mathbf{k}_{IV} = +\mathbf{k}_1 + \mathbf{k}_2 + \mathbf{k}_3. \quad (3.8)$$

The fast oscillating \mathbf{k}_{IV} signal is usually neglected within the rotating wave approximation. The remaining signal vectors are graphically illustrated in Fig. 3.2 (c). The detected wave vector combination can be extracted from the full signal using

$$\mathbf{P}^{(3)}(\mathbf{r}, t) = \sum_{\mathbf{k}_s} \mathbf{P}_{\mathbf{k}_s}(\mathbf{r}, t) e^{i\mathbf{k}_s \cdot \mathbf{r}}. \quad (3.9)$$

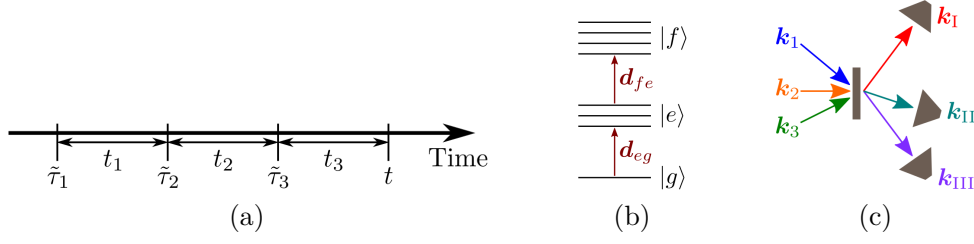


Figure 3.2: (a) Timeline for the successive interactions in a FWM experiment. (b) Level scheme of the three-band model consisting of the ground state $|g\rangle$ and the excited state manifolds $|e\rangle$ (singly excited) and $|f\rangle$ (doubly excited). The manifolds are connected by the dipole transitions d_{eg} and d_{fe} . (c) Wave vector combinations that can be extracted from the experiment by direction selection of the signal. They form the distinct Liouville space pathways.

The sum refers to the possible values of $u_j = \pm 1$. Plugging the expression for the electrical field Eq. (3.1) into Eq. (3.3), substituting Eq. (3.9), and reordering the terms leads to [Abr09]

$$\begin{aligned}
(P_{\mathbf{k}_s}^{(3)})_{\alpha}(\mathbf{r}, t) &= e^{-i\omega_s(t-\tau_3) - i(u_2\omega_2 + u_1\omega_1)(\tau_3 - \tau_2) - iu_1\omega_1(\tau_2 - \tau_1)} \int_0^{\infty} dt_3 \int_0^{\infty} dt_2 \int_0^{\infty} dt_1 \\
&\times \sum_{\beta, \gamma, \delta=1}^3 R_{\alpha\beta\gamma\delta}^{(3)}(t_3, t_2, t_1) e^{i\omega_s t_3 + i(u_2\omega_2 + u_1\omega_1)t_2 + iu_1\omega_1 t_1} \\
&\times \mathcal{E}_{3\beta}^{u_3}(\mathbf{r}, t - t_3 - \tau_3) \mathcal{E}_{2\gamma}^{u_2}(\mathbf{r}, t - t_3 - t_2 - \tau_2) \mathcal{E}_{1\delta}^{u_1}(\mathbf{r}, t - t_3 - t_2 - t_1 - \tau_1).
\end{aligned} \tag{3.10}$$

$\omega_s = u_1\omega_1 + u_2\omega_2 + u_3\omega_3$ is the signal frequency.

3.3.2 Liouville space pathways and double-sided Feynman diagrams

Double-sided Feynman diagrams [Muk95] allow a direct graphical representation of the temporal evolution of the density matrix when applying the pulse sequence. They enable a diagrammatic understanding of the different excitation pathways contributing to the full signal measured along a specific direction given by the wave vector combinations of Eqs. (3.5), (3.6), (3.7), and (3.8). They are called *Liouville space pathways*. Therefore, learning how to read this type of diagram greatly simplifies the understanding and interpretation of the 2D signals and the underlying excitation pathways. As an example, Fig. 3.3 shows the double-sided Feynman diagrams belonging to the DQC k_{III} signal, which is treated in Chap. 4 of this thesis.

The diagrams are constructed in the following way [Abr09]:

- The letters g , e , and f denote the ground state and the singly and doubly excited state manifolds that are involved in $\chi^{(3)}$ measurements where a maximum of two excitations in the system is achieved. The corresponding three-band model is shown in Fig. 3.2 (b).
- The density matrix is illustrated by the two vertical lines. The left line represents the *ket*, the right line the *bra* state of the density operator.
- The *ket* and *bra* labels indicate the state of the density matrix during the intervals t_j between two subsequent light-matter interactions.
- Time flows from bottom to top. The system always starts in the ground state $\hat{\rho}(t_0) = |g\rangle\langle g|$.
- Each interaction with the light field is indicated by a wavy arrow that begins or ends at a vertex of the diagram.

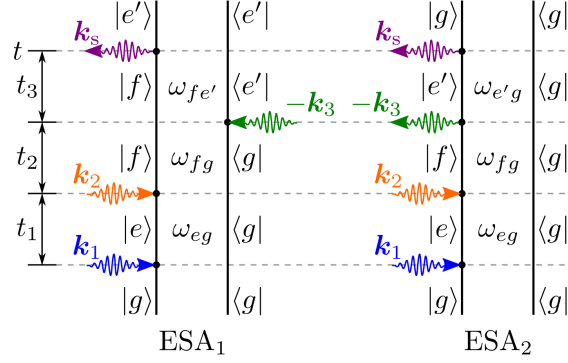


Figure 3.3: Feynman diagrams representing the Liouville space pathways of the density matrix that contribute to the **DQC** signal $\mathbf{k}_{\text{III}} = \mathbf{k}_1 + \mathbf{k}_2 - \mathbf{k}_3$.

- A wavy arrow pointing to the right (left) represents an interaction with a field component of positive (negative) frequency \mathcal{E}_j (\mathcal{E}_j^*).
- Incoming (outgoing) arrows indicate a photon absorption (emission) that comes along with a transition to a higher (lower) excitonic state of the density matrix. Each absorption and emission process is described by a transition dipole moment \mathbf{d}_{ab} .
- If the system is in a coherence, the corresponding oscillation frequency $\omega_{ab} = \frac{1}{\hbar}(\lambda_a - \lambda_b)$ is written in between the two vertical lines.
- The final arrow labeled \mathbf{k}_s marks the outgoing signal field and points to the left.
- The global sign for a specific Liouville space pathway is $(-1)^n$ with n being the number of light-field interactions along the right line, and each third-order pathway is multiplied by a factor $\left(\frac{i}{\hbar}\right)^3$.

All possible excitation pathways belonging to a specific wave vector combination can be constructed this way, and the corresponding third-order response functions can be directly read out from the diagrams.

3.3.3 Double quantum coherence signal

The **DQC** signal detected in the $\mathbf{k}_{\text{III}} = \mathbf{k}_1 + \mathbf{k}_2 - \mathbf{k}_3$ direction is composed of two excited state absorption (ESA) pathways (cf. Fig. 3.3), both of them involving the doubly excited state manifold. The **DQC** signal in frequency domain is obtained by Fourier transforming the signal function with respect to (at least) two of the three pulse delay times. Often, the first two intervals T_1 and T_2 are chosen, since they describe the single coherence time with an $e \leftrightarrow g$ coherence and the double coherence time with a $f \leftrightarrow g$ coherence (identical for both pathways), giving the technique its name. The signal is the sum of the two **ESA** contributions:

$$S_{\text{DQC}}^{(3)}(T_3, \Omega_2, \Omega_1) = S_{\text{ESA}_1}^{(3)}(T_3, \Omega_2, \Omega_1) + S_{\text{ESA}_2}^{(3)}(T_3, \Omega_2, \Omega_1). \quad (3.11)$$

The heterodyned signals for the distinct pathways are calculated according to Eq. (3.2). The response functions entering the third-order polarization given in Eq. (3.10) can be directly read out from the Feynman diagrams following the recipe detailed in Sec. 3.3.2. This procedure is presented in detail for the so-called rephasing or **photon echo** \mathbf{k}_1 signal in App. A. The two

ESA pathways contributing to the DQC \mathbf{k}_{III} signal are calculated analogously, yielding:

$$S_{\text{ESA}_1}^{(3)}(T_3, \Omega_2, \Omega_1) = -i \frac{(2\pi)^4}{\hbar^3} \sum_{e, e', f} (\mathbf{d}_{f e'}^* \cdot \mathcal{E}_s^*(\omega_{f e'} - \omega_s)) (\mathbf{d}_{e' g}^* \cdot \mathcal{E}_3^*(\omega_{e' g} - \omega_3)) e^{-i\xi_{f e'} T_3} \\ \times \frac{\mathbf{d}_{f e} \cdot \mathcal{E}_2(\omega_{f e} - \omega_2)}{\Omega_2 - \xi_{f g}} \frac{\mathbf{d}_{e g} \cdot \mathcal{E}_1(\omega_{e g} - \omega_1)}{\Omega_1 - \xi_{e g}}, \quad (3.12)$$

$$S_{\text{ESA}_2}^{(3)}(T_3, \Omega_2, \Omega_1) = i \frac{(2\pi)^4}{\hbar^3} \sum_{e, e', f} (\mathbf{d}_{e' g}^* \cdot \mathcal{E}_s^*(\omega_{e' g} - \omega_s)) (\mathbf{d}_{f e'}^* \cdot \mathcal{E}_3^*(\omega_{f e'} - \omega_3)) e^{-i\xi_{e' g} T_3} \\ \times \frac{\mathbf{d}_{f e} \cdot \mathcal{E}_2(\omega_{f e} - \omega_2)}{\Omega_2 - \xi_{f g}} \frac{\mathbf{d}_{e g} \cdot \mathcal{E}_1(\omega_{e g} - \omega_1)}{\Omega_1 - \xi_{e g}}. \quad (3.13)$$

$\mathbf{d}_{ab} = \mathbf{d}_{ba}^* = \langle a | \hat{\mathbf{d}} | b \rangle$ denotes the dipole moment in the basis of the (potentially delocalized) exciton states, ω_{ab} the resonance frequency and γ_{ab} the homogeneous broadening of the $b \rightarrow a$ transition. $\xi_{ab} \equiv \omega_{ab} - i\gamma_{ab}$ was introduced as a complex transition frequency including dephasing. Having derived the signal functions for the contributing pathways, it is now possible to calculate 2D maps of the DQC signal depending on the Fourier transformed pulse delays.

In the *impulsive limit*, the exciting laser pulses are short compared to the timescale of any material dynamics. Hence, the pulse bandwidth is large compared to the exciton bandwidth and one can set $\mathcal{E}_j(\omega) = 1$. However, bandwidth limitations of the exciting pulses can play a role if a broad energy range is covered, cf. Chaps. 5 and 6.

The Feynman diagrams allow a straightforward interpretation of the underlying physical processes: After the arrival of the first pulse, the density matrix in both ESA pathways is in a coherence between the ground state g and a single exciton state e , oscillating at an optical frequency ω_{eg} during the time interval t_1 . The second pulse creates a coherence between the ground state and a two-exciton state f . The third laser pulse \mathbf{k}_3 acts differently in the two pathways: It generates a $|f\rangle\langle e'|$ coherence in pathway 1 and a $|e'\rangle\langle g|$ coherence in pathway 2. The last, outgoing pulse \mathbf{k}_{III} represents the signal field.

3.3.4 Phase cycling

The directional selection of the signal field by varying the directions of the ingoing laser pulses through spatial separation is only possible for spatially extended systems. However, if single nanostructures of sizes smaller than the wavelength are probed, the emitted signal from an individual state is in general isotropic. In this case, the excitation pathways can be controlled using *phase cycling* [Sei95, Mey00, Tia03, Bri10, Muk11]. Here, it is used that all pulses have a defined phase, such that the total applied field is given by

$$\mathbf{E}(\mathbf{r}, t) = \sum_{j=1}^3 \sum_{u_j=\pm 1} \mathcal{E}_j^{u_j}(\mathbf{r}, t - \tau_j) e^{-iu_j\omega_j(t-\tau_j) + iu_j\varphi_j} \quad (3.14)$$

and the detected signal phase combination is

$$\varphi_s = u_1\varphi_1 + u_2\varphi_2 + u_3\varphi_3 \quad (3.15)$$

with $u_j = \pm 1$. The experiment is conducted several times with varying phase relations between the applied collinear pulses. Finally, a system of linear equations can be solved by matrix inversion and the desired phase contribution can be extracted. The signals obtained via phase cycling are derived in complete analogy to the signals presented earlier in this chapter, but with phases φ_j instead of wave vector products $\mathbf{k}_j \cdot \mathbf{r}$.

Part II

Multidimensional spectroscopy of semiconductor nanostructures

4

Probing spin-dependent exciton wave functions of coupled quantum emitters with localized 2D spectra

4.1 Introduction

In quantum theory, microscopic couplings between quantum emitters are modeled in order to predict macroscopic observables such as polarizations that are experimentally probed in optical spectra. The microscopic key ingredients for theory such as wave functions or (reduced) density matrices that characterize the quantum state of nanoscaled systems are in most cases not accessible in experiments [Ger10]. Quantum state tomography therefore aims at the development of techniques to infer the quantum state of a nanostructured material from measurements [Fan57, Gal68, Ban70, Woo86, Fre98, Ste10]. The information on the wave function gained by retrieving the quantum state of a system can then be used to derive further properties of the system, e.g., magnetic moments and transport properties [Ric12].

A research focus in the design of optoelectronic devices lies in optically active nanostructured materials that are composed of several quantum emitters in close vicinity. As a consequence, collective optical excitations due to (Coulomb) couplings between the individual constituents arise. For example, dipole-dipole coupling between quantum emitters leads to the formation of hybridized excitonic states that are potentially delocalized over the whole structure [Gue02, Lov03, Ger05, Eng07, Chr10, Sch12, Ber03]. Typical examples of such nanomaterials are quantum dot (QD) molecules [Lov03, Dan06, Del17], proteins and pigments in light-harvesting complexes [Eng07, Ric07, Chr10], plasmon lasers [Ber03, Nog09], and hybrid materials [Vas08, Mal11].

Experimental methods applying optical far-field techniques are restricted by the fundamental diffraction limit dictating a resolution barrier at $\lambda/2$. However, the spatial dimension of the above mentioned composite quantum systems is very small compared to the optical wavelength. Therefore, the external optical fields are not able to selectively excite the individual emitters. Instead, only the collective optical resonances are probed and the internal structural properties cannot be resolved.

To overcome this fundamental limitation, the idea is to realize a spatiotemporal control of optical excitations localized on a spatial scale well below the diffraction limit [Sto02, Aes11]. The applied near-field techniques range from nanoplasmonic antennas [Zha09, Kin09, Hua09, Mer08, Nov11] to metal tips or (metalized) fiber tips [Gue02, Bri05, vFr98, Pet04, Web11].

An overview over the theoretical treatment of spatially localized excitation and detection schemes and its application to linear optics and pump-probe spectroscopy is given in [Ric13]. In [Ric12], a novel quantum tomography protocol is suggested that combines coherent two-dimensional (2D) spectroscopy with near-field excitation to decompose the delocalized single-exciton wavefunctions in coupled QD systems into the contributions from the single emitters. This reconstruction scheme was extended to two-exciton wave functions in [Sch13]. Both works treat the case of probing one exciton per QD. This simplified model applies, e.g., to trions or to systems where the spin-orbit coupling is larger than the inter-QD couplings.

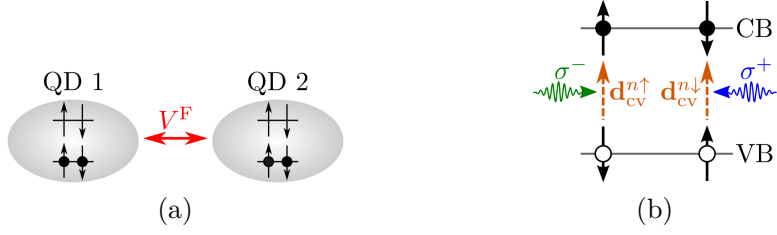


Figure 4.1: (a) Two coupled QDs modeled as spin-degenerate two-level systems. (b) Optically allowed, spin-selective dipole transitions between the heavy-hole valence and conduction band of a zincblende-type semiconductor. [Spe16b]

However, it breaks down for QDs where spin-orbit coupling is small compared to the homogeneous linewidth (in the order of few μeV for the zero-phonon line [Bor01, Sto11]). This is the case for QDs with only few electrons [Jac98] and energetically degenerate spin states. There, the Förster interaction can couple identical and opposite spin states of the excited electron [Spe15]. To resolve these spin-dependent couplings, the reconstruction scheme of [Ric12, Sch13] is generalized to energy degenerate, spin-dependent exciton states in this work. This provides a tool to examine and quantify the impact of Förster-induced spin flip processes.

Also, if a circularly polarized excitation cannot be realized in the specific nanoplasmonic setup, a combination of spin states \uparrow and \downarrow is created [Jac98]. Thus, in the case of weak Förster coupling, the proposed protocol allows to resolve the contributions from different spin states in the case of mixed polarizations of the exciting near-field pulses. Parts of this chapter have been published in [Spe16b, Spe15].

This chapter is structured as follows: First, the QD model is introduced in terms of its Hamiltonian, optical selection rules, and local and delocalized basis states in Sec. 4.2. In Sec. 4.3, the linear absorption and 2D spectra in the far-field limit are discussed. Next, the concept of localized double quantum coherence (DQC) spectroscopy using nanooptical fields is presented and the corresponding spectra are discussed (cf. Sec. 4.4). Finally, the quantum state tomography protocol for retrieving the single and two-exciton wave functions is described and its accuracy is analyzed in Sec. 4.5.

4.2 Coupled quantum dots

4.2.1 Model system

In this work, a typical example of coupled nanoemitters is studied, namely two self-organized InAs/GaAs QDs that interact with each other via the non-radiative dipole-dipole (Förster) coupling [Lov03, Dan06, Spe15]. In the following, spin-orbit splitting is neglected and only the energetically lowest dominant exciton transition between the highest valence (v) and lowest conduction band (c) state is considered. Thus, each QD is described by a spin-degenerate two-level system as illustrated in Fig. 4.1 (a). The distance between the two QDs is assumed to be large enough that the electronic wave-function overlap between the QDs is negligible. Electron-phonon coupling is not included in the treatment, since (i) it is usually weak in semiconductors at low temperatures and would only cause an additional dephasing of the coherences without significantly affecting the results of the reconstruction and (ii) the zero-phonon line dominates over the phonon sidebands in the low-temperature regime [Bor01, Kru02, Ric06, Sto11].

The double QD system is modeled as in Ref. [Spe15]: In the envelope function approximation, the wave functions are given by products of the lattice periodic Bloch function $u_{\lambda i \sigma, \mathbf{k} \approx 0}(\mathbf{r})$ and the envelope function $\phi_{\lambda i}(\mathbf{r})$ of an electron with spin $\sigma \in \{\uparrow, \downarrow\}$ in the valence or

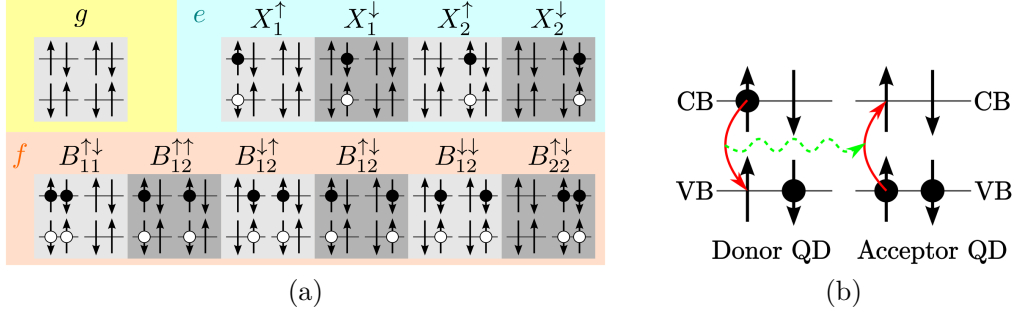


Figure 4.2: (a) Scheme of the ground state and optically bright excited state configurations in the double QD system. Superpositions of these states form the excited state manifolds e and f . (b) Sketch of the Förster excitation energy transfer process between two QDs. The initially excited donor QD relaxes, whereas the acceptor QD is excited via interdot dipole-dipole coupling. [Spe16b]

conduction band $\lambda \in \{v, c\}$ of QD $i \in \{1, 2\}$ [Hau04, Yu05]. QD indices will be labeled with Latin letters and spin indices with Greek letters throughout this chapter. The field operators are then given by: $\hat{\psi}^{(\dagger)}(\mathbf{r}) = \sum_{\lambda, i, \sigma} \phi_{\lambda i}^{(*)}(\mathbf{r}) u_{\lambda i \sigma}^{(*)}(\mathbf{r}) \hat{a}_{\lambda i \sigma}^{(\dagger)}$, where $\hat{a}_{\lambda i \sigma}^{(\dagger)}$ denotes the electronic annihilation (creation) operator. In the effective mass approximation, $\phi_{\lambda i}(\mathbf{r})$ is a solution of the single-particle Schrödinger equation for the confinement potential $U_C^\lambda(\mathbf{r})$ of the QD structure: $(-\hbar^2 \nabla^2 / (2m_\lambda^*) + U_C^\lambda(\mathbf{r})) \phi_{\lambda i}(\mathbf{r}) = E_{\lambda i} \phi_{\lambda i}(\mathbf{r})$. $m_v^* = 0.45 m_0$ and $m_c^* = 0.07 m_0$ denote the valence and conduction band effective masses.

The two ellipsoidal QDs are located in the xy plane with growth direction (crystalline c axis) along the z axis. The confinement $U_C^\lambda(\mathbf{r})$ is separated into the three spatial directions $U_C^\lambda(\mathbf{r}) = U_C^\lambda(x) + U_C^\lambda(y) + U_C^\lambda(z)$, yielding a product ansatz for the envelope functions $\phi_{\lambda i}(\mathbf{r}) = \phi_{\lambda i}^x(x) \phi_{\lambda i}^y(y) \phi_{\lambda i}^z(z)$. Harmonic potentials are assumed in y and z direction with minima at $y, z = 0$, such that the ground state envelopes in y and z direction are given by Gaussian functions of widths $b = 5$ nm in y direction and $h = 2.5$ nm in z direction [Gro08]. The confinement potential in x direction, i.e., along the connecting axis between the two QDs, is described by two Gaussian functions with minima at the QD centers and center-to-center distance $R_{12} = 13$ nm [Spe15]:

$$U_C^\lambda(x) = -U_0^\lambda \exp \left[-\frac{1}{2} \left(\frac{x + R_{12}/2}{l_{0,x}} \right)^2 \right] - (U_0^\lambda + \Delta U^\lambda) \exp \left[-\frac{1}{2} \left(\frac{x - R_{12}/2}{l_{0,x}} \right)^2 \right] \quad (4.1)$$

with potential depths $U_0^v = 330$ meV and $U_0^c = 770$ meV [Fon98] and offsets $\Delta U^v = -0.05$ meV and $\Delta U^c = -0.5$ meV. The one-dimensional (1D) Schrödinger equation for $\phi_{\lambda i}^x(x)$ is solved numerically using eighth order finite differences [For94]. The lowest two eigenstates are taken as the single-particle envelope functions of the two QDs, since they are predominantly localized at the lower-energy QD 1 at $x = -R_{12}/2$ and the higher-energy QD 2 at $x = R_{12}/2$, respectively.

4.2.2 Local states and dipole selection rules

Since the $\chi^{(3)}$ signal is of interest, a three-band model of the ground state g , the single-exciton manifold e , and the two-exciton manifold f is considered (cf. Chap. 3 Fig. 3.2 (b)). The nanostructure is assumed to be initially in the ground state g where the conduction band is not occupied. The microscopic interband dipole moment for transitions between the valence and conduction band is defined per unit cell using the Bloch functions [Web08]

$$\mathbf{d}_{\lambda\mu}^{i\sigma} = \frac{1}{V_{UC}} \int_{UC} d^3 \tilde{r} u_{\lambda i \sigma}^*(\tilde{\mathbf{r}}) e \tilde{\mathbf{r}} u_{\mu i \sigma}(\tilde{\mathbf{r}}), \quad (4.2)$$

where V_{UC} denotes the unit cell volume. In the considered zincblende type semiconductor material, circularly polarized transition dipole moments describe the optically allowed interband transitions from the heavy hole valence to the conduction band: $\mathbf{d}_{\text{cv}}^{i\uparrow} = d(\hat{\mathbf{e}}_x - i\hat{\mathbf{e}}_y)/\sqrt{2}$ for a spin-up and $\mathbf{d}_{\text{cv}}^{i\downarrow} = d(\hat{\mathbf{e}}_x + i\hat{\mathbf{e}}_y)/\sqrt{2}$ for a spin-down electron in the i -th QD [Sch04], as indicated by the dashed orange arrows in Fig. 4.1 (b). \mathbf{e}_x and \mathbf{e}_y denote orthogonal Cartesian unit vectors. This way, different conduction band spin states can be selectively excited using circularly polarized light. In particular, right-hand circularly polarized light (σ^-) will excite the spin-up states, whereas left-hand circularly polarized light (σ^+) will induce the transition of a spin-down electron.

As shown in Fig. 4.2 (a), four bright single and six bright double excitation configurations are possible. They are generated from the ground state using the electronic annihilation and creation operators introduced in Sec. 4.2.1: The states $|X_i^\sigma\rangle = a_{\text{ci}\sigma}^\dagger a_{\text{vi}\sigma}|g\rangle$ describe the configurations where a single electron with spin σ in QD i is excited. The double excitation states have the form $|B_{ij}^{\sigma\mu}\rangle = a_{\text{ci}\sigma}^\dagger a_{\text{vi}\sigma} a_{\text{cj}\mu}^\dagger a_{\text{vj}\mu}|g\rangle$.¹ A small band gap detuning $\Delta = 0.48$ meV (determined by the potential offsets $\Delta U^{\text{v/c}}$) between the two QDs causes that the six double-excitation states cover three different energies.² These states are referred as *local basis states*, since they represent the electronic configurations of the system without delocalization induced by off-diagonal couplings (such as Förster interaction). Note that the local basis set is unique up to an arbitrary phase.

4.2.3 Hamilton operator

The full Hamilton operator $\hat{H} = \hat{H}_0 + \hat{H}_C + \hat{H}_{\text{el-L}}$ comprises three parts. The non-interacting electron part H_0 contains the electronic single-particle energies ε_i . In the local state basis introduced in Sec. 4.2.2, it reads in bra-ket notation

$$\hat{H}_0 = \varepsilon_0|g\rangle\langle g| + \sum_{i=1}^2 \sum_{\sigma \in \{\uparrow, \downarrow\}} \varepsilon_i |X_i^\sigma\rangle\langle X_i^\sigma| + \frac{1}{2} \sum_{i,j=1}^2 \sum_{\sigma, \mu \in \{\uparrow, \downarrow\}} (\varepsilon_i + \varepsilon_j) |B_{ij}^{\sigma\mu}\rangle\langle B_{ij}^{\sigma\mu}|. \quad (4.3)$$

In a semiclassical treatment of the electron-light interaction, the quantized electronic system couples to an external classical light field $\mathbf{E}(t)$ that is assumed to be constant on the spatial scale of the considered nanostructure in the far-field limit:

$$\hat{H}_{\text{el-L}} = - \sum_i \sum_{\sigma} \mathbf{d}_{gX_i^\sigma} \cdot \mathbf{E}(t) |g\rangle\langle X_i^\sigma| - \sum_{i,j} \sum_{\sigma, \mu} \mathbf{d}_{gX_i^\sigma} \cdot \mathbf{E}(t) |X_j^\mu\rangle\langle B_{ij}^{\sigma\mu}| + h.c. \quad (4.4)$$

with the transition dipole matrix elements in the local basis

$$\mathbf{d}_{gX_i^\sigma} \equiv \langle g | \hat{\mathbf{d}} | X_i^\sigma \rangle = \int d^3r \phi_{\text{vi}}^*(\mathbf{r}) \phi_{\text{ci}}(\mathbf{r}) \mathbf{d}_{\text{cv}}^{i\sigma}. \quad (4.5)$$

Finally, the Coulomb interaction \hat{H}_C is given by

$$\begin{aligned} \hat{H}_C = & V_0^{\text{mono}} |g\rangle\langle g| + \sum_i \sum_{\sigma} V_i^{\text{mono}} |X_i^\sigma\rangle\langle X_i^\sigma| + \frac{1}{2} \sum_{i,j} \sum_{\sigma, \mu} V_{ij}^{\text{mono}} |B_{ij}^{\sigma\mu}\rangle\langle B_{ij}^{\sigma\mu}| \\ & + \left\{ \sum_{\sigma, \mu} V_{\sigma\mu}^{\text{F}} |X_2^\mu\rangle\langle X_1^\sigma| + \sum_i \sum_{\sigma, \mu, \nu} V_{\sigma\mu}^{\text{F}} |B_{i2}^{\nu\mu}\rangle\langle B_{i1}^{\sigma\nu}| + h.c. \right\} \end{aligned} \quad (4.6)$$

¹ This construction ensures that Pauli-forbidden biexciton states $|B_{ij}^{\sigma\mu}\rangle$ with $i = j$ and $\sigma = \mu$ where two electrons with identical spins reside within the same QD are excluded.

² The four two-exciton states $B_{12}^{\sigma\mu}$ with one electron-hole pair in each QD are energetically degenerate. However, due to the detuning, the biexciton states $B_{11}^{\uparrow\downarrow}$ and $B_{22}^{\uparrow\downarrow}$ are energetically separated.

The Coulomb coupling elements V are obtained by performing a Taylor expansion of the Green's function $G(\mathbf{r}, \mathbf{r}') = 1/(4\pi\epsilon_0\epsilon_r|\mathbf{r} - \mathbf{r}'|)$ around the center of each unit cell. $\epsilon_r = 10.9$ denotes the relative medium permittivity [Mac09]. The zeroth order coupling elements V^{mono} represent the diagonal monopole-monopole shifts of the Coulomb Hamiltonian. They describe the electrostatic interaction between the electronic charge densities. The dipole-dipole coupling elements $V_{\sigma\mu}^{\text{F}}$ incorporate Förster excitation transfer:

$$V_{\sigma\mu}^{\text{F}} = \frac{1}{4\pi\epsilon_0\epsilon_r} \int d^3r \int d^3r' \left(\frac{\mathbf{d}_{\text{vc}}^{1\sigma} \cdot \mathbf{d}_{\text{cv}}^{2\mu}}{|\mathbf{r} - \mathbf{r}'|^3} - 3 \frac{(\mathbf{d}_{\text{vc}}^{1\sigma} \cdot (\mathbf{r} - \mathbf{r}')) (\mathbf{d}_{\text{cv}}^{2\mu} \cdot (\mathbf{r} - \mathbf{r}'))}{|\mathbf{r} - \mathbf{r}'|^5} \right) \times \phi_{v1}^*(\mathbf{r}) \phi_{c2}^*(\mathbf{r}') \phi_{v2}(\mathbf{r}') \phi_{c1}(\mathbf{r}). \quad (4.7)$$

A scheme of the Förster transfer mechanism is shown in Fig. 4.2 (b). The spin of the transferred electron changes from σ to μ during the transfer. As a consequence, both spin-preserving ($\sigma = \mu$) and spin-flipping ($\sigma \neq \mu$) Förster transfer processes occur in the considered QD geometry. The monopole-monopole and Förster coupling elements are taken from the calculations in Ref. [Spe15]: $|V_{\uparrow\uparrow}^{\text{F}}| = |V_{\downarrow\downarrow}^{\text{F}}| = 0.05$ meV and $|V_{\uparrow\downarrow}^{\text{F}}| = |V_{\downarrow\uparrow}^{\text{F}}| = 0.14$ meV.

Later on, the terms ‘‘uncoupled system’’ and ‘‘interaction shifted energies’’ refer to the exclusion of Förster coupling. The diagonal monopole-monopole shifts are always included.

4.2.4 Delocalized exciton basis

The Förster interaction is off-diagonal in the local basis, i.e., it couples different local excited state configurations. Consequently, the local states hybridize into new, delocalized exciton states e and f that represent the eigenstates of the Coulomb-coupled electronic system (without light-matter interaction). They are numerically obtained by diagonalizing the purely electronic Hamiltonian $\hat{H}_0 + \hat{H}_C$, yielding linear combinations of the local states with spin-dependent coefficients $c_{i,\sigma}^e$ and $c_{ij,\sigma\mu}^f$:

$$|e\rangle = \sum_{i=1}^2 \sum_{\sigma \in \{\uparrow, \downarrow\}} c_{i,\sigma}^e |X_i^\sigma\rangle \quad \text{and} \quad |f\rangle = \frac{1}{2} \sum_{i,j=1}^2 \sum_{\sigma,\mu \in \{\uparrow, \downarrow\}} c_{ij,\sigma\mu}^f |B_{ij}^{\sigma\mu}\rangle. \quad (4.8)$$

The two-exciton coefficients $c_{ii,\sigma\sigma}^f$ with $i = j$, $\sigma = \mu$ describe Pauli-forbidden states and are therefore set to zero.

Knowledge of the spin-dependent coefficients of Eq. (4.8) provides access to the composition of the delocalized exciton states, i.e., it reveals to which extent they contain contributions from the different local states. This enables a detailed understanding of the underlying microscopic coupling processes. In this chapter, a quantum state tomography protocol is developed for retrieving c^e and c^f from measured 2D DQC signals obtained by applying nano-optical fields [Spe16b]. It constitutes an extension of the non spin-dependent protocol from Refs. [Ric12, Sch13].

In the new basis of delocalized eigenstates, the electronic Hamilton operator takes the simple form

$$\hat{H}_0 + \hat{H}_C = \hbar\omega_0 |g\rangle\langle g| + \sum_e \hbar\omega_e |e\rangle\langle e| + \sum_f \hbar\omega_f |f\rangle\langle f| \quad (4.9)$$

with the eigenenergies of the ground state ($\hbar\omega_0$), single exciton states ($\hbar\omega_e$), and two-exciton states ($\hbar\omega_f$).

The electron-light coupling Hamiltonian in the delocalized basis is given by

$$\hat{H}_{\text{el-L}} = - \sum_e \mathbf{d}_{ge} \cdot \mathbf{E}(t) |g\rangle\langle e| - \sum_{e,f} \mathbf{d}_{ef} \cdot \mathbf{E}(t) |e\rangle\langle f| + h.c. \quad (4.10)$$

with the delocalized dipole matrix elements

$$\mathbf{d}_{ge} = \langle g|\hat{\mathbf{d}}|e\rangle = \sum_i \sum_\sigma c_{i,\sigma}^e \hat{\mathbf{d}}_{gX_i^\sigma} \quad \text{and} \quad \mathbf{d}_{ef} = \langle e|\mathbf{d}|f\rangle = \sum_{i,j} \sum_{\sigma,\mu} c_{j,\mu}^{e*} c_{i,\sigma}^f \mathbf{d}_{gX_i^\sigma} \quad (4.11)$$

for the ground-state to single-exciton and single-exciton to two-exciton transitions, respectively. Note that $\mathbf{d}_{eg} = \mathbf{d}_{ge}^*$ and $\mathbf{d}_{fe} = \mathbf{d}_{ef}^*$.

4.3 Linear and nonlinear far-field spectroscopy

4.3.1 Linear absorption

A far-field linear absorption measurement serves to study the single-exciton resonance energies. The linear absorption coefficient is calculated as [Hau04]

$$\alpha(\omega) \propto \omega \operatorname{Im} \left(\frac{\mathbf{P}^{(1)}(\omega) \cdot \mathbf{e}_{\text{Pol}}}{\mathbf{E}(\omega) \cdot \mathbf{e}_{\text{Pol}}} \right). \quad (4.12)$$

with frequency ω and normalized polarization vector \mathbf{e}_{Pol} of the incident light field. $\mathbf{P}^{(1)}(\omega)$ denotes the (Fourier transformed) polarization in first order of the electron-light interaction given by $\mathbf{P}^{(1)}(t) = \operatorname{tr} [\hat{\mathbf{d}}\rho^{(1)}(t)]$ (cf. Sec. 2.1). To account for radiative dephasing, a phenomenological dephasing constant $\gamma = 1/(500 \text{ ps})$ is added [Bor01], leading to [Abr09, Hau04]

$$\alpha(\omega) \propto \omega \sum_e |\mathbf{d}_{eg} \cdot \mathbf{e}_{\text{Pol}}|^2 \frac{\gamma}{\gamma^2 + (\omega_{eg} - \omega)^2}. \quad (4.13)$$

$\omega_{eg} = \omega_e - \omega_0$ denotes the resonance frequency for a transition from the ground state to the single-exciton state e .

4.3.2 Two-dimensional DQC spectroscopy

The additional frequency axis and the possibility to extract specific pulse combinations of the full system response makes coherent multidimensional spectroscopy a valuable tool for studying the internal structure of complex quantum systems such as coupled semiconductor nanostructures and molecular assemblies [Muk95, Muk00, Tia03, Lan07, Yan08, Abr09, Kar10, Fin12, Nar15], cf. Sec. 3.1. This has stimulated the idea to combine 2D DQC spectroscopy with local excitation for disentangling the collective resonances and restoring the wave function coefficients c^e and c^f , which is demonstrated in the following. As a first step, the far-field signal is analyzed.

Since a single nanostructure is treated, the DQC pulse configuration can be extracted using a phase-cycling technique with heterodyne detection, where the experiment is repeated several times for different phase contributions, cf. Sec. 3.3.4. The DQC spectra with a signal phase $\varphi_s = \varphi_1 + \varphi_2 - \varphi_3$ are studied. The corresponding nonlinear optical far-field signal is given in Eqs. (3.11), (3.12), and (3.13) and illustrated in the Feynman diagrams of Fig. 3.3, where \mathbf{d}_{eg} and \mathbf{d}_{fe} are the transition dipole matrix elements in the delocalized exciton basis defined in Eq. (4.11). The complex frequencies $\xi_{ab} \equiv \omega_{ab} - i\gamma_{ab}$ contain the exciton resonances ω_{ab} and the dephasing constants $\gamma_{ab} \equiv \gamma = 1/(500 \text{ ps})$. The signal is plotted in frequency domain as a 2D map depending on the Fourier transforms Ω_1 and Ω_2 of the first two pulse intervals. The ground-state to single-exciton resonances ω_{eg} show up along the Ω_1 axis, whereas the resonances ω_{fg} for ground-state to two-exciton transitions are associated with the Ω_2 axis. This way, the positions and oscillator strengths of the resonance peaks in the 2D frequency map give a first impression of how each two-exciton state is built up of the different single-exciton states.

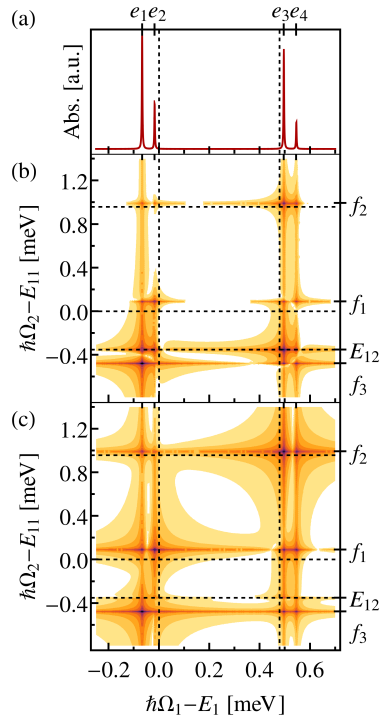


Figure 4.3: (a) Linear absorption spectrum and **2D DQC** spectra for far-field excitation with laser pulses of (b) identical circular polarizations $\sigma^- \sigma^- \sigma^- \sigma^-$ and (c) alternating circular polarizations $\sigma^- \sigma^+ \sigma^- \sigma^+$. The vertical and horizontal dashed lines mark the uncoupled resonances before the transition into the delocalized state basis. The calculations were performed for a fixed delay time $T_3 = 1$ ps.

4.3.3 Evaluation of the linear and 2D far-field spectra

Figure 4.3 shows the linear and **2D DQC** spectra for a far-field excitation with circularly polarized pulses. The single- and two-exciton energy scales are shifted with respect to the energies E_1 for the creation of a single exciton in **QD 1** and E_{11} for the creation of a biexciton in **QD 1**, respectively. The signal function is plotted in a nonlinear scaling in order to make both weak and strong features visible on the same scale: $\mathcal{S}_{nl} = \text{arsinh}[S_{\text{DQC}}^{(3)}/N]$ with normalization constant N [Fin13].

The signatures showing up in the spectra of Fig. 4.3 can be understood after a thorough inspection of the possible excitation pathways dictated by the optical selection rules (cf. Sec. 4.2.2). Fig. 4.4 shows a level scheme of the bright single- and two-exciton states in the local basis. The excitation pathways that are addressed by the circular polarization sequences used for the **2D** spectra in Fig. 4.3 are marked by green (σ^-) and blue (σ^+) arrows. Fig. 4.3 (a) shows the linear absorption spectrum for excitation with right-hand circularly polarized light. A σ^- pulse can generate a spin-up conduction band electron either in **QD 1** (X_1^\uparrow) or in **QD 2** (X_2^\uparrow), cf. Fig. 4.4. The states are energetically separated by the band gap detuning Δ . A bright single exciton in one **QD** couples to both bright single excitons in the other **QD** via F orster interaction, resulting in a hybridization of all four bright single-exciton states. Therefore, four peaks show up in the linear absorption spectrum (denoted e_1 to e_4) that are shifted by the F orster interaction with respect to the uncoupled single-excitation resonances at E_1 and $E_2 = E_1 + \Delta$ marked by the vertical dashed lines in Fig. 4.3 (a).

The nonlinear **2D** spectra of Fig. 4.3 (b) and (c) allow to inspect also the two-exciton resonances along the additional Ω_2 axis. The three horizontal dashed lines mark the double

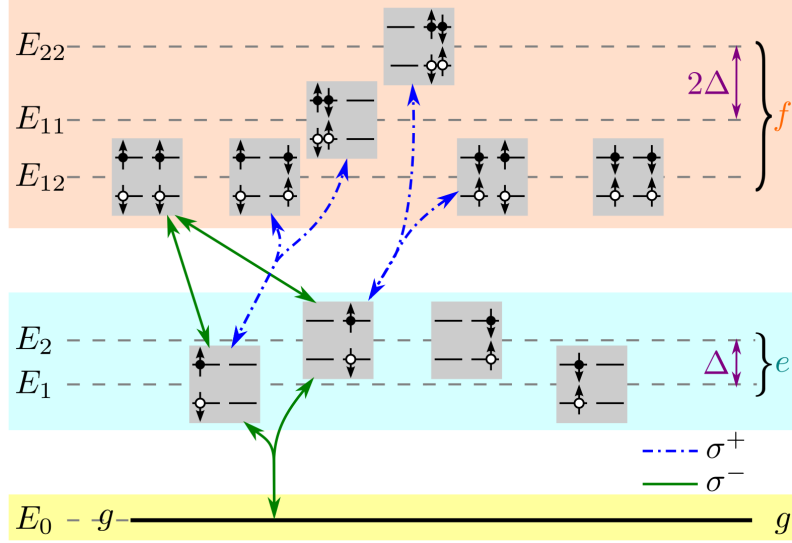


Figure 4.4: Level scheme showing the local states of the uncoupled double QD system and the possible light-induced excitation pathways between them. E_0 denotes the energy of the ground state g , E_i the energy of the uncoupled single excitation states X_i^σ (electron with spin σ in QD i excited) and E_{ij} the energy of the local double excitation states $B_{ij}^{\sigma\mu}$ (two electron-hole pairs at QDs i and j with electron spins σ and μ). The band gap detuning Δ between the QDs denotes the energetic difference between the uncoupled single-excitation energies E_1 and E_2 . The uncoupled biexciton energies E_{11} and E_{22} are separated by 2Δ . The blue and green arrows indicate the possible spin-selective transitions for excitation with left-hand and right-hand circularly polarized light, respectively. After state diagonalization with respect to Förster coupling, the local states hybridize into new delocalized states forming the singly and doubly excited state manifold e and f . [Spe16b]

excitation energies E_{12} , E_{11} , and E_{22} of the uncoupled (local) system states, as indicated in the level scheme of Fig. 4.4. The local two-exciton states $B_{12}^{\sigma\mu}$ with one electron-hole pair in each QD contribute mainly to the delocalized resonance f_3 close to the uncoupled two-exciton energy E_{12} . In contrast, the resonance f_1 (f_2) located close to E_{11} (E_{22} marked by the upper dashed line) is primarily assigned to the biexciton states with both excitons in the lower-energy QD 1 (higher-energy QD 2).

The far-field DQC spectrum of Fig. 4.3 (b) is calculated for an excitation with a sequence of four identically right-hand circularly polarized pulses: $\sigma^- \sigma^- \sigma^- \sigma^-$. According to the selection rules illustrated in Fig. 4.4, only the local state $B_{12}^{\uparrow\uparrow}$ composed of one spin-up electron at each QD at the degenerate energy level E_{12} can be directly generated through purely right-hand circular excitation. However, the spin-flipping Förster transfer couples the two-exciton state to the biexciton states $B_{11}^{\uparrow\downarrow}$ at energy E_{11} and $B_{22}^{\uparrow\downarrow}$ at energy E_{22} . As a consequence, weak resonance peaks are also visible at the interaction shifted energies f_1 and f_2 .

The 2D spectrum for a pulse sequence of alternating circular polarizations $\sigma^- \sigma^+ \sigma^- \sigma^+$ in Fig. 4.3 (c) shows a similar peak pattern. In contrast to Fig. 4.3 (b), the oscillator strengths of the peaks at f_1 and f_2 are substantially increased, since here the biexciton states $B_{11}^{\uparrow\downarrow}$ and $B_{22}^{\uparrow\downarrow}$ are directly excited by the second, left-hand circularly polarized pulse (cf Fig. 4.4), whereas in the case of identical polarizations they can only be accessed due to the Förster induced formation of hybridized states.

This way, off-diagonal couplings such as Förster interaction relax the strict optical selection rules introduced in Sec. 4.2.2 due to excited state hybridization, thus leading to highly delocalized exciton states. The aim of the following section is to disentangle these exciton states into their local state contributions using spatiotemporal pulse control.

4.4 Localized DQC spectroscopy

4.4.1 Spatiotemporal pulse control

The combination of **2D** spectroscopy with localized nanooptical fields allows to unravel how the delocalized exciton wave functions are spread over the individual emitters [Ric12, Sch13]. **DQC** spectroscopy is ideally suited for the proposed quantum state tomography protocol, since the first pulse generates a ground-state to single-exciton coherence and the second pulse excites a ground-state to two-exciton coherence in both involved Liouville space pathways. Hence, localizing the first or the second pulse of the pulse sequence at a specific **QD** limits the respective coherence to this particular **QD**. This opens the possibility to access the single- and two-exciton expansion coefficients that determine to what extent the delocalized wave functions are composed of the single local exciton states. As mentioned in Sec. 4.1, there are several experimental implementations of spatial field control, e.g., by the use of nanoantennas [Zha09, Kin09, Hua09, Mer08, Nov11], metal tips, or (metalized) fiber tips [Gue02, Bri05, vFr98, Pet04, Web11]. The quantum state tomography protocol presented in this chapter is independent of the applied near-field technique. However, for a successful application of the protocols, there are some requirements concerning the nanoplasmonic setup: First, the chosen localization technique must ensure that the electric field strength applied to the selected **QD** is at least a factor of 10 higher than the residual field strength at the other **QDs** (cf. the evaluation in Sec. 4.5). Second, the localization should be applicable to every **QD** in the nanostructure [Spe16b].

Note that the zincblende optical selection rules for circularly polarized spin-selective excitation are relaxed in the case of band mixing. Here, the heavy hole valence band states have a slight admixture of light-hole states, causing an elliptical polarization of the optical dipole transitions [Kou04, Sit12]. However, light-hole admixture is typically only in the range of few percent [Gaw12], thus having no significant effect on the spectra.

4.4.2 Modification of the electron-light coupling for localized excitation

The electron-light interaction has to be adapted to the situation where one or two pulses of the pulse sequence are replaced by localized fields with a spatial control on the nanometer scale, such that it excites only one selected **QD**. The remaining pulses are assumed to excite both **QDs** simultaneously as in the far-field case. The light-matter coupling Hamiltonian for an electric field localized at the **QD** positions is modified as follows:

$$\hat{H}_{\text{el-L}} = - \sum_i \sum_{\sigma} \mathbf{d}_{gX_i^{\sigma}} \cdot \mathbf{E}(\mathbf{r}_i, t) |g\rangle \langle X_i^{\sigma}| - \sum_{i,j} \sum_{\sigma,\mu} \mathbf{d}_{gX_i^{\sigma}} \cdot \mathbf{E}(\mathbf{r}_i, t) |X_j^{\mu}\rangle \langle B_{ij}^{\sigma\mu}| + h.c. \quad (4.14)$$

Here, $\mathbf{E}(\mathbf{r}_i, t)$ describes the spatial field distribution of the field localized at **QD** i . To express this Hamiltonian in terms of the delocalized eigenstates, the unitary basis transformations of Eq. (4.8) are inverted:

$$|X_i^{\sigma}\rangle = \sum_e c_{i,\sigma}^e |e\rangle \quad \text{and} \quad |B_{ij}^{\sigma\mu}\rangle = \sum_f c_{ij,\sigma\mu}^f |f\rangle. \quad (4.15)$$

Plugging these expansions of the local exciton states into Eq. (4.14) yields

$$\hat{H}_{\text{el-L}} = - \sum_i \sum_{\sigma} \sum_e c_{i,\sigma}^e \mathbf{d}_{gX_i^{\sigma}} \cdot \mathbf{E}(\mathbf{r}_i, t) |g\rangle \langle e| - \sum_{i,j} \sum_{\sigma,\mu} \sum_{e,f} c_{j,\mu}^e c_{ij,\sigma\mu}^f \mathbf{d}_{gX_i^{\sigma}} \cdot \mathbf{E}(\mathbf{r}_i, t) |e\rangle \langle f| + h.c. \quad (4.16)$$

Here, the spatial variation of the localized electric field prevents the formation of delocalized dipole matrix elements (cf. Eq. (4.11)). However, the diagonalized exciton states e and f (in

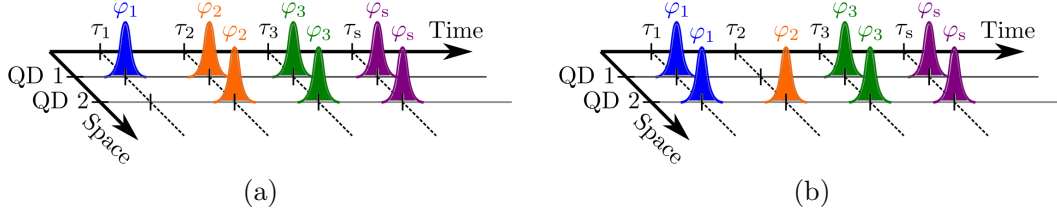


Figure 4.5: Graphical illustration of the spatial and temporal pulse control in a partially localized FWM experiment probing a double QD structure for (a) localization of the first pulse at QD 1 and (b) localization of the second pulse at QD 2. All remaining pulses excite both QDs equally.

terms of the coefficients $c_{i,\sigma}^e$ and $c_{ij,\sigma\mu}^f$) account for the Förster-induced delocalization taking place right after the excitation. The far-field Hamiltonian of Eq. (4.10) can be restored from this equation by assuming a spatially constant electric field and rewriting the expression in terms of the delocalized dipole moments (Eq. (4.11)). This is however not possible for near-field excitation since the electric field distribution $\mathbf{E}(\mathbf{r}_i, t)$ is different at every QD i .

4.4.3 Localization of the first pulse

To develop a reconstruction protocol for the delocalized single-exciton wave functions, the first pulse of the pulse sequence and thus the ground-state to single-exciton coherence is localized at a specific QD. All subsequent pulses still excite all QDs equally. This partially localized excitation protocol is schematically depicted in Fig. 4.5 (a). The DQC signal function of Eq. (3.11) is modified in a way that the first electron-light interaction is given by a localized excitation as introduced in Eq. (4.16). The new signal function depends on the selected QD i :

$$\begin{aligned}
S_{\text{DQC}}^{\text{loc}}(\mathcal{E}_1^i, T_3, \Omega_2, \Omega_1) &= S_{\text{ESA}_1}^{\text{loc}}(\mathcal{E}_1^i, T_3, \Omega_2, \Omega_1) + S_{\text{ESA}_2}^{\text{loc}}(\mathcal{E}_1^i, T_3, \Omega_2, \Omega_1), \\
S_{\text{ESA}_1}^{\text{loc}}(\mathcal{E}_1^i, T_3, \Omega_2, \Omega_1) &= -i \frac{(2\pi)^4}{\hbar^3} \sum_{e,e',f} (\mathbf{d}_{fe'}^* \cdot \mathcal{E}_s^*(\omega_{fe'} - \omega_s)) \left(\mathbf{d}_{e'g}^* \cdot \mathcal{E}_3^*(\omega_{e'g} - \omega_3) e^{-i\xi_{fe'} T_3} \right) \\
&\quad \times \frac{\mathbf{d}_{fe} \cdot \mathcal{E}_2(\omega_{fe} - \omega_2)}{\Omega_2 - \xi_{fg}} \sum_j \sum_{\sigma} \frac{c_{j,\sigma}^e \mathbf{d}_{X_j^{\sigma g}} \cdot \mathcal{E}_1^i(\mathbf{r}_j, \omega_{eg} - \omega_1)}{\Omega_1 - \xi_{eg}}, \\
S_{\text{ESA}_2}^{\text{loc}}(\mathcal{E}_1^i, T_3, \Omega_2, \Omega_1) &= i \frac{(2\pi)^4}{\hbar^3} \sum_{e,e',f} (\mathbf{d}_{e'g}^* \cdot \mathcal{E}_s^*(\omega_{e'g} - \omega_s)) \left(\mathbf{d}_{fe'}^* \cdot \mathcal{E}_3^*(\omega_{fe'} - \omega_3) e^{-i\xi_{e'g} T_3} \right) \\
&\quad \times \frac{\mathbf{d}_{fe} \cdot \mathcal{E}_2(\omega_{fe} - \omega_2)}{\Omega_2 - \xi_{fg}} \sum_j \sum_{\sigma} \frac{c_{j,\sigma}^e \mathbf{d}_{X_j^{\sigma g}} \cdot \mathcal{E}_1^i(\mathbf{r}_j, \omega_{eg} - \omega_1)}{\Omega_1 - \xi_{eg}}.
\end{aligned} \tag{4.17}$$

The first pulse denoted $\mathcal{E}_1^i(\mathbf{r}_j, \omega_{eg} - \omega_1)$ is assumed to predominantly excite QD i .

Fig. 4.6 shows the calculated spectra for a localization of the first pulse at QD 1 (left spectrum) and QD 2 (right spectrum). The remaining far-field pulses are assumed to have circular polarizations. However, depending on the specific nanoplasmonic setup, the polarization of the localized electromagnetic field may be difficult to control since depolarization effects can occur at the nanoantenna or (metal) tip after exciting it with linearly polarized light or polarization shaped pulses [Hua09, Bri05, vFr98, Web11]. According to recent experiments, coaxial antennae structures are able to maintain the linear far-field polarization imprinted by the excitation pulse [Web11, Bao12]. Moreover, it has been shown that cross antenna structures [Bia09, Kla15] and aperture antennas with V-groove structures [Cai15] are able to strongly enhance circularly polarized light while maintaining a high degree of circular

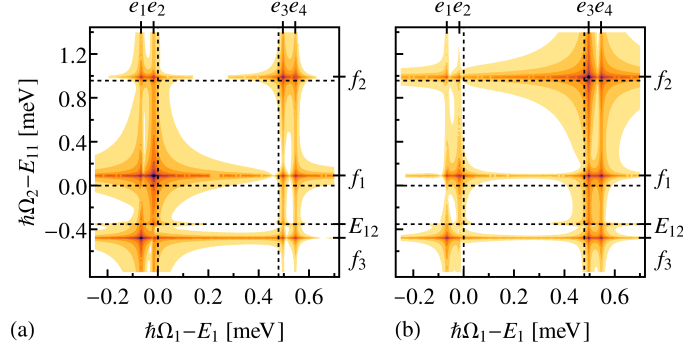


Figure 4.6: 2D DQC spectra for localized excitation with the first pulse at QD 1 (a) and 2 (b). The first (localized) pulse has an arbitrary mixed polarization $\hat{e}_{\text{Pol}}^{\text{loc}} = (3\hat{e}_{\sigma^-} + \hat{e}_{\sigma^+})/\sqrt{10}$, whereas the subsequent three far-field pulses have alternating circular polarizations: $\hat{e}_{\text{Pol}}^{\text{loc}}\hat{e}_{\sigma^+} + \hat{e}_{\sigma^-}\hat{e}_{\sigma^+}$. The DQC signals were calculated for a fixed delay time $T_3 = 1$ ps.

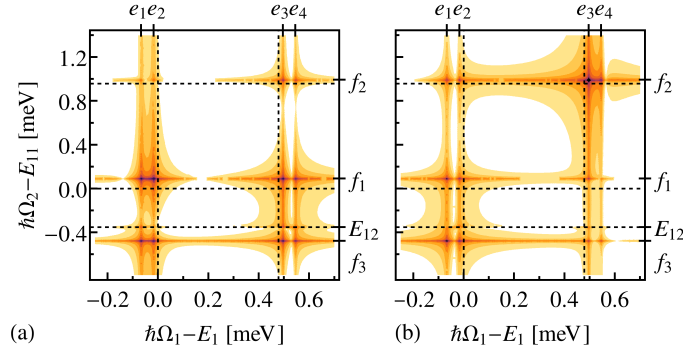


Figure 4.7: 2D DQC spectra for localized excitation with the second pulse at QD 1 (a) and 2 (b). The second (localized) pulse has an arbitrary mixed polarization $\hat{e}_{\text{Pol}}^{\text{loc}} = (3\hat{e}_{\sigma^-} + \hat{e}_{\sigma^+})/\sqrt{10}$, whereas the three far-field pulses have alternating circular polarizations: $\hat{e}_{\sigma^-}\hat{e}_{\text{Pol}}^{\text{loc}}\hat{e}_{\sigma^-} + \hat{e}_{\sigma^+}$. The DQC signals were calculated for a fixed delay time $T_3 = 1$ ps.

polarization. Still, nano-optical fields can exhibit a mixed polarization given by a superposition of right- and left-hand circularly polarized components, and a dynamic localization protocol (including a controlled circular polarization) is not generally feasible in every nanoplasmonic setup [Spe16b]. Therefore, as an example, a normalized polarization $\hat{e}_{\text{Pol}}^{\text{loc}} = (3\hat{e}_{\sigma^-} + \hat{e}_{\sigma^+})/\sqrt{10}$ of the localized pulse is arbitrarily chosen for the calculation of the 2D spectra shown in this work. As cross-check, the reconstruction protocol was carried out for several different random polarizations of the localized pulse and its result was almost unaffected by the particular choice of polarization.

According to Eq. (4.17), the signal $S_{\text{DQC}}^{\text{loc}}(\mathcal{E}_1^i, T_3, \Omega_2, \Omega_1)$ is directly proportional to the single-exciton coefficients $c_{j,\sigma}^{e,*}$. Therefore, the DQC signal for a localization of the first pulse at QD 1 depicted in Fig. 4.6 (a) provides information about the contribution of QD 1 to the ground-state to single-exciton coherence induced by the first pulse. Due to its spatial localization at QD 1, the first pulse excites the states X_1^\uparrow and X_1^\downarrow within QD 1 depending on its polarization. The single-exciton resonances at e_1 and e_2 are energetically close to the uncoupled energy E_1 and are therefore predominantly located at QD 1. Their signal strengths are significantly enhanced compared to the e_3 and e_4 peaks close the resonance energy E_2 of QD 2. Moreover, the oscillator strengths of the resonances at (e_1, f_1) and (e_2, f_1) for the creation of a biexciton in QD 1 are large compared to the biexciton resonances at f_2 (biexciton located at QD 2). This reflects the fact that a direct optical excitation of a biexciton within QD

2 is not possible due to the pulse localization at **QD** 1. The resonances at f_2 stem from Förster coupling processes. The picture is inverted if the first pulse is localized at **QD** 2, cf. Fig. 4.6 (b): Here, the resonances at the single-exciton states e_3 and e_4 close to the uncoupled resonance energy E_2 of **QD** 2 dominate and the resonances at (e_3, f_2) and (e_4, f_2) for a biexciton within **QD** 2 are significantly enhanced compared to the biexciton resonances at f_1 .

4.4.4 Localization of the second pulse

In order to retrieve the two-exciton coefficients $c_{ij,\sigma\mu}^f$ and thus the two-exciton wave functions, a localization of the second incident pulse at **QD** i is necessary, whereas a far-field excitation with circular polarizations is applied for the remaining first, third and fourth pulse. The corresponding partially localized pulse sequence is schematically shown in Fig. 4.5 (b). The signal function for a localized second pulse has the form

$$\begin{aligned}
S_{\text{DQC}}^{\text{loc}}(\mathcal{E}_2^i, T_3, \Omega_2, \Omega_1) &= S_{\text{ESA}_1}^{\text{loc}}(\mathcal{E}_2^i, T_3, \Omega_2, \Omega_1) + S_{\text{ESA}_2}^{\text{loc}}(\mathcal{E}_2^i, T_3, \Omega_2, \Omega_1), \\
S_{\text{ESA}_1}^{\text{loc}}(\mathcal{E}_2^i, T_3, \Omega_2, \Omega_1) &= -i \frac{(2\pi)^4}{\hbar^3} \sum_{e,e',f} (\mathbf{d}_{fe'}^* \cdot \mathcal{E}_s^*(\omega_{fe'} - \omega_s)) \left(\mathbf{d}_{e'g}^* \cdot \mathcal{E}_3^*(\omega_{e'g} - \omega_3) e^{-i\xi_{fe'} T_3} \right) \\
&\quad \times \sum_{j,k} \sum_{\sigma,\mu} \frac{c_{k,\mu}^e c_{jk,\sigma\mu}^{f*} \mathbf{d}_{X_j^\sigma} \cdot \mathcal{E}_2^i(\mathbf{r}_j, \omega_{fe} - \omega_2) \mathbf{d}_{eg} \cdot \mathcal{E}_1(\omega_{eg} - \omega_1)}{\Omega_2 - \xi_{fg} \Omega_1 - \xi_{eg}}, \\
S_{\text{ESA}_2}^{\text{loc}}(\mathcal{E}_2^i, T_3, \Omega_2, \Omega_1) &= i \frac{(2\pi)^4}{\hbar^3} \sum_{e,e',f} (\mathbf{d}_{e'g}^* \cdot \mathcal{E}_s^*(\omega_{e'g} - \omega_s)) \left(\mathbf{d}_{fe'}^* \cdot \mathcal{E}_3^*(\omega_{fe'} - \omega_3) e^{-i\xi_{e'g} T_3} \right) \\
&\quad \times \sum_{j,k} \sum_{\sigma,\mu} \frac{c_{k,\mu}^e c_{jk,\sigma\mu}^{f*} \mathbf{d}_{X_j^\sigma} \cdot \mathcal{E}_2^i(\mathbf{r}_j, \omega_{fe} - \omega_2) \mathbf{d}_{eg} \cdot \mathcal{E}_1(\omega_{eg} - \omega_1)}{\Omega_2 - \xi_{fg} \Omega_1 - \xi_{eg}}.
\end{aligned} \tag{4.18}$$

It depends on a product of single-exciton and two-exciton coefficients $c_{k,\mu}^e c_{jk,\sigma\mu}^{f*}$. Therefore, it is not connected to the two-exciton states as directly as the signal for localization of the first pulse is assigned to the single-exciton states. Nevertheless, the composition of the two-exciton states can be analyzed by means of the calculated spectra for a localization of the second incident laser pulse at **QD** 1 and **QD** 2 as shown in Fig. 4.7 (a) and (b), respectively. This time, the single-exciton to two-exciton coherence induced by the second pulse is localized at the focused **QD**. The resonances projected onto the single-exciton Ω_1 axis are more or less equally distributed over all single-exciton states, since the first pulse acts on the full system and does not selectively excite a specific **QD**. Comparing the biexciton resonances at f_1 and f_2 reveals that the peak intensities at level f_1 are stronger for a localization of the second pulse at **QD** 1 (cf. Fig. 4.7 (a)), whereas the resonances at f_2 predominate for a localization at **QD** 2 (Fig. 4.7 (b)), since f_1 is mainly located at **QD** 1 and f_2 at **QD** 2. The two-exciton states at level E_{12} are predominantly composed of local states with one electron-hole pair in each **QD**. Therefore, the resonance peaks at the two-exciton energy $\hbar\Omega_2 = f_3$ exhibit a higher signal strength close to the single-exciton energy $\hbar\Omega_1 = E_2$ ($\hbar\Omega_1 = E_1$) for generating an exciton in **QD** 2 (**QD** 1) if the second pulse is localized at **QD** 1 (**QD** 2), cf. Fig. 4.7 (a) (Fig. 4.7 (b)).

4.5 Reconstruction schemes

Having discussed the **DQC** signal for localized excitation in the previous section, now an algorithm for reconstructing the exciton wave functions of coupled nanostructures is suggested, providing a protocol to dissect the spin-degenerate delocalized excitons. Therefore, a scheme

to extract the single- and two-exciton expansion coefficients is required, based on the protocols presented in Refs. [Ric12] and [Sch13]. The algorithms are however modified with respect to a treatment of the spin-degenerate exciton states, which appear as sums over σ and μ in Eqs. (4.17) and (4.18). Once the expansion coefficients $c_{i,\sigma}^e$ and $c_{ij,\sigma\mu}^f$ are derived, the full delocalized wave functions $|e\rangle$ and $|f\rangle$ are retrieved using Eq. (4.8) [Spe16b].

4.5.1 Extraction of the single-exciton coefficients

The reconstruction algorithm for the single-exciton wave functions is based on the signal in Eq. (4.17), where the first pulse is localized and mainly excites QD i . So far, the sums over e , j , and σ impede the retrieval of the coefficient $c_{j,\sigma}^{e*}$. Therefore, an ideal pulse localization is assumed in order to remove the sum over j :

$$\mathcal{E}_1^i(\mathbf{r}_j, \omega_{eg} - \omega_1) \approx \delta_{i,j} \mathcal{E}_1^i(\mathbf{r}_i, \omega_{eg} - \omega_1). \quad (4.19)$$

As a second step, the sum over e is eliminated by selecting only the spectroscopic signal at a particular single-exciton resonance \bar{e} . Therefore, the DQC signal close to the frequencies $\Omega_1 = \bar{\Omega}_1 \approx \omega_{\bar{e}g}$ and $\Omega_2 = \bar{\Omega}_2 \approx \omega_{\bar{f}g}$ is extracted. \bar{f} must be selected in a way that the signal at $(\bar{\Omega}_1, \bar{\Omega}_2)$ has a strong contribution only from the chosen single-exciton state \bar{e} . For this purpose, other delocalized states have to be spectrally well separated from this resonance. The localized signal reads

$$\begin{aligned} S_{\text{DQC}}^{\text{loc}}(\mathcal{E}_1^i, T_3, \bar{\Omega}_2, \bar{\Omega}_1) &= S_{\text{ESA}_1}^{\text{loc}}(\mathcal{E}_1^i, T_3, \bar{\Omega}_2, \bar{\Omega}_1) + S_{\text{ESA}_2}^{\text{loc}}(\mathcal{E}_1^i, T_3, \bar{\Omega}_2, \bar{\Omega}_1), \\ S_{\text{ESA}_1}^{\text{loc}}(\mathcal{E}_1^i, T_3, \bar{\Omega}_2, \bar{\Omega}_1) &= -i \frac{(2\pi)^4}{\hbar^3} \sum_{e'} \left(\mathbf{d}_{\bar{f}e'}^* \cdot \mathcal{E}_s^*(\omega_{\bar{f}e'} - \omega_s) \right) \left(\mathbf{d}_{e'g}^* \cdot \mathcal{E}_3^*(\omega_{e'g} - \omega_3) e^{-i\xi_{\bar{f}e'} T_3} \right) \\ &\quad \times \frac{\mathbf{d}_{\bar{f}\bar{e}} \cdot \mathcal{E}_2(\omega_{\bar{f}\bar{e}} - \omega_2)}{\bar{\Omega}_2 - \xi_{\bar{f}g}} \sum_{\sigma} \frac{c_{i,\sigma}^{\bar{e}*} \mathbf{d}_{X_i^{\sigma}g} \cdot \mathcal{E}_1^i(\mathbf{r}_i, \omega_{\bar{e}g} - \omega_1)}{\bar{\Omega}_1 - \xi_{\bar{e}g}}, \\ S_{\text{ESA}_2}^{\text{loc}}(\mathcal{E}_1^i, T_3, \bar{\Omega}_2, \bar{\Omega}_1) &= i \frac{(2\pi)^4}{\hbar^3} \sum_{e'} \left(\mathbf{d}_{e'g}^* \cdot \mathcal{E}_s^*(\omega_{e'g} - \omega_s) \right) \left(\mathbf{d}_{\bar{f}e'}^* \cdot \mathcal{E}_3^*(\omega_{\bar{f}e'} - \omega_3) e^{-i\xi_{e'g} T_3} \right) \\ &\quad \times \frac{\mathbf{d}_{\bar{f}\bar{e}} \cdot \mathcal{E}_2(\omega_{\bar{f}\bar{e}} - \omega_2)}{\bar{\Omega}_2 - \xi_{\bar{f}g}} \sum_{\sigma} \frac{c_{i,\sigma}^{\bar{e}*} \mathbf{d}_{X_i^{\sigma}g} \cdot \mathcal{E}_1^i(\mathbf{r}_i, \omega_{\bar{e}g} - \omega_1)}{\bar{\Omega}_1 - \xi_{\bar{e}g}}. \end{aligned} \quad (4.20)$$

The signal for a selected resonance is proportional to the spin sum over σ containing the single-exciton coefficients and a scalar product of the local dipole moment and the electric field. A proportionality factor $A_{\bar{e}}^f$ is introduced that subsumes the part independent of i or σ :

$$A_{\bar{e}}^f \sum_{\sigma} c_{i,\sigma}^{\bar{e}*} \mathbf{d}_{X_i^{\sigma}g} \cdot \mathcal{E}_1^i(\mathbf{r}_i, \omega_{\bar{e}g} - \omega_1) = S_{\text{DQC}}^{\text{loc}}(\mathcal{E}_1^i, T_3, \bar{\Omega}_2, \bar{\Omega}_1). \quad (4.21)$$

Still, the spin-dependent coefficients $c_{i,\sigma}^{\bar{e}*}$ appear under a sum over σ together with the scalar product $\mathbf{d}_{X_i^{\sigma}g} \cdot \mathcal{E}_1^i(\mathbf{r}_i, \omega_{\bar{e}g} - \omega_1)$ and cannot be extracted. To overcome this obstacle, the DQC measurement has to be carried out for two linearly independent polarization directions of the localized electric field $\mathcal{E}_1^i(\mathbf{r}_i, \omega_{\bar{e}g} - \omega_1)$.³ In the following, the index $\eta \in \{1, 2\}$ labels the two different polarizations, whereas i labels the QD at which the field is localized as before. Evaluating Eq. (4.21) for the two polarization directions of $\mathcal{E}_1^{i,\eta=1/2}$ results in a system of

³ This is possible since the transition dipole moments $\mathbf{d}_{X_i^\uparrow}$ and $\mathbf{d}_{X_i^\downarrow}$ are linearly independent.

Table 4.1: Absolute values $|c_{i,\sigma}^e|$ and phases $\arg(c_{i,\sigma}^e)$ of the original (O) and reconstructed (R) single-exciton wave-function coefficients. Different cases are considered: perfect pulse localization (0%) and more realistic scenarios where still 10% or 20% of the optical field strength applied at the focused **QD** reaches also the other **QD** not in focus. The phases are given in multiples of 2π with phase factors $p \in [0, 1]$: $p(c_{i,\sigma}^e) = \arg(c_{i,\sigma}^e)/(2\pi)$. Due to the periodicity, a phase factor of 0 is equivalent to a phase factor of 1. The last column contains the squared error (cf. Eq. (4.24).)

State	Type	$ c_{1,\uparrow}^e $	$ c_{1,\downarrow}^e $	$ c_{2,\uparrow}^e $	$ c_{2,\downarrow}^e $	$p(c_{1,\uparrow}^e)$	$p(c_{1,\downarrow}^e)$	$p(c_{2,\uparrow}^e)$	$p(c_{2,\downarrow}^e)$	Error
e_1	O	0.667	0.667	0.234	0.234	0.500	0.000	0.500	0.000	
	R(0%)	0.667	0.667	0.234	0.234	0.499	0.995	0.495	0.011	0.000
	R(10%)	0.648	0.648	0.282	0.282	0.500	0.996	0.496	0.008	0.050
	R(20%)	0.629	0.629	0.323	0.324	0.500	0.997	0.497	0.006	0.100
e_2	O	0.695	0.695	0.130	0.130	0.500	0.500	0.000	0.000	
	R(0%)	0.695	0.694	0.131	0.132	0.478	0.496	0.010	0.016	0.001
	R(10%)	0.705	0.703	0.066	0.066	0.464	0.482	0.031	0.024	0.025
	R(20%)	0.708	0.706	0.030	0.019	0.332	0.350	0.147	0.171	0.033
e_3	O	0.130	0.130	0.695	0.695	0.500	0.500	0.500	0.500	
	R(0%)	0.130	0.130	0.695	0.695	0.506	0.494	0.497	0.503	0.001
	R(10%)	0.192	0.192	0.680	0.681	0.503	0.497	0.497	0.503	0.040
	R(20%)	0.247	0.247	0.662	0.663	0.501	0.499	0.497	0.503	0.088
e_4	O	0.234	0.234	0.667	0.667	0.000	0.500	0.500	0.000	
	R(0%)	0.234	0.234	0.667	0.668	0.997	0.503	0.505	0.994	0.001
	R(10%)	0.178	0.177	0.684	0.685	0.994	0.506	0.506	0.994	0.046
	R(20%)	0.113	0.113	0.697	0.699	0.986	0.514	0.506	0.993	0.084

linear equations that is written in matrix form:

$$A_{\bar{e}}^{\bar{f}} \underbrace{\begin{pmatrix} d_{i,\uparrow}^1 & d_{i,\downarrow}^1 \\ d_{i,\uparrow}^2 & d_{i,\downarrow}^2 \end{pmatrix}}_{\equiv D_S} \begin{pmatrix} c_{i,\uparrow}^{e*} \\ c_{i,\downarrow}^{e*} \end{pmatrix} = \begin{pmatrix} S_{\text{DQC}}^{\text{loc}}(\mathcal{E}_1^{i,\eta=1}, T_3, \bar{\Omega}_2, \bar{\Omega}_1) \\ S_{\text{DQC}}^{\text{loc}}(\mathcal{E}_1^{i,\eta=2}, T_3, \bar{\Omega}_2, \bar{\Omega}_1) \end{pmatrix} \quad (4.22)$$

with $d_{i,\sigma}^\eta \equiv \mathbf{d}_{X_i^\sigma} \cdot \mathcal{E}_1^{i,\eta}(\mathbf{r}_i, \omega_{\bar{e}g} - \omega_1)$. The two polarizations of the near-field pulses have to be chosen in a way that (i) they are linearly independent and (ii) a sufficient signal strength at the selected resonances is achieved as required for the reconstruction. Then, the dipole matrix D_S in Eq. (4.22) has a non-vanishing determinant and can be inverted:

$$A_{\bar{e}}^{\bar{f}} \begin{pmatrix} c_{i,\uparrow}^{e*} \\ c_{i,\downarrow}^{e*} \end{pmatrix} = D_S^{-1} \begin{pmatrix} S_{\text{DQC}}^{\text{loc}}(\mathcal{E}_1^{i,\eta=1}, T_3, \bar{\Omega}_2, \bar{\Omega}_1) \\ S_{\text{DQC}}^{\text{loc}}(\mathcal{E}_1^{i,\eta=2}, T_3, \bar{\Omega}_2, \bar{\Omega}_1) \end{pmatrix}. \quad (4.23)$$

With that, the single-exciton coefficients are determined up to a proportionality factor provided that all local ground-state to single-exciton transition dipole moments $\mathbf{d}_{gX_i^\sigma}$ and the localized fields $\mathcal{E}_1^{i,\eta}(\mathbf{r}_i, \omega_{\bar{e}g} - \omega_1)$ are known. To complete the reconstruction, the normalization condition $\sum_{i,\sigma} |A_{\bar{e}}^{\bar{f}} c_{i,\sigma}^{e*}|^2 = |A_{\bar{e}}^{\bar{f}}|^2$ is used to calculate the normalized wave function coefficients (except for a global phase) [Spe16b].

In order to evaluate the suggested protocol, the reconstructed single-exciton coefficients are compared to the original coefficients obtained from the diagonalization of the electronic Hamiltonian. This is demonstrated in Tab. 4.1. For the reconstruction, the signal was calculated for the two arbitrary linearly independent normalized polarizations $1/\sqrt{10}(3\hat{e}_{\sigma-} + \hat{e}_{\sigma+})$ and $1/\sqrt{13}(2\hat{e}_{\sigma-} - 3\hat{e}_{\sigma+})$ of the localized field. The three subsequent far-field pulses have circular

polarizations. The choice of the specific two-exciton frequency $\bar{\Omega}_2$ for which the signal at the single-exciton resonance \bar{e} is measured is in principle arbitrary.⁴ In general, it is beneficial to select a value of $\bar{\Omega}_2$ where low interference with neighboring peaks along the Ω_1 axis occurs. Moreover, a measurement point close to a pronounced system resonance should be chosen for a strong, distortion-free signal. However, test calculations show that the accuracy of the reconstruction is not very sensitive to the particular choice of $\bar{\Omega}_2$. Therefore, the two-exciton resonance f_2 is chosen for the reconstruction of all single-exciton resonances in the example given here. In the case of more significant peak overlaps than in the shown example, it is advisable to average over several measurement points on the Ω_2 axis in order to reduce the interference from other resonances.

To estimate the quality of the reconstruction, the squared error

$$\sqrt{\sum_{i=1}^2 \sum_{\sigma \in \{\uparrow, \downarrow\}} \left| |c_{i,\sigma}^{e,\text{rec}}|^2 - |c_{i,\sigma}^{e,\text{org}}|^2 \right|^2} \quad (4.24)$$

of the difference between the reconstructed and original coefficients is calculated [Sch13] and shown in the last column of Tab. 4.1.

In the case of ideal pulse localization, the reconstructed values agree perfectly with the original ones. The coupling parameters in the low meV range are high compared to the homogeneous linewidth of only few μeV [Bor01]. As a consequence, the resonance peaks are sharp and well separated from neighboring resonances. However, the existence of significant phonon side bands would be detrimental for the reconstruction quality, since they are likely to mix with neighboring resonances. Fortunately, the zero phonon line dominates the spectrum in most cases, since its amplitude is one to two orders of magnitude higher than the amplitude of the phonon side peaks [Bor01, Sto11].

To simulate a more realistic spatial distribution of the localized field, further calculations are performed where the amplitude of the localized electric field at the other QD is assumed to be still (i) 10% and (ii) 20% compared to the focused QD [Ric12], cf. Tab. 4.1. The reconstruction accuracy decreases, since the condition of an ideal field localization formulated in Eq. (4.19) is violated. The reconstruction still shows an acceptable overall agreement, however the error goes up to around 10% for a localization with 20% residual field strength at the QD out of focus. The bar charts in Fig. 4.8 provide a direct graphical comparison of the original and reconstructed single-exciton coefficients in the case of 20% field deviation. It is shown that the amplitudes and phases of the original coefficients (darker red and blue bars, respectively) are nicely reproduced by the reconstructed ones (lighter red and blue bars).

4.5.2 Extraction of the two-exciton coefficients

As a prerequisite for the extraction of the two-exciton coefficients, all single-exciton coefficients have to be determined, e.g., by applying the reconstruction scheme introduced in Sec. 4.5.1. The protocol for extracting the two-exciton coefficients is based on the procedure derived in Ref. [Sch13], but generalized to the case of spin-degenerate exciton states [Spe16b]. The starting point for the reconstruction is Eq. (4.18). First, the j sum is removed by assuming an ideal pulse localization as in the previous chapter:

$$\mathcal{E}_2^i(\mathbf{r}_j, \omega_{fe} - \omega_2) \simeq \delta_{ij} \mathcal{E}_2^i(\mathbf{r}_i, \omega_{fe} - \omega_2). \quad (4.25)$$

As a second step, the sums over e and f are eliminated: A specific resonance at frequencies $\Omega_1 = \bar{\Omega}_1 \approx \omega_{\bar{e}g}$ and $\Omega_2 = \bar{\Omega}_2 \approx \omega_{\bar{f}g}$ is selected where states \bar{e} and \bar{f} make the main spectral

⁴ It is not even necessary that $\bar{\Omega}_2$ coincides with a two-exciton resonance.

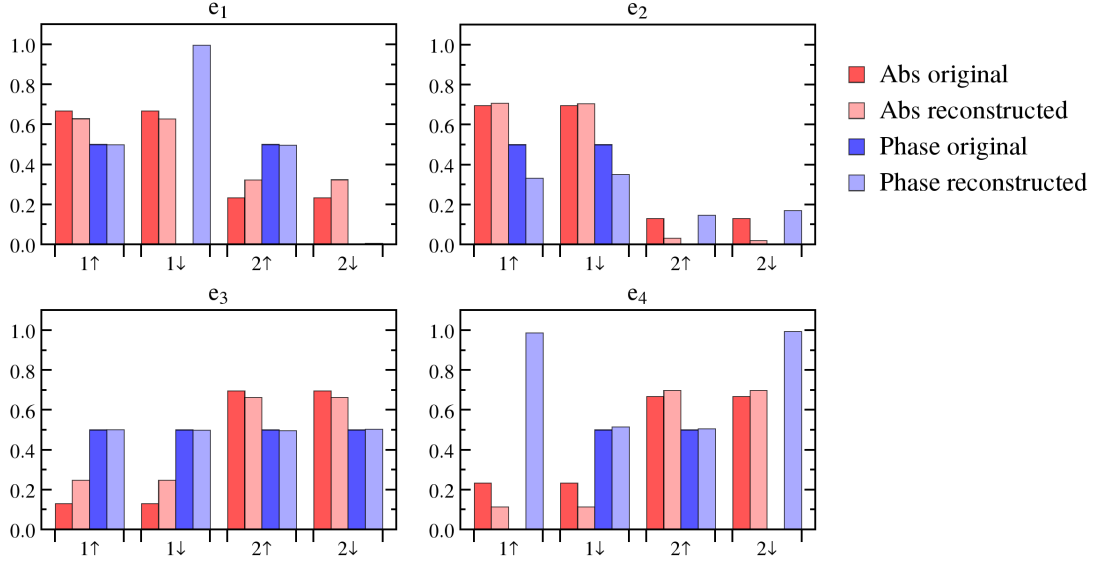


Figure 4.8: Absolute values and phases of the original and reconstructed single-exciton wave function coefficients $c_{i,\sigma}^e$ for an imperfect field localization with 20% residual field strength at the other QD. Each bar chart shows the contributions from the different local states characterized by the quantum numbers $i\sigma$ to a specific delocalized exciton state e . Note that a phase factor of 0 (no bar visible) is equivalent to a phase factor of 1.

contribution, yielding

$$\begin{aligned}
S_{\text{DQC}}^{\text{loc}}(\mathcal{E}_2^i, T_3, \bar{\Omega}_2, \bar{\Omega}_1) &= S_{\text{ESA}_1}^{\text{loc}}(\mathcal{E}_2^i, T_3, \bar{\Omega}_2, \bar{\Omega}_1) + S_{\text{ESA}_2}^{\text{loc}}(\mathcal{E}_2^i, T_3, \bar{\Omega}_2, \bar{\Omega}_1), \\
S_{\text{ESA}_1}^{\text{loc}}(\mathcal{E}_2^i, T_3, \bar{\Omega}_2, \bar{\Omega}_1) &= -i \frac{(2\pi)^4}{\hbar^3} \sum_{e'} \left(\mathbf{d}_{\bar{f}e'}^* \cdot \mathcal{E}_s^*(\omega_{\bar{f}e'} - \omega_s) \right) \left(\mathbf{d}_{e'g}^* \cdot \mathcal{E}_3^*(\omega_{e'g} - \omega_3) e^{-i\xi_{\bar{f}e'} T_3} \right) \\
&\quad \times \sum_k \sum_{\sigma, \mu} \frac{c_{k,\mu}^{\bar{e}} c_{ik,\sigma\mu}^{\bar{f}*} \mathbf{d}_{X_i^{\sigma}g} \cdot \mathcal{E}_2^i(\mathbf{r}_i, \omega_{\bar{f}\bar{e}} - \omega_2) \mathbf{d}_{\bar{e}g} \cdot \mathcal{E}_1(\omega_{\bar{e}g} - \omega_1)}{\bar{\Omega}_2 - \xi_{\bar{f}g}} \frac{1}{\bar{\Omega}_1 - \xi_{\bar{e}g}}, \\
S_{\text{ESA}_2}^{\text{loc}}(\mathcal{E}_2^i, T_3, \bar{\Omega}_2, \bar{\Omega}_1) &= i \frac{(2\pi)^4}{\hbar^3} \sum_{e'} \left(\mathbf{d}_{e'g}^* \cdot \mathcal{E}_s^*(\omega_{e'g} - \omega_s) \right) \left(\mathbf{d}_{\bar{f}e'}^* \cdot \mathcal{E}_3^*(\omega_{\bar{f}e'} - \omega_3) e^{-i\xi_{e'g} T_3} \right) \\
&\quad \times \sum_k \sum_{\sigma, \mu} \frac{c_{k,\mu}^{\bar{e}} c_{ik,\sigma\mu}^{\bar{f}*} \mathbf{d}_{X_i^{\sigma}g} \cdot \mathcal{E}_2^i(\mathbf{r}_i, \omega_{\bar{f}\bar{e}} - \omega_2) \mathbf{d}_{\bar{e}g} \cdot \mathcal{E}_1(\omega_{\bar{e}g} - \omega_1)}{\bar{\Omega}_2 - \xi_{\bar{f}g}} \frac{1}{\bar{\Omega}_1 - \xi_{\bar{e}g}}.
\end{aligned} \tag{4.26}$$

Introducing the proportionality factor $B_{\bar{e}}^{\bar{f}}$ that contains all terms independent of i, k, σ , or μ , Eq. (4.26) is rewritten as:

$$B_{\bar{e}}^{\bar{f}} \sum_k \sum_{\sigma, \mu} c_{k,\mu}^{\bar{e}} c_{ik,\sigma\mu}^{\bar{f}*} \mathbf{d}_{X_i^{\sigma}g} \cdot \mathcal{E}_2^i(\mathbf{r}_i, \omega_{\bar{f}\bar{e}} - \omega_2) = S_{\text{DQC}}^{\text{loc}}(\mathcal{E}_2^i, T_3, \bar{\Omega}_2, \bar{\Omega}_1). \tag{4.27}$$

The goal is to isolate the two-exciton coefficients $c_{ik,\sigma\mu}^{\bar{f}*}$. However, they show up under sums over $k \in \{1, 2\}$ and $\sigma, \mu \in \{\uparrow, \downarrow\}$ together with the single-exciton coefficients $c_{k,\mu}^{\bar{e}}$ and the dipole scalar products $\mathbf{d}_{X_i^{\sigma}g} \cdot \mathcal{E}_2^i(\mathbf{r}_i, \omega_{\bar{f}\bar{e}} - \omega_2)$. Therefore, in its present form, Eq. (4.27) is not suited for retrieving the two-exciton coefficients. As in the single-exciton reconstruction, Eq. (4.27) is rewritten into a system of linear equations for two linearly independent polarizations $\eta \in \{1, 2\}$

of the second pulse:

$$B_{\bar{e}}^{\bar{f}} \underbrace{\begin{pmatrix} d_{i,\uparrow}^1 & d_{i,\downarrow}^1 \\ d_{i,\uparrow}^2 & d_{i,\downarrow}^2 \end{pmatrix}}_{\equiv D_B} \begin{pmatrix} \sum_k \sum_{\mu} c_{k,\mu}^{\bar{e}} c_{ik,\uparrow\mu}^{\bar{f}*} \\ \sum_k \sum_{\mu} c_{k,\mu}^{\bar{e}} c_{ik,\downarrow\mu}^{\bar{f}*} \end{pmatrix} = \begin{pmatrix} S_{\text{DQC}}^{\text{loc}}(\mathcal{E}_2^{i,\eta=1}, T_3, \bar{\Omega}_2, \bar{\Omega}_1) \\ S_{\text{DQC}}^{\text{loc}}(\mathcal{E}_2^{i,\eta=2}, T_3, \bar{\Omega}_2, \bar{\Omega}_1) \end{pmatrix} \quad (4.28)$$

with $d_{i,\sigma}^n \equiv \mathbf{d}_{X_i^\sigma} \cdot \mathcal{E}_2^{i,\eta}(\mathbf{r}_i, \omega_{\bar{f}\bar{e}} - \omega_2)$. By applying the inverse of the matrix D_B to Eq. (4.28), the dipole scalar products can be brought to the right-hand side and only the single- and two-exciton coefficients under the sums over k and μ remain on the left-hand side:

$$B_{\bar{e}}^{\bar{f}} \begin{pmatrix} \sum_k \sum_{\mu} c_{k,\mu}^{\bar{e}} c_{ik,\uparrow\mu}^{\bar{f}*} \\ \sum_k \sum_{\mu} c_{k,\mu}^{\bar{e}} c_{ik,\downarrow\mu}^{\bar{f}*} \end{pmatrix} = D_B^{-1} \begin{pmatrix} S_{\text{DQC}}^{\text{loc}}(\mathcal{E}_2^{i,\eta=1}, T_3, \bar{\Omega}_2, \bar{\Omega}_1) \\ S_{\text{DQC}}^{\text{loc}}(\mathcal{E}_2^{i,\eta=2}, T_3, \bar{\Omega}_2, \bar{\Omega}_1) \end{pmatrix}. \quad (4.29)$$

Separating the lines of Eq. (4.29) again into an upper line whose right-hand side is abbreviated by $S_1^{\text{loc}}(\mathcal{E}_2^i, T_3, \bar{\Omega}_2, \bar{\Omega}_1)$ and a lower line whose right-hand side is denoted $S_2^{\text{loc}}(\mathcal{E}_2^i, T_3, \bar{\Omega}_2, \bar{\Omega}_1)$ yields

$$B_{\bar{e}}^{\bar{f}} \sum_k \sum_{\mu} c_{k,\mu}^{\bar{e}} c_{ik,\uparrow\mu}^{\bar{f}*} = S_1^{\text{loc}}(\mathcal{E}_2^i, T_3, \bar{\Omega}_2, \bar{\Omega}_1), \quad (4.30)$$

$$B_{\bar{e}}^{\bar{f}} \sum_k \sum_{\mu} c_{k,\mu}^{\bar{e}} c_{ik,\downarrow\mu}^{\bar{f}*} = S_2^{\text{loc}}(\mathcal{E}_2^i, T_3, \bar{\Omega}_2, \bar{\Omega}_1). \quad (4.31)$$

The next step is to remove the single-exciton coefficients $c_{k,\mu}^{\bar{e}}$ from the left-hand side of the equations by applying the orthogonality relation. However, this is not yet possible because the unknown proportionality factors $B_{\bar{e}}^{\bar{f}}$ depend on \bar{e} [Spe16b]. In order to restore the spin sum over σ and make Eqs. (4.30) and (4.31) symmetric, Eq. (4.30) is multiplied by $c_{i,\uparrow}^{\bar{e}}$ and Eq. (4.31) by $c_{i,\downarrow}^{\bar{e}}$ on both sides of the equations. After that, a sum over the QD index i is performed and both equations are added:

$$B_{\bar{e}}^{\bar{f}} \sum_{i,k} \sum_{\sigma,\mu} c_{i,\sigma}^{\bar{e}} c_{k,\mu}^{\bar{e}} c_{ik,\sigma\mu}^{\bar{f}*} = \sum_i \left(c_{i,\uparrow}^{\bar{e}} S_1^{\text{loc}}(\mathcal{E}_2^i, T_3, \bar{\Omega}_2, \bar{\Omega}_1) + c_{i,\downarrow}^{\bar{e}} S_2^{\text{loc}}(\mathcal{E}_2^i, T_3, \bar{\Omega}_2, \bar{\Omega}_1) \right). \quad (4.32)$$

The summation indices $i \leftrightarrow k$ and $\sigma \leftrightarrow \mu$ on the left-hand side are swapped and \bar{e} and \tilde{e} are exchanged. Using $c_{ik,\sigma\mu}^{\bar{f}*} = c_{ki,\mu\sigma}^{\tilde{f}*}$, one obtains

$$B_{\tilde{e}}^{\tilde{f}} \sum_{i,k} \sum_{\sigma,\mu} c_{k,\mu}^{\tilde{e}} c_{i,\sigma}^{\tilde{e}} c_{ik,\sigma\mu}^{\tilde{f}*} = \sum_i \left(c_{i,\uparrow}^{\tilde{e}} S_1^{\text{loc}}(\mathcal{E}_2^i, T_3, \bar{\Omega}_2, \tilde{\Omega}_1) + c_{i,\downarrow}^{\tilde{e}} S_2^{\text{loc}}(\mathcal{E}_2^i, T_3, \bar{\Omega}_2, \tilde{\Omega}_1) \right). \quad (4.33)$$

For computing the ratio $B_{\tilde{e}}^{\tilde{f}}/B_{\bar{e}}^{\bar{f}}$ for two arbitrary exciton states \bar{e} and \tilde{e} , Eq. (4.32) is divided by Eq. (4.33) [Sch13]:

$$\frac{B_{\tilde{e}}^{\tilde{f}}}{B_{\bar{e}}^{\bar{f}}} = \frac{\sum_i \left(c_{i,\uparrow}^{\tilde{e}} S_1^{\text{loc}}(\mathcal{E}_2^i, T_3, \bar{\Omega}_2, \tilde{\Omega}_1) + c_{i,\downarrow}^{\tilde{e}} S_2^{\text{loc}}(\mathcal{E}_2^i, T_3, \bar{\Omega}_2, \tilde{\Omega}_1) \right)}{\sum_i \left(c_{i,\uparrow}^{\bar{e}} S_1^{\text{loc}}(\mathcal{E}_2^i, T_3, \bar{\Omega}_2, \bar{\Omega}_1) + c_{i,\downarrow}^{\bar{e}} S_2^{\text{loc}}(\mathcal{E}_2^i, T_3, \bar{\Omega}_2, \bar{\Omega}_1) \right)}. \quad (4.34)$$

Going back to Eqs. (4.30) and (4.31), the relation found in Eq. (4.34) can now be used to replace the factors $B_{\tilde{e}}^{\tilde{f}} = B_{\bar{e}}^{\bar{f}} \times B_{\tilde{e}}^{\tilde{f}}/B_{\bar{e}}^{\bar{f}}$ on the left-hand side by a factor $B_{\tilde{e}}^{\tilde{f}}$ which is independent of \bar{e} . Therefore, an arbitrary single-exciton state \hat{e} is selected, and Eqs. (4.30) and (4.31) are multiplied by $B_{\hat{e}}^{\hat{f}}$ and divided by $B_{\bar{e}}^{\bar{f}}$:

$$B_{\hat{e}}^{\hat{f}} \sum_{k,\mu} c_{k,\mu}^{\hat{e}} c_{ik,\uparrow\mu}^{\hat{f}*} = S_1^{\text{loc}}(\mathcal{E}_2^i, T_3, \bar{\Omega}_2, \bar{\Omega}_1) \times B_{\hat{e}}^{\hat{f}}/B_{\bar{e}}^{\bar{f}}, \quad (4.35)$$

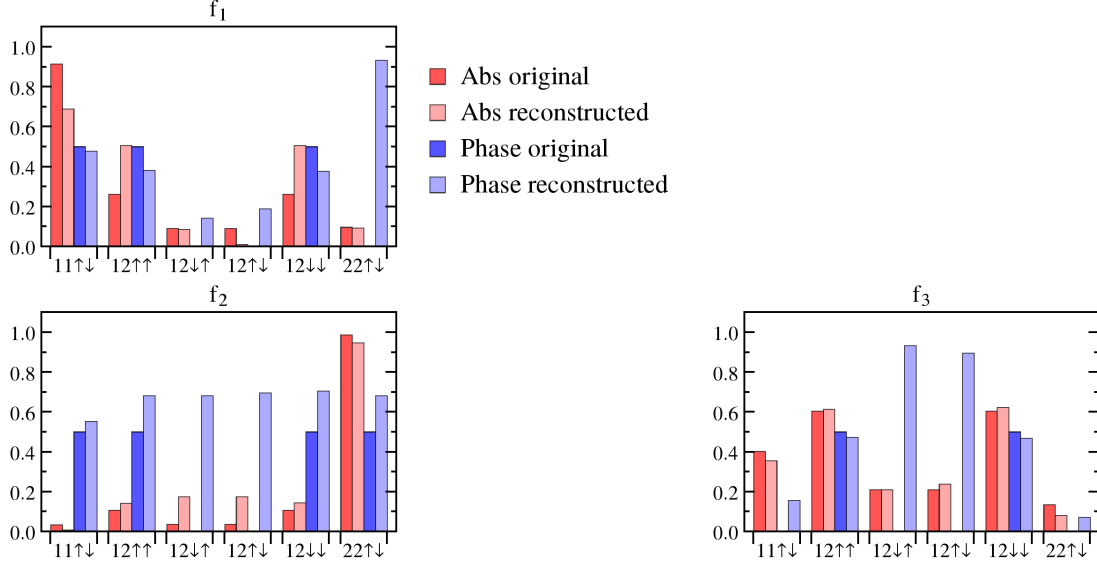


Figure 4.9: Absolute values and phases of the original and reconstructed two-exciton wave function coefficients $c_{ij,\sigma\mu}^g$ for an imperfect field localization with 20% residual field strength at the other QD. Each bar chart shows the contributions from the different local states characterized by the quantum numbers $ij\sigma\mu$ to a specific delocalized two-exciton state f . Note that a phase factor of 0 (no bar visible) is equivalent to a phase factor of 1.

$$B_{\bar{e}}^{\bar{f}} \sum_{k,\mu} c_{k,\mu}^{\bar{e}} c_{ik,\downarrow\mu}^{\bar{f}*} = S_2^{\text{loc}}(\mathcal{E}_2^i, T_3, \bar{\Omega}_2, \bar{\Omega}_1) \times B_{\bar{e}}^{\bar{f}} / B_{\bar{e}}^{\bar{f}}. \quad (4.36)$$

Finally, for applying the orthogonality relation $\sum_{\bar{e}} c_{k,\mu}^{\bar{e}} c_{j,\sigma}^{\bar{e}*} = \delta_{kj} \delta_{\mu\sigma}$, both equations are multiplied with $c_{j,\sigma}^{\bar{e}*}$ and a sum over \bar{e} is performed, ending up with

$$c_{ij,\uparrow\sigma}^{\bar{f}*} B_{\bar{e}}^{\bar{f}} = \sum_{\bar{e}} c_{j,\sigma}^{\bar{e}*} S_1^{\text{loc}}(\mathcal{E}_2^i, T_3, \bar{\Omega}_2, \bar{\Omega}_1) \times B_{\bar{e}}^{\bar{f}} / B_{\bar{e}}^{\bar{f}}, \quad (4.37)$$

$$c_{ij,\downarrow\sigma}^{\bar{f}*} B_{\bar{e}}^{\bar{f}} = \sum_{\bar{e}} c_{j,\sigma}^{\bar{e}*} S_2^{\text{loc}}(\mathcal{E}_2^i, T_3, \bar{\Omega}_2, \bar{\Omega}_1) \times B_{\bar{e}}^{\bar{f}} / B_{\bar{e}}^{\bar{f}}. \quad (4.38)$$

The two-exciton coefficients $c_{ij,\sigma\mu}^f$ are normalized using $\frac{1}{2} \sum_{i,j} \sum_{\sigma,\mu} |c_{ij,\sigma\mu}^f|^2 = 1$. All ingredients for the two-exciton reconstruction are now at hand: The localized DQC measurements, the dipole scalar products entering S_{η}^{loc} , the reconstructed single-exciton coefficients, and the ratio $B_{\bar{e}}^{\bar{f}} / B_{\bar{e}}^{\bar{f}}$ (from Eq. (4.34)).

Table 4.2 shows the calculated two-exciton coefficients of the states f_1 , f_2 , and f_3 . In the case of a perfect field localization (0%), the protocol works well and the original and reconstructed coefficients agree nicely. However, compared to the single-exciton case, the quality of the reconstruction is reduced and the error goes as high as 45% for a residual electric field of 20% at the QD out of focus. This scenario of an imperfect field localization is illustrated in the bar diagrams of Fig. 4.9. Still, most values show an acceptable overall agreement and it is at least possible to identify the local two-exciton states that make dominant and negligible contributions to the considered delocalized two-exciton state.

There are several reasons for the decreased reconstruction quality: Interferences between different two-exciton resonances (e.g. between f_3 and E_{12}) cause inaccuracies. The problem of overlapping resonances can in principle be tackled by applying a filtering method in the data postprocessing, as suggested in Refs. [Ric12] and [Sch13]. However, in the considered case, this

Table 4.2: Absolute values $|c_{ij,\sigma\mu}^f|$ and phases $\arg(c_{ij,\sigma\mu}^f)$ of the original (O) and reconstructed (R) two-exciton expansion coefficients of the states $f_1, f_2,$ and f_3 , for a perfect pulse localization (0%) and more realistic scenarios, where the electric field strength at the other QD still is 10% or 20% of the field magnitude at the focused QD. The phases are given in multiples of 2π with phase factors $p \in [0, 1]$: $\arg(c_{ij,\sigma}^e) = 2\pi p(c_{ij,\sigma}^e)$. Due to the periodicity, a phase factor of 0 is equivalent to a phase factor of 1.

State	Type	$ c_{11,\uparrow\downarrow}^f $	$ c_{12,\uparrow\uparrow}^f $	$ c_{12,\uparrow\downarrow}^f $	$ c_{22,\uparrow\downarrow}^f $	$ c_{11,\uparrow\downarrow}^f $	$p(c_{12,\uparrow\downarrow}^f)$	$ c_{12,\uparrow\uparrow}^f $	$ c_{12,\uparrow\downarrow}^f $	$ c_{22,\uparrow\downarrow}^f $	$p(c_{12,\uparrow\uparrow}^f)$	$p(c_{12,\uparrow\downarrow}^f)$	$p(c_{22,\uparrow\downarrow}^f)$	Error
f_1	O	0.915	0.262	0.091	0.262	0.500	0.000	0.500	0.000	0.096	0.500	0.000	0.000	0.000
	R(0%)	0.814	0.380	0.151	0.378	0.511	0.026	0.492	0.966	0.072	0.490	0.941	0.015	0.205
	R(20%)	0.778	0.431	0.090	0.430	0.513	0.063	0.490	0.941	0.093	0.486	0.941	0.006	0.285
f_2	O	0.688	0.505	0.087	0.505	0.477	0.143	0.382	0.189	0.093	0.382	0.189	0.933	0.449
	R(0%)	0.034	0.108	0.037	0.108	0.500	0.000	0.500	0.986	0.986	0.500	0.000	0.500	0.000
	R(20%)	0.081	0.104	0.003	0.105	0.525	0.105	0.524	0.986	0.972	0.618	0.667	0.670	0.032
f_3	O	0.008	0.143	0.175	0.144	0.552	0.682	0.681	0.947	0.947	0.682	0.697	0.682	0.087
	R(0%)	0.403	0.605	0.210	0.605	0.000	0.000	0.500	0.134	0.134	0.000	0.000	0.000	0.000
	R(20%)	0.262	0.677	0.051	0.680	0.026	0.061	0.500	0.061	0.061	0.874	0.874	0.496	0.173
f_3	R(10%)	0.286	0.662	0.120	0.667	0.039	0.012	0.496	0.068	0.068	0.930	0.930	0.491	0.140
	R(20%)	0.356	0.613	0.211	0.624	0.156	0.933	0.474	0.082	0.082	0.896	0.896	0.072	0.047

will not considerably improve the reconstruction results, since the peaks are already very sharp and well-separated from each other [Spe16b]. Another reason for the increased inaccuracy is that the reconstructed single-exciton wave functions enter multiple times in the calculation of the two-exciton coefficients, leading to an accumulation of their errors. However, this error is of minor relevance in the considered case, since a very accurate single-exciton reconstruction could be achieved. The most important error source is that the signal for reconstructing a specific two-exciton state \tilde{f} is not only recorded for one selected single-exciton frequency, but it has to be measured for all single-exciton resonances along the selected two-exciton resonance. Since the measured signals enter multiple times in different sums, products and quotients of Eqs. (4.34), (4.37), and (4.38), the two-exciton reconstruction is highly sensitive to variations in the signal strengths of the resonances. Hence, weak oscillator strengths of single resonances can cause a substantial error in the reconstruction. Therefore, if possible it is beneficial to choose excitation polarizations for which all peaks have a significant contribution to the selected two-exciton state [Spe16b].

In general, a circularly polarized far-field excitation through the three remaining pulses (as assumed for the example) is not mandatory. The non-localized pulses can also have mixed polarizations and the far-field condition does not have to be fulfilled as long as they are more or less equally distributed over the system such that a signal can be measured for all exciton states [Spe16b].

A shortcoming of the proposed protocol is that the coefficients of the three remaining two-exciton states f_4 , f_5 , and f_6 cannot be reconstructed, since these states are degenerate at energy E_{12} and therefore only span the same subspace as the original wave function coefficients but are not identical.

4.6 Summary

To recapitulate the procedure, the subsequent steps of the reconstruction schemes for the single- and two-exciton states are summarized and visualized in the flow chart of Fig. 4.10.

In this chapter, reconstruction protocols were derived for dissecting the spin-dependent single- and two-exciton wave functions into the contributions from the local (uncoupled) basis states of coupled self-organized InAs/GaAs QDs, cf. Ref. [Spe16b]. Therefore, 2D DQC spectroscopy was combined with localized nanooptical fields in order to selectively excite a specific emitter. The proportionality of the signal to the expansion coefficients of the wave functions in the delocalized exciton basis was exploited to retrieve the local state contributions. It was demonstrated that the localized excitation does not necessarily have to be spin-selective. The experiment only has to be carried out for two linearly independent polarizations of the local field in order to resolve the internal spin structure of the QDs.

In principle, the proposed algorithms are not limited to the specific QD model system considered in this work. They are applicable to any coupled, spin-degenerate two-level quantum emitters with defined spin states, for which the dynamics are described by the Hamilton operator in Sec. 4.2.3 and a localized excitation is possible. Moreover, a polarization control of the localized pulses must be feasible in order to be able to record the signal for two linearly independent polarizations.

The quantum emitters should exhibit a detuning in the same order of magnitude as the coupling strength, such that the exciton states of the two nanostructures are energetically separate. To avoid spectral overlap between the peaks, the coupling strength between the quantum states should be high compared to the homogeneous linewidth of the resonances.

In the considered model system, the reconstruction of the single-exciton coefficients has turned out to be very accurate even for non-ideal field distributions. The two-exciton reconstruction scheme is analytically and experimentally more challenging and is subjected to multiple error

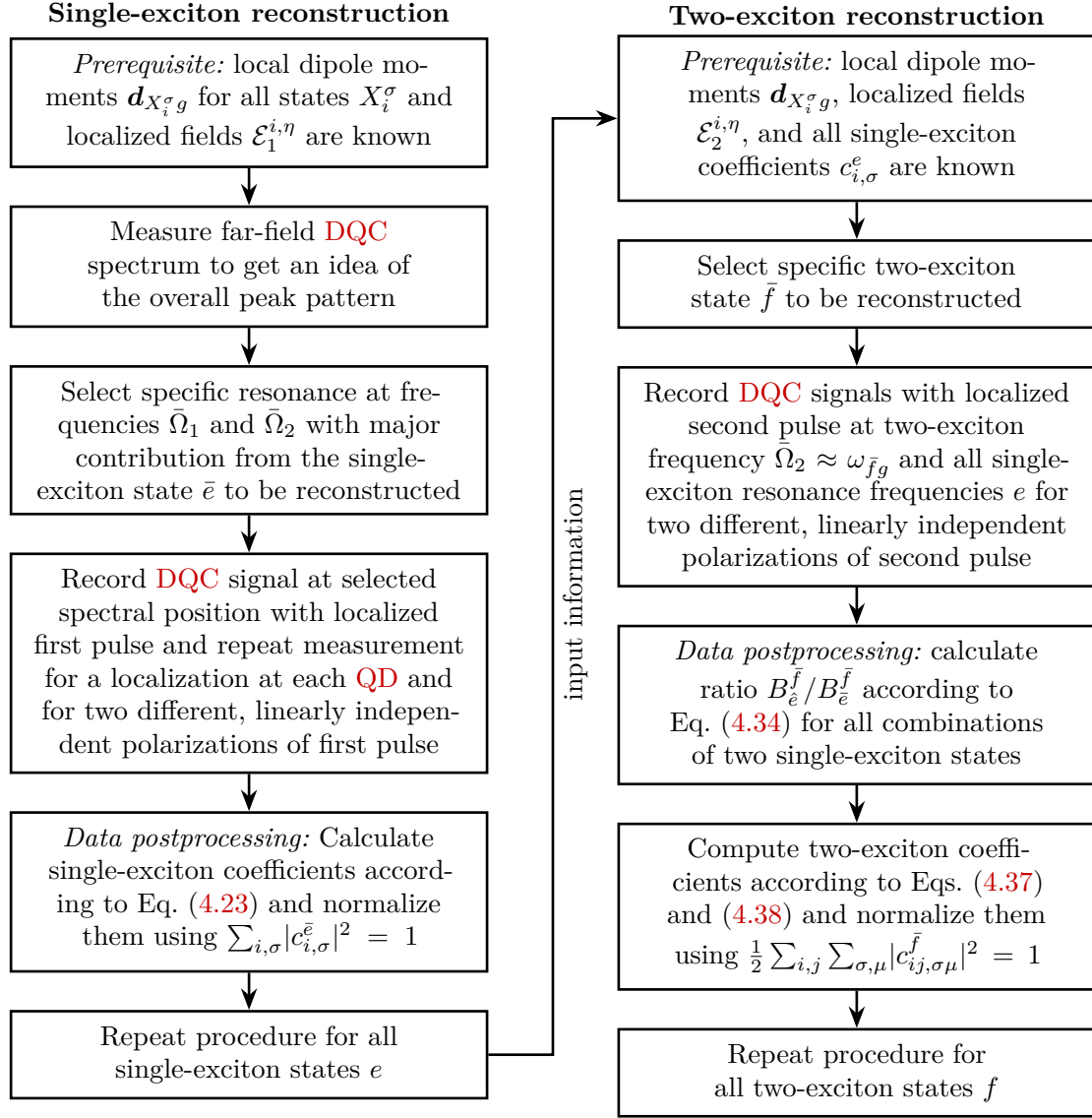


Figure 4.10: Flow chart of the quantum state tomography protocol for the retrieval of the single- and two-exciton wave functions in a double **QD** structure.

sources such as resonance peak interferences, insufficient signal strengths, and shortcomings in the spatiotemporal control of the localized fields. Still, a good overall reconstruction result is achieved, giving a unique insight into the microscopic spin- and polarization-dependent coupling mechanisms that would not be accessible in far-field experiments and without the proposed data postprocessing.

5

Coherent coupling of excitons and trions in monolayer transition metal dichalcogenides

5.1 Introduction

Over the last years, the fabrication and characterization of monolayer transition-metal dichalcogenides has evolved an emerging research field in semiconductor physics [Wan12, But13]. Atomically thin transition-metal dichalcogenides (TMDs) constitute a novel material class of **two-dimensional** direct band gap semiconductors in the visible frequency range with remarkable optoelectronic properties such as strong and structural rich photoluminescence due to a large interband dipole moment [Mak10, Spl10, Ple16]. They exhibit two energetically degenerate direct band gaps in momentum space, namely the K and K' valley at the corners of the first Brillouin zone. Using circularly polarized light, a valley- and spin-selective optical control of charge carriers is possible (valley polarization), giving rise to rich coupled spin-valley physics referred to as “valleytronics” [Xia12, Zen12, Mak12, Cao12].

Excitons, i.e., bound electron-hole pairs, constitute the fundamental optical excitations in semiconductors and dominate the optical properties. In systems with strong Coulomb interaction, excitons can couple to an extra charge carrier and even higher-order correlations between four and more charge carriers such as bound biexcitons can be formed. In two-dimensional (2D) **TMD** films, reduced dielectric screening and strong quantum confinement due to the monolayer thickness cause the formation of strongly correlated many-body quasiparticle states. Several experimental and theoretical works have reported on neutral excitons [Mak10, Spl10, Kom12, Ram12, Qiu13, Yu14, Ber14, Gla14], trions (charged excitons) [Mak13, Ros13, Ber13, Zha14, Wan14, Sri15, Sin16], biexcitons [Mai14a, Sie15, You15, Kyl15, Lee16, Szy17], and even coupled exciton-trion states [Sin14]. The large exciton binding energies of several hundred meV [Ram12, He14, Che14, Uge14, Klo14] and trion binding energies of 20 – 40 meV with respect to the excitonic resonance [Ros13, Mak13, Wan14, Sin14] are roughly one order of magnitude larger than in other quasi-2D and bulk semiconductors. As a consequence, excitonic states in monolayer **TMDs** are stable up to room temperature, making them ideally suited candidates for optoelectronic device applications such as ultrathin biexciton lasers and polarization-entangled photon sources.

Therefore, a precise classification of the rich excitonic features in optical spectra of atomically thin **TMDs** is a crucial step towards assessing the full functionality of this promising new material class. However, an unambiguous identification especially of higher excitonic states in optical spectra as well as their theoretical prediction using effective mass models [Ber13], the Stochastic Variational Method [Zha15], and path integral [Kyl15] and diffusion quantum Monte Carlo calculations [May15, Szy17], is extremely challenging. As a consequence, experimental and theoretical works come to different results concerning, e.g., the magnitude of the biexciton binding energy: Experimental studies suggest that the biexciton binding energy is about twice as large as the trion binding energy [Mai14a, You15, Sie15, Sha15, Ple16]. In contrast, theoretical studies come to the opposite conclusion that the biexciton is spectrally located between the

trion and the exciton [Kyl15, Zha15, May15, Kid16, Kez16, Szy17]. The discrepancy originates on the one hand from the difficult assignment of peaks growing super-linearly with pump fluence in photoluminescence (PL) measurements.¹ On the other hand, it is a demanding task for theory to calculate higher-order correlated states. Furthermore, it remains an unresolved question whether, in addition to intervalley biexcitons, also bound intervalley exciton-trion complexes (as suggested in Refs. [Sin14, Kyl15, Kid16]) and trion-trion couplings can be observed in monolayer TMDs.

Here, polarization-resolved 2D coherent spectroscopy comes into play as ideal tool to disentangle the complex optical response, since in pump/probe experiments the biexciton resonances are spectrally masked by the broad trion peak. Moreover, the rephasing photon echo (PE) signal offers two unique advantages: First, off-diagonal cross peaks reveal coherent couplings between the excited states and second, the inhomogeneous broadening is eliminated along the cross-diagonal. Considering the valley- and spin-dependent optical selection rules, the detected spectral signatures can be traced back to the underlying correlated many-body states. The signal functions derived in Sec. 5.2.1 are calculated incorporating possible excitation pathways and inhomogeneous broadening, which allows to estimate the binding energies of neutral and charged intervalley biexcitons as well as intervalley trions from measured spectra.

This chapter presents a collaboration with Galan Moody from the National Institute of Standards & Technology in Boulder and the group of Xiaoqin (Elaine) Li from the University of Texas (UT) in Austin, where the experiments were conducted under guidance of Kai Hao. Parts of this chapter have been published in Ref. [Hao17]. The presented theoretical model was used to identify the resonance peaks and couplings in the spectra and estimate the binding energies. To the best of our knowledge, Ref. [Hao17] constitutes the first theoretically supported measurement of the charged and uncharged biexciton binding energies of MoSe₂ and of a coupled six-particle correlated state arising due to trion-trion coupling.

The chapter is organized as follows: First, the PE signal is calculated based on the Liouville space formalism introduced in Chap. 3 and its specific properties are discussed. In Sec. 5.3, the spin- and valley-dependent optical selection rules in monolayer TMDs are analyzed and translated into a theoretical model. The experimental setup is briefly described in Sec. 5.4. The measured and calculated spectra are presented in Sec. 5.5.1 and analyzed in more detail in Sec. 5.4.

5.2 Coherent photon echo spectroscopy

In the group of X. Li, rephasing PE spectra of monolayer MoSe₂ were recorded. In this section, the corresponding signal function is presented in Sec. 5.2.1 and the specific advantages of PE spectroscopy are highlighted, making this technique an ideal candidate to probe the excitonic structure of monolayer TMDs: First, off-diagonal peaks in the spectrum clearly indicate coherent couplings (cf. Sec. 5.2.2) and second, the strong inhomogeneous broadening observed in these materials can be eliminated along the cross-diagonal (Sec. 5.2.3).

5.2.1 Calculation of the rephasing one-quantum signal

The rephasing PE signal is measured along the phase-matching direction $\mathbf{k}_1 = -\mathbf{k}_1 + \mathbf{k}_2 + \mathbf{k}_3$ direction (cf. Sec. 3.3.1). It has three Liouville space pathway contributions called excited state emission (ESE), ground state bleaching (GSB), and excited state absorption (ESA) [Abr09], as illustrated in the double-sided Feynman diagrams of Fig. 5.1. Its 2D representation in

¹ These peaks may be associated with the neutral biexciton, but also the charged biexciton, electron plasma excitations, and excitons localized by impurities and defects can show up at similar energies and make a clear identification challenging [Der16, Hua16].

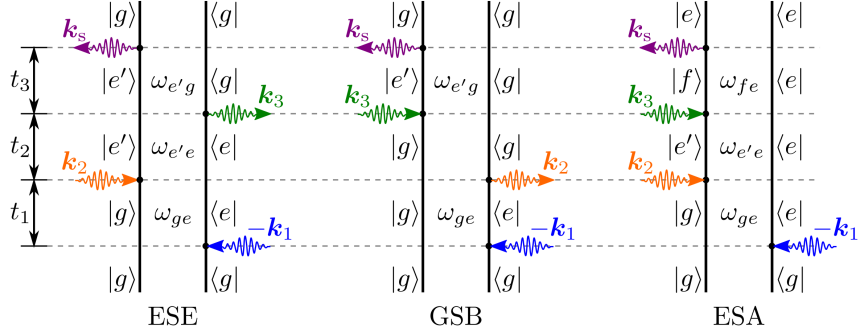


Figure 5.1: Feynman diagrams representing the Liouville space pathways of the density matrix that contribute to the PE signal $\mathbf{k}_1 = -\mathbf{k}_1 + \mathbf{k}_2 + \mathbf{k}_3$.

frequency domain is calculated by Fourier transforming the third-order heterodyne-detected signal with respect to the first and third time intervals T_1 and T_3 between the pulses, whereas T_2 is fixed. This way, in the 2D frequency representation depending on Ω_1 (excitation axis) and Ω_3 (emission axis), the formation of the photon echo can be observed along the diagonal, as discussed later.

The heterodyne-detected signal is calculated using the induced polarization, cf. Chap. 3. It depends on the third-order response function that can be deduced from the double-sided Feynman diagrams. Details on the derivation are given in App. A. The total (measured) rephasing PE signal is the sum of all three contributions [Abr09]:

$$S_{\text{PE}}^{(3)}(\Omega_3, T_2, \Omega_1) = S_{\text{ESE}}^{(3)}(\Omega_3, T_2, \Omega_1) + S_{\text{GSB}}^{(3)}(\Omega_3, T_2, \Omega_1) + S_{\text{ESA}}^{(3)}(\Omega_3, T_2, \Omega_1). \quad (5.1)$$

They are superimposed in the experiment, however separable in theory with distinct signal functions:

$$S_{\text{ESE}}^{(3)}(\Omega_3, T_2, \Omega_1) = i \frac{(2\pi)^4}{\hbar^3} \sum_{e, e'} (\mathbf{d}_{e'g}^* \cdot \mathcal{E}_s^*(\omega_{e'g} - \omega_s)) (\mathbf{d}_{e'g} \cdot \mathcal{E}_2(\omega_{e'g} - \omega_2)) e^{-i\xi_{e'e}T_2} \times \frac{\mathbf{d}_{eg} \cdot \mathcal{E}_3(\omega_{eg} - \omega_3)}{\Omega_3 - \xi_{e'g}} \frac{\mathbf{d}_{eg}^* \cdot \mathcal{E}_1^*(\omega_{eg} - \omega_1)}{\Omega_1 - \xi_{ge}}, \quad (5.2)$$

$$S_{\text{GSB}}^{(3)}(\Omega_3, T_2, \Omega_1) = i \frac{(2\pi)^4}{\hbar^3} \sum_{e, e'} (\mathbf{d}_{e'g}^* \cdot \mathcal{E}_s^*(\omega_{e'g} - \omega_s)) (\mathbf{d}_{eg} \cdot \mathcal{E}_2(\omega_{eg} - \omega_2)) \times \frac{\mathbf{d}_{e'g} \cdot \mathcal{E}_3(\omega_{e'g} - \omega_3)}{\Omega_3 - \xi_{e'g}} \frac{\mathbf{d}_{eg}^* \cdot \mathcal{E}_1^*(\omega_{eg} - \omega_1)}{\Omega_1 - \xi_{ge}}, \quad (5.3)$$

$$S_{\text{ESA}}^{(3)}(\Omega_3, T_2, \Omega_1) = -i \frac{(2\pi)^4}{\hbar^3} \sum_{e, e', f} (\mathbf{d}_{fe}^* \cdot \mathcal{E}_s^*(\omega_{fe} - \omega_s)) (\mathbf{d}_{e'g} \cdot \mathcal{E}_2(\omega_{e'g} - \omega_2)) e^{-i\xi_{e'e}T_2} \times \frac{\mathbf{d}_{fe'} \cdot \mathcal{E}_3(\omega_{fe'} - \omega_3)}{\Omega_3 - \xi_{fe}} \frac{\mathbf{d}_{eg}^* \cdot \mathcal{E}_1^*(\omega_{eg} - \omega_1)}{\Omega_1 - \xi_{ge}} \quad (5.4)$$

with $\xi_{ab} \equiv \omega_{ab} - i\gamma_{ab}$. \mathbf{d}_{ab} denotes the dipole moment, ω_{ab} the resonance frequency and γ_{ab} the homogeneous broadening of the $b \rightarrow a$ transition. \mathcal{E}_i is the envelope of the i -th pulse. e and e' label the singly excited and f the doubly excited state manifold.

5.2.2 Off-diagonal peaks as indicators of coherent couplings

The ESA pathway (cf. Eq. (5.4)) enters the total signal with a negative sign in contrast to the first two contributions, which has an important consequence concerning the peak patterns in

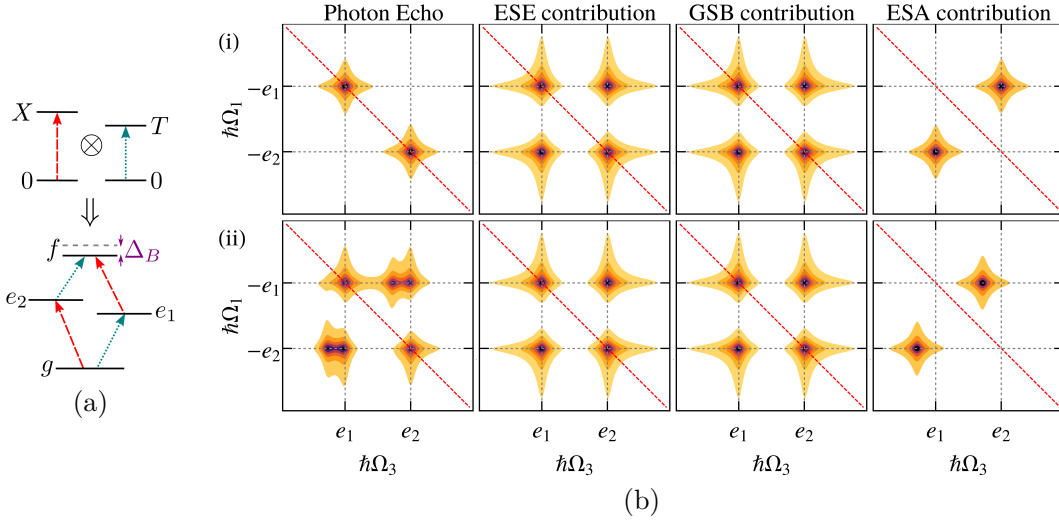


Figure 5.2: (a) Two two-level systems representing, e.g., an exciton ($0 \rightarrow X$) and a trion ($0 \rightarrow T$) transition, can be equivalently expressed by a four-level system with ground state g , singly excited trion (e_1) and exciton (e_2) states, and the doubly excited exciton-trion state f (cf. [Sin14]). Electrostatic coupling between the two excited states leads to an energy shift Δ_B of the two-exciton state. (b) Full PE spectra (left panel) with ESE, GSB, and ESA contributions (from left to right) for the four-level system of (a) in the absence ((i), upper row) and presence ((ii), lower row) of coupling in terms of the biexciton shift. The diagonals are marked by the red dashed lines.

the spectra: A diagonal peak occurs when the oscillation frequencies ω_{ge} and $-\omega_{e'g}$ during the time intervals t_1 between the interaction with the first and second pulse and t_3 between the interaction with the third pulse and the emission of the signal field are identical, cf. Fig. 5.1. In the ESE and GSB pathway, this is the case if $e = e'$, designated as “photon echo”. It immediately follows that the Ω_1 axis has to be plotted as negative excitation photon energy since the coherences oscillate at negative frequencies during t_1 compared to t_3 . In contrast, an off-diagonal peak shows up if $e \neq e'$, which indicates excitation at one energy and emission at the other. The ESA pathway incorporates the doubly-excited state manifold. In the absence of many-body interactions, the lower $g \leftrightarrow e$ and upper $e \leftrightarrow f$ transitions are equivalent and cannot be distinguished.

This is demonstrated for a typical four-level scheme of an exciton-biexciton system composed of two single-exciton transitions, as shown in Fig. 5.2 (a) [Sin14]. If they are coupled, the energy of the biexciton is reduced with respect to the sum of the energies of e_1 and e_2 by the biexciton binding energy Δ_B . Without many-body interactions (i.e., $\Delta_B = 0$), the $g \rightarrow e_1$ ($g \rightarrow e_2$) and $e_2 \rightarrow f$ ($e_1 \rightarrow f$) transitions marked by the dotted (dashed) arrows are degenerate. This way, off-diagonal peaks induced either from ESE and GSB or from ESA coincide. The different signs of the pathways lead to a cancellation of the off-diagonal peaks. This is shown in the upper row of Fig. 5.2 (b), where the off-diagonal peaks vanish in the full PE spectrum due to destructive interference and only diagonal peaks remain visible (left panel).² In contrast, many-body interactions lift this degeneracy by introducing a finite biexciton shift $\Delta_B \neq 0$. As a consequence, the cancellation is incomplete and off-diagonal peaks are observed, as depicted in the lower row of Fig. 5.2 (b). Here, the biexciton binding energy leads to an interaction-induced shift of the ESA signal along the Ω_3 axis (right panel).

² Note that the diagonal goes from the upper left to the lower right corner due to the negative scaling of the Ω_1 axis.

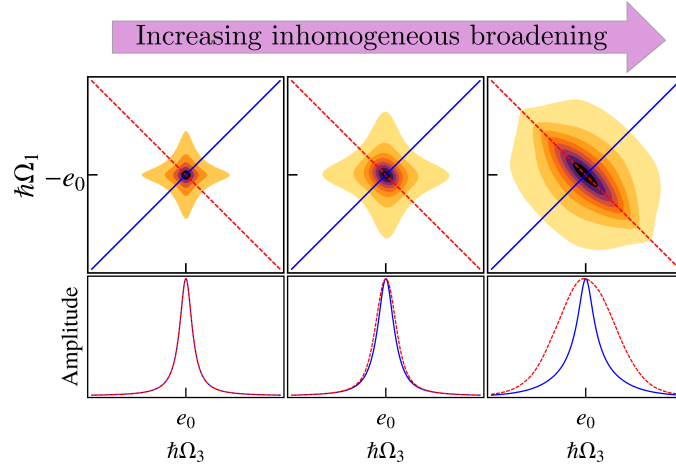


Figure 5.3: Upper row: Calculated PE spectra for a single-exciton resonance e_0 at a fixed homogeneous linewidth γ_{e_0g} . Three cases are considered: no inhomogeneous broadening (left panel), equal homogeneous and inhomogeneous broadenings $\gamma_{\text{inhom}} = \gamma_{e_0g}$ (middle panel) and a dominant inhomogeneous broadening $\gamma_{\text{inhom}} = 4\gamma_{e_0g}$ (right panel). The red dashed line marks the diagonal and the solid blue line the cross-diagonal. The lower row shows slices of the upper row PE spectra along the diagonal (red dashed curve) and cross-diagonal (blue solid curve). A similar model was discussed in Ref. [Sie10].

5.2.3 Elimination of inhomogeneous broadening along the cross-diagonal

The spectral lineshapes of resonance peaks are governed by the homogeneous and inhomogeneous broadening, however the latter can be partially eliminated in 2D PE spectra [Kuz07, Sie10], which is briefly discussed in this section and exemplified for a simple two-level system.

Based on Eq. (A.9) given in the App. A, the signal function of a two-level system consisting of states g and e_0 in time-domain can be determined:

$$S_{\text{PE}}^{(3)}(T_3, T_1) \propto e^{-(\gamma_{e_0g}(T_3+T_1)+i\omega_{e_0g}(T_3-T_1))}\theta(T_1)\theta(T_3). \quad (5.5)$$

The expression does not depend on the fixed delay T_2 since a single resonance $e_0 = e = e'$ is considered with $\xi_{e'e} = 0$. Inhomogeneous broadening is now included by assuming a Gaussian distribution of the resonance energy ω_{e_0g} with half width at half maximum $\gamma_{\text{inh}}^{e_0} = \sqrt{2 \ln 2} \sigma_{\text{inh}}^{e_0}$. An integration over all possible fluctuations $\Delta\omega_{e_0g}$ around the central value ω_{e_0g} is performed:

$$\begin{aligned} S_{\text{PE}}^{(3)}(T_3, T_1) &\propto \int_{-\infty}^{\infty} d(\Delta\omega_{e_0g}) \frac{1}{\sqrt{2\pi}\sigma_{\text{inh}}^{e_0}} e^{-\frac{1}{2}\left(\frac{\Delta\omega_{e_0g}}{\sigma_{\text{inh}}^{e_0}}\right)^2} e^{-(\gamma_{e_0g}(T_3+T_1)+i(\omega_{e_0g}+\Delta\omega_{e_0g})(T_3-T_1))}\theta(T_1)\theta(T_3) \\ &= e^{-(\gamma_{e_0g}(T_3+T_1)+i\omega_{e_0g}(T_3-T_1)+\frac{\sigma_{\text{inh}}^{e_0 2}}{2}(T_3-T_1)^2)}\theta(T_1)\theta(T_3). \end{aligned} \quad (5.6)$$

The signal function shows a homogeneous (Lorentzian) decay with γ_{e_0g} along the diagonal photon echo direction $T_3 = T_1$ that is not affected by the oscillation with the eigenfrequency ω_{e_0g} and the Gaussian envelope. This relation is inverse after a Fourier transform with respect to T_1 and T_3 , as shown in Fig. 5.3: For increasing inhomogeneous broadening, the Gaussian-shaped broadening along the diagonal increases strongly, whereas along the cross-diagonal the narrow Lorentzian line shape dictated by the homogeneous broadening remains almost unchanged. This way, the inhomogeneous broadening is effectively eliminated along the cross-diagonal. Taking a closer look, a very slight broadening of the cross-diagonal slice can be observed as a consequence of the time ordering: Through the Heaviside step functions, the diagonal ($T_1 + T_3$)

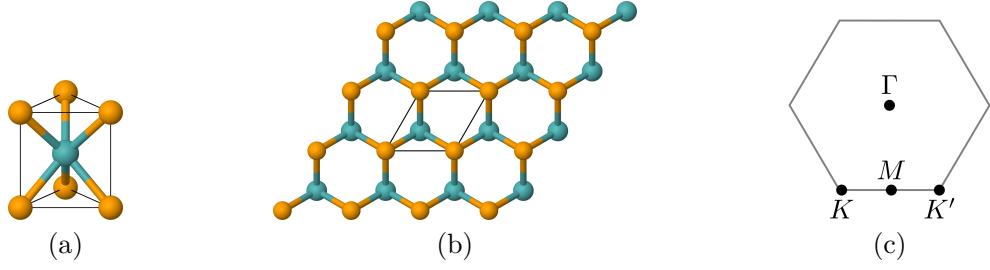


Figure 5.4: (a) Unit cell, (b) top view on the honeycomb lattice, and (c) Brillouin zone with high-symmetry points K and K' of monolayer MoSe_2 . The Mo atoms are light blue, the Se atoms orange.

and cross-diagonal ($T_3 - T_1$) directions are not completely separable, but the homogeneous and inhomogeneous broadenings mix [Sie10].

In systems with more than two levels, a cancellation of the inhomogeneous broadening in the cross-diagonal direction will only occur if the fluctuations in the resonance energies during T_1 and T_3 are perfectly correlated. This is usually the case in the considered optical experiments, since the pulse sequence with delays in the sub-ps range takes place on a shorter timescale than spectral diffusion processes and therefore, the relative change in the transition energies should be stable over one measurement cycle [Sin14].

5.3 Spin- and valley-selective optical transitions in monolayer MoSe_2

Transition-metal dichalcogenides are chemical compound materials consisting of a transition metal and a chalcogen atom in a 1 : 2 stoichiometry of the form MX_2 (e.g., with $M = \text{Mo}$, W and $X = \text{S}$, Se). When going from multilayers to monolayers, **TMDs** exhibit a crossover from an indirect-gap to a direct-gap semiconductor with direct band gaps at the K and K' valley [Mak10]. Fig. 5.4 shows the unit cell, the typical honeycomb structure appearing in top view, and the Brillouin zone of monolayer MoSe_2 . The inversion symmetry in monolayer **TMDs** is broken since the two sublattices that form the **TMD** lattice exhibit different atomic sites. This leads, together with spin-orbit coupling, to coupled spin and valley physics [Xia12]. Within the effective-mass approximation, a parabolic bandstructure is approximated around the optically relevant high-symmetry K and K' points (with nearly identical effective masses for the electrons and holes).

The spin-orbit coupling leads to a splitting of the spin \uparrow and spin \downarrow bands, which is particularly pronounced for the valence bands with $E_{\text{s-o}}^{\text{v}} \approx 180 \text{ meV}$ in MoSe_2 [Zhu11] (factor 50 larger than the conduction band splitting). Therefore, an A transition from the energetically higher and a B transition from the energetically lower valence band to the conduction band are distinguished. They constitute the lowest dipole-allowed optical transitions in MoSe_2 . In this chapter, the focus is on the energetically lowest allowed optical transitions (A excitons) with an optical gap of roughly 1.66 eV [Ros13]. The highest valence and lowest conduction band spin states are energetically reversely ordered at the K and K' point, such that the optical excitation of the A transition with circularly polarized light is both spin and valley selective. Fig. 5.5 (a) shows the lowest allowed optical A transitions that can be accessed under excitation with circularly polarized light: Left-hand (σ^+) polarized light with polarization vector $\hat{e}_{\text{Pol}}^{\sigma^+} = (\hat{e}_x + i\hat{e}_y)/\sqrt{2}$ excites the spin \uparrow electron in the K valley and right-hand (σ^-) polarized light with $\hat{e}_{\text{Pol}}^{\sigma^-} = (\hat{e}_x - i\hat{e}_y)/\sqrt{2}$ the spin \downarrow electron in the K' valley. The optical

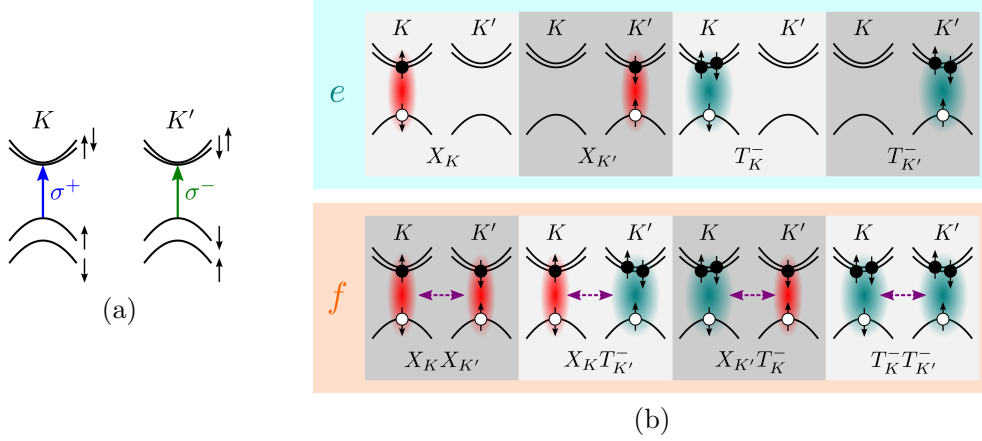


Figure 5.5: (a) Band structure of MoSe₂ at the K and K' points. The green (σ^-) and blue arrows (σ^+) indicate the possible optical transitions using circularly polarized light at a wavelength matching the A transition. (b) Schematic illustration of the neutral (red) and charged (teal) singly excited (upper row) and doubly excited (lower row) bound state configurations associated with the lowest-energy direct-gap A transitions accessible using circularly polarized light. The purple arrows mark many-body interactions responsible for the formation of bound biexcitons. [Hao17]

transitions are described by the following dipole moments:

$$\mathbf{d}_{eg}^{K\uparrow} = d_e \frac{1}{\sqrt{2}} (\hat{e}_x + i\hat{e}_y) \quad \text{and} \quad \mathbf{d}_{eg}^{K'\downarrow} = d_e \frac{1}{\sqrt{2}} (\hat{e}_x - i\hat{e}_y) \quad (5.7)$$

with the magnitude d_e depending on the chosen singly excited state e .

Besides neutral excitons X composed of an electron and a hole with opposite spins in the same valley, also negatively charged excitons, i.e., trions (T^-) can be created in the case of n -type sample doping. They comprise an exciton in one valley bound to an additional electron with opposite spin in the same or the other valley. The treatment is restricted to these singlet trions since triplet trions where the two electrons have identical spins have not yet been observed in the absence of magnetic fields [Zha14].

In the nonlinear $\chi^{(3)}$ regime, doubly excited states enter the optical response. In general, the lowest-energy bound doubly excited state is an *intervalley* biexciton composed of two excitons in opposite valleys, since the energy for generating an *intravalley* biexciton by simultaneous excitation of two excitons in the same valley is roughly 20 meV higher [Sie15, Kyl15]. Besides neutral intervalley biexcitons (XX), also bound five- and six-particle states such as mixed exciton-trion (XT) and trion-trion (TT) states can form.

The lowest-energy bound state configurations belonging to the singly (e) and the doubly excited state manifold (f) are illustrated in Fig. 5.5 (b). They are accessible using circularly polarized light tuned close to the A exciton resonance. The singly excited state configurations consist of two exciton ($X_K, X_{K'}$) and two trion ($T_K^-, T_{K'}^-$) states (one in each valley), whereas the doubly excited states are given by one intervalley biexciton ($X_K X_{K'}$), one trion-trion state ($T_K^- T_{K'}^-$), and two mixed exciton-trion states ($X_K T_{K'}^-, X_{K'} T_K^-$).³

In Fig. 5.6, the polarization-specific optical excitation scheme involving these excited state configurations is shown. Exciton-exciton, trion-trion, and exciton-trion couplings (indicated by

³ Note that the excited state configurations included in the calculations are the lowest-energy bound states. However, depending on multiple parameters such as the sample quality and preparation, the doping, and the excitation energy and power, also other bound state configurations are possible, e.g., B excitons, excited biexcitons [Zha15], intravalley AB biexcitons, triplet trions, etc. [Zha14, Zha15, Kyl15, Sie15, Ser01, San02]. However, they are at higher energies than the states considered here and thus not within the spectral bandwidth [Hao17].

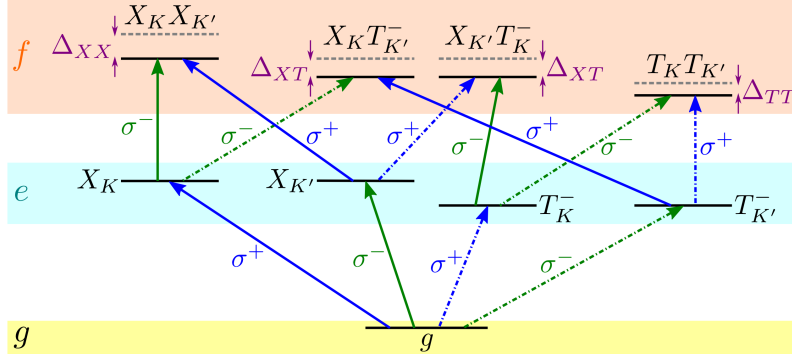


Figure 5.6: Level scheme used to calculate the signal function. The arrows represent the possible excitation pathways using right-hand σ^- (green arrows) and left-hand σ^+ (blue arrows) circularly polarized light according to the valley-specific polarization selection rules. Solid lines mark the excitation of exciton states, dashed-dotted lines indicate the excitation of trion states. The energy diagram consists of the ground state g as well as the singly and doubly excited state manifolds e and f , respectively, as introduced in Fig. 5.5 (b). Due to many-body interactions, the doubly excited states are shifted by Δ_{XX} , Δ_{TT} , and Δ_{XT} with respect to the sum of the individual transitions they are built of (gray, dashed levels). [Hao17]

the purple arrows in Fig. 5.5 (b)) lead to Coulomb-induced shifts Δ_{ij} in the energies of the doubly excited states with respect to the sum of the individual (isolated) exciton and trion transitions (with energies E_X and E_T , respectively) they are built of:

$$E_{XX} = 2E_X - \Delta_{XX}, \quad E_{TT} = 2E_T - \Delta_{TT}, \quad E_{XT} = E_X + E_T - \Delta_{XT}. \quad (5.8)$$

As discussed in Sec. 5.2.2, off-diagonal peaks in PE spectra indicate coherent couplings between the excited states, since in the absence of many-body interactions the Liouville space pathways involving singly excited states (lower transitions) are completely canceled out by the pathway including the doubly excited states (upper transitions). The interactions between the excited states cause shifts Δ_{XX} , Δ_{TT} , and Δ_{XT} , thus breaking the symmetry between the $g \rightarrow e$ and $e \rightarrow f$ transitions and leading to off-diagonal signatures in the 2D spectra.

Note that the considered model system (cf. Fig. 5.6) exhibits a common ground state for both the excitons and trions. This ground state is assumed to incorporate the background charge carrier density of unbound electrons and holes [Ess01]. An optical excitation then generates an additional electron-hole pair, which can either form a neutral bound exciton or capture a background carrier to form a bound trion state.

5.4 Experimental setup and numerical implementation

The biexcitons in monolayer MoSe₂ are probed using coherent 2D PE spectroscopy with polarization control. The sample, an atomically thin flake of roughly $80 \times 40 \mu\text{m}^2$, is mechanically exfoliated onto a sapphire substrate and the optical experiments are performed at a constant temperature of 20 K. 40 fs pulses are generated from a mode-locked Ti:Sapphire laser at a repetition rate of 80 MHz. A system of Michelson interferometers creates a sequence of four phase-stabilized pulses, three of which are focused on the sample and interact with it coherently. The delay T_1 is scanned with interferometric precision and subsequently Fourier transformed. T_2 is held at 0 fs in order to obtain maximum signal-to-noise ratio. The four-wave mixing signal is heterodyne detected in the phase-matched direction using the fourth reference pulse. The interference signal is directly resolved with a spectrometer. The generated 2D spectra correlate the excitation energies $\hbar\Omega_1$ of the system during T_1 with the emission energies $\hbar\Omega_3$ during

Table 5.1: Parameter set (dipole moment d_e in e nm and transition energies E in meV) used to calculate the spectra in Fig. 5.7 (c) and (d). Note that the two exciton states X_K and $X_{K'}$ are subsumed under X , the two trion states T_K and $T_{K'}$ are subsumed under T^- and the two mixed exciton-trion $X_K T_{K'}$ and $X_{K'} T_K$ states are subsumed under XT^- . This is possible since the respective transitions have identical properties. All parameters were chosen in agreement with the experiment.

	$g \leftrightarrow X$	$X \leftrightarrow XX$	$T \leftrightarrow XT$	$g \leftrightarrow T$	$T \leftrightarrow TT$	$X \leftrightarrow XT$
d_e	1.0	1.0	1.0	0.8	0.8	0.8
E	$E_X = 1648.5$	$E_X - \Delta_{XX}$ $\Delta_{XX} = 20.3$	$E_X - \Delta_{XT}$ $\Delta_{XT} = 5.0$	$E_T = 1620.8$	$E_T - \Delta_{TT}$ $\Delta_{TT} = 2.0$	$E_T - \Delta_{XT}$ $\Delta_{XT} = 5.0$

T_3 . The fluence of the exciting pulses is kept below $\sim 4 \mu\text{J cm}^{-2}$ ($\sim 10^{12}$ excitons per cm^2) to ensure that the signal is in the $\chi^{(3)}$ regime, thus excluding higher-order nonlinearities [Hao17]. The laser frequency distribution is centered around the trion resonance ~ 1620 meV, which is tuned well below the exciton resonance at ~ 1650 meV [Hao16] in order to predominantly spectrally address signatures of energetically lower bound biexcitons. The laser bandwidth covers an energy range of roughly 80 meV.

In order to incorporate laser bandwidth effects into the calculations presented in this chapter, the excitation laser spectrum is approximated by a Gaussian-shaped spectral distribution centered at the wavelength $\lambda_c = 765$ nm (corresponding to the trion resonance at 1620.8 meV) with broadening $\gamma_{\text{laser}} = 30$ meV (half width at half maximum). With that, the normalized pulse envelope reads

$$\mathcal{E}(\omega) = \frac{\hbar\sqrt{\ln 2}}{\gamma_{\text{laser}}\sqrt{\pi}} \exp\left(-\hbar^2 \ln 2 \frac{(\omega - \frac{2\pi c}{\lambda_{\text{laser}}})^2}{\gamma_{\text{laser}}^2}\right). \quad (5.9)$$

The excitation laser spectrum is shown in the topmost panels of Figs. 5.9 and 5.10.

As discussed in Sec. 5.2.3, the inhomogeneous broadening is included into the calculations by averaging the signal functions of Eqs. (5.2), (5.3), and (5.4) over normally distributed values of the system resonances. A perfect correlation of the transition energies during T_1 and T_3 is assumed, i.e., the changes in the transition energies during T_1 and during T_3 are directly correlated. This is a reasonable assumption since the (fixed) delay time T_2 between the second and third pulse is vanishing and therefore no spectral diffusion processes will occur between T_1 and T_3 . The inhomogeneous broadening is set to $\gamma_{\text{inh}} = 4$ meV. As a consequence, the resonance peaks are elongated along the diagonal ($\Omega_1 = -\Omega_3$), whereas the broadening along the cross-diagonal is predominantly governed by the homogeneous linewidth, which is set to $\gamma_{\text{hom}} = 2.0$ meV for all transitions. The signals are averaged over 250 normally distributed values of the resonance energies in order to obtain smooth curves.

5.5 Evaluation of the spectra

5.5.1 Comparison between experiment and theory

The rephasing spectra were recorded by K. Hao and coworkers employing two different polarization combinations of the pulse sequence: First, in a co-circular configuration with four left-hand circularly polarized pulses $\sigma^+\sigma^+\sigma^+\sigma^+$ and second, in a cross-circular configuration with alternating polarizations $\sigma^+\sigma^-\sigma^+\sigma^-$. The two corresponding polarization-resolved spectra are shown in Fig. 5.7 (a) and (b). (c) and (d) represent the simulated rephasing signals for the two polarization combinations including exciton-exciton, exciton-trion, and trion-trion

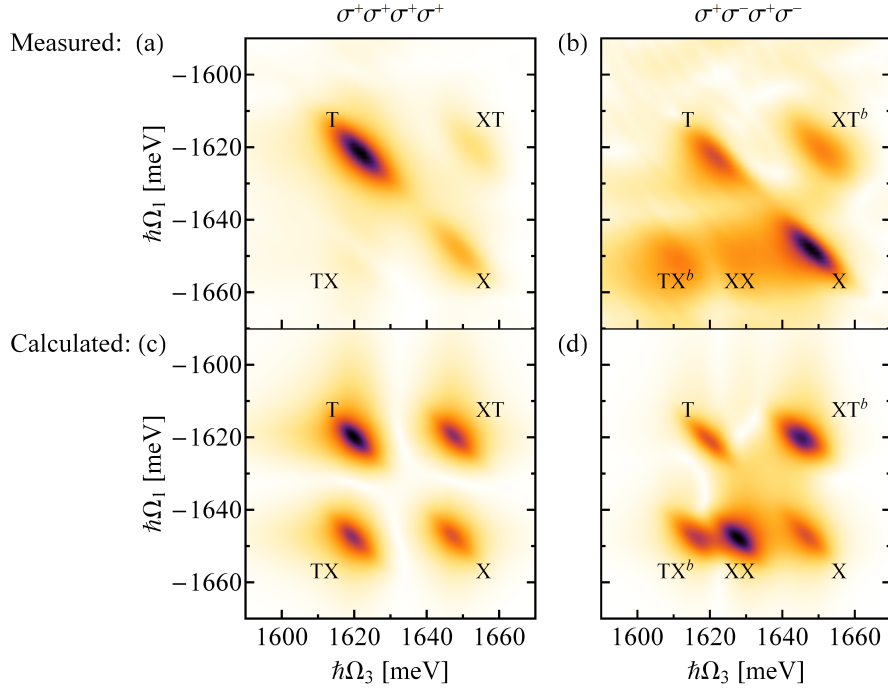


Figure 5.7: Amplitudes of the measured ((a)-(b)) and calculated ((c)-(d)) 2D coherent PE spectra. (a) and (c) are obtained using identical left-hand circular polarizations of the excitation pulses and the detected FWM signal (left column). Along the diagonal two peaks show up that are assigned to the degenerate excitation and emission of the exciton (X) and trion (T) resonances. In addition, two off-diagonal peaks (TX and XT) appear as a consequence of Pauli blocking (saturation) nonlinearities. (b) and (d) show the measured and simulated spectra for excitation using a cross-circular configuration with σ^+ polarization of the first and third pulse and σ^- polarization of the second and signal field (right column). An additional peak (XX) is featured in the spectra that is associated with the neutral bound biexciton. The shift of the off-diagonal XT^b and TX^b peaks along the Ω_3 axis towards lower emission energies is assigned to the charged bound biexciton. The measurements were performed by K. Hao et al. in the group of X. Li and the postprocessed plot data was provided by G. Moody. [Hao17]

couplings phenomenologically using the level scheme of Fig. 5.6 and the parameter set given in Tab. 5.1. Along the diagonals, two peaks show up that can be assigned to the trion resonance at $(E_T, -E_T)$ with $E_T \approx 1620$ meV and the exciton resonance at $(E_X, -E_X)$ with $E_X \approx 1650$ meV. In the co-circular excitation case, two additional peaks show up at the cross-diagonal intersections of the exciton and trion lines: TX at $(E_T, -E_X)$ connecting the $g \rightarrow X_K$ transition during T_1 with the $g \rightarrow T_K^-$ transition during T_3 and XT at $(E_X, -E_T)$ associated with the $g \rightarrow T_K^-$ transition during T_1 and the $g \rightarrow X_K$ transition during T_3 .

Next, the polarization combination is changed to cross-circular excitation $\sigma^+\sigma^-\sigma^+\sigma^-$. This allows to access the doubly excited state manifold via the ESA pathway, as illustrated in Fig. 5.1. In Fig. 5.7 (b), an additional peak labeled XX shows up whose emission energy along the Ω_3 axis is redshifted by $\Delta_{XX} \approx 20$ meV with respect to the exciton X . This spectral feature is attributed to the bound biexciton state. The time and polarization ordered pulse sequence and the energy level diagram shown in Fig. 5.8 gives a first graphical impression of the underlying processes in terms of the density matrix evolution: The first pulse (σ^+) resonantly drives the $g \rightarrow X_K$ transition, thus creating a coherence between the ground state g and the neutral K valley exciton during T_1 . Subsequently, the second pulse (σ^-) excites the exciton transition in the K' valley. During the T_2 interval, the density matrix is in a

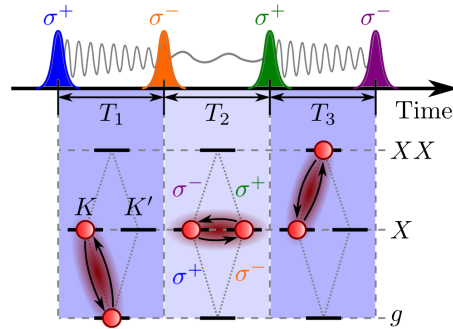


Figure 5.8: Graphical illustration of the **ESA** quantum pathway for cross-circular polarization of the exciting and signal fields. Their time and polarization ordering is shown by the pulse sequence in the upper part of the graph. The interactions are demonstrated below using a simple four-level system. The first pulse (σ^+) generates an exciton coherence in the K valley during T_1 . The second pulse (σ^-) drives the exciton transition in the K' valley. The third pulse (σ^+) excites the exciton-to-biexciton transition, which subsequently radiates as the four-wave mixing signal. [Hao17]

dipole-forbidden, non-radiative coherence between the excitons in the K and K' valleys due to Coulomb coupling. Finally, the third pulse (σ^+) drives the $X'_K \rightarrow XX$ transition, resulting in an optical exciton-to-biexciton coherence during T_3 , which then radiates as the **FWM** signal.

In the **ESA** quantum pathway, the density matrix oscillates with energy E_X during T_1 and with $E_X - \Delta_{XX}$ during T_3 with Δ_{XX} being the neutral biexciton binding energy. Accordingly, in frequency space the spectral contribution from the neutral biexciton (labeled XX) appears at the excitation energy $-E_X$ along the Ω_1 axis and emits redshifted by $\Delta_{XX} \approx 20$ meV with respect to the exciton resonance. In the same way, using cross-circular excitation it is possible to create charged five-particle doubly excited exciton-trion states, where an exciton in one valley is coupled to a trion in the other valley. As a consequence, the cross peaks TX^b and XT^b are redshifted along the Ω_3 axis by $\Delta_{XT} \approx 5$ meV with respect to TX and XT in the co-circular spectrum of Fig. 5.7 (a).

Interestingly, the intensity of the trion peak T relative to the exciton peak X is substantially reduced in the cross-circular excitation scheme compared to the co-circular case. This implies that trion-trion interactions associated with charged six-particle bound states composed of one trion per valley are considerably weaker than the tightly bound neutral biexciton XX . It is estimated to be an order of magnitude smaller: $\Delta_{TT} \approx 2$ meV, possibly due to spatial separation and weak localization of trions [Moo14]. As a consequence, the quantum pathways involving the singly and doubly excited states of the trion interfere destructively, thus reducing the amplitude of the trion peak T . This is discussed in more detail in the next section.

Within the considered spectral bandwidth, biexcitonic signatures are only visible if the first two pulses have opposite helicity. This confirms the level scheme of Fig. 5.6, where all doubly excited states in the f manifold are composed of two excitons with opposite valley indices. Hence, since only the K valley is addressed using solely left-hand circularly polarized light, the corresponding spectrum of Fig. 5.7 (a) does not involve the doubly excited state manifold.

Some differences in the relative peak intensities of the measured and calculated spectra are observed. Possible reasons for that are effects that are not included in the phenomenological model applied for the calculations, such as the electron density in the doped sample, disorder, excitation power, admixture of unwanted polarization components, fluctuations in the pulse bandwidth, higher-order effects beyond $\chi^{(3)}$, and varying dipole coupling strengths. However, the key features and overall peak patterns in the calculated signals are in agreement with the measured spectra.

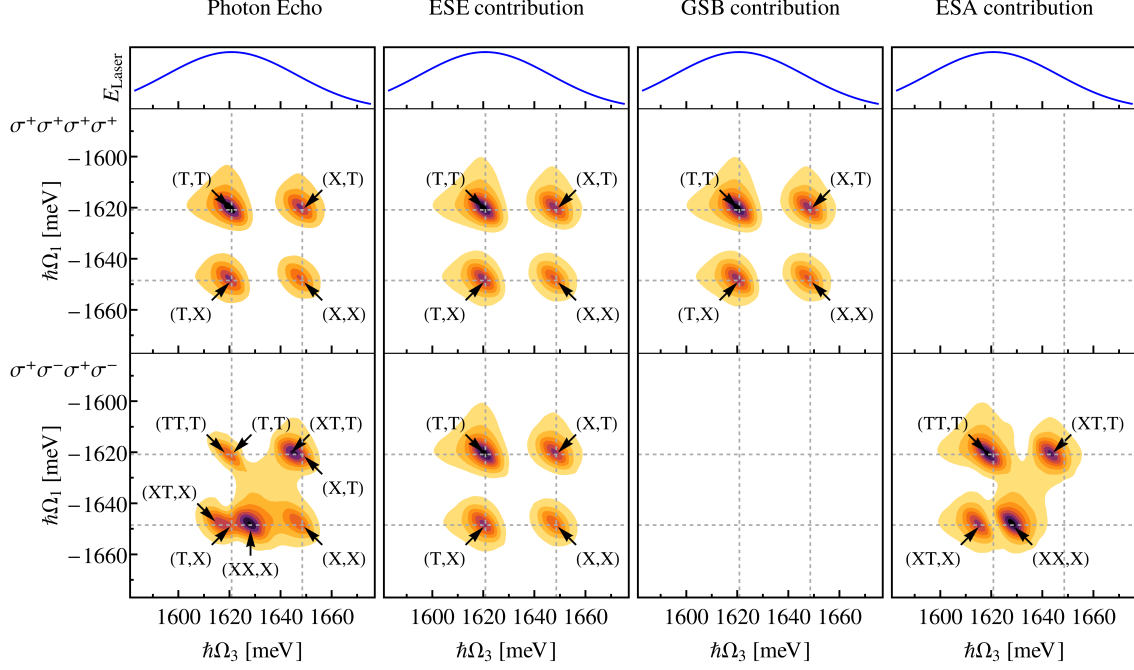


Figure 5.9: Simulated total photon-echo spectra, **ESE**, **GSB**, and **ESA** contributions (from left to right) for identical (upper row) and alternating (lower row) circular polarization combinations. The left column corresponds to the calculated spectra shown in Fig. 5.7 (c) and (d). The topmost curves show the excitation laser spectrum. The resonance peaks are labeled and marked by arrows. The spectra were calculated for the parameter set given in Tab. 5.1. Gray dashed lines have been inserted at the exciton and trion resonances of each frequency axis.

5.5.2 Discussion of the calculated spectra

The simulated rephasing signals for the co- and cross-circular polarization sequences are analyzed in more detail in this section. The distinct spectral features can be traced back to their microscopic origin by decomposing the full **PE** signal into its three different contributions stemming from the **ESE**, **GSB**, and **ESA** Liouville space pathways illustrated in the Feynman diagrams of Fig. 5.1. They are of course not separable in the experiment, however the theoretical treatment allows to inspect them individually, thus providing direct insight into the microscopic evolution of the system state and the complex interplay of the different space pathways.

As stated in the previous section, the rephasing **PE** spectrum for co-circular excitation (upper row of Fig. 5.9) features four resonances marked in the upper left spectrum: Two diagonal peaks labeled (X, X) and (T, T) at the spectral positions $(E_X, -E_X)$ and $(E_T, -E_T)$ as well as two off-diagonal peaks labeled (T, X) and (X, T) at the spectral positions $(E_T, -E_X)$ and $(E_X, -E_T)$, respectively. The diagonal population peaks are associated with the singly excited exciton and trion state in the K valley. The lower (upper) off-diagonal cross-peak (T, X) ((X, T)) combines an excitation at the exciton (trion) energy $\hbar\Omega_1 = -E_X$ ($\hbar\Omega_1 = -E_T$) with an emission at the trion (exciton) energy $\hbar\Omega_3 = E_T$ ($\hbar\Omega_3 = E_X$). According to the optical selection rules discussed in Sec. 5.3, only one valley is addressed using a co-circular excitation scheme within the considered spectral bandwidth: When a σ^- pulse excites the system, the spin \uparrow exciton in the K valley is populated. A second σ^- pulse resonant with the A transition can then not be absorbed any more due to Pauli blocking. Therefore, due to the co-circular excitation scheme and the valley-specific optical selection rules, the **ESA** quantum pathway involving bound biexciton states composed of one (charged) exciton in each valley does not

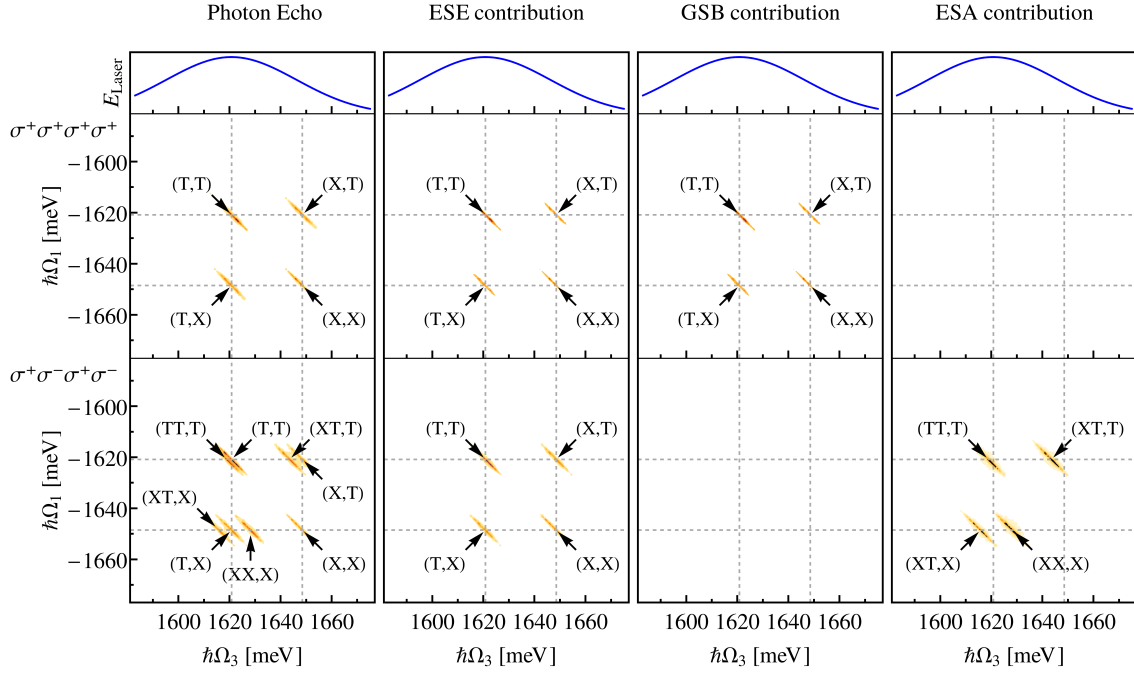


Figure 5.10: The same spectra as in Fig. 5.9, but for artificially low homogeneous broadening of $\gamma_{\text{hom}} = 0.1$ meV in order to resolve all signatures.

contribute. Many-body effects associated with interaction-induced shifts or binding between multiple quasiparticles will not contribute, since the doubly-excited state manifold does not enter the nonlinear optical response within the spectral bandwidth. As a consequence, the cross-diagonal peaks (T, X) and (X, T) are unshifted in the excitation and emission energies with respect to the exciton and trion marked by the intersections of the dashed gray lines. Pauli blocking causes that the cancellation of the **ESE** and **GSB** pathways through the **ESA** pathway (entering with opposite sign, cf. Eq. (5.4)) is incomplete due to the vanishing **ESA** signal [Hao17].

The situation changes in the case of cross-circular excitation with alternating circular polarizations (cf. lower row of Fig. 5.9). Here, the doubly-excited state manifold is accessible via the **ESA** pathway that involves transitions to biexcitons composed of one exciton per valley. This leads to additional spectral signatures in the calculated spectra that agree nicely with the measured spectrum shown in Fig. 5.7 (b). As stated in Sec. 5.2.2, the appearance of several off-diagonal resonance peaks implies the existence of many-body effects. These additional peaks indicate the formation of intervalley doubly-excited states composed of two Coulomb coupled quasi-particles (excitons or trions). This time, the **GSB** pathway does not contribute, which can again be understood by recalling the optical selection rules and the **GSB** Feynman diagram of Fig. 5.1: After the σ^+ polarized first pulse has excited a transition in the K valley, the second pulse cannot induce stimulated emission of this K valley transition at the opposite circular polarization σ^- . Instead, the **GSB** pathway requires the same helicity of the first and second excitation pulses. Due to the interaction-induced energy shifts of the doubly excited states f , the $e \rightarrow f$ transition energies are reduced compared to the corresponding $g \rightarrow e$ excitation energies. As a consequence, the emission energies (along the Ω_3 axis) of the $e \rightarrow f$ resonances in the **ESA** signal (lower right panel of Fig. 5.9) are redshifted with respect to the exciton and trion resonances marked by the dashed lines by the binding energies of the exciton-exciton (Δ_{XX}), trion-trion (Δ_{TT}), and exciton-trion (Δ_{XT}) complexes.

Table 5.2: Resonances contributing to the peak patterns for co- and cross-circular polarizations. A checkmark in the last two columns marks that the respective signature shows up in the co- and cross-circular polarized spectra, respectively. The upper four resonances correspond to the singly excited state manifold (**ESE** and **GSB** pathways), whereas the lower four peaks belong to the doubly excited state manifold (**ESA** pathway) and can therefore only be addressed using alternating circular polarizations due to the optical selection rules.

Label	Name	Spectral position (x, y) in meV	co	cross
(X, X)	exciton	$(E_X, -E_X) = (1648.5, -1648.5)$	✓	✓
(T, T)	trion	$(E_T, -E_T) = (1620.8, -1620.8)$	✓	✓
(T, X)	lower cross peak	$(E_T, -E_X) = (1620.8, -1648.5)$	✓	✓
(X, T)	upper cross peak	$(E_X, -E_T) = (1648.5, -1620.8)$	✓	✓
(XX, X)	exciton-exciton	$(E_X - \Delta_{XX}, -E_X) = (1628.2, -1648.5)$	✗	✓
(TT, T)	trion-trion	$(E_T - \Delta_{TT}, -E_T) = (1618.8, -1620.8)$	✗	✓
(XT, X)	lower exciton-trion	$(E_T - \Delta_{XT}, -E_X) = (1615.8, -1648.5)$	✗	✓
(XT, T)	upper exciton-trion	$(E_X - \Delta_{XT}, -E_T) = (1643.5, -1620.8)$	✗	✓

These multiple contributions from different states and pathways give rise to a rich peak pattern consisting of a total of 8 peaks in the full **PE** spectrum shown in the lower left panel of Fig. 5.9. For reasons of clarity, they are indicated by arrows. Due to the homogeneous and inhomogeneous broadening present in the sample, several of the resonances merge into one: The TX peak in the measured spectrum of Fig. 5.7 (b) is actually composed of the two peaks labeled (XT, X) and (T, X) . The measured XX and X peaks are here denoted (XX, X) and (X, X) , respectively. The two peaks (TT, T) and (T, T) again melt into one peak (T) in the experimental spectrum. Finally, the measured XT peak is composed of the two resonances (XT, T) and (X, T) . In order to resolve the full peak structure, the spectra are calculated again but this time with an artificially reduced homogeneous broadening of only 0.1 meV instead of 2 meV in Fig. 5.10. Here, all signatures are clearly visible. The individual resonances forming the peak patterns for the two polarization combinations are listed in Tab. 5.2.

The off-diagonal peaks showing up in the **PE** spectrum of Fig. 5.10 for alternating circular polarizations $\sigma^+\sigma^-\sigma^+\sigma^-$ (lower left panel) are: exciton-trion cross peaks, exciton-exciton peaks, and trion-trion peaks. They are discussed in the following subsections.

Exciton-trion peaks

The lower cross peak (T, X) in the spectrum connects the $g \rightarrow X_K$ transition at $\hbar\Omega_1$ and the $g \rightarrow T_K^-$ transition at $\hbar\Omega_3$. The upper cross peak (X, T) combines the $g \rightarrow T_K^-$ transition at $\hbar\Omega_1$ with the $g \rightarrow X_K$ transition at $\hbar\Omega_3$. Both cross peaks are unaffected by interaction-induced shifts, since the doubly excited state manifold is not involved in the formation of these peaks.

The lower exciton-trion peak (XT, X) is composed of the $g \rightarrow X_{K'}$ transition at $\hbar\Omega_1$ and the $X_{K'} \rightarrow X_{K'}T_K^-$ transition at $\hbar\Omega_3$. The upper exciton-trion peak (XT, T) combines the $g \rightarrow T_{K'}^-$ transition at $\hbar\Omega_1$ and the $T_{K'}^- \rightarrow X_K T_{K'}^-$ transition at $\hbar\Omega_3$. These exciton-trion peaks represent the **ESA** contributions from the charged five-particle bound states $X_{K'}T_K^-$ and $X_K T_{K'}^-$, composed of an exciton in one and a trion in the other valley. The associated exciton-trion binding energy $\Delta_{XT} = 5$ meV is considerably smaller than the tightly bound biexciton state XX , which is consistent with previous experimental and theoretical studies [Kyl15, Sin14].

Since Δ_{XT} is in the same order of magnitude as the homogeneous and inhomogeneous broadenings, the unshifted cross-diagonal peaks (T, X) and (X, T) stemming from the singly-excited state (**ESE**) contribution spectrally overlap and interfere with the doubly-excited

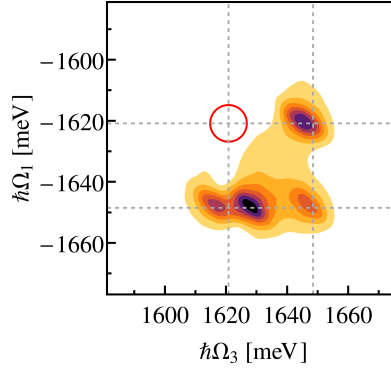


Figure 5.11: PE spectrum for cross-circular $\sigma^+\sigma^-\sigma^+\sigma^-$ polarization with the trion-trion coupling set to zero: $\Delta_{TT} = 0$. As a result, the diagonal trion peak vanishes, as marked by the red circle.

exciton-trion peaks from the **ESA** pathway. The spectral shifts of these superposed resonances denoted XT^b and TX^b peaks in the experimental and theoretical spectra of Fig. 5.7 (b) and (d) depend on the relative intensities and phases of the two system resonances they are built of and do not have to be identical for the lower and upper cross peaks. Therefore, in the experiment (cf. Fig. 5.7), a shift by 3 meV for the superposed upper cross peak is observed, while the superposed lower cross peak is shifted by 4.6 meV.

Exciton-exciton peak

The exciton-exciton peak (XX, X) is composed of the $g \rightarrow X_{K'}$ transition at $\hbar\Omega_1$ and the $X_{K'} \rightarrow XX$ transition at $\hbar\Omega_3$. It represents the intervalley biexciton composed of one exciton in each valley. Therefore, it is spectrally shifted from the exciton peak (X, X) by the biexciton binding energy $\Delta_{XX} = 20.3$ meV (cf. Tab. 5.1) along the emission energy Ω_3 axis. This value agrees very well with the biexciton binding energy predicted from previous microscopic calculations [Zha15, Ky15, May15, Kid16, Kez16].

Trion-trion peak

The trion-trion peak (TT, T) is composed of the $g \rightarrow T_{K'}^-$ transition at $\hbar\Omega_1$ and the $T_{K'}^- \rightarrow T_{K'}^-T_{K'}^-$ transition at $\hbar\Omega_3$. It represents the charged six-particle state composed of one trion in each valley with an estimated trion-trion binding energy of $\Delta_{TT} = 2$ meV. This small binding energy causes that the $T_{K'}^- \rightarrow T_{K'}^-T_{K'}^-$ transition in the **ESA** contribution is only slightly shifted along the Ω_3 axis and thus spectrally not well separated from the $g \rightarrow T_{K'}^-$ transition in the **ESE** contribution. As a consequence, they partly cancel each other out, resulting in a smaller overall amplitude of the superposed diagonal trion T peak compared to the trion peak in the co-circular spectrum. However, the appearance of the diagonal T peak in the measured spectrum in cross-circular configuration (cf. Fig. 5.7 (b)) is an indicator for a non-zero (but small) trion-trion coupling: Rerunning the simulations for $\Delta_{TT} = 0$ leads to a complete cancellation of the diagonal (T, T) peak, as shown in Fig. 5.11. This contradicts the experimental observation of an intense T peak. However, there are also other possible explanations for this T peak such as spectral diffusion, admixture of unwanted polarization components, or higher order effects.

5.6 Conclusion

In this chapter, polarization-resolved 2D rephasing PE signals of monolayer MoSe₂ were calculated and compared to the experiment. The optical response was derived from Liouville space pathways representing the evolution of the density matrix [Abr09]. Both the specific properties of the chosen spectroscopy technique and the characteristics of the material class were exploited in order to unfold the complex optical response in third order of the electric field and identify multiple higher-order correlated states by:

- employing FWM spectroscopy to spread the nonlinear signal across two axes,
- eliminating inhomogeneous broadening using the PE technique,
- using circularly polarized pulses for spin- and valley-selective excitation,
- restricting the system response to the *A* transitions between the highest valence and lowest conduction band through a careful choice of the pulse bandwidth,
- decomposing the simulated signal into the contributions from the different Liouville space pathways.

Spectral signatures showing up in the cross-polarized spectra were assigned to neutral and charged biexcitons. The quantum pathways giving rise to these states were analyzed taking into account the optical selection rules. It was found that all formed doubly excited states are intervalley states consisting of one (charged) exciton in the *K* and the other in the *K'* valley with large difference in crystal momentum. This makes them novel higher-order bound states with no direct analogue in conventional semiconductors [Hao17].

The microscopic evaluation of the calculated spectra helped to interpret the signatures showing up in the measured spectra based on a phenomenological model. Exciton-exciton and exciton-trion binding energies for the neutral and charged bound biexcitons were estimated as ~ 20 meV and ~ 5 meV, respectively. These values are in reasonable agreement with previous theoretical works [Kyl15, Zha15]. Moreover, the theoretical analysis showed that the diagonal trion peak *T* appearing with reduced relative intensity in the measured spectrum of Fig. 5.7 (b) is an indicator of a weak trion-trion coupling. This leads to the formation of bound six-particle states composed of one trion per valley that has so far not been observed in monolayer TMDs. However, the presented results contradict most previous experimental studies on TMDs where biexciton binding energies in the range of 40 – 80 meV (significantly higher than the trion binding energy) were found. Possibly, charged biexcitons or excited-state biexcitons have been observed and misclassified in these previous measurements [Zha15].

Comparing the calculated and measured spectra shows that the overall resonance peak structure coincides and the optical selection rules used to model the system are confirmed by the experimental findings. However, the relative peak intensities of the measured and calculated spectra show some deviations. This is likely connected to experimental parameters that are not taken into account by the phenomenological model applied for the calculations, such as doping concentrations, sample quality, variations in the excitation power and bandwidth, the experimentally achieved degree of circular polarization, higher-order contributions beyond $\chi^{(3)}$, etc. These effects may alter the spectral signatures and the bound quasi-particle states.

In summary, a very good agreement of the simulated and measured spectra was achieved using polarization-resolved 2D spectroscopy in the rephasing pulse geometry. The presented study contributes to a better understanding of the Coulomb-driven many-body interactions leading to the formation of correlated many-particle complexes in 2D TMDs. This could in turn support experimental studies in their search for even higher-order multiple-exciton correlations that are likely to form in this exciting new material class due to the long-range Coulomb

interactions [Tur10]. The intervalley composition of all found types of doubly excited states and the efficient control of light-matter interaction might pave the way towards the generation of novel polarization- and valley-entangled photon states.

6

Two-dimensional rephasing and double-quantum spectroscopy of single QDs and QD molecules

6.1 Introduction

Four-wave mixing (FWM) spectroscopy has been widely used to probe the ultrafast dynamics and coherent couplings of higher-order excited states in ensemble measurements of semiconductors [Cum94, Che01, Len04, Lan04, Vos06, Moo13a]. However, with regard to quantum information processing in solid-state implementations such as semiconductor quantum dots (QDs) [Los98, Bon98, Bay01, Mic03, Ram10], coherent control of individual excitons and their interactions on a local (Coulomb) and long-range (radiative) spatial scale draws increasing scientific interest. Coupling parameters such as the biexciton binding energy and fine-structure splitting in individual QDs forming exciton-biexciton systems [Fin13] are of particular interest for the generation of entangled photon pairs [Ben00, Seg05, Ste06, Ako06, Din10, Sal10, Car10, Mer16b]. Coherent couplings between different QDs and the underlying microscopic mechanisms play a major role for possible two-qubit operations [Nie00, Kas10]. Also, investigating the polarization-specific excitation pathways is important to selectively excite optical transitions in quantum optical applications [Ton12].

Studying individual transitions in single QDs also has the advantage to circumvent the strong inhomogeneous broadening due to the QD size dispersion which frequently masks the optical response in ensemble experiments. Only a residual spectral wandering of the resonance energies in time-averaged measurements causes a slight inhomogeneous broadening [Pat06, Kas13, Mer16a, Mer16b, Jak16].¹ For a high sample quality, the inhomogeneous linewidth is in the few μeV range, which is often in the same order as the homogeneous broadening and the temporal sensitivity of the experimental FWM setup dictated by the spectrometer resolution (~ 120 ps in the experiment discussed in this chapter) [Del17].

However, due to the bad signal-to-background ratio, probing individual excitonic transitions is a demanding task. In addition, a directional selection of the signal field is not possible for single nanostructures, which makes more challenging experimental detection techniques with a collinear geometry of the exciting pulses necessary. These problems are tackled using photonic nanostructures to improve the intrinsically weak FWM signal intensity of single QDs by enhancing the coupling to the external laser field [Fra16, Mer16a, Jak16].

In this chapter, the internal coupling mechanisms within individual InAs QDs and QD molecules embedded in a low- Q semiconductor microcavity [Mai14b] are analyzed using heterodyne detected two-dimensional (2D) coherent, nonlinear optical spectroscopy. The considered two-beam experiment conducted by Valentin Delmonte and conceptualized by Jacek Kasprzak at the Institut Néel in Grenoble, France, allows to exploit the rephasing photon echo (PE) as well as the double-quantum coherence FWM configurations by swapping the time ordering of the pulse sequence.

¹ Typical data acquisition times are in the range of tens to hundreds of seconds, where slow spectral diffusion processes can take place.

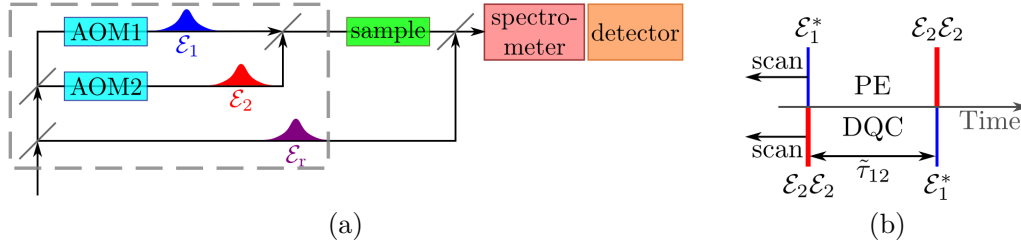


Figure 6.1: (a) Schematic setup of a heterodyne detected **FWM** experiment for a sub-wavelength sized nanostructure in a collinear geometry using acousto-optic modulators (AOM). The beam paths are encapsulated (marked by the dashed frame) in order to prevent air turbulence, thus suppressing phase fluctuations (passive stabilization) [Lan07]. (b) Pulse sequence applied in a two-beam **FWM** experiment. Two configurations are possible: A positive (negative) delay corresponds to the rephasing one-quantum **PE** (two-quantum **DQC**) pathways in the upper (lower) part of the graphics.

This chapter presents calculations of the corresponding **FWM** signals that allow to ascertain the coherent coupling mechanisms between individual quantum systems. This way, the intra- and interdot biexciton binding energies as well as the fine-structure splitting and the relative alignment of the laser polarization and **QD** axis can be determined. Thus, combining **2D** single and double quantum coherence spectroscopy is a powerful tool to study coherent couplings, representing a step forward in the quantum control of optically active two- and few-level systems present in semiconductor nanostructures. The main results of this chapter have been published in [Del17].

The chapter is organized as follows: First, the two-beam experiment with variable pulse ordering and the applied phase referencing technique for heterodyne detection is briefly introduced in Sec. 6.2. In Sec. 6.3, the corresponding signal functions are derived. The model system and Hamiltonian incorporating the optical selection rules are introduced in Sec. 6.4. Section 6.5 is dedicated to the analysis of the distinct spectral signatures and a comparison to the experiment. Finally, in Sec. 6.6 the situation including Förster coupling between the **QDs** is discussed. Section 6.7 briefly summarizes this chapter.

6.2 Two-beam four-wave mixing spectroscopy

In the considered two-beam **FWM** experiment conducted by V. Delmonte and J. Kasprzak, a pulse train spectrally centered around the optical resonance of interest is split up into two excitation pulses described by the electric field envelopes \mathcal{E}_1 and \mathcal{E}_2 and a reference pulse \mathcal{E}_r [Lan10]. The setup is schematically shown in Fig. 6.1 (a). An optical delay line enables a variable interval $\tilde{\tau}_{12}$ between the pulses \mathcal{E}_1 and \mathcal{E}_2 , which is positive for \mathcal{E}_1 leading. Using acousto-optic modulators, pulse 1 and pulse 2 are frequency upshifted by $\tilde{\omega}_1 = 80$ MHz and $\tilde{\omega}_2 = 80.77$ MHz. The two pulses are recombined in a beam splitter and interact with the sample (stored in a cryostat at 5 K) in the active region of a waveguide. The emitted signal then is recombined and interferes with the reference beam, whose temporal separation from \mathcal{E}_2 can also be varied. Finally, the signal is detected at the frequency $2\tilde{\omega}_2 - \tilde{\omega}_1 = 81.54$ MHz, corresponding in lowest-order (pulse 2 interacts twice, pulse 1 once) to the response $\mathcal{E}_1^* \mathcal{E}_2 \mathcal{E}_2$. The signal is spectrally dispersed using a spectrometer, detected with a CCD camera and retrieved in amplitude and phase by employing spectral interferometry [Del17].

Using optical delay lines, both the delay $\tilde{\tau}_{12}$ as well as the arrival time of the reference pulse can be adjusted. As mentioned in the introduction, by swapping the temporal ordering of the two light pulses, one- and two-quantum configurations can be distinguished experimentally. For positive delay $\tilde{\tau}_{12} > 0$, the rephasing **PE** pathway is recorded where $\tilde{\tau}_{12} = T_1$ represents the

delay between the first and second pulse and $T_2 = 0$ for the subsequent interactions induced by \mathcal{E}_2 according to the nomenclature introduced in Chap. 3. A negative delay $\tilde{\tau}_{12} < 0$ in turn corresponds to the **DQC** pathway with $\tilde{\tau}_{12} = -T_2$ and $T_1 = 0$.

In order to obtain the typical **FWM** frequency maps for the different pulse orderings by Fourier transforming the pulse delays, referencing the signal phase is a necessary precondition. In the experiment discussed in this chapter, a post-treatment protocol was established which uses auxiliary spectral interferences of the reference pulse \mathcal{E}_r with the individual excitation pulses \mathcal{E}_1 and \mathcal{E}_2 for phase-referencing. This way, the necessity of active phase stabilization during acquisition [Bri08, Hel11] is overcome. Further details on the implementation of this phase-referencing protocol are given in [Del17].

6.3 Calculation of the four-wave mixing signals

In this section, the rephasing one-quantum and two-quantum signals are calculated following [Abr09]. The applied optical field is described as a sequence of three pulses centered at times τ_j with frequencies ω_j and phases $\varphi_j = \tilde{\omega}_j T_j$:

$$\mathbf{E}(\mathbf{r}, t) = \sum_{j=1}^3 \sum_{u_j=\pm 1} \mathcal{E}_j^{u_j}(\mathbf{r}, t - \tau_j) e^{-iu_j\omega_j(t-\tau_j) + iu_j\varphi_j} \quad (6.1)$$

with $\mathcal{E}_2 = \mathcal{E}_3$, $\varphi_2 = \varphi_3$, and $\tau_2 = \tau_3$ in the considered two-beam experiment. As introduced in Sec. 3.2.2, the heterodyned signal in the optical $\chi^{(3)}$ regime is a function of the delay times T_j between the pulses:

$$S_{\tilde{\omega}_s}^{(3)}(T_3, T_2, T_1) = \int_{-\infty}^{+\infty} dt \mathbf{P}_{\tilde{\omega}_s}(t) \cdot \mathcal{E}_r^*(t - \tau_s) e^{i\tilde{\omega}_s(t - \tau_s)} \quad (6.2)$$

with reference field \mathcal{E}_r and third-order induced polarization $\mathbf{P}_{\tilde{\omega}_s}$ given in Eq. (3.3). In the considered experiment, the detected frequency combination is $\tilde{\omega}_s = 2\tilde{\omega}_2 - \tilde{\omega}_1$. If the field \mathcal{E}_1 interacts first, this corresponds to the rephasing **PE** phase combination $\varphi_I = -\varphi_1 + 2\varphi_2$ retrieved by the phase-referencing protocol of [Del17]. If the time ordering of the two driving pulses is swapped such that \mathcal{E}_2 is the leading pulse, the extracted phase combination $\varphi_{III} = 2\varphi_2 - \varphi_1$ coincides with the **DQC** configuration.

6.3.1 Rephasing photon echo signal

Three types of excitation quantum pathways contribute to the rephasing signal denoted excited state emission (ESE), ground state bleaching (GSB), and excited state absorption (ESA), as discussed in detail in Sec. 5.2.1. The corresponding double-sided Feynman diagrams are shown in Fig. 6.2 (a).² Remember that the **ESE** and **GSB** pathways incorporate only the ground state g and the singly excited state manifold e , whereas the **ESA** pathway includes also the doubly excited states f . In the absence of many-body interactions, the off-diagonal resonances stemming from the two Liouville space pathways involving singly excited states (lower transitions) destructively interfere with the ones from the **ESA** pathway including doubly excited states (upper transitions). This leads to a cancellation of all off-diagonal peaks [Kas10, Dai12, Moo13a].

The rephasing one-quantum signal in the frequency domain is obtained by Fourier transforming the third-order heterodyne-detected signal with respect to the time delays T_1 between

² Compared to Sec. 5.2.1, this time the pulses carry characteristic phases φ_j instead of wave vectors \mathbf{k}_j due to the collinear measurement setup used for single nanostructures.

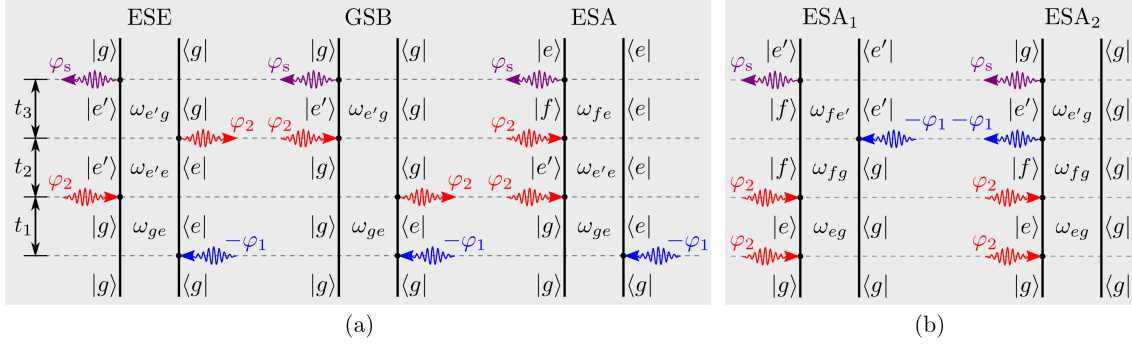


Figure 6.2: Double-sided Feynman diagrams for the rephasing (a) and double-quantum (b) signal representing the Liouville space pathways of the density matrix evolution in the considered two-beam experiment.

pulse 1 and 2 and T_3 between pulse 2 and the reference pulse, whereas T_2 is vanishing in the two-pulse experiment. The total rephasing PE signal is given by [Abr09]

$$S_{\text{PE}}^{(3)}(\Omega_3, \Omega_1) = S_{\text{ESE}}^{(3)}(\Omega_3, \Omega_1) + S_{\text{GSB}}^{(3)}(\Omega_3, \Omega_1) + S_{\text{ESA}}^{(3)}(\Omega_3, \Omega_1). \quad (6.3)$$

with

$$S_{\text{ESE}}^{(3)}(\Omega_3, \Omega_1) = i \frac{(2\pi)^4}{\hbar^3} \sum_{e, e'} (\mathbf{d}_{e'g}^* \cdot \mathcal{E}_s^*(\omega_{e'g} - \omega_s)) (\mathbf{d}_{e'g} \cdot \mathcal{E}_2(\omega_{e'g} - \omega_2)) \times \frac{\mathbf{d}_{eg} \cdot \mathcal{E}_3(\omega_{eg} - \omega_3) \mathbf{d}_{eg}^* \cdot \mathcal{E}_1^*(\omega_{eg} - \omega_1)}{\Omega_3 - \xi_{e'g} \Omega_1 - \xi_{ge}}, \quad (6.4)$$

$$S_{\text{GSB}}^{(3)}(\Omega_3, \tau_2, \Omega_1) = i \frac{(2\pi)^4}{\hbar^3} \sum_{e, e'} (\mathbf{d}_{e'g}^* \cdot \mathcal{E}_s^*(\omega_{e'g} - \omega_s)) (\mathbf{d}_{eg} \cdot \mathcal{E}_2(\omega_{eg} - \omega_2)) \times \frac{\mathbf{d}_{e'g} \cdot \mathcal{E}_3(\omega_{e'g} - \omega_3) \mathbf{d}_{eg}^* \cdot \mathcal{E}_1^*(\omega_{eg} - \omega_1)}{\Omega_3 - \xi_{e'g} \Omega_1 - \xi_{ge}}, \quad (6.5)$$

$$S_{\text{ESA}}^{(3)}(\Omega_3, \Omega_1) = -i \frac{(2\pi)^4}{\hbar^3} \sum_{e, e', f} (\mathbf{d}_{fe}^* \cdot \mathcal{E}_s^*(\omega_{fe} - \omega_s)) (\mathbf{d}_{e'g} \cdot \mathcal{E}_2(\omega_{e'g} - \omega_2)) \times \frac{\mathbf{d}_{fe'} \cdot \mathcal{E}_3(\omega_{fe'} - \omega_3) \mathbf{d}_{eg}^* \cdot \mathcal{E}_1^*(\omega_{eg} - \omega_1)}{\Omega_3 - \xi_{fe} \Omega_1 - \xi_{ge}}. \quad (6.6)$$

Here, $\xi_{ab} \equiv \omega_{ab} - i\gamma_{ab}$ has been defined, where \mathbf{d}_{ab} denotes the dipole moment, ω_{ab} the resonance energy and γ_{ab} the homogeneous broadening of the $b \rightarrow a$ transition. A detailed derivation can be found in App. A.

6.3.2 Double quantum coherence signal

Similarly, the two-quantum DQC signal is obtained by Fourier transforming the signal function with respect to the delay times T_2 between the leading pulse 2 and the subsequent pulse 1 and T_3 between pulse 1 and the reference pulse. In contrast to Sec. 3.3.3 where the signal was Fourier transformed with respect to T_1 and T_2 , here the 2D frequency map is calculated depending on Ω_2 and Ω_3 . This has practical reasons: First, the delay $T_1 = 0$ is fixed and second, the Fourier transform with respect to Ω_3 is directly achieved by the spectrometer, thus facilitating the data postprocessing. The DQC signal has two contributing ESA pathways

shown in Fig. 6.2 (b):

$$S_{\text{DQC}}^{(3)}(\Omega_3, \Omega_2) = S_{\text{ESA}_1}^{(3)}(\Omega_3, \Omega_2) + S_{\text{ESA}_2}^{(3)}(\Omega_3, \Omega_2) \quad (6.7)$$

with

$$S_{\text{ESA}_1}^{(3)}(\Omega_3, \Omega_2) = -i \frac{(2\pi)^4}{\hbar^3} \sum_{e, e', f} (\mathbf{d}_{fe'}^* \cdot \boldsymbol{\mathcal{E}}_s^*(\omega_{fe'} - \omega_s)) (\mathbf{d}_{eg} \cdot \boldsymbol{\mathcal{E}}_1(\omega_{eg} - \omega_1)) \times \frac{\mathbf{d}_{e'g}^* \cdot \boldsymbol{\mathcal{E}}_3^*(\omega_{e'g} - \omega_3)}{\Omega_3 - \xi_{fe'}} \frac{\mathbf{d}_{fe} \cdot \boldsymbol{\mathcal{E}}_2(\omega_{fe} - \omega_2)}{\Omega_2 - \xi_{fg}}, \quad (6.8)$$

$$S_{\text{ESA}_2}^{(3)}(\Omega_3, \Omega_2) = i \frac{(2\pi)^4}{\hbar^3} \sum_{e, e', f} (\mathbf{d}_{e'g}^* \cdot \boldsymbol{\mathcal{E}}_s^*(\omega_{e'g} - \omega_s)) (\mathbf{d}_{eg} \cdot \boldsymbol{\mathcal{E}}_1(\omega_{eg} - \omega_1)) \times \frac{\mathbf{d}_{fe'}^* \cdot \boldsymbol{\mathcal{E}}_3^*(\omega_{fe'} - \omega_3)}{\Omega_3 - \xi_{e'g}} \frac{\mathbf{d}_{fe} \cdot \boldsymbol{\mathcal{E}}_2(\omega_{fe} - \omega_2)}{\Omega_2 - \xi_{fg}}. \quad (6.9)$$

These signal functions allow to calculate **2D** maps of the rephasing and double-quantum pathways depending on the Fourier transformed pulse delays.

6.4 Quantum dot model system

6.4.1 Individual QD exciton-biexciton system with fine-structure splitting

An isolated **QD** with zincblende crystal structure located in a microcavity exhibits two *s*-shell transitions, namely the circularly polarized spin \uparrow and spin \downarrow excitons. In the following, the spectral bandwidth is chosen in a way that no higher transitions are driven.³ In the presence of an anisotropic confinement potential of the **QD**, the degeneracy of the two exciton states is lifted [Mer16b]. The reason is an exchange interaction between the two singly excited states within one **QD**, resembling a coupling between the transition dipoles of the two spatially superimposed circularly polarized excitons [Kas10]. This coupling within the single **QD** system leads to a new, linearly polarized basis of two excitonic eigenstates separated by the fine-structure splitting (FSS) δ , as shown in Fig. 6.3 (a). They are selectively addressed by driving the system along one of its polarization axes. This **FSS** is accompanied by a strong biexciton shift Δ_B altering the energy of the doubly excited state.

6.4.2 Quantum dot molecule

Now, a **QD** molecule is considered consisting of two electrostatically coupled **QDs** with resonance energies E_1 and E_2 , each with a **FSS** δ_1 and δ_2 , respectively. The level scheme and possible excitation pathways of such a **QD** molecule are schematically depicted in Fig. 6.3 (b). The electrostatic Coulomb interaction shifts the energy of each doubly excited state with respect to the sum of the energies of the contributing (isolated) single exciton states. Δ_1 (Δ_2) denotes the intradot biexciton shift within **QD** 1 (**QD** 2) and Δ_{12} represents the electrostatic interdot coupling between an exciton in **QD** 1 and an exciton in **QD** 2, forming a bound interdot biexciton B_{12} . The **FSS** determines the optical selection rules for linear polarization, cf. Sec. 6.4.1: Vertically polarized optical transitions are marked by red arrows, horizontally polarized by teal arrows in Fig. 6.3 (b).

³ This has the consequence that exciton complexes without a doubly excited state within the excitation bandwidth such as trions do not contribute to the **DQC** signal since they represent a single two-level system [Del17].

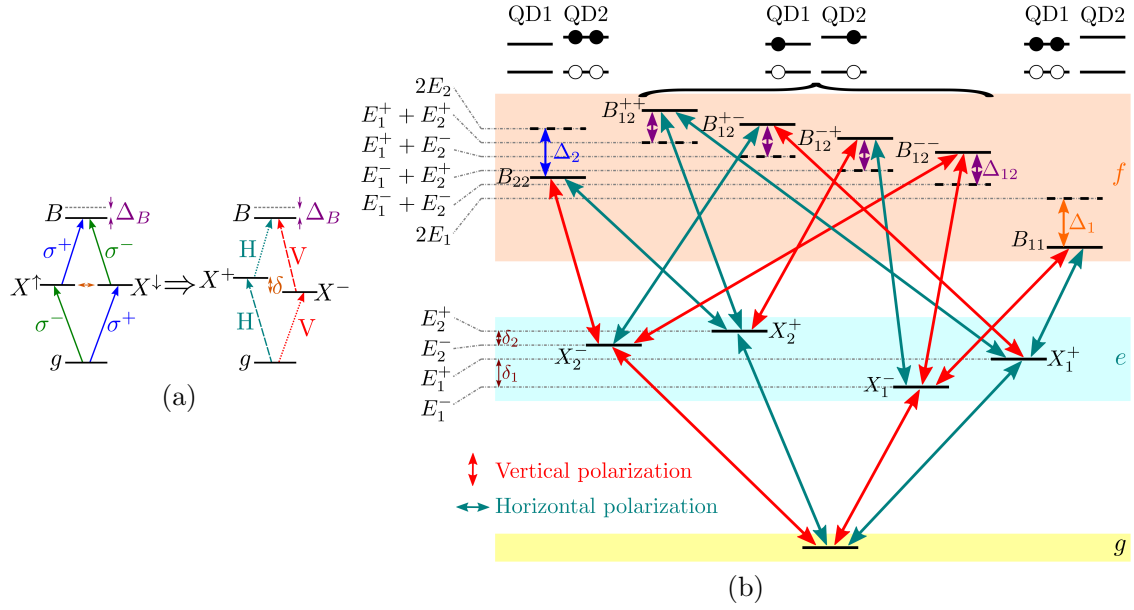


Figure 6.3: (a) Four-level system representing the s -shell excitons of a neutral single QD described as exciton-biexciton system. FSS lifts the degeneracy of the singly excited states, resulting in a transition from a circularly polarized to a linearly polarized excitation. ΔB denotes the biexciton binding energy. (b) Schematic level scheme of a QD molecule consisting of two QDs. The single exciton energies of the two QDs are E_1 and E_2 . Δ_{12} is the electrostatic coupling of a doubly excited interdot two-exciton state with one exciton in each QD. Both QDs exhibit a FSS δ_i , which separates the QD excitons into an upper state $E_i^+ = E_i + \frac{\delta_i}{2}$ and a lower state $E_i^- = E_i - \frac{\delta_i}{2}$ ($i = 1, 2$). For the considered QD molecule, the intradot biexciton binding energies Δ_1 and Δ_2 shift the biexciton states B_{11} at energy $2E_1$ and B_{22} at energy $2E_2$ towards lower energies. In contrast, the interdot coupling is repulsive, i.e., shifts the B_{12} states towards higher energies. [Del17]

6.4.3 Hamiltonian and model parameters

The procedure for deriving the energies and transition dipole moments in the delocalized basis of eigenstates of the electronic Hamiltonian is similar to the one presented in Chap. 4. The electronic Hamiltonian containing the free electron part, the FSS and the diagonal and Förster-type Coulomb part for a system of N_{QD} QDs reads in the local state basis:

$$\begin{aligned} \hat{H}_0 + \hat{H}_C = & E_0 |g\rangle\langle g| + \sum_{i=1}^{N_{\text{QD}}} \sum_{\sigma \in \{\uparrow, \downarrow\}} E_i |X_i^\sigma\rangle\langle X_i^\sigma| + \frac{1}{2} \sum_{i,j} \sum_{\sigma, \mu} (E_i + E_j + \Delta_{ij}) |B_{ij}^{\sigma\mu}\rangle\langle B_{ij}^{\sigma\mu}| \\ & + \left\{ \sum_i \frac{\delta_i}{2} |X_i^\uparrow\rangle\langle X_i^\downarrow| + \frac{1}{2} \sum_{i,j} \sum_{\sigma} \frac{\delta_i}{2} (|B_{ij}^{\uparrow\sigma}\rangle\langle B_{ij}^{\downarrow\sigma}| + |B_{ji}^{\sigma\uparrow}\rangle\langle B_{ji}^{\sigma\downarrow}|) + h.c. \right\} \quad (6.10) \\ & + \left\{ \sum_{i < j} \sum_{\sigma, \mu} V_{\sigma\mu}^F |X_i^\mu\rangle\langle X_j^\sigma| + \sum_{i,j < k} \sum_{\sigma, \mu, \nu} V_{\sigma\mu}^F |B_{ij}^{\nu\mu}\rangle\langle B_{ik}^{\nu\sigma}| + h.c. \right\} \end{aligned}$$

Note that Pauli-forbidden biexciton states such as $B_{11}^{\uparrow\uparrow}$ where two electrons with identical spins reside within the same QD are excluded. As introduced in Sec. 6.4.2, E_i denotes the energy (renormalized by the electrostatic Coulomb coupling) of a singly excited state in QD i . Δ_{ij} denotes the two-exciton shift for a doubly excited state composed of two single excitons in QD i and j with $\Delta_{ii} \equiv \Delta_i$ in the level scheme of Fig. 6.3 (b). The FSS δ_i lifts the degeneracy of the two excitons within one QD, as discussed in Sec. 6.4.1. Finally, $V_{\sigma\mu}^F$ denotes the spin-preserving

Table 6.1: Model parameters used to calculate the optical response of a QD molecule composed of two coupled QDs and an individual QD.

	QD 1	QD 2	QD 3
resonance energy	$E_1 = 1358.95 \text{ meV}$	$E_2 = 1359.7 \text{ meV}$	$E_3 = 1360.1 \text{ meV}$
transition dipole moment	$d_1 = 0.5 \text{ e nm}$	$d_2 = 0.5 \text{ e nm}$	$d_3 = 0.6 \text{ e nm}$
fine-structure splitting	$\delta_1 = 140 \mu\text{eV}$	$\delta_2 = 60 \mu\text{eV}$	-
biexciton binding energy	$\Delta_1 = -3.6 \text{ meV}$	$\Delta_2 = -3.3 \text{ meV}$	$\Delta_3 = -3.5 \text{ meV}$
interdot coupling	$\Delta_{12} = +0.09 \text{ meV}$		-

($\sigma = \mu$) and -flipping ($\sigma \neq \mu$) Förster coupling between different QDs.

In the experimental spectra recorded by V. Delmonte, signatures of a QD molecule consisting of two electrostatically coupled InAs QDs labeled 1 and 2 and an isolated QD 3 were observed, as verified by the calculations performed as part of this work (cf. Sec. 6.5). Therefore, the Hamiltonian of Eq. (6.10) was adapted to the specific three-QD situation and the energies and coupling elements were chosen in agreement with the experimental data [Del17]. All parameters used to calculate the one- and two-quantum 2D FWM spectra are given in Tab. 6.1. In order to obtain the system eigenstates and energies as well as the dipole moments in the delocalized exciton basis, the electronic Hamiltonian of Eq. (6.10) was numerically diagonalized, as demonstrated in more detail in Sec. 4.2.4. This yields the electron-light coupling Hamiltonian in the new exciton basis of delocalized singly (e) and doubly (f) excited states:

$$\hat{H}_{\text{el-L}} = - \sum_e \mathbf{d}_{ge} \cdot \mathbf{E}(t) |g\rangle \langle e| - \sum_{e,f} \mathbf{d}_{ef} \cdot \mathbf{E}(t) |e\rangle \langle f| + h.c. \quad (6.11)$$

The Förster coupling was found to be vanishing in the measured spectra, as discussed later in Sec. 6.6.

The homogeneous linewidth in QD systems is typically in the order of several μeV , corresponding to a dephasing time of few hundred picoseconds [Sto11, Ost12]. Here, $\gamma = 1/(500 \text{ ps})$ is used for the calculations [Bor01]. Additionally, the spectrometer resolution of $\sim 25 \mu\text{eV}$ is accounted for by incorporating it into the homogeneous linewidth [Kas10]. The transition dipole moments of the two QDs forming the QD molecule are chosen equally. Spectral wandering causes an inhomogeneous broadening of $10 \mu\text{eV}$ [Mer16b]. This is included in the calculations by averaging the contributions to the signal functions for normally distributed values of the system resonances. However, it does not have a noticeable effect on the line shapes since they are dominated by the homogeneous broadening due to the spectrometer resolution.

6.5 Discussion of the spectral signatures

The left panel of Fig. 6.4 shows the measured PE (a) and DQC (c) spectra of the three-QD system described in the previous section. The corresponding simulations of the rephasing and DQC signals calculated for the parameter set of Tab. 6.1 are presented in the right panel. The multiple off-diagonal peaks in the PE spectrum are decisive signatures of multiple interdot and intradot exciton couplings in the QD system, which are analyzed in the following. Figure 6.5 illustrates the expected peak pattern and the underlying energies and couplings determining the measured and calculated spectra of Fig. 6.4.

Both the rephasing and the two-quantum spectra share a common $\hbar\Omega_3$ axis displaying the FWM frequency recorded by the spectrometer. Along this axis, ground state to single exciton ($G \rightarrow X$) and single exciton to two exciton transitions ($X \rightarrow B$) appear. For positive delays $\tilde{\tau}_{12} > 0$, the $\hbar\Omega_1$ axis contains the $G \rightarrow X$ transitions, such that the photon echo of all single

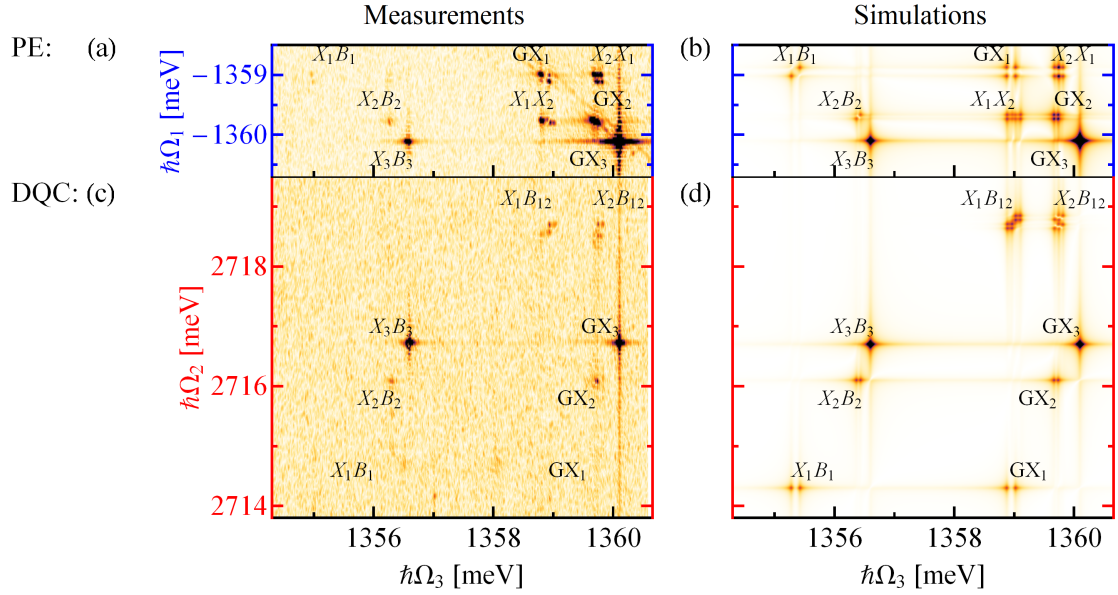


Figure 6.4: Measured ((a) and (c)) and calculated ((b) and (d)) single and double quantum 2D FWM spectra of a system of three QDs, two of which are electrostatically coupled and form a QD molecule. The coherent couplings between QD 1 and 2 as well as the intradot couplings in all three QDs are revealed using 2D rephasing PE ((a) and (b)) and DQC ((c) and (d)) spectroscopy. The plot data for the experimental spectra were provided by J. Kasprzak. [Del17]

exciton resonances shows up along the diagonal $\Omega_1 = -\Omega_3$. Three main resonances GX_1 , GX_2 , and GX_3 are visible on the diagonal at frequencies $E_1 = 1358.95$ meV, $E_2 = 1359.7$ meV, and $E_3 = 1360.1$ meV, belonging to the three QDs.⁴ For negative delay times, the ground state to two-exciton coherences driven by the second pulse emerge along the $\hbar\Omega_2$ axis, corresponding to the sum of the $G \rightarrow X$ and $X \rightarrow B$ transitions.

A single exciton-biexciton pair (peaks GX_3 and X_3B_3) shows up in both PE and DQC spectra at the FWM frequencies $E_3 = 1360.1$ meV and $E_3 + \Delta_3 = 1356.6$ meV.⁵ This pair can be attributed to the isolated QD 3 that is not involved in the molecule formation. The $X \rightarrow B$ transition marked by the X_3B_3 peak in the PE and DQC spectra of Fig. 6.4 is redshifted along the $\hbar\Omega_3$ axis by the binding energy $\Delta_3 = -3.5$ meV with respect to GX_3 . The resonance peaks belonging to the isolated QD 3 exhibit a higher oscillator strength than the other two QDs, which is reflected by a slightly larger transition dipole moment $d_3 = 0.6$ e nm compared to the two coupled QDs 1 and 2 with $d_1 = d_2 = 0.5$ e nm. The peaks exhibit no FSS, suggesting that QD 3 is driven along its polarization axis.

Similar exciton-biexciton peak pairs can be identified for the QDs 1 and 2: The X_1B_1 and X_2B_2 resonance peaks are off-diagonally shifted along the FWM axis by the intradot biexciton binding energies $\Delta_1 = -3.6$ meV and $\Delta_2 = -3.3$ meV with respect to the GX_1 and GX_2 peaks, respectively (see also Fig. 6.5). However, the peak pattern belonging to the QD molecule composed of the QDs 1 and 2 exhibits further features that significantly differ from the exciton-biexciton resonance peak pair of the individual QD 3 in two major respects:

⁴ It is important to note that no biexciton signatures show up on the diagonal of the measured rephasing spectrum. This observation confirms that the first pulse \mathcal{E}_1 does not excite any $X \rightarrow B$ transition, ensuring that the measurements indeed take place in the low-excitation $\chi^{(3)}$ regime.

⁵ Note that the biexciton binding energies Δ_i are negative, i.e., they reduce the energy of the biexciton state composed of two excitons in QD i with respect to the sum of the exciton resonances.

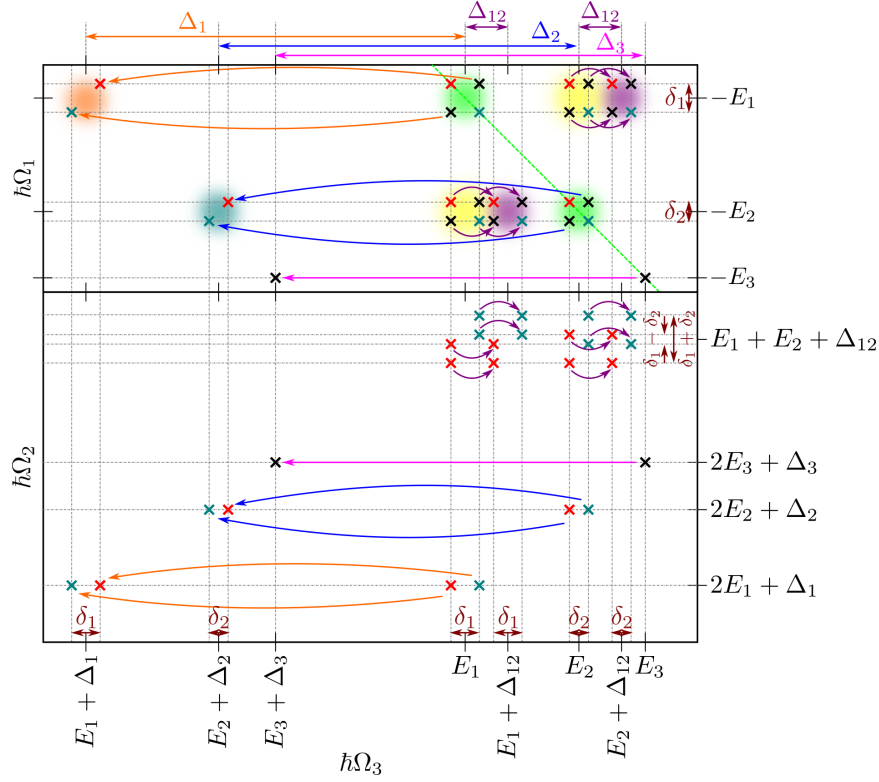


Figure 6.5: Sketch of the resonance peak patterns in the one- (upper panel) and two-quantum spectrum (lower panel) of the considered system of three QDs with resonance energies E_i , FSS δ_i , and biexciton binding energies $\Delta_i < 0$ (not true to scale). The electrostatic coupling $\Delta_{12} > 0$ between QDs 1 and 2 leads to the formation of a QD molecule, whereas QD 3 is independent. In contrast to the intradot couplings Δ_i , the interdot coupling Δ_{12} is positive and shifts the resonance peaks towards higher energies. The dashed green line marks the diagonal $\Omega_1 = -\Omega_3$ in the PE spectrum. Teal markers label the spectral positions of peaks that are observed when all pulses have a linear horizontal polarization, whereas red markers denote the peaks visible when applying a vertically polarized pulse sequence. If the polarization is somewhere in between these two cases, all marked positions show up in the spectrum. The arrows in the plot mark the interaction-shifted peaks due to intradot (orange, blue, and pink) and interdot (purple) exciton couplings. These shifted peaks showing up in addition to the unshifted cross peaks indicate coherent couplings.

1. In contrast to the isolated exciton-biexciton system of QD 3, the two coupled QDs 1 and 2 show a pronounced FSS in the order of $\delta_1 = 140 \mu\text{eV}$ and $\delta_2 = 60 \mu\text{eV}$, respectively. This leads to a splitting of each exciton resonance GX_1 and GX_2 along the diagonal of the rephasing spectrum into clusters of four peaks. In the measured spectra of Fig. 6.4 (a) and (c), the resonance peaks of the two exciton levels of each QD 1 and 2 separated by the FSS are (more or less) equally pronounced. Therefore, an angle of 45° between the linear polarization direction of the driving/reference pulse and the anisotropy axis of the two dots is assumed for the theoretical calculation. This way, all the interaction pathways shown in the level scheme of Fig. 6.3 (b) contribute to the measured signal. Compared to the FSS of only $35 - 40 \mu\text{eV}$ found in similar systems [Mer16b], here a much higher FSS is observed for the resonances associated with the QD molecule. This suggests that the spatial proximity of the two coupled QDs alters the local symmetry of the confinement, thus changing the magnitude of the FSS and the polarization of the excitonic transitions [Del17].

2. Two off-diagonal cross peaks labeled X_2X_1 (upper cross peak) and X_1X_2 (lower cross peak) appear in the rephasing spectrum at the spectral positions ($\hbar\Omega_3 = E_2, \hbar\Omega_1 = -E_1$) and ($\hbar\Omega_3 = E_1, \hbar\Omega_1 = -E_2$), respectively. They form a square with the two diagonal GX_1 and GX_2 resonances at energies $E_1 = 1359.7$ meV and $E_2 = 1358.95$ meV. The existence of these off-diagonal cross peaks clearly indicates a coherent interdot exciton-exciton coupling between the two QDs: The energy of the interdot biexciton B_{12} consisting of one exciton in each QD is renormalized by the electrostatic Coulomb coupling. This biexciton shift breaks the symmetry of the lower $G \rightarrow X_1$ ($G \rightarrow X_2$) and higher $X_1 \rightarrow B_{12}$ ($X_2 \rightarrow B_{12}$) transitions such that the Liouville space pathways involving the singly excited states do not destructively interfere with the ESA pathway including doubly excited states any more. As a consequence, cross peaks show up due to the incomplete cancellation.

The electrostatic interdot coupling Δ_{12} between an exciton in QD 1 and an exciton in QD 2 is small compared to the intradot biexciton binding energies of several meV as well as the linewidth and spectrometer resolution. As a result, the corresponding interaction-shifted resonances marked by the purple peak clusters in the sketch of Fig. 6.5 cannot be identified as separate peaks in the measured rephasing spectrum of Fig. 6.4 (a). To better resolve the signatures, three horizontal slices through the measured PE spectra at the fixed excitation energies $\hbar\Omega_1 = -E_1, -E_2, -E_3$ are plotted in the left column of Fig. 6.6, depicting the FWM amplitude as a function of the emission energy $\hbar\Omega_3$. The corresponding simulations are shown in the right column. The cuts at energies E_1 and E_2 reveal that Δ_{12} shifts the interdot two-exciton resonances towards higher energies (repulsion), showing up as blueshifted high-energy shoulders of the exciton cross peaks marked by the red circles in Fig. 6.6. The calculations suggest that the interdot biexciton binding energy is of the order $\Delta_{12} = +0.09$ meV.

In addition to the FWM amplitude, the orange traces in Fig. 6.6 depict the phases of the FWM signals in the rephasing configuration. As expected for a single Lorentzian resonance, a phase shift of π is observed for the diagonal peaks. The off-diagonal cross peaks in the upper two panels exhibit a 2π phase shift, since they are – although not well separated in the spectra – composed of two resonances: the unshifted cross peak and the interaction-shifted peak, each inducing a π phase shift [Kas10, Ard16]. The intersection through the exciton-biexciton pair of QD 3 (lowermost panels of Fig. 6.5) reveals that both the GX_3 and X_3B_3 resonances are accompanied by a π phase shift each in the absence of coherent couplings to other QDs. Note that the calculated amplitudes and phases shown in the intersections of Fig. 6.6 quantitatively differ from the measured ones, since in the calculations the FSS is better resolved. On the other hand, the overlap with neighboring Lorentzian-shaped resonance peaks has a stronger impact in the simulated spectra, resulting in phase interferences and amplitude superpositions. For example, the slight jitter in the calculated phase and amplitude traces of QD 3 (lowermost panel on the right-hand side) stems from spectral wings of the GX_2 , X_1X_2 , and X_2B_2 resonance peaks. They are not observed in the measured intersections, since here they are covered by the strong background.

In the DQC spectra of Fig. 6.4 (c) and (d), the three QDs form exciton-biexciton complexes at the two-photon frequencies $\hbar\Omega_2 = 2E_1 + \Delta_1 = 2714.3$ meV, $2E_2 + \Delta_2 = 2716.1$ meV, and $2E_3 + \Delta_3 = 2716.7$ meV respectively. The corresponding peak pairs are labeled GX_i and X_iB_i with $i = 1, 2, 3$. Note that the peak pair GX_1 and X_1B_1 is hardly visible in the measured DQC spectrum of Fig. 6.4 (c), since it is outside the spectral bandwidth. The coupling of the two QDs 1 and 2 manifests itself in a peak pair labeled X_1B_{12} and X_2B_{12} representing the interaction-shifted $G \rightarrow B_{12}$ transition (energy $\hbar\Omega_2 = E_1 + E_2 + \Delta_{12} = 2718.74$ meV) with FWM frequencies $\hbar\Omega_3 = E_1 = 1359.7$ meV and $\hbar\Omega_3 = E_2 = 1358.95$ meV, respectively. In the absence of interdot interactions, these peaks would cancel each other out due to the opposite signs of the two ESA pathways entering the full DQC signal.

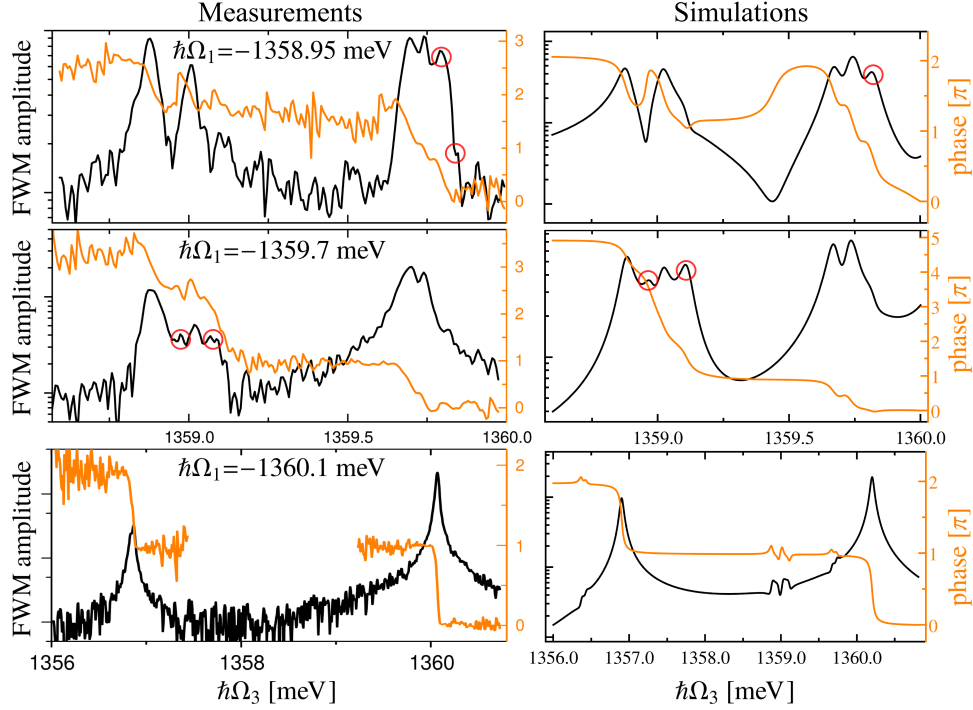


Figure 6.6: FWM amplitudes (black traces) and phases (orange traces) retrieved from horizontal cuts through the 2D maps of the measured (left column) and calculated (right column) rephasing signals shown in Fig. 6.4 (a) and (b), respectively, at the three QD resonance energies $E_1 = 1358.95$ meV, $E_2 = 1359.7$ meV, and $E_3 = 1360.1$ meV. [Del17]

6.6 Comparison to a Förster-coupled quantum dot molecule

Hyperspectral imaging reveals that the two QDs 1 and 2 forming the molecule are simultaneously excited by a laser spot focused down to the diffraction limit of around $0.85 \mu\text{eV}$. Thus the two coupled dots are found to be within a few hundred nm vicinity [Del17, Kas10]. This raises the question whether other short-ranged interaction mechanisms such as dipole-induced Förster coupling or Dexter-type coupling via wave-function overlap are present in the QD molecule, possibly contributing to the extraordinarily high FSS.

However, the Förster coupling strength is expected to be in the order of μeV [Spe15], which is too small to be detected within the given spectrometer resolution of $25 \mu\text{eV}$. To inspect a possible dipole-dipole coupling anyways, a (large) Förster coupling of $V_{\sigma\mu}^F = 0.1$ meV was included in the calculated spectra of Fig. 6.7. This Förster coupling leads to an additional slight splitting of the exciton resonances. However, this so-called Förster shift scales nonlinearly with the ratio $V_{\sigma\mu}^F/|E_1 - E_2|$, making a considerable Förster coupling strength necessary to have a noticeable effect on the spectral signatures.

Moreover, the Förster coupling leads to two additional peaks in the rephasing PE spectrum of Fig. 6.7 (a) that show up at frequencies ($\hbar\Omega_3 = E_1 - (E_2 - E_1) + \Delta_1 = 1354.6$ meV, $\hbar\Omega_1 = -E_2$) and ($\hbar\Omega_3 = E_2 - (E_1 - E_2) + \Delta_2 = 1357.15$ meV, $\hbar\Omega_1 = -E_1$), as highlighted by the green circles in Fig. 6.7. These peaks mark spectral positions where the third pulse creates an XB coherence involving an intradot biexciton in one QD after the first pulse has created a GX coherence involving a single exciton in the other QD. Speaking in terms of the level scheme of Fig. 6.3 (b), the Förster coupling connects the X_2^\pm (X_1^\pm) states with the biexciton state B_{11} (B_{22}). This process is only possible due to the Förster exciton transfer between the QDs. In a similar manner, four additional peaks show up in the DQC spectrum of Fig. 6.7 (b)

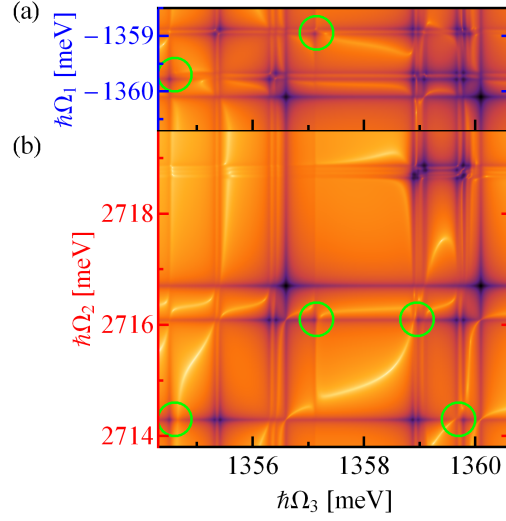


Figure 6.7: Calculated rephasing one-quantum (a) and non-rephasing two-quantum (b) 2D FWM spectra including Förster coupling. The additional peaks arising due to exciton transfer processes between the QDs are highlighted by green circles.

marking spectral positions where the second pulse creates a GB coherence involving an intradot biexciton in one QD before the third pulse induces a GX or XB coherence involving a single exciton in the other QD. However, these peaks are not observed in the experimentally measured spectra, meaning that Förster and Dexter coupling processes (that have a similar effect on the spectral signatures) are negligible and electrostatic couplings dominate the spectral signatures.

6.7 Summary

In this chapter, calculations reproducing the measured one- and two-quantum spectra of individual QDs were presented, allowing to identify different intradot and interdot coupling types and strengths and providing evidence of an isolated QD and a QD molecule consisting of two electrostatically coupled QDs at the probed sample spot. It was demonstrated that the combination of rephasing and double-quantum spectroscopy by swapping the pulse ordering in a two-beam experiment constitutes a valuable tool to detect and characterize coherent coupling mechanisms between excitons and the structure of the involved (bi)exciton states.

The theoretical model incorporates the optical selection rules, the FSS and intradot biexciton binding energies, and the interdot coupling between the excitons addressed within the spectral bandwidth. The electrostatic Coulomb interaction turns out to be the dominant coupling mechanism, whereas Förster-type coupling processes are not relevant in the considered quantum system. Moreover, while the isolated QD is driven along its polarization axis, the resonances associated with the QD molecule exhibit a pronounced FSS of a factor 2 to 3 higher than expected from earlier experimental studies [Mer16b]. A possible explanation is that the interdot coupling affects the confinement geometry and thus the magnitude of the FSS and the polarization of the excitonic eigenstates.

In summary, the presented study suggests a methodology to infer Coulomb-mediated couplings in QD molecules, which serve as possible building blocks for quantum information processing units, e.g., in terms of electrostatically coupled qubits [Par05, Shu12, Ard16].

Part III

Excitation transfer in hybrid inorganic/organic systems

7

Excitation transfer from semiconductor continuum states into an ordered molecular layer

7.1 Introduction

The construction and characterization of hybrid inorganic/organic systems (HIOS) has evolved into a vibrant research field over the last years [Bas99, Blu06, Its07, Nev08, Blu10, Vay12, Lia13, Qia15, Fri15, Sch15, Lju17]. By exploiting the benefits of both constituents, they form highly flexible building blocks for a large variety of optoelectronic applications, ranging from photovoltaics using dye-sensitized solar cells [Bac98, Ima09, Har12, Lju17] to light-emitting devices [Nev08, Bia14]. In this chapter, the Coulomb induced excitation transfer from continuum states of a semiconductor substrate into a highly ordered molecular single layer across the hybrid interface as well as within the organic layer is studied on a microscopic level, cf. Fig. 7.1 (c). Parts of this chapter have been published in [Spe16a, Spe18].

Electronic states in an inorganic semiconductor can couple non-radiatively to Frenkel excitons in organic molecules via dipole-dipole interaction. This Förster-type excitation transfer [För48] in hybrid systems has been studied both experimentally [Blu06, Blu08a, Nev08, Its07, Ple15, Qia15] and theoretically [Agr94, Agr98, Nev08, Ver14]. To ideally exploit the beneficial properties this novel material class is capable of, extensive parameter studies are of major interest in order to explore the operating regimes for optimized device performance. Therefore, this chapter aims at an in-depth theoretical understanding of the Coulomb-mediated excitation transfer efficiency in such HIOS depending on the specific geometry and preparation of the heterostructure.¹

The optical absorption and Förster coupling characteristics have been investigated by E. Verdenhalven et al. [Ver14], where a Heisenberg equation of motion technique based on the density matrix formalism was used to derive Bloch equations for the composite inorganic-organic system. Here, a von Neumann equation technique is used, where the Coulomb interactions between the inorganic and organic constituent (referred to as “interlayer coupling”) as well as between different molecular exciton states within the organic layer (referred to as “intermolecular coupling”) are taken into account, cf. Fig. 7.1 (c). Besides the above-mentioned dipole-dipole excitation transfer processes, also electrostatic monopole-monopole coupling terms enter the considered Coulomb Hamiltonian, inducing monopole-monopole shifts in the resonance energies that strongly depend on the molecular coverage. The microscopic Coulomb coupling elements are calculated using so-called atomic (transition) partial charges. They are obtained from density-functional theory (DFT) calculations employing the hybrid xc-functional HSE06, provided by B. Bieniek and P. Rinke from the Fritz-Haber-Institut (FHI) Berlin.

In this chapter, strong electrical pumping of the semiconductor substrate is considered,

¹ Note that depending on the growth technique and material, a quantum well is usually embedded in a heterostructure [Blu06] and an organometallic donor or acceptor layer can be inserted to reduce the interlayer energy-level offset by work-function tuning [Sch15]. This is not included in the simple model system used here, since it is not supposed to change the electron dynamics considerably.

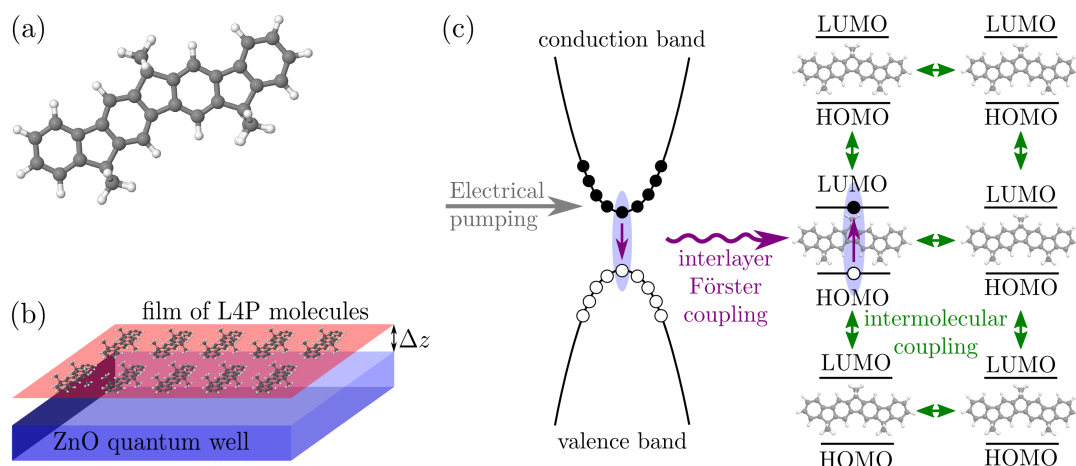


Figure 7.1: (a) Atomic structure of the L4P molecule. C atoms are colored in gray, H atoms in white. (b) The model system consisting of an organic molecular single layer adsorbed on an inorganic semiconductor QW with interlayer separation Δz . (c) Scheme of Förster energy transfer from an electrically pumped semiconductor into the molecular film. The interlayer Förster coupling is marked by purple arrows, the intermolecular Coulomb coupling is indicated by green arrows.

where Förster coupling transfers the excitation into the optically active, weakly bonded organic film (cf. Fig. 7.1 (c)). This represents the case of operating an inorganic/organic structure as hybrid light emitter, where the efficient electrical charge carrier injection into the semiconductor substrate is combined with the radiative emission yield of molecules [Bia14]. Note that electronic wave-function overlap between the two layers as well as between different molecules is assumed to be negligible. The intermolecular Coulomb interaction leads to the formation of (flat) electronic bands within the molecular system. This plays a role especially for small intermolecular distances, i.e., densely packed molecular films. Molecular excitons can couple either to bound semiconductor excitons or continuum states of the substrate. The coupling to semiconductor excitons resembles a typical molecular Förster resonance excitation transfer. However, it requires an exact energetic match between the molecular HOMO-LUMO transition energy and the exciton resonance in the semiconductor substrate. Therefore, this work focuses on the interaction with the electrically pumped, i.e., occupied electron-hole continuum that covers a broad energy range, thereby overcoming possible transition energy mismatches between the organic and inorganic constituent.

The chapter is structured as follows: First, the model system and Hamiltonian is introduced (Sec. 7.2). A partial charge approximation is employed for modeling the Coulomb coupling elements (Sec. 7.3) and the problem is transformed into a Bloch basis representation assuming a periodic arrangement of the molecules (Sec. 7.4). In Sec. 7.5, an exciton basis for the organic part is constructed and in Sec. 7.6, equations of motion are derived for the full hybrid structure. Finally, the transfer rate is calculated (Sec. 7.7) and numerically evaluated for different parameter regimes (Sec. 7.8).

7.2 Modeling the hybrid inorganic/organic system

7.2.1 Model system

The inorganic-organic heterostructure is described by the following model system, schematically shown in Fig. 7.1 (b): A single layer of flat organic ladder-type quarterphenyl (L4P) molecules (cf. Fig. 7.1 (a)) forms a quasi **two-dimensional** film that is weakly (non-covalently) bound to a

ZnO **QW** of wurtzite crystal structure with a (10 $\bar{1}$ 0) surface acting as inorganic semiconductor substrate. The distance between this molecular overlayer and the semiconductor surface is denoted as Δz . **DFT** calculations of this heterostructure show that the system relaxes at a distance of $\Delta z \approx 0.4$ nm. ZnO is ideally suited for this kind of application since it is a wide-gap semiconductor ($\varepsilon_{\text{gap}} \approx 3.4$ eV [Yos97, Dju06, Tek04]) of high structural quality and with a large exciton-binding energy of 60 meV, such that excitonic effects can occur up to room temperature [Tek04, Özg05]. It is cheap, non-toxic, and chemically stable towards the deposition of molecules at its surface, such that no additional passivation layers on top of the **QW** are required and organic molecules can be deposited in a controlled manner [Blu06, Dju06, Blu08a, Sch15]. Consequently, ZnO has raised broad scientific interest as a promising candidate for future photovoltaic applications [Blu08b, Vay12, Shi12, Nev08]. On the other hand, it is desirable that the organic molecules exhibit a high radiative emission yield, narrow fluorescence and absorption linewidths, and a small polaron shift for efficient energy migration within the molecular overlayer. This is achieved using the above mentioned ladder oligo(*p*-phenylene)s due to their fixed planar geometry compared to the less rigid oligo phenyls [Sch15, Kob12], cf. Fig. 7.1 (a). It has been observed that these kinds of molecules can form highly ordered films when they are deposited on the smooth surface of a semiconductor substrate [Kob12, Lju17]. Therefore, the molecules are assumed to arrange periodically on top of the substrate, which will simplify the theoretical description. This way, the study is restricted to **HIOS** with a lattice periodic arrangement of molecules and thereby represents an idealized first approach to derive a microscopic description of such heterostructures. It marks a first step towards the description of more complex systems with, e.g., a disordered molecular layer and imperfect semiconductor substrates, cf. Chap. 8.

Due to the resonant excitation, only the energetically lowest allowed electronic transitions are considered between the highest occupied molecular orbital (HOMO) and lowest unoccupied molecular orbital (LUMO) of the molecules and between the valence and the conduction band in the semiconductor substrate.

7.2.2 Hamilton operator

The Hamilton operator of the composite system is defined as follows:

$$\hat{H} = \hat{H}_0^m + \hat{H}_0^s + \hat{H}_C^{m-m} + \hat{H}_C^{m-s}, \quad (7.1)$$

The free-particle part

$$\hat{H}_0 = \hat{H}_0^m + \hat{H}_0^s = \sum_{A,\nu} \varepsilon_{A,\nu} \hat{a}_{A,\nu}^\dagger \hat{a}_{A,\nu} + \sum_{\lambda,\mathbf{k}} \varepsilon_{\lambda,\mathbf{k}} \hat{a}_{\lambda,\mathbf{k}}^\dagger \hat{a}_{\lambda,\mathbf{k}} \quad (7.2)$$

contains the undisturbed electronic eigenenergies $\varepsilon_{A,\nu}$ and $\varepsilon_{\lambda,\mathbf{k}}$ of the electrons in the molecular orbitals and in the semiconductor bands, respectively. The index $A \in \{\text{H}, \text{L}\}$ denotes the **HOMO** (H) and **LUMO** (L) of the ν -th molecule described by the electronic wave function $\psi_{A,\nu}$. Assuming identical molecules, $\varepsilon_{A,\nu} \equiv \varepsilon_A$ holds. The index $\lambda \in \{\text{v}, \text{c}\}$ parametrizes the valence (v) and conduction (c) band and $\mathbf{k} \equiv \mathbf{k}_\parallel$ the two-dimensional (2D) wave vector of the semiconductor electrons in the **QW** plane with wave function $\psi_{\lambda,\mathbf{k}}$. The three-dimensional spatial coordinate $\mathbf{r} = (\mathbf{r}_\parallel, r_\perp)$ is decomposed into the **2D** in-plane component \mathbf{r}_\parallel within the **QW** plane and the one-dimensional (1D) component $r_\perp \equiv z$ perpendicular to the **QW** plane, here arbitrarily chosen as z direction. Within the envelope-function approximation, the electronic wave functions $\psi_{\lambda,\mathbf{k}}(\mathbf{r})$ are given by [Cho99, Hau04, Yu05]:

$$\psi_{\lambda,\mathbf{k}}(\mathbf{r}) = \frac{1}{\sqrt{A_{\text{QW}}}} e^{i\mathbf{k} \cdot \mathbf{r}_\parallel} u_{\lambda,\mathbf{k}}(\mathbf{r}) \xi_\lambda(z). \quad (7.3)$$

They contain a plane-wave contribution with quantization area A_{QW} in the **QW** plane, the lattice periodic Bloch function $u_{\lambda,\mathbf{k}}(\mathbf{r})$, and the envelope function $\xi_\lambda(z)$ that accounts for the **QW** confinement in z -direction. $\xi_\lambda(z)$ is obtained by solving the **1D** Schrödinger equation for an appropriate confinement potential. $A_{\text{QW}} = N_{\text{uc}}A_{\text{uc}}$ is the total sample area, consisting of N_{uc} **unit cells** of size A_{uc} .

$\hat{a}_{A,\nu}^{(\dagger)}$ and $\hat{a}_{\lambda,\mathbf{k}}^{(\dagger)}$ denote the annihilation (creation) operators for an electron in a molecule and in the semiconductor **QW**, respectively, obeying the fermionic anticommutator relations:

$$[\hat{a}_{A,\nu}^\dagger, \hat{a}_{A',\nu'}]_+ = \delta_{A,A'}\delta_{\nu,\nu'}, \quad [\hat{a}_{\lambda,\mathbf{k}}^\dagger, \hat{a}_{\lambda',\mathbf{k}'}]_+ = \delta_{\lambda,\lambda'}\delta_{\mathbf{k},\mathbf{k}'}. \quad (7.4)$$

The Heisenberg field operator of an electron in the semiconductor substrate is given by

$$\hat{\Psi}_s^{(\dagger)}(\mathbf{r}) = \sum_{\lambda,\mathbf{k}} \psi_{\lambda,\mathbf{k}}^{(*)}(\mathbf{r}) \hat{a}_{\lambda,\mathbf{k}}^{(\dagger)}. \quad (7.5)$$

Correspondingly, the molecular field operator is defined as

$$\hat{\Psi}_m^{(\dagger)}(\mathbf{r}) = \sum_{A,\nu} \psi_{A,\nu}^{(*)}(\mathbf{r}) \hat{a}_{A,\nu}^{(\dagger)}. \quad (7.6)$$

Starting from the Coulomb interaction Hamiltonian in second quantization,

$$\hat{H}_C = \frac{1}{2} \int d^3r \int d^3r' \hat{\Psi}^\dagger(\mathbf{r}) \hat{\Psi}^\dagger(\mathbf{r}') e^2 G(\mathbf{r}, \mathbf{r}') \hat{\Psi}(\mathbf{r}') \hat{\Psi}(\mathbf{r}) \quad (7.7)$$

with the Green's function $G(\mathbf{r}, \mathbf{r}') = 1/(4\pi\epsilon_0\epsilon_r|\mathbf{r} - \mathbf{r}'|)$ arising from Poisson's equation for interacting charges, two different types of Coulomb interaction are obtained: Intermolecular coupling $\hat{H}_C^{\text{m-m}}$ between molecules in the organic film and molecule-semiconductor interlayer coupling $\hat{H}_C^{\text{m-s}}$ between the molecules and the **QW** electrons. Couplings among the semiconductor electrons within the **QW** substrate are not considered here, since strong, incoherent electrical pumping of the semiconductor leads to high carrier densities, which will suppress the formation of Wannier-exciton like bound states within the semiconductor [Cho99].

The intermolecular Coulomb coupling Hamiltonian reads

$$\hat{H}_C^{\text{m-m}} = \underbrace{\frac{1}{2} \sum_{A,B} \sum_{\substack{\nu_a, \nu_b \\ \nu_a \neq \nu_b}} V_{A,\nu_a}^{A,\nu_a} V_{B,\nu_b}^{B,\nu_b} \hat{a}_{A,\nu_a}^\dagger \hat{a}_{B,\nu_b}^\dagger \hat{a}_{B,\nu_b} \hat{a}_{A,\nu_a}}_{\text{diagonal part}} + \underbrace{\sum_{\substack{\nu_a, \nu_b \\ \nu_a \neq \nu_b}} V_{L,\nu_a}^{\text{H},\nu_a} V_{\text{H},\nu_b}^{\text{L},\nu_b} \hat{a}_{\text{H},\nu_a}^\dagger \hat{a}_{\text{L},\nu_b}^\dagger \hat{a}_{\text{H},\nu_b} \hat{a}_{\text{L},\nu_a}}_{\text{Förster part}} \quad (7.8)$$

with the Coulomb coupling matrix element

$$V_{A',\nu_a}^{A,\nu_a} V_{B',\nu_b}^{B,\nu_b} = \int d^3r \int d^3r' \psi_{A,\nu_a}^*(\mathbf{r}) \psi_{B,\nu_b}^*(\mathbf{r}') e^2 G^{\text{m-m}}(\mathbf{r}, \mathbf{r}') \psi_{B',\nu_b}(\mathbf{r}') \psi_{A',\nu_a}(\mathbf{r}). \quad (7.9)$$

$G^{\text{m-m}}(\mathbf{r}, \mathbf{r}')$ denotes the Green's function for the Coulomb interaction between two charges at \mathbf{r} and \mathbf{r}' , which is derived treating dielectric screening at the hybrid interface, cf. App. B.1. The matrix element given in Eq. (7.9) describes the Coulomb coupling between a molecule numbered ν_a with electronic states $A, A' \in \{\text{H}, \text{L}\}$ and a molecule numbered ν_b with electronic states $B, B' \in \{\text{H}, \text{L}\}$. Two types of Coulomb coupling are distinguished in the Hamiltonian of Eq. (7.8) [Ric06]: The first term represents the diagonal monopole-monopole shifts. They describe the electrostatic interaction between two charge densities and cause an energy renormalization,

thus shifting the system resonances. The second term contains the off-diagonal Förster coupling that describes an excitation energy transfer between different molecules ν_a and ν_b .²

The molecule-substrate Hamiltonian is given by:

$$\begin{aligned} \hat{H}_C^{\text{m-s}} = & \underbrace{\sum_{\lambda, \mathbf{k}, \mathbf{k}'} \sum_{A, \nu} V_{\lambda, \mathbf{k}'}^{\lambda, \mathbf{k}, A, \nu} \hat{a}_{\lambda, \mathbf{k}}^\dagger \hat{a}_{A, \nu}^\dagger \hat{a}_{A, \nu} \hat{a}_{\lambda, \mathbf{k}}}_{\text{diagonal part}} \\ & + \underbrace{\sum_{\mathbf{k}, \mathbf{k}'} \sum_{\nu} \left(V_{\nu, \mathbf{k}'}^{\text{c}, \mathbf{k}, \text{H}, \nu} \hat{a}_{\nu, \mathbf{k}}^\dagger \hat{a}_{\text{H}, \nu}^\dagger \hat{a}_{\text{L}, \nu} \hat{a}_{\nu, \mathbf{k}'} + V_{\text{c}, \mathbf{k}'}^{\text{v}, \mathbf{k}, \text{H}, \nu} \hat{a}_{\nu, \mathbf{k}}^\dagger \hat{a}_{\text{L}, \nu}^\dagger \hat{a}_{\text{H}, \nu} \hat{a}_{\text{c}, \mathbf{k}'} \right)}_{\text{Förster part}} \quad (7.10) \end{aligned}$$

with the Coulomb coupling matrix element

$$V_{\lambda', \mathbf{k}'}^{\lambda, \mathbf{k}, A, \nu} = \int d^3 r \int d^3 r' \psi_{\lambda, \mathbf{k}}^*(\mathbf{r}) \psi_{A, \nu}^*(\mathbf{r}') e^2 G^{\text{m-s}}(\mathbf{r}, \mathbf{r}') \psi_{B, \nu}(\mathbf{r}') \psi_{\lambda', \mathbf{k}'}(\mathbf{r}). \quad (7.11)$$

Again, $G^{\text{m-s}}(\mathbf{r}, \mathbf{r}')$ denotes the Green's function of the interlayer coupling derived in App. B.1. Note that $V_{\lambda', \mathbf{k}'}^{\lambda, \mathbf{k}, A, \nu} = V_{\lambda, \mathbf{k}}^{\lambda', \mathbf{k}', B, \nu}$.

7.3 Partial charge approximation of the Coulomb matrix elements

Usually, a dipole approximation is applied as a microscopic model for the Coulomb coupling elements of Eqs. (7.9) and (7.11) (cf., e.g., Refs. [Lov03, Dan06, Cur08, Mac09, Spe15]). However, this common and simple approximation breaks down if two spatially extended constituents interact over small distances, e.g., in the case of two neighbored interacting molecules. Therefore, the Coulomb coupling matrix elements in this work are derived using so-called atomic (transition) partial charges [Mad06, Cam09] that are obtained numerically by fitting to the electrostatic potential. Within the partial charge approximation, the Coulomb interaction is described as a Coulomb coupling between the atomic partial charges that are, for example, centered at the nuclei of the molecule or the unit cell (UC) atoms of the semiconductor, respectively. This way, the complex field distribution of the molecules and the semiconductor is created by point charges located at the atomic positions. Note that this is only valid outside the characteristic van der Waals (vdW) radius of the atoms, representing the radius of imaginary hard spheres defined by the contact distance of the atoms [Pau60].

In this work, the partial charges are taken from *ab initio* calculations provided by Björn Bieniek and Patrick Rinke from the Fritz-Haber-Institut, Berlin. The hybrid xc-functional HSE06 [Hey03] implemented in the FHI-aims code [Blu09] is employed to determine the equilibrium adsorption geometry for an organic L4P molecule relaxed on top of the (10 $\bar{1}$ 0) surface of a ZnO QW. This geometry is maintained for deriving the partial charges of each

² Note that all non-energy preserving coupling elements are excluded, e.g., of the form $A = B$ but $A' = B'$ with $A \neq A'$, since they would describe a synchronous transition of both interacting electronic molecular states either into the ground or the excited state via Coulomb interaction. The same holds for matrix elements where one constituent is excited or relaxes while the other one remains in the same electronic configuration, since this would describe a creation or annihilation of an excited state that is not outweighed by the annihilation or creation of another state. Also, a wave function overlap between the electronic states of two different molecules has been neglected by choosing the same molecular index ν_i for molecular wave functions that belong to the same integration variable. Moreover, the condition $\nu_a \neq \nu_b$ expresses the assumption that only one electronic transition (between the respective HOMO and LUMO state) is considered in each molecule.

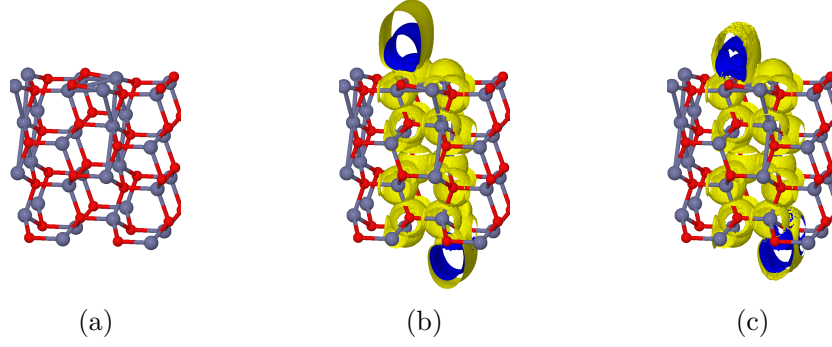


Figure 7.2: (a) Atomic structure of the ZnO (1010) unit cell that is repeated periodically in the lateral directions. (b) Electrostatic potential obtained from a **DFT** calculation. (c) Electrostatic potential reconstructed from the partial charges located at the atomic positions. The graphics were provided by B. Bieniek [Spe18].

component in separate calculations. In the case of ZnO, a **UC** is defined with perpendicular lattice vectors along the Cartesian coordinates and a thickness of 4.3 nm corresponding to the **QW** thickness. In order to model the surface, these **UCs** are repeated periodically and the periodic images of the slab in z direction (perpendicular to the **QW** plane) are separated by a vacuum layer of $> 30 \text{ \AA}$ width. Fig. 7.2 (a) shows the ZnO **UC** employed in the DFT calculations. The parameterization of the TS-scheme from Ref. [Zha11] was used. For the molecule, the long-range electrostatic interactions were accounted for by the TS-scheme [Tka09].

Poisson's equation for the *full* electron density is solved in order to obtain the full electrostatic potential that is approximated by the partial charges $q_i^{\lambda\lambda}$ and q_j^{AA} entering the monopole-monopole coupling elements. The *transition* partial charges generating the transition potential of the involved electronic states are calculated to approximate the Förster-type coupling elements. The charges are fitted to the electrostatic potential obtained from a **DFT** calculation employing the hybrid xc-functional HSE06 [Hey03]. Fig. 7.2 (b) shows the calculated electrostatic potential and Fig. 7.2 (c) shows the potential reconstructed from the partial charges. A comparison of (b) and (c) shows that the calculated electrostatic potential of (b) is well represented by the reconstruction with partial charges of (c).

7.3.1 Partial charge technique for the intermolecular Coulomb coupling

In [Mad06], the partial charge technique is used for the Coulomb coupling between two molecules described by many-particle wave functions. Here, the Hamiltonian is considered in a second quantization formalism. First, the partial charge technique is applied to the intermolecular Coulomb coupling element given in Eq. (7.9). The one-particle density $\rho_\nu^{AB}(\mathbf{r})$ of the ν -th molecule [Sch03] is introduced as follows:

$$\rho_\nu^{AB}(\mathbf{r}) \equiv \psi_{A,\nu}^*(\mathbf{r})\psi_{B,\nu}(\mathbf{r}). \quad (7.12)$$

For $A \neq B$, this product of two molecular wave functions is called **HOMO-LUMO** transition density. The intermolecular Coulomb matrix element of Eq. (7.9) thus becomes:

$$V_{A',\nu_a}^{A,\nu_a}{}_{B',\nu_b}^{B,\nu_b} = - \int d^3r e\rho_{\nu_a}^{AA'}(\mathbf{r})\phi_{\nu_b}^{BB'}(\mathbf{r}), \quad (7.13)$$

where the potential $\phi_{\nu_b}^{BB'}(\mathbf{r})$ of molecule ν_b has been introduced, stemming from Poisson's equation $\Delta_{\mathbf{r}}\phi_{\nu_b}^{BB'}(\mathbf{r}) = e/\epsilon_0(\rho_{\nu_b}^{BB'}(\mathbf{r})/\epsilon_m - \rho_{\nu_b}^{BB'}(x, y, -z)/\epsilon_{\text{eff}}^{\text{m-m}})$:

$$\phi_{\nu_b}^{BB'}(\mathbf{r}) \equiv - \int d^3r' eG^{\text{m-m}}(\mathbf{r}, \mathbf{r}')\rho_{\nu_b}^{BB'}(\mathbf{r}') \approx \sum_J G^{\text{m-m}}(\mathbf{r}, \mathbf{R}_{J\nu_b})q_{J\nu_b}^{BB'}. \quad (7.14)$$

Here, $\mathbf{R}_{J\nu_b} = \mathbf{R}_{\nu_b} + \mathbf{r}_{J\nu_b}$ denotes the position of the J -th atom of molecule ν_b , which can be expressed as a sum of the position \mathbf{R}_{ν_b} of molecule ν_b and the position $\mathbf{r}_{J\nu_b}$ of the J -th atom of molecule ν_b relative to \mathbf{R}_{ν_b} . Assuming identical, uniformly oriented molecules, the relative atomic positions and partial charges are equal for each molecule: $\mathbf{r}_{J\nu_b} \equiv \mathbf{r}_J$ and $q_{J\nu}^{AB} \equiv q_J^{AB}$. In the last step of Eq. (7.14), the molecular potential has been approximated by the electrostatic potential generated by point charges, namely the aforementioned atomic partial charges $q_{J\nu_b}^{BB'}$. They are in this case located at the atomic positions $\mathbf{R}_{J\nu_b}$. The Coulomb coupling matrix element thereby becomes

$$V_{A',\nu_a}^{A,\nu_a}{}_{B',\nu_b}^{B,\nu_b} \approx \sum_J q_J^{BB'} \times \left(- \int d^3r eG^{\text{m-m}}(\mathbf{r}, \mathbf{R}_{J\nu_b}) \rho_{\nu_a}^{AA'}(\mathbf{r}) \right) = \sum_J q_J^{BB'} \phi_{\nu_a}^{AA'}(\mathbf{R}_{J\nu_b}). \quad (7.15)$$

The potential $\phi_{\nu_a}^{AA'}(\mathbf{R}_{J\nu_b})$ of molecule ν_a is also approximated by partial charges:

$$\phi_{\nu_a}^{AA'}(\mathbf{R}_{J\nu_b}) \approx \sum_I G^{\text{m-m}}(\mathbf{R}_{I\nu_a}, \mathbf{R}_{J\nu_b}) q_I^{AA'}, \quad (7.16)$$

where the index I runs over all atoms in molecule ν_a . Combining Eqs. (7.14) and (7.15), the Coulomb coupling is obtained as the electrostatic interaction between atomic partial charges [Mad06]:

$$V_{A',\nu_a}^{A,\nu_a}{}_{B',\nu_b}^{B,\nu_b} \approx \sum_{I,J} G^{\text{m-m}}(\mathbf{R}_{I\nu_a}, \mathbf{R}_{J\nu_b}) q_I^{AA'} q_J^{BB'} \quad (7.17)$$

with $\mathbf{R}_{I\nu_a} \equiv \mathbf{R}_{\nu_a} + \mathbf{r}_I$, $\mathbf{R}_{J\nu_b} \equiv \mathbf{R}_{\nu_b} + \mathbf{r}_J$, and $q_I^{AB} = q_I^{BA}$.

In this partial charge approximation, the diagonal and Förster matrix elements entering the intermolecular Coulomb coupling Hamiltonian given in Eq. (7.8) take the form:

$$V_{A,\nu_a}^{A,\nu_a}{}_{B,\nu_b}^{B,\nu_b} \approx \sum_{I,J} G^{\text{m-m}}(\mathbf{R}_{\nu_a} + \mathbf{r}_I, \mathbf{R}_{\nu_b} + \mathbf{r}_J) q_I^{AA} q_J^{BB}, \quad (7.18)$$

$$V_{L,\nu_a}^{H,\nu_a}{}_{H,\nu_b}^{L,\nu_b} \approx \sum_{I,J} G^{\text{m-m}}(\mathbf{R}_{\nu_a} + \mathbf{r}_I, \mathbf{R}_{\nu_b} + \mathbf{r}_J) q_I^{\text{HL}} q_J^{\text{LH}}. \quad (7.19)$$

7.3.2 Partial charge technique for the interlayer Coulomb coupling

The technique of the partial charge approximation for intermolecular Coulomb matrix elements can also be applied to the interfacial coupling between molecular and semiconductor electrons. First, the one-particle density for the semiconductor substrate

$$\rho_{\mathbf{k}\mathbf{k}'}^{\lambda\lambda'}(\mathbf{r}) \equiv \psi_{\lambda,\mathbf{k}}^*(\mathbf{r}) \psi_{\lambda',\mathbf{k}'}(\mathbf{r}) \quad (7.20)$$

is defined in analogy to the molecular one-particle density. This way, a more compact notation for the interfacial molecule-semiconductor coupling element of Eq. (7.11) can be employed:

$$V_{\lambda',\mathbf{k}'}^{\lambda,\mathbf{k}}{}_{B,\nu}^{A,\nu} = \int d^3r \int d^3r' \rho_{\mathbf{k}\mathbf{k}'}^{\lambda\lambda'}(\mathbf{r}) e^2 G^{\text{m-s}}(\mathbf{r}, \mathbf{r}') \rho_{\nu}^{AB}(\mathbf{r}') = -e \int d^3r \rho_{\mathbf{k}\mathbf{k}'}^{\lambda\lambda'}(\mathbf{r}) \phi_{\nu}^{AB}(\mathbf{r}). \quad (7.21)$$

In the last step, the potential $\phi_{\nu}^{AB}(\mathbf{r})$ of the ν -th molecule was plugged in, which is defined and approximated by the electrostatic potential of the partial charges according to Eq. (7.16):

$$\phi_{\nu}^{AB}(\mathbf{r}) = - \int d^3r' eG^{\text{m-s}}(\mathbf{r}, \mathbf{r}') \rho_{\nu}^{AB}(\mathbf{r}') \approx \sum_J G^{\text{m-s}}(\mathbf{r}, \mathbf{R}_{J\nu}) q_J^{AB}. \quad (7.22)$$

Compared to molecular systems, setting up the electrostatic potential generated by the atomic partial charges is more demanding in the case of solids with periodic boundary conditions, since

the charges are repeated infinitely and long-range electrostatic interactions take place [Cam09]. An electrostatic potential for the i -th UC of the semiconductor substrate is introduced:

$$\phi_i^{\lambda\lambda',\mathbf{k}\mathbf{k}'}(\mathbf{r}) = -\frac{1}{A_{\text{uc}}} \int_{\text{UC}_i} d^3\tilde{\mathbf{r}} eG^{\text{m-s}}(\mathbf{r}, \mathbf{R}_i + \tilde{\mathbf{r}}) e^{i(\mathbf{k}'-\mathbf{k})\cdot\tilde{\mathbf{r}}_{\parallel}} u_{\lambda,\mathbf{k}}^*(\tilde{\mathbf{r}}) u_{\lambda',\mathbf{k}'}(\tilde{\mathbf{r}}) \xi_{\lambda}^*(Z_i + \tilde{z}) \xi_{\lambda'}(Z_i + \tilde{z}) \quad (7.23)$$

where A_{uc} is the UC area, \mathbf{R}_i represents the lattice vector of the i -th semiconductor UC and \mathbf{r}' denotes the variation within this cell. Again, the semiconductor potential is approximated by the electrostatic potential of the partial charges $q_I^{\lambda\lambda',\mathbf{k}\mathbf{k}'}$ at the relative positions \mathbf{r}_I within one unit cell:

$$\phi_i^{\lambda\lambda',\mathbf{k}\mathbf{k}'}(\mathbf{r}) \approx \sum_I G^{\text{m-s}}(\mathbf{r}, \mathbf{R}_{I_i}) q_I^{\lambda\lambda',\mathbf{k}\mathbf{k}'}. \quad (7.24)$$

Here, $\mathbf{R}_{I_i} = \mathbf{R}_i + \mathbf{r}_I$ denotes the position of the I -th atom within the i -th semiconductor unit cell, where \mathbf{r}_I is the relative position of the I -th atom within this unit cell. In this study, only electronic states close to the band edges are considered. Therefore, the momentum dependence of the semiconductor partial charges $q_I^{\lambda\lambda',\mathbf{k}\mathbf{k}'}$ is neglected and the value at the Γ point ($\mathbf{k} = \mathbf{0}$) is taken: $q_I^{\lambda\lambda',\mathbf{k}\mathbf{k}'} \approx q_I^{\lambda\lambda',\mathbf{0}\mathbf{0}} \equiv q_I^{\lambda\lambda'}$.

The integral over \mathbf{r} is decomposed into a sum of integrals over the single UCs and split into the lattice vector \mathbf{R}_i of the i -th UC and a variation $\tilde{\mathbf{r}}$ within this cell in order to separate the scales:

$$V_{\lambda',\mathbf{k}'}^{\lambda,\mathbf{k}}{}_{B,\nu}{}^{A,\nu} = -\sum_J q_J^{AB} \sum_{i=1}^{N_{\text{uc}}} \int_{\text{UC}_i} d^3\tilde{\mathbf{r}} eG^{\text{m-s}}(\mathbf{R}_i + \tilde{\mathbf{r}}, \mathbf{R}_{J\nu}) \frac{1}{A_{\text{QW}}} e^{i(\mathbf{k}'-\mathbf{k})\cdot(\mathbf{R}_i+\tilde{\mathbf{r}})_{\parallel}} \times u_{\lambda,\mathbf{k}}^*(\mathbf{R}_i + \tilde{\mathbf{r}}) u_{\lambda',\mathbf{k}'}(\mathbf{R}_i + \tilde{\mathbf{r}}) \xi_{\lambda}^*(Z_i + \tilde{z}) \xi_{\lambda'}(Z_i + \tilde{z}), \quad (7.25)$$

where the expression of the one-particle density Eq. (7.20) was evaluated by inserting the QW wave function of Eq. (7.3). Next, the invariance of the Bloch functions under a lattice translation is used, $u_{\lambda,\mathbf{k}}(\mathbf{R}_i + \tilde{\mathbf{r}}) = u_{\lambda,\mathbf{k}}(\tilde{\mathbf{r}})$, and the QW area A_{QW} is replaced by $N_{\text{uc}}A_{\text{uc}}$ with N_{uc} being the number of UCs in the QW substrate. This yields a form where the electrostatic potential of Eq. (7.23) can be identified and approximated by the partial charges according to Eq. (7.24):

$$V_{\lambda',\mathbf{k}'}^{\lambda,\mathbf{k}}{}_{B,\nu}{}^{A,\nu} \approx \frac{1}{N_{\text{uc}}} \sum_{i=1}^{N_{\text{uc}}} e^{i(\mathbf{k}'-\mathbf{k})\cdot\mathbf{R}_{i\parallel}} \sum_{I,J} G^{\text{m-s}}(\mathbf{R}_{I_i}, \mathbf{R}_{J\nu}) q_I^{\lambda\lambda'} q_J^{AB} \quad (7.26)$$

with $\mathbf{R}_{I_i} \equiv \mathbf{R}_i + \mathbf{r}_I$ and $\mathbf{R}_{J\nu} \equiv \mathbf{R}_\nu + \mathbf{r}_J$. \mathbf{R}_ν denotes the position of the ν -th molecule in the organic film and \mathbf{R}_i the position of the i -th UC in the QW substrate. The atomic partial charges are located at \mathbf{r}_I within one semiconductor UC and \mathbf{r}_J within the ν -th molecule, respectively. The matrix elements entering the molecule-semiconductor Coulomb Hamiltonian given in Eq. (7.10) are hence approximated by the partial charges according to

$$V_{\lambda,\mathbf{k}'}^{\lambda,\mathbf{k}}{}_{A,\nu}{}^{A,\nu} \approx \frac{1}{N_{\text{uc}}} \sum_{i=1}^{N_{\text{uc}}} e^{i(\mathbf{k}'-\mathbf{k})\cdot\mathbf{R}_{i\parallel}} \sum_{I,J} G^{\text{m-s}}(\mathbf{R}_i + \mathbf{r}_I, \mathbf{R}_\nu + \mathbf{r}_J) q_I^{\lambda\lambda} q_J^{AA}, \quad (7.27)$$

$$V_{\nu,\mathbf{k}'}^{\text{c},\mathbf{k}}{}_{L,\nu}{}^{\text{H},\nu} \approx \frac{1}{N_{\text{uc}}} \sum_{i=1}^{N_{\text{uc}}} e^{i(\mathbf{k}'-\mathbf{k})\cdot\mathbf{R}_{i\parallel}} \sum_{I,J} G^{\text{m-s}}(\mathbf{R}_i + \mathbf{r}_I, \mathbf{R}_\nu + \mathbf{r}_J) q_I^{\text{cv}} q_J^{\text{HL}}. \quad (7.28)$$

Effective transition dipole moments can be assigned to the inorganic and organic component by summing over the transition partial charges at the atomic position,

$$\mathbf{D}_{\text{cv}} = \sum_I q_I^{\text{cv},\mathbf{k}\mathbf{k}'} \mathbf{r}_I = (0.003, -0.027, -0.007) \text{ e nm} \quad (7.29)$$

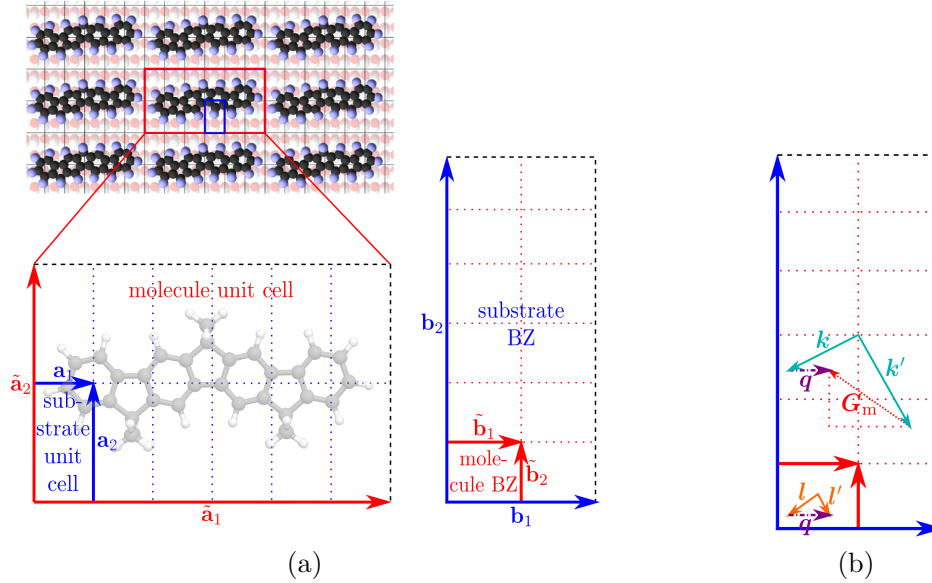


Figure 7.3: (a) Unit cells (UCs, left) and Brillouin zones (BZs, right) of the hybrid system with the maximum coverage of 1 molecule per 12 substrate UCs (6×2). $\tilde{\mathbf{a}}_{1/2}$ and $\mathbf{a}_{1/2}$ denote the lattice vectors of the molecule and ZnO unit cell, respectively. $\tilde{\mathbf{b}}_{1/2}$ and $\mathbf{b}_{1/2}$ represent the corresponding reciprocal lattice vectors. The upper 3D graphics is taken from Ref. [Ver14]. (b) Illustration of the quasi-momentum selection rules during interlayer Coulomb coupling ensured by the Kronecker delta. The momentum difference $\mathbf{k}' - \mathbf{k}$ in the substrate BZ has to equal the momentum transfer $\mathbf{q} = \mathbf{l}' - \mathbf{l}$ in the molecule except for a molecular reciprocal lattice vector \mathbf{G}_m .

and

$$D_{\text{LH}} = \sum_J q_J^{\text{LH}} \mathbf{r}_J = (0.187, 0.006, 0.004) \text{ e nm}. \quad (7.30)$$

The values given here correspond to the relaxed geometry of the heterostructure found in DFT calculations performed by B. Bieniek. Note that, in order to study also other molecular arrangements, the molecules are rotated on top of the semiconductor surface in the later evaluation. For the numerical implementation of these rotations, the concept of quaternions is used, which is briefly introduced in App. B.2.

7.4 Transformation of the molecular orbitals into a Bloch basis

Up to now, the electrons in the ZnO QW were described in a lattice-periodic Bloch basis representation, whereas the molecules were treated in a localized, non-periodic basis in position space. In order to introduce a consistent description of both constituents, the molecular parts of the Hamilton operator are transformed into a momentum representation. This is easily feasible since a lattice-periodic arrangement of the molecules in the organic film is assumed, as demonstrated in Fig. 7.3 (a). Moreover, the substrate UCs are assumed to match the molecular UCs, meaning that the molecular lattice vectors are integer multiples of the substrate lattice vectors (cf. Fig. 7.3 (a)). This relation is inverted in reciprocal space, as shown in the reciprocal space schematic (right panel) of Fig. 7.3 (a).

2D wave vectors \mathbf{l} for the molecular electrons are introduced. They are restricted to the first BZ of the molecular reciprocal lattice. This way, the electronic operators of the molecules are

transformed into momentum space according to [Sla34, Ver14]:

$$\hat{a}_{A,\nu} = \frac{1}{\sqrt{N_m}} \sum_{\mathbf{l}} e^{-i\mathbf{l}\cdot\mathbf{R}_{\nu\parallel}} \hat{a}_{A,\mathbf{l}}, \quad \hat{a}_{A,\mathbf{l}} = \frac{1}{\sqrt{N_m}} \sum_{\nu=1}^{N_m} e^{i\mathbf{l}\cdot\mathbf{R}_{\nu\parallel}} \hat{a}_{A,\nu}, \quad (7.31)$$

where the new electronic molecule operators $\hat{a}_{A,\mathbf{l}}^{(\dagger)}$ obey the fermionic commutation relations $[\hat{a}_{A,\mathbf{l}}^\dagger, \hat{a}_{A',\nu'}]_+ = \delta_{A,A'}\delta_{\mathbf{l},\nu'}$. To satisfy the periodic in-plane boundary conditions, the volume $V = N_m V_m$ containing N_m molecular UCs of volume V_m must equal the volume $V = N_{uc} V_{uc}$ containing N_{uc} semiconductor UCs of volume V_{uc} . The lattice-periodic ordering of the molecules allows to define the lattice vectors $\tilde{\mathbf{a}}_1$ and $\tilde{\mathbf{a}}_2$ in real space and the reciprocal lattice vectors $\tilde{\mathbf{b}}_1$ and $\tilde{\mathbf{b}}_2$ that span the molecular BZ, cf. right panel of Fig. 7.3 (a). They are determined by the condition $\tilde{\mathbf{a}}_i \cdot \tilde{\mathbf{b}}_j = 2\pi\delta_{i,j}$. The in-plane component of the position \mathbf{R}_{ν} of the ν -th molecule is then just a linear combination of the lattice vectors, $\mathbf{R}_{\nu\parallel} = n'_1 \tilde{\mathbf{a}}_1 + n'_2 \tilde{\mathbf{a}}_2$ with integers n'_1 and n'_2 . Later on, the following relation will be used [Ver14]:³

$$\frac{1}{N_m} \sum_{\nu=1}^{N_m} e^{i\mathbf{Q}\cdot\mathbf{R}_{\nu\parallel}} \approx \sum_{m_1, m_2 \in \mathbb{Z}} \delta_{\mathbf{Q}, m_1 \tilde{\mathbf{b}}_1 + m_2 \tilde{\mathbf{b}}_2} \equiv \sum_{\mathbf{G}_m} \delta_{\mathbf{Q}, \mathbf{G}_m} \quad (7.32)$$

with $\mathbf{G}_m = m_1 \tilde{\mathbf{b}}_1 + m_2 \tilde{\mathbf{b}}_2$ being a reciprocal lattice vector in the molecular layer.

The individual parts of the Hamilton operator involving the operators of the molecular electrons (Eq. (7.1)) can now be transformed. A detailed derivation is given in App. B.3. The free electron part takes the form:

$$\hat{H}_0^m = \sum_A \varepsilon_A \sum_{\mathbf{l}} \hat{a}_{A,\mathbf{l}}^\dagger \hat{a}_{A,\mathbf{l}}. \quad (7.33)$$

The intermolecular Coulomb Hamiltonian in the new basis has the form

$$\begin{aligned} \hat{H}_C^{m-m} = & \frac{1}{2} \frac{1}{N_m} \sum_{A,B} \sum_{\mathbf{l}_1, \dots, \mathbf{l}_4} \sum_{\mathbf{G}_m} \delta_{\mathbf{l}_1 - \mathbf{l}_4 + \mathbf{l}_2 - \mathbf{l}_3, \mathbf{G}_m} \mathcal{V}_{A \ B}^A \ (\mathbf{l}_2 - \mathbf{l}_3) \hat{a}_{A,\mathbf{l}_1}^\dagger \hat{a}_{B,\mathbf{l}_2}^\dagger \hat{a}_{B,\mathbf{l}_3} \hat{a}_{A,\mathbf{l}_4} \\ & + \frac{1}{N_m} \sum_{\mathbf{l}_1, \dots, \mathbf{l}_4} \sum_{\mathbf{G}_m} \delta_{\mathbf{l}_1 - \mathbf{l}_4 + \mathbf{l}_2 - \mathbf{l}_3, \mathbf{G}_m} \mathcal{V}_{L \ H}^H \ (\mathbf{l}_2 - \mathbf{l}_3) \hat{a}_{H,\mathbf{l}_1}^\dagger \hat{a}_{L,\mathbf{l}_2}^\dagger \hat{a}_{H,\mathbf{l}_3} \hat{a}_{L,\mathbf{l}_4}, \end{aligned} \quad (7.34)$$

with the redefined Coulomb matrix element in partial charge approximation

$$\mathcal{V}_{A' \ B'}^A \ (\mathbf{q}) = \sum_{\Delta_{m-m} \neq \mathbf{0}} e^{i\mathbf{q}\cdot\Delta_{m-m\parallel}} \sum_{I,J} G^{m-m}(\mathbf{r}_I, \mathbf{r}_J + \Delta_{m-m}) q_I^{AA'} q_J^{BB'}. \quad (7.35)$$

The sum over $\Delta_{m-m} \equiv \mathbf{R}_{\nu_b} - \mathbf{R}_{\nu_a}$ runs over all possible positions of a molecular UC relative to another molecule at a fixed position. The sum over the reciprocal lattice vectors \mathbf{G}_m accounts for Umklapp processes and $\mathbf{q} \equiv \mathbf{l}_2 - \mathbf{l}_3 = -(\mathbf{l}_1 - \mathbf{l}_4) + \mathbf{G}_m$ describes the momentum transfer. The Kronecker delta in Eq. (7.34) accounts for momentum conservation except for a reciprocal lattice vector. Note that the coupling element solely depends on the momentum transfer \mathbf{q} and is invariant under a translation of the momentum transfer vector by a reciprocal lattice vector \mathbf{G}_m of the molecular layer: $\mathcal{V}_{A' \ B'}^A \ (\mathbf{q} + \mathbf{G}_m) = \mathcal{V}_{A' \ B'}^A \ (\mathbf{q})$.

In a similar fashion, the molecule-semiconductor Coulomb Hamiltonian of Eq. (7.10) is transformed into momentum space (a detailed derivation is shown in App. B.3). It consists of

³ This approximation is valid for a sufficiently extended sample and thus large N_m , where the exponential term $e^{i\mathbf{Q}\cdot\mathbf{R}_{\nu\parallel}}$ for any $\mathbf{Q} \neq \mathbf{G}_m$ averages out when carrying out the sum over all molecular positions \mathbf{R}_{ν} .

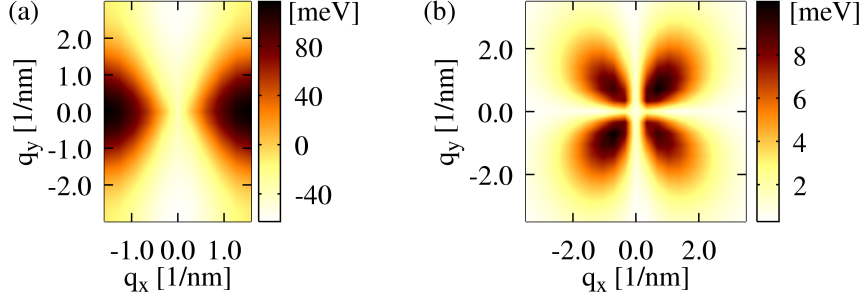


Figure 7.4: (a) Contour plot showing the magnitude of the intermolecular Förster coupling element $\mathcal{V}_{L,H}^H(\mathbf{q})$ over all \mathbf{q} values within the first molecule Brillouin zone for a maximum coverage of 1 molecule per 12 substrate unit cells (6×2). (b) Contour plot of the coupling strength $|\mathcal{V}_v^H(\mathbf{q})|$ of the interlayer Förster interaction.

a monopole-monopole part and a Förster part:

$$\begin{aligned} \hat{H}_C^{m-s} = & \frac{1}{N_{uc}} \sum_{\lambda, \mathbf{k}, \mathbf{k}'} \sum_{A, l, l'} \sum_{\mathbf{G}_m} \delta_{l-l'+\mathbf{k}'-\mathbf{k}, \mathbf{G}_m} \mathcal{V}_{\lambda, A}^{\lambda, A}(\mathbf{k}' - \mathbf{k}) \hat{a}_{\lambda, \mathbf{k}}^\dagger \hat{a}_{A, l}^\dagger \hat{a}_{A, l'} \hat{a}_{\lambda, \mathbf{k}'} \\ & + \frac{1}{N_{uc}} \left(\sum_{\mathbf{k}, \mathbf{k}'} \sum_{l, l'} \sum_{\mathbf{G}_m} \delta_{l-l'+\mathbf{k}'-\mathbf{k}, \mathbf{G}_m} \mathcal{V}_v^c(\mathbf{k}' - \mathbf{k}) \hat{a}_{c, \mathbf{k}}^\dagger \hat{a}_{H, l}^\dagger \hat{a}_{L, l'} \hat{a}_{v, \mathbf{k}'} + h.c. \right). \end{aligned} \quad (7.36)$$

The sum over Δ_{m-s} runs over the positions \mathbf{R}_i of all substrate UCs relative to a fixed molecular position \mathbf{R}_ν . The redefined Coulomb coupling element in momentum space is given by

$$\mathcal{V}_{\lambda', A'}^{\lambda, A}(\mathbf{q}) = \sum_{\Delta_{m-s}} e^{i\mathbf{q} \cdot \Delta_{m-s}} \sum_{I, J} G^{m-s}(\mathbf{r}_I + \Delta_{m-s}, \mathbf{r}_J) q_I^{\lambda \lambda'} q_J^{A A'}. \quad (7.37)$$

The Kronecker deltas in Eq. (7.36) ensure momentum conservation during Förster transfer and thereby impose microscopic quasi-momentum selection rules on the system. This is graphically illustrated in Fig. 7.3 (b). Later on, it is shown that these selection rules will govern the effect of Coulomb coupling.

For a numerically efficient calculation of the interlayer Förster coupling elements, a two-dimensional discrete Fourier transform using the FFTW library is performed, cf. App. B.4.

In Fig. 7.4 (a), the intermolecular Förster coupling element $\mathcal{V}_{L,H}^H(\mathbf{q})$ is plotted as function of the momentum transfer \mathbf{q} . Its shape resembles a dumbbell along the x direction, since the effective dipole moments of all uniformly oriented molecules in the organic layer point into the x direction (cf. Eq. (7.30)). As a result, the maximum coupling strength is shown up along the x axis. Fig. 7.4 (b) shows the interlayer Förster coupling strength $|\mathcal{V}_v^H(\mathbf{q})|$ as function of the momentum transfer \mathbf{q} . The shape of the transfer element consists of four lobes oriented roughly along the diagonals, since the effective transition dipole moments given in Eqs. (7.29) and (7.30) are oriented almost perpendicular to each other along the coordinate axes.

7.5 Molecular exciton basis

The ground state of the molecular layer where the HOMOs of all molecules are fully occupied is denoted $|\phi_0^m\rangle$. An orthonormal two-particle basis can be generated from this ground state using the annihilation (creation) operators $\hat{a}_{A, l}^{(\dagger)}$ for electrons in the molecule:

$$|l_1, l_2\rangle \equiv \hat{a}_{L, l_1}^\dagger \hat{a}_{H, l_2}^\dagger |\phi_0^m\rangle. \quad (7.38)$$

The Coulomb coupling between the molecules leads to molecular exciton states designated by the parameter α . They can be expressed as superpositions of the two-particle states (with coefficients $c_{\mathbf{l}_1, \mathbf{l}_2}^\alpha = \langle \mathbf{l}_1, \mathbf{l}_2 | X_\alpha^m \rangle$) that are potentially delocalized over the molecular film:

$$|X_\alpha^m\rangle = \sum_{\mathbf{l}_1, \mathbf{l}_2} c_{\mathbf{l}_1, \mathbf{l}_2}^\alpha |\mathbf{l}_1, \mathbf{l}_2\rangle = \sum_{\mathbf{l}, \mathbf{q}} c_{\mathbf{l}+\mathbf{q}, \mathbf{l}}^\alpha |\mathbf{l} + \mathbf{q}, \mathbf{l}\rangle. \quad (7.39)$$

In the last step, the two-particle basis was expressed by specifying offset $\mathbf{l} \equiv \mathbf{l}_2$ and momentum difference $\mathbf{q} \equiv \mathbf{l}_1 - \mathbf{l}_2$. Note that the coefficients $c_{\mathbf{l}+\mathbf{q}, \mathbf{l}}^\alpha$ are only defined for wave vector sums $\mathbf{l} + \mathbf{q}$ within the first molecular **BZ**. Therefore, if the sum $\mathbf{l} + \mathbf{q}$ exceeds the first **BZ**, it is mapped back into the first **BZ** by means of a reciprocal lattice vector.

In this section, the eigenvalue problem for these molecular Frenkel excitons $|X_\alpha^m\rangle$ in the organic layer will be treated. It is given by the Schrödinger equation:

$$\hat{H}^m |X_\alpha^m\rangle = (\hat{H}_0^m + \hat{H}_C^{m-m}) |X_\alpha^m\rangle = (E_0^m + E_\alpha^m) |X_\alpha^m\rangle, \quad (7.40)$$

where the molecular eigenenergy $E_0^m + E_\alpha^m$ was introduced. The ground state energy E_0^m of the molecular layer acts as a constant offset:

$$E_0^m = \langle \phi_0^m | \hat{H}^m | \phi_0^m \rangle = N_m \varepsilon_H + \frac{1}{2} N_m \mathcal{V}_{\text{H H}}^{\text{H H}}(\mathbf{0}) - \frac{1}{2} \frac{1}{N_m} \sum_{\mathbf{l}, \mathbf{l}'} \mathcal{V}_{\text{H H}}^{\text{H H}}(\mathbf{l} - \mathbf{l}'). \quad (7.41)$$

A representation of the eigenproblem in the two-particle basis has the form:

$$\langle \mathbf{l} + \mathbf{q}, \mathbf{l} | \hat{H}^m | X_\alpha^m \rangle = (E_0^m + E_\alpha^m) c_{\mathbf{l}+\mathbf{q}, \mathbf{l}}^\alpha. \quad (7.42)$$

A detailed derivation of the matrix elements $\langle \mathbf{l} + \mathbf{q}, \mathbf{l} | \hat{H}^m | X_\alpha^m \rangle$ is given in App. B.5.1.

For a sufficiently large material sample, the **2D** molecular wave vectors are continuous and the sums can be replaced by integrals [Hau04]:

$$\sum_{\mathbf{l}} \rightarrow \frac{N_m A_m}{(2\pi)^2} \int_{\text{1st BZ}} d^2 l, \quad (7.43)$$

where A_m denotes the area of one molecular **UC** and the area of the first molecular **BZ** is given by $A_{\text{BZ}}^m = \frac{(2\pi)^2}{A_m}$. This leads to

$$E_\alpha^m c_{\mathbf{l}+\mathbf{q}, \mathbf{l}}^\alpha = c_{\mathbf{l}+\mathbf{q}, \mathbf{l}}^\alpha \left[\varepsilon_{\text{gap}}^m - \mathcal{V}_{\text{H H}}^{\text{H H}}(\mathbf{0}) + \mathcal{V}_{\text{H L}}^{\text{H L}}(\mathbf{0}) + \frac{A_m}{4\pi^2} \int d^2 l' \left(\mathcal{V}_{\text{H H}}^{\text{H H}}(\mathbf{l}') - \mathcal{V}_{\text{L H}}^{\text{L H}}(\mathbf{l}') \right) \right] \\ + \frac{A_m}{4\pi^2} \int d^2 l' c_{\mathbf{l}'+\mathbf{q}, \mathbf{l}'}^\alpha \left[\mathcal{V}_{\text{L H}}^{\text{L H}}(\mathbf{q}) - \mathcal{V}_{\text{H L}}^{\text{H L}}(\mathbf{l} - \mathbf{l}') \right], \quad (7.44)$$

where the lattice periodicity of the Coulomb coupling elements in momentum space has been used, cf. App. B.5.1. $\varepsilon_{\text{gap}}^m \equiv \varepsilon_{\text{L}} - \varepsilon_{\text{H}}$ denotes the molecular **HOMO-LUMO** gap.

To make the problem numerically tractable, the continuous wave vectors have to be discretized. Therefore, the integrals over the first **BZ** are rewritten into sums over N_{d}^m small surface segments of size $\Delta A \equiv \frac{A_{\text{BZ}}^m}{N_{\text{d}}^m}$, where ΔA is determined by the discretization grid:

$$\int d^2 l' f(\mathbf{l}') \rightarrow \sum_{i=1}^{N_{\text{d}}^m} \Delta A f(\mathbf{l}_i). \quad (7.45)$$

Since the monopole-monopole coupling elements exhibit only a slight variation of few percent over the first **BZ**, one can approximate $\mathcal{V}_{\text{H L}}^{\text{H L}}(\mathbf{l} - \mathbf{l}') \approx \mathcal{V}_{\text{H L}}^{\text{H L}}(\mathbf{0})$. This will greatly simplify the

eigenvalue problem derived for the molecular Frenkel excitons in matrix form and enable its analytical solution (see below). Nevertheless, the exact eigenproblem was solved numerically in the context of this work using the PETSc [Bal15a, Bal15b] and SLEPc [Her05] libraries for efficient computation of eigenvalue problems. A comparison of the numerical solutions for the exact eigenproblem with the analytical results for the simplified eigenproblem shows that the approximation introduced above is valid.

The eigenproblem for the energy E_α^m and the coefficients $c_{\mathbf{l}_i+\mathbf{q}_j, \mathbf{l}_i}^\alpha$ can be rewritten in matrix form. It is diagonal with respect to the momentum transfer \mathbf{q}_j , yielding a block-diagonal form for the entire index space $(\mathbf{l}_i, \mathbf{q}_j)$ of dimension $N_d^{m2} \times N_d^{m2}$. Using the abbreviations

$$a_{\mathbf{q}_j} \equiv \frac{1}{N_d^m} \left[\mathcal{V}_{\mathbf{L} \ \mathbf{H}}^{\mathbf{H} \ \mathbf{L}}(\mathbf{q}_j) - \mathcal{V}_{\mathbf{H} \ \mathbf{L}}^{\mathbf{H} \ \mathbf{L}}(\mathbf{0}) \right], \quad (7.46)$$

$$d_{\mathbf{q}_j} \equiv a_{\mathbf{q}_j} + \varepsilon_{\text{gap}}^m - \mathcal{V}_{\mathbf{H} \ \mathbf{H}}^{\mathbf{H} \ \mathbf{H}}(\mathbf{0}) + \mathcal{V}_{\mathbf{H} \ \mathbf{L}}^{\mathbf{H} \ \mathbf{L}}(\mathbf{0}) + \frac{1}{N_d^m} \sum_{k=1}^{N_d^m} \left(\mathcal{V}_{\mathbf{H} \ \mathbf{H}}^{\mathbf{H} \ \mathbf{H}}(\mathbf{l}_k) - \mathcal{V}_{\mathbf{L} \ \mathbf{H}}^{\mathbf{H} \ \mathbf{L}}(\mathbf{l}_k) \right), \quad (7.47)$$

each $N_d^m \times N_d^m$ block for a given \mathbf{q}_j has the form

$$E_{\mathbf{q}_j}^m \begin{pmatrix} c_{\mathbf{l}_1+\mathbf{q}_j, \mathbf{l}_1}^{\mathbf{q}_j} \\ c_{\mathbf{l}_2+\mathbf{q}_j, \mathbf{l}_2}^{\mathbf{q}_j} \\ \vdots \\ c_{\mathbf{l}_{N_d^m}+\mathbf{q}_j, \mathbf{l}_{N_d^m}}^{\mathbf{q}_j} \end{pmatrix} = \begin{pmatrix} d_{\mathbf{q}_j} & a_{\mathbf{q}_j} & \cdots & a_{\mathbf{q}_j} \\ a_{\mathbf{q}_j} & \ddots & & \vdots \\ \vdots & & \ddots & a_{\mathbf{q}_j} \\ a_{\mathbf{q}_j} & \cdots & a_{\mathbf{q}_j} & d_{\mathbf{q}_j} \end{pmatrix} \begin{pmatrix} c_{\mathbf{l}_1+\mathbf{q}_j, \mathbf{l}_1}^{\mathbf{q}_j} \\ c_{\mathbf{l}_2+\mathbf{q}_j, \mathbf{l}_2}^{\mathbf{q}_j} \\ \vdots \\ c_{\mathbf{l}_{N_d^m}+\mathbf{q}_j, \mathbf{l}_{N_d^m}}^{\mathbf{q}_j} \end{pmatrix}. \quad (7.48)$$

This way, $\alpha = \mathbf{q}_j, n$ uniquely determines a particular solution of the full eigenproblem, where n enumerates the N_d^m solutions of the reduced $N_d^m \times N_d^m$ eigenproblem in the \mathbf{l}_i index space for a given \mathbf{q}_j . The excitonic states of the molecular layer introduced in Eq. (7.39) are then expressed in the discretized basis set of vectors $(\mathbf{l}_i, \mathbf{q}_j)$ by:

$$|X_\alpha^m\rangle = |X_{\mathbf{q}_j, n}^m\rangle = \frac{N_m}{N_d^m} \sum_{i=1}^{N_d^m} c_{\mathbf{l}_i+\mathbf{q}_j, \mathbf{l}_i}^{\mathbf{q}_j, n} |\mathbf{l}_i + \mathbf{q}_j, \mathbf{l}_i\rangle \quad (7.49)$$

with eigenenergies $E_\alpha^m = E_{\mathbf{q}_j, n}^m$ for $n, j = 1, \dots, N_d^m$.

Each $N_d^m \times N_d^m$ block for a given \mathbf{q}_j is highly symmetric with identical entries $d_{\mathbf{q}_j}$ (Eq. (7.47)) on the diagonal and identical off-diagonal elements $a_{\mathbf{q}_j}$ (Eq. (7.46)). This symmetric eigenproblem in matrix form can be solved analytically. It has only two distinct eigenvalues: $E_-^m \equiv E_{\mathbf{q}_j, n=1}^m = \cdots = E_{\mathbf{q}_j, n=N_d^m-1}^m = d_{\mathbf{q}_j} - a_{\mathbf{q}_j}$ and $E_+^m \equiv E_{\mathbf{q}_j, n=N_d^m}^m = d_{\mathbf{q}_j} + (N_d^m - 1)a_{\mathbf{q}_j}$. Plugging in Eqs. (7.46) and (7.47) yields:

$$E_-^m = \varepsilon_{\text{gap}}^m - \mathcal{V}_{\mathbf{H} \ \mathbf{H}}^{\mathbf{H} \ \mathbf{H}}(\mathbf{0}) + \mathcal{V}_{\mathbf{H} \ \mathbf{L}}^{\mathbf{H} \ \mathbf{L}}(\mathbf{0}) + \frac{1}{N_d^m} \sum_{k=1}^{N_d^m} \left(\mathcal{V}_{\mathbf{H} \ \mathbf{H}}^{\mathbf{H} \ \mathbf{H}}(\mathbf{l}_k) - \mathcal{V}_{\mathbf{L} \ \mathbf{H}}^{\mathbf{H} \ \mathbf{L}}(\mathbf{l}_k) \right), \quad (7.50)$$

$$E_+^m = E_-^m + \mathcal{V}_{\mathbf{L} \ \mathbf{H}}^{\mathbf{H} \ \mathbf{L}}(\mathbf{q}_j) - \mathcal{V}_{\mathbf{H} \ \mathbf{L}}^{\mathbf{H} \ \mathbf{L}}(\mathbf{0}). \quad (7.51)$$

The normalized components of the $(N_d^m - 1)$ eigenvectors corresponding to the degenerate eigenvalue E_-^m are given by

$$c_{\mathbf{l}_i+\mathbf{q}_j, \mathbf{l}_i}^{\mathbf{q}_j, n} = \frac{N_d^m}{N_m} \times \begin{cases} \frac{1}{\sqrt{2}} & \text{for } i = 1, \\ -\frac{1}{\sqrt{2}} & \text{for } i = n + 1, \\ 0 & \text{else} \end{cases} \quad (7.52)$$

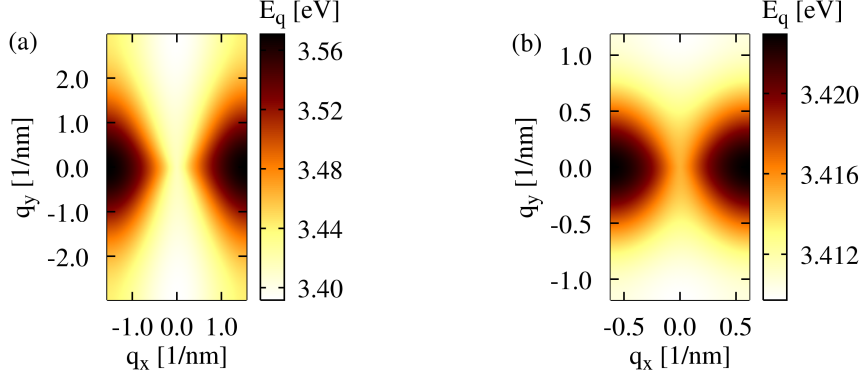


Figure 7.5: Molecular energy dispersion $E_{\mathbf{q}_j}^m$ corresponding to the symmetric solutions of the molecular eigenvalue problem for (a) the closest possible molecular packing without steric overlap of one molecule per 6×2 substrate UCs and (b) a lower molecular coverage density with identical aspect ratio of one molecule per 15×5 substrate UCs.

for $n \in \{1, \dots, N_d^m - 1\}$, fulfilling the normalization condition derived in Eq. (B.35) of App. B.5.2. The $N_d^m - 1$ excitonic basis states corresponding to E^{m-} are pairwise antisymmetric linear combinations of the two-particle basis functions with equal momentum transfer \mathbf{q}_j :

$$|X_{\mathbf{q}_j, n}^m\rangle = \frac{1}{\sqrt{2}}(|l_1 + \mathbf{q}_j, l_1\rangle - |l_{n+1} + \mathbf{q}_j, l_{n+1}\rangle) \quad \text{for } n \in \{1, \dots, N_d^m - 1\}. \quad (7.53)$$

It appears that only the symmetric eigenvalue $E_{\mathbf{q}_j}^m$ shows a \mathbf{q}_j dispersion, whereas the degenerate antisymmetric eigenenergy E^{m-} as well as the corresponding eigenvector components do not depend on \mathbf{q}_j .⁴

$E_{\mathbf{q}_j}^m$ has identical eigenvector components

$$c_{l_i}^{\mathbf{q}_j, n=N_d^m} = \frac{\sqrt{N_d^m}}{N_m} \quad \text{for all } i, \quad (7.54)$$

so that the corresponding excitonic basis state is symmetric:

$$|X_{\mathbf{q}_j}^m\rangle \equiv |X_{\mathbf{q}_j, n=N_d^m}^m\rangle = \frac{1}{\sqrt{N_d^m}} \sum_{i=1}^{N_d^m} |l_i + \mathbf{q}_j - \mathbf{G}_m^{l_i + \mathbf{q}_j}, l_i\rangle. \quad (7.55)$$

Figure 7.5 shows the symmetric energy eigenvalues $E_{\mathbf{q}_j}^m$ as a function of the molecular wave vector \mathbf{q}_j for two different coverage densities of the semiconductor substrate with molecules. The interlayer Coulomb coupling among the molecules causes the formation of energy bands in the organic film. The effect is particularly pronounced in the case of densely packed molecular films and thus small intermolecular distances, since then the coupling strength increases and excitations in the molecular layer get more and more delocalized over several molecules placed in close proximity. This relaxes the assumed electronic two-level configuration for each molecule, resulting in a band dispersion reflecting the hybridized molecular states. The range of \mathbf{q} vectors shown in Fig. 7.5 represents the first molecule BZ. In the case of a maximum coverage without steric overlap of one molecule per 6×2 ZnO UCs (Fig. 7.5 (a)), the energetic dispersion ranges over roughly 150 meV within the molecular BZ, thus making the energy of the molecular states

⁴ Note that the eigenvectors given in Eq. (7.53) represent only a generating set of vectors that span the degenerate subspace associated with E^{m-} . However, it is numerically possible to obtain an orthogonal basis by applying, e.g., the Gram-Schmidt orthogonalization scheme.

strongly wave-vector dependent. This effect is weakened for reduced coverage densities, since the coupling strength decreases for larger intermolecular separations until reaching the limit of distant single, non-interacting molecules represented by simple two-level systems. Fig. 7.5 (b) shows an intermediate case with a coverage density of one molecule per 15×5 substrate UCs (and the same aspect ratio of 3 : 1 as in Fig. 7.5 (a)), where the dispersion over the first molecule **BZ** is still in the order of 10 meV. As can be seen in Eq. (7.51), the energy $E_{\mathbf{q}_j+}^m$ is proportional to the intermolecular Förster coupling element $\mathcal{V}_{\mathbf{L}}^{\text{H}} \mathcal{V}_{\mathbf{H}}^{\text{L}}(\mathbf{q}_j)$. Therefore, its shape resembles a dumbbell oriented along the x direction, since all molecules are assumed to be uniformly oriented with the effective dipole moments pointing in the x direction (cf. Eq. (7.30)).

In conclusion, the intermolecular monopole-monopole coupling leads to a substantial energy renormalization for high molecular coverages. In the case of the closest molecular packing without steric overlap of one molecule per 6×2 substrate unit cells (cf. Fig. 7.5), the molecular gap $\varepsilon_{\text{gap}}^m$ is adjusted by several tens of meV in order to get the inorganic and organic system into resonance.

Later, it will be shown that the antisymmetric eigenvectors do not contribute to the charge transfer across the hybrid interface, i.e., they form dispersionless dark states.

7.6 Equations of motion of the hybrid system

In this chapter, the equations of motion (EOM) of the hybrid system are derived in the molecular exciton basis using the von Neumann equation

$$i\hbar \frac{\partial}{\partial t} \text{tr}_s[\langle a^m | \hat{O}_s \hat{\rho} | b^m \rangle] = \text{tr}_s[\langle a^m | \hat{O}_s [\hat{H}, \hat{\rho}] | b^m \rangle] \quad (7.56)$$

for the density operator $\hat{\rho} \equiv \hat{\rho}_m \otimes \hat{\rho}_s$. Here, $|a^m\rangle$ and $|b^m\rangle$ represent states of the molecular system, whereas \hat{O}_s is either an observable operating on the semiconductor system or the identity. The Hamilton operator of the considered composite inorganic/organic system is given by $\hat{H} = \hat{H}_0^m + \hat{H}_0^s + \hat{H}_C^{m-m} + \hat{H}_C^{m-s}$. The quantity of interest is the population of the molecular exciton states $|X_{\mathbf{q}_j,n}^m\rangle$ whose eigenproblem has been solved in Sec. 7.5:

$$\rho_{\mathbf{q}_j,n}^m \equiv \text{tr}_s[\langle X_{\mathbf{q}_j,n}^m | \hat{\rho} | X_{\mathbf{q}_j,n}^m \rangle]. \quad (7.57)$$

The EOM for this exciton density is given by

$$\frac{\partial}{\partial t} \rho_{\mathbf{q}_j,n}^m = -\frac{2}{\hbar} \sum_{\mathbf{k}, \mathbf{k}'} \text{Im} \left[\mathcal{V}_{\mathbf{q}_j,n}^{\text{F}}(\mathbf{k}' - \mathbf{k}) \sigma_{\mathbf{q}_j,n}^{\mathbf{k}, \mathbf{k}'} \right], \quad (7.58)$$

where the effective interlayer Förster coupling element has been defined as

$$\mathcal{V}_{\mathbf{q}_j,n}^{\text{F}}(\mathbf{k}' - \mathbf{k}) \equiv \frac{N_m}{N_d^m} \sum_{i=1}^{N_d^m} c_{\mathbf{l}_i}^{\mathbf{q}_j,n} \frac{1}{N_{\text{uc}}} \sum_{\mathbf{G}_m} \delta_{\mathbf{q}_j, \mathbf{k}' - \mathbf{k} + \mathbf{G}_m} \mathcal{V}_{\mathbf{v}}^{\text{c}} \mathcal{V}_{\mathbf{L}}^{\text{H}}(\mathbf{k}' - \mathbf{k}). \quad (7.59)$$

It contains the expansion coefficient and the Kronecker delta ensuring quasi-momentum conservation during interlayer Förster coupling, as illustrated in Fig. 7.3 (b). The full calculation is demonstrated in App. B.6.1. $\rho_{\mathbf{q}_j,n}^m$ couples to the assisted molecule–semiconductor coherence

$$\sigma_{\mathbf{q}_j,n}^{\mathbf{k}, \mathbf{k}'} \equiv \text{tr}_s[\hat{a}_{\mathbf{c}, \mathbf{k}}^\dagger \hat{a}_{\mathbf{v}, \mathbf{k}'} \langle X_{\mathbf{q}_j,n}^m | \hat{\rho} | \phi_0^m \rangle] \quad (7.60)$$

whose EOM is given by

$$\begin{aligned} \frac{\partial}{\partial t} \sigma_{\mathbf{q}_j,n}^{\mathbf{k}, \mathbf{k}'} &= \frac{i}{\hbar} (-E_{\mathbf{q}_j,n}^m + \varepsilon_{\mathbf{c}, \mathbf{k}} - \varepsilon_{\mathbf{v}, \mathbf{k}'} + \mathcal{V}_{\text{mono}}^{m-s}) \sigma_{\mathbf{q}_j,n}^{\mathbf{k}, \mathbf{k}'} \\ &+ \frac{i}{\hbar} \mathcal{V}_{\mathbf{q}_j,n}^{\text{F}*}(\mathbf{k}' - \mathbf{k}) ((1 - f_{\mathbf{h}, \mathbf{k}'}) (1 - f_{\mathbf{e}, \mathbf{k}}) \rho_{\mathbf{q}_j,n}^m - f_{\mathbf{h}, \mathbf{k}'} f_{\mathbf{e}, \mathbf{k}} \rho_0^m), \end{aligned} \quad (7.61)$$

with $\rho_0^m \equiv \text{tr}_s[\langle \phi_0^m | \hat{\rho} | \phi_0^m \rangle]$. The calculation is shown in more detail in App. B.6.2. $f_{e/h,\mathbf{k}}$ denotes the carrier population probability given by Fermi functions for electrons (e) and holes (h). $\mathcal{V}_{\text{mono}}^{m-s}$ subsumes all diagonal monopole-monopole shifts and is given in Eq. (B.51). It describes the self-energy due to the electrostatic coupling of the electronic states in the molecular layer and the semiconductor substrate.

In order to derive the above EOM, the following steps and approximations were undertaken:

- Only single excitations in the molecular system were considered, neglecting terms describing doubly excited states in the organic layer.
- A Hartree-Fock factorization was applied to expectation values of four electronic operators of the substrate (cf. Sec. 2.3).
- Spatial homogeneity was assumed both in the semiconductor QW for fixed semiconductor populations as well as in the molecular layer. Thus, expectation values of two electronic operators are diagonalized with respect to their (quasi-)momenta:⁵ $\langle \hat{a}_{\lambda,\mathbf{k}}^\dagger \hat{a}_{\lambda,\mathbf{k}'} \rangle \approx \delta_{\mathbf{k},\mathbf{k}'} \langle \hat{a}_{\lambda,\mathbf{k}}^\dagger \hat{a}_{\lambda,\mathbf{k}} \rangle$ and, analogously, $\frac{N_m^2}{N_d^2} \text{tr}_s[\langle X_{\mathbf{q}_j,n}^m | \hat{\rho} | X_{\mathbf{q}_l,n'}^m \rangle] \approx \delta_{j,l} \delta_{n,n'} \rho_{\mathbf{q}_j,n}^m$.
- Inhomogeneous monopole-monopole contributions (cf. Eq. (B.50)) have been neglected. Later on, the energetic detuning between the resonance energies of the two constituents will be varied anyway, such that monopole-monopole shifts are only of minor interest here.
- The electronic semiconductor coherences $\langle \hat{a}_{v,\mathbf{k}}^\dagger \hat{a}_{c,\mathbf{k}'} \rangle$ are assumed to decay rapidly, such that their products vanish: $\langle \hat{a}_{v,\mathbf{k}_2}^\dagger \hat{a}_{c,\mathbf{k}_1} \rangle \langle \hat{a}_{c,\mathbf{k}}^\dagger \hat{a}_{v,\mathbf{k}'} \rangle \approx 0$.
- The system is assumed to be in the thermodynamic quasi-equilibrium, such that the carrier populations in the respective bands are described by Fermi distribution functions $f_{e/h,\mathbf{k}}$ for electrons (e) and holes (h) [Hau04, But04, Cho12]:

$$\rho_{v,\mathbf{k}} \equiv \langle \hat{a}_{v,\mathbf{k}}^\dagger \hat{a}_{v,\mathbf{k}} \rangle = f_{v,\mathbf{k}} = 1 - f_{h,\mathbf{k}}, \quad \rho_{c,\mathbf{k}} \equiv \langle \hat{a}_{c,\mathbf{k}}^\dagger \hat{a}_{c,\mathbf{k}} \rangle = f_{c,\mathbf{k}} = f_{e,\mathbf{k}} \quad (7.62)$$

with the Fermi function

$$f_{i,\mathbf{k}} = \frac{1}{\exp\left(\frac{\varepsilon_{i,\mathbf{k}} - \mu_i}{k_B T_i}\right) + 1} \quad \text{with } i \in \{e, h\}. \quad (7.63)$$

μ_i denotes the quasi-equilibrium chemical potential in the respective band. For a two-band system consisting of a valence and a conduction band with dispersion, it can be calculated analytically [Hau04]:

$$\mu_i(n_i, T_i) = k_B T_i \ln \left(\exp\left(\frac{\pi w \hbar^2 n_i}{m_i k_B T_i}\right) - 1 \right) = k_B T_i \ln \left(\exp\left(\frac{\pi \hbar^2 n_i^{2D}}{m_i k_B T_i}\right) - 1 \right), \quad (7.64)$$

with the carrier density $n_i = N_i/V$ in 3D, and the two-dimensional carrier density $n_i^{2D} = N_i/A_{\text{QW}} = n_i w$. T_i is the non-equilibrium charge carrier temperature that can differ for electrons and holes. The carrier temperature can exceed the surrounding lattice temperature if the energy gained by the electrons from the external field or pumping is no longer negligible compared to the thermal energy of the system. This effect is particularly strong in the low-temperature regime and the electrons are called *hot electrons*.

⁵ This is a consequence of the translational invariance of the Wigner function [Kuh94, Ric05]

$$f_{\lambda,\mathbf{k}}(\mathbf{r}, t) \equiv \sum_{\mathbf{k}'} e^{i\mathbf{k}' \cdot \mathbf{r}} \langle \hat{a}_{\lambda,\mathbf{k} - \frac{1}{2}\mathbf{k}'}^\dagger \hat{a}_{\lambda,\mathbf{k} + \frac{1}{2}\mathbf{k}'} \rangle.$$

- In the effective-mass approximation, a parabolic dispersion relation with effective masses $m_v^* < 0$ and $m_c^* > 0$ is assumed:

$$\varepsilon_{h,\mathbf{k}} = \frac{\hbar^2 k^2}{2m_h} = -\frac{\hbar^2 k^2}{2m_v^*} = -\varepsilon_{v,\mathbf{k}}, \quad \varepsilon_{e,\mathbf{k}} = \frac{\hbar^2 k^2}{2m_e} = \frac{\hbar^2 k^2}{2m_c^*} = \varepsilon_{c,\mathbf{k}} - \varepsilon_{\text{gap}}^s \quad (7.65)$$

where $\varepsilon_{\text{gap}}^s$ represents the band gap energy in the absence of excited electrons [Cho99]. Note that the point of zero energy was arbitrarily set at the valence band edge. The effective masses $m_v^* = -8.3035 m_0$ of the valence and $m_c^* = 1.4463 m_0$ of the conduction band electrons are obtained from a fit to the DFT band structure of ZnO surface bands [Ver14]. They translate as $m_e = m_c^*$ and $m_h = -m_v^*$ into the electron-hole picture.

- For applying the effective mass approximation, it is a necessary precondition that only \mathbf{k} states close to the Γ point ($\mathbf{k} = \mathbf{0}$) are occupied. As a consequence, Umklapp processes where the sum of two \mathbf{k} vectors equals a molecular reciprocal lattice vector are not possible and therefore neglected in the calculation by setting: $\delta_{\mathbf{k}-\mathbf{k}',\mathbf{G}_m} = \delta_{\mathbf{k},\mathbf{k}'}\delta_{\mathbf{G}_m,\mathbf{0}}$.

Since the electron-hole states in both constituents form a continuum, the linear, inhomogeneous differential Eq. (7.61) for the molecular exciton–substrate polarization $\sigma_{\mathbf{q}_j,n}^{\mathbf{k},\mathbf{k}'} = \text{tr}_s[\hat{a}_{c,\mathbf{k}}^\dagger \hat{a}_{v,\mathbf{k}'} \langle X_{\mathbf{q}_j,n}^m | \hat{\rho} | \phi_0^m \rangle]$ is solved via Markov approximation (cf. Sec. 2.4). Formal integration leads to:

$$\sigma_{\mathbf{q}_j,n}^{\mathbf{k},\mathbf{k}'}(t) = -\frac{i}{\hbar} \int_{-\infty}^t dt' e^{-\frac{i}{\hbar}(\varepsilon_{e,\mathbf{k}} + \varepsilon_{h,\mathbf{k}'} - \Delta_{\mathbf{q}_j,n})(t'-t)} \quad (7.66)$$

$$\begin{aligned} & \times \mathcal{V}_{\mathbf{q}_j,n}^{\text{F}*}(\mathbf{k}' - \mathbf{k})(f_{h,\mathbf{k}'} f_{e,\mathbf{k}} \rho_0^m(t') - (1 - f_{h,\mathbf{k}'})(1 - f_{e,\mathbf{k}}) \rho_{\mathbf{q}_j,n}^m(t')) \\ & = -\frac{i}{\hbar} \int_0^\infty ds e^{+\frac{i}{\hbar}(\varepsilon_{e,\mathbf{k}} + \varepsilon_{h,\mathbf{k}'} - \Delta_{\mathbf{q}_j,n})s} \\ & \times \mathcal{V}_{\mathbf{q}_j,n}^{\text{F}*}(\mathbf{k}' - \mathbf{k})(f_{h,\mathbf{k}'} f_{e,\mathbf{k}} \rho_0^m(t-s) - (1 - f_{h,\mathbf{k}'})(1 - f_{e,\mathbf{k}}) \rho_{\mathbf{q}_j,n}^m(t-s)), \end{aligned} \quad (7.67)$$

where $\Delta_{\mathbf{q}_j,n} \equiv E_{\mathbf{q}_j,n}^m - \varepsilon_{\text{gap}}^s - \mathcal{V}_{\text{mono}}^{\text{m-s}}$ has been introduced as energetic detuning between the renormalized resonances of the two constituents.⁶ The memory kernel of the densities $\rho_{\mathbf{q}_j,n}^m$ and ρ_0^m is truncated by neglecting their s dependence. The solution for the assisted molecular exciton–substrate polarization in Markov approximation is then given by:

$$\sigma_{\mathbf{q}_j,n}^{\mathbf{k},\mathbf{k}'} = -i\pi \mathcal{V}_{\mathbf{q}_j,n}^{\text{F}*}(\mathbf{k}' - \mathbf{k})(f_{h,\mathbf{k}'} f_{e,\mathbf{k}} \rho_0^m - (1 - f_{h,\mathbf{k}'})(1 - f_{e,\mathbf{k}}) \rho_{\mathbf{q}_j,n}^m) \delta(\varepsilon_{e,\mathbf{k}} + \varepsilon_{h,\mathbf{k}'} - \Delta_{\mathbf{q}_j,n}). \quad (7.68)$$

It is inserted into the EOM for the population of the molecular layer (Eq. (7.58)):

$$\frac{\partial}{\partial t} \rho_{\mathbf{q}_j,n}^m = \frac{2\pi}{\hbar} \sum_{\mathbf{k},\mathbf{k}'} \left| \mathcal{V}_{\mathbf{q}_j,n}^{\text{F}}(\mathbf{k},\mathbf{k}') \right|^2 (f_{h,\mathbf{k}'} f_{e,\mathbf{k}} \rho_0^m - (1 - f_{h,\mathbf{k}'})(1 - f_{e,\mathbf{k}}) \rho_{\mathbf{q}_j,n}^m) \delta(\varepsilon_{e,\mathbf{k}} + \varepsilon_{h,\mathbf{k}'} - \Delta_{\mathbf{q}_j,n}). \quad (7.69)$$

This EOM describes the transfer from the semiconductor electron-hole continuum into the organic layer. It will be used to calculate the microscopic rate equations for Coulomb scattering processes between the organic and inorganic component of the hybrid structure.

⁶ Later on, the parameters will be chosen in a way that the detuning $\Delta_{\mathbf{q}_j,n}$ is at least two orders of magnitude larger than the interlayer Förster coupling strength $|\mathcal{V}_{\mathbf{q}_j,n}^{\text{F}}(\mathbf{k}' - \mathbf{k})|$. This ensures that the inhomogeneity temporally varies much slower than the oscillation resulting from the exponential function.

7.7 Calculation of the interlayer transfer rate

Starting from the **EOM** for the molecular population $\rho_{\mathbf{q}_j,n}^m$ derived in Sec. 7.6, the energy transfer rates between the electrically pumped semiconductor and the molecular layer are calculated in partial charge approximation. Using Eq. (7.69) and the expression for the effective interlayer Förster coupling element $\mathcal{V}_{\mathbf{q}_j,n}^F(\mathbf{k}, \mathbf{k}')$ given in Eq. (7.59), the in-scattering rate from the semiconductor substrate into the exciton state $X_{\mathbf{q}_j,n}^m$ of the molecular layer is determined as:

$$\Gamma_{\mathbf{q}_j,n}^{\text{in}} = \sum_{\mathbf{k}, \mathbf{k}'} \gamma_{\mathbf{q}_j,n}(\mathbf{k}, \mathbf{k}') f_{h,\mathbf{k}'} f_{e,\mathbf{k}} \quad (7.70)$$

with

$$\begin{aligned} \gamma_{\mathbf{q}_j,n}(\mathbf{k}, \mathbf{k}') \equiv & \frac{2\pi}{\hbar} \frac{1}{N_{\text{uc}}^2} \frac{N_m^2}{N_d^{m^2}} \sum_{i=1}^{N_d^m} c_{\mathbf{l}_i}^{\mathbf{q}_j,n} \sum_{k=1}^{N_d^m} c_{\mathbf{l}_k}^{\mathbf{q}_j,n*} \sum_{\mathbf{G}_m} \delta_{\mathbf{q}_j, \mathbf{k}' - \mathbf{k} + \mathbf{G}_m} \left| \mathcal{V}_{\text{v L}}^{\text{c H}}(\mathbf{k}' - \mathbf{k}) \right|^2 \\ & \times \delta(\varepsilon_{e,\mathbf{k}} + \varepsilon_{h,\mathbf{k}'} - \Delta_{\mathbf{q}_j,n}). \end{aligned} \quad (7.71)$$

It is governed by the interlayer Förster coupling strength, the Fermi functions $f_{h,\mathbf{k}'} f_{e,\mathbf{k}}$ representing the quasi-equilibrium carrier distributions in the **QW**, and the delta conditions for momentum and energy conservation. In the same way, the back-scattering rate into the **QW** substrate is identified as:

$$\Gamma_{\mathbf{q}_j,n}^{\text{out}} = \sum_{\mathbf{k}, \mathbf{k}'} \gamma_{\mathbf{q}_j,n}(\mathbf{k}, \mathbf{k}') (1 - f_{h,\mathbf{k}'}) (1 - f_{e,\mathbf{k}}), \quad (7.72)$$

with the typical Pauli blocking terms $(1 - f_{h,\mathbf{k}'}) (1 - f_{e,\mathbf{k}})$ preventing back-scattering into the substrate when the relevant states are already occupied.

In order to implement the expressions for the in- and out-scattering rates numerically, the Kronecker and Dirac delta functions are evaluated and the remaining physical wave vector sums are transformed into integrals and then numerically discretized and truncated, which is shown in App. B.7. To obtain the total transfer rates involving all molecular exciton states, a sum over all n solutions of the molecular eigenproblem and over all numerically discrete \mathbf{q}_j vectors within the first molecular **BZ** of the molecules is performed, cf. Eq. (B.62). Note that the factor

$$\sum_{i=1}^{N_d^m} c_{\mathbf{l}_i}^{\mathbf{q}_k,n} = \frac{N_d^m}{N_m} \left(\frac{1}{\sqrt{2}} - \frac{1}{\sqrt{2}} \right) = 0 \quad (7.73)$$

is zero for the antisymmetric eigenvectors with $n = 1, \dots, N_d^m$ belonging to the $(N_d^m - 1)$ -fold degenerate eigenvalue E_-^m (cf. Eqs. (7.50) and (7.53)). As a consequence, only the symmetric solutions with eigenvalues $E_{\mathbf{q}_j,+}^m$ will contribute (cf. Eqs. (7.51) and (7.55)). The sum over the corresponding eigenvector components given in Eq. (7.54) reads

$$\frac{N_m^2}{N_d^{m^3}} \sum_{i=1}^{N_d^m} c_{\mathbf{l}_i}^{\mathbf{q}_j,n} \sum_{k=1}^{N_d^m} c_{\mathbf{l}_k}^{\mathbf{q}_j,n*} = 1. \quad (7.74)$$

With that, the total in-scattering rate is given by:

$$\begin{aligned} \Gamma_{\text{tot}}^{\text{in}} = & N_m \times \frac{|m_v^*| m_c^* A_{\text{uc}} \Delta k_y'}{2\pi \hbar^3} \frac{N_m}{N_{\text{uc}}} \frac{1}{N_d^m} \sum_{j=1}^{N_d^m} \sum_{m_y=1}^{N_d^s} \sum_{\gamma \in \{+, -\}} \sum_{\mathbf{G}_m} \left| \mathcal{V}_{\text{v L}}^{\text{c H}}(\mathbf{q}_j - \mathbf{G}_m) \right|^2 \\ & \times f_{h,\mathbf{k}_{m,\gamma}} f_{e,\mathbf{k}_{m,\gamma} - \mathbf{q}_j + \mathbf{G}_m} \frac{1}{\left(|m_v^*| + m_c^* \right) k_{m,x\gamma} - |m_v^*| (q_{j,x} - G_{m,x})} \theta(\dots). \end{aligned} \quad (7.75)$$

Table 7.1: Material parameters used to calculate the **HIOS** transfer rates (if not varied in the plots).

L4P relative permittivity	ϵ_m	1.0
ZnO relative permittivity [Yos97]	ϵ_s	7.9
ZnO band gap [Yos97]	ϵ_{gap}^s	3.4 eV
2D electron density in ZnO	n_e^{2D}	$1.5 \times 10^{13} / \text{cm}^2$
2D hole density in ZnO	n_h^{2D}	$1.5 \times 10^{13} / \text{cm}^2$
Electron temperature in ZnO	T_e	10 K
Hole temperature in ZnO	T_h	10 K
Interlayer separation	Δz	0.4 nm
Molecular coverage	N_m/N_{uc}	10×10 unit cells ²
Detuning	Δ_0	15 meV

with $\mathbf{k}_{m_\gamma} \equiv \begin{pmatrix} k_{m_x\gamma} \\ k_{m_y} \end{pmatrix}$ and $\mathbf{k}_{m_\pm} = \frac{1}{|m_v^*| + m_c^*} (|m_v^*| q'_{k_x} \pm \sqrt{\dots})$ with

$$\sqrt{\dots} = \left[\frac{2}{\hbar^2} |m_v^*| m_c^* (|m_v^*| + m_c^*) \Delta_{\mathbf{q}_j, n} - (|m_v^*| + m_c^*)^2 k_{m_y}^2 + 2|m_v^*| (|m_v^*| + m_c^*) k_{m_y} (q_{j_y} - G_{m_y}) - |m_v^*| m_c^* (q_{j_x} - G_{m_x})^2 + |m_v^*| (|m_v^*| + m_c^*) (q_{j_y} - G_{m_y})^2 \right]^{1/2}. \quad (7.76)$$

$\Delta_{k_y}^l$ defines the discretization step size of the k_y^l sum, cf. App. B.7. The factor $\frac{N_m}{N_{\text{uc}}}$ defines the coverage density of the sample. The out-scattering rate has the same form except for the Fermi factor which is instead given by $(1 - f_{h, \mathbf{k}_{m_\gamma}})(1 - f_{e, \mathbf{k}_{m_\gamma} - \mathbf{q}_j + \mathbf{G}_m})$.

This total rate scales linearly with the total number N_m of molecules in the system. Therefore, the rate $\Gamma_{\text{tot}}^{\text{in/out}}/N_m$ referring to one molecule (mean in/out-scattering from the inorganic layer into one molecule of the organic layer) is numerically evaluated in the following.

7.8 Evaluation of the numerical results

For the systematic analysis of the transfer efficiency, all material parameters are kept fixed at the values given in Tab. 7.1 except for one parameter that is varied within a physically reasonable range.

7.8.1 Variation of the resonance energy detuning

First, the excitation transfer rate is calculated for increasing detunings $\Delta_{\mathbf{q}_j=\mathbf{0}} \equiv \Delta_0 = E_{\mathbf{q}_j=\mathbf{0}}^{m+} - \mathcal{V}_{\text{mono}}^{m-s} - \epsilon_{\text{gap}}^s$ between the resonance energy of the molecular layer renormalized by the interlayer monopole-monopole shifts, $E_{\mathbf{q}_j=\mathbf{0}}^{m+}$, and the semiconductor band gap ϵ_{gap}^s , cf. Fig. 7.6 (a). This inorganic-organic resonance energy detuning enters the energy conserving delta distribution in Eqs. (7.70) and (7.72) and determines which states fulfill the energy matching restriction for excitation transfer coupling. One way to tune Δ_0 is to manipulate the molecular structure (e.g., by exchanging ligands [Sch15]), which is beyond the scope of this work. To include these effects into the considered simple model system focusing on the transfer and to achieve a qualitative understanding of the involved transfer processes, the detuning Δ_0 is varied.

Fig. 7.6 (b) depicts the total in- and out-scattering rates depending on Δ_0 . The rates have values in the range of several ns^{-1} , which is consistent with experimentally measured transfer times of 100 to 300 ps in comparable hybrid structures [Blu06, Sch15]. The in-scattering rate

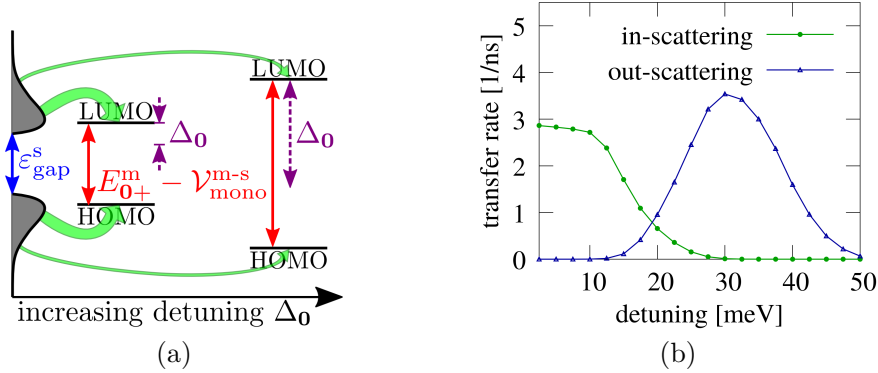


Figure 7.6: (a) Scheme of the system states in the semiconductor substrate (left) and molecule (right) for increasing detuning $\Delta_0 = E_0^{m+} - \varepsilon_{\text{gap}}^s - \mathcal{V}_{\text{mono}}^{m-s}$ (not true to scale). To simplify the picture, the organic part is represented by a simple two-level **HOMO-LUMO** system, ignoring the formation of flat molecular bands due to the intermolecular Coulomb coupling. However, these bands cover a very small energetic range compared to the electrically pumped semiconductor states for the considered coverage density of one molecule per 10×10 substrate **UCs**. (b) Total in- and out-scattering rates from the inorganic to the organic component depending on the detuning between the renormalized resonance energies of the substrate and the molecular layer. [Spe18]

into the molecular film decreases for increasing Δ_0 and vanishes for detunings larger than 30 meV, whereas the out-scattering rate has a maximum at ~ 30 meV and drops to zero towards higher (~ 50 meV) and lower detunings (~ 10 meV). This suggests that an efficient device operation is only possible for small resonance energy detunings below 10-15 meV.

The scheme of system states of Fig. 7.6 (a) enables an intuitive understanding of the observed behavior: The carrier population in the semiconductor substrate given by the product of the Fermi function and the density of states is depicted along the y axis. The discrete **HOMO** and **LUMO** levels representing the molecular states are plotted for two different detunings Δ_0 . Low detunings correspond to a close energetic match between the resonances of the inorganic and organic component (cf. the left two-level system of Fig. 7.6 (a)). Since the semiconductor substrate exhibits a high population filling in regions that obey the energy and momentum conservation for excitation transfer, this results in an efficient in-scattering into the molecular layer indicated by the fat green arrows in Fig. 7.6 (a). In contrast, the **HOMO-LUMO** level system on the right-hand side of Fig. 7.6 (a) depicts a higher detuning and thus an increased energy mismatch. The number of available scattering partners in the high-energy band states of the semiconductor substrate is reduced, such that the in-scattering is attenuated (and finally fully suppressed) for increasing detunings, as illustrated by the thin green arrow.

Up to $\Delta_0 = 30$ meV, the out-scattering rate in Fig. 7.6 (b) shows the opposite behavior governed by the Pauli blocking terms that prevent back-scattering into the substrate. However, Pauli blocking gets weaker with increased detuning and the out-scattering rate increases until the energy mismatch between the molecular and semiconductor gap is too large to be bridged by any of the populated states in the semiconductor electron-hole continuum [Spe18].

The relevant processes that determine how the transfer rate depends on the detuning can also be discussed by means of a reciprocal space analysis, as shown in App. B.8.

7.8.2 Variation of the molecular coverage

In Fig. 7.7 (a), the excitation transfer rate from the electrically pumped ZnO substrate into the organic film is depicted as a function of the molecular coverage density given as the number of molecules divided by the number of semiconductor unit cells, N_m/N_{uc} , for different aspect

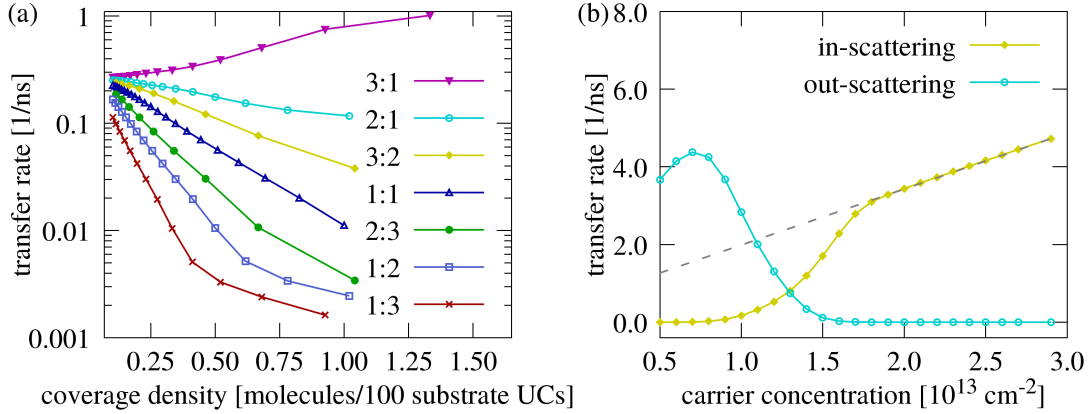


Figure 7.7: (a) Excitation transfer rates as functions of the molecular coverage density for different aspect ratios of the molecular coverage. (b) Total in- and out-scattering rates depending on the **2D** carrier concentration in the ZnO substrate for a fix aspect ratio of 1 : 1 (10×10 coverage) and charge carrier temperature of 10 K. The dashed gray line marks the linear growing regime the in-scattering rate enters at $n_{e/h}^{2D} \approx 1.8 \times 10^{13} \text{ cm}^{-2}$. [Spe18]

ratios of molecular coverage. The aspect ratio $n_x : n_y$ is defined as the ratio between the number of semiconductor UCs matching a molecular UC in x direction and the number in y direction. It turns out that a variation of the coverage densities and aspect ratios changes the transfer efficiency dramatically (by orders of magnitude). To make the calculation numerically feasible over a large parameter range, the transfer rate is calculated for a high detuning of $\Delta_0 = 30 \text{ meV}$. Smaller detunings show the same qualitative behavior.

When going towards low molecular coverages, the size of the molecular UC in real space is increased, whereas the size of the molecular BZ is reduced [Ver14]: The molecular reciprocal grid points get denser until a quasi-continuous density of reciprocal lattice vectors is reached. As a consequence, momentum conservation is fulfilled more easily, thus increasing the interlayer Coulomb coupling per molecule in the case of low molecular coverages. For very small molecular coverages (left-hand side of Fig. 7.7), the distance between two neighboring molecules gets so large that they do not interact and the particular UC geometry determined by the aspect ratio does not play a role. Therefore, independent of the aspect ratio, the transfer rates tend towards a common low-coverage limit.

In contrast, for increasing molecular coverages, the behavior of the transfer rate strongly depends on the aspect ratio. This is a consequence of two counteracting processes: On the one hand, increasing the total number of molecules per 100 substrate UCs improves the coupling to the substrate, since the coverage density N_m/N_{uc} enters the transfer rate of Eq. (7.75). On the other hand, the number of allowed momentum transfer processes decreases for increasing coverages due to the reduced reciprocal grid density.

The dependence on the aspect ratio reflects the spatial orientation of the molecular transition dipole moment \mathbf{D}_{LH} along the x axis (cf. Eq. (7.30)). For aspect ratios less than 1, the UC has a larger extent in y direction than in x direction. This increases the number of unfavorable scattering channels perpendicular to the effective dipole moment and results in a weaker interaction for smaller aspect ratios. In fact, the transfer rate (normalized to the molecule number) decreases by orders of magnitude when increasing the molecular coverage inside typical ranges due to the reduction of allowed transfer processes, which is detrimental for the device performance. For aspect ratios greater than 1 that coincide with the dipole orientation, this effect is strongly attenuated or even inverted in the case of a 3 : 1 coverage. Here, the increase in transfer efficiency for high coverages outweighs the counteracting decrease of allowed

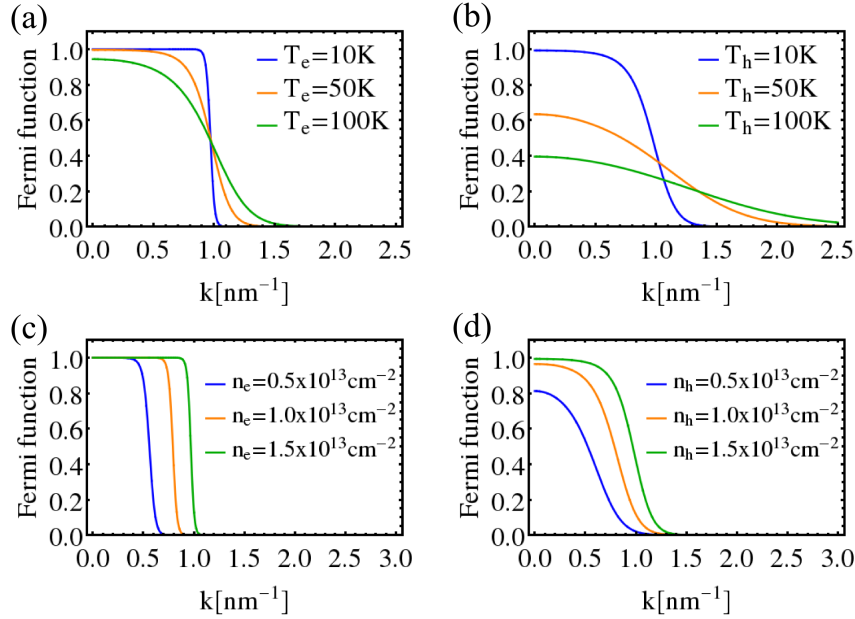


Figure 7.8: Electron ((a) and (c)) and hole ((b) and (d)) Fermi distributions for the parameter set given in Tab. 7.1 and varying temperatures ((a) and (b)) and charge carrier concentrations ((c) and (d)). [Spe18]

momentum transfer processes. The maximum molecular coverage without steric overlap is one molecule per 6×2 substrate UCs with an aspect ratio of 3 : 1 (cf. purple curve in Fig. 7.7). This configuration will be most likely in the experiment with one or few fully closed organic layers on top of the substrate. The presented calculations show that such a dense coverage in combination with a high aspect ratio is beneficial for the device performance [Spe18].

7.8.3 Tuning the electrical driving

In this section, it is analyzed how changes in the charge carrier distribution in the semiconductor bands of the ZnO substrate in terms of the carrier concentration and temperature (determined by the electrical pump strength) influence the excitation transfer efficiency across the hybrid interface. The charge carrier densities $n_{e/h}^{2D}$ and temperatures T_i enter the Fermi distribution of the electron and hole continuum in the semiconductor substrate through the chemical potential in Eq. (7.64), as shown in Fig. 7.8 for different values of $n_{e/h}^{2D}$ and T_i . Therefore, it is expected that the transfer rate is highly sensitive to changes in the charge carrier occupation determined by the density and temperature.

Variation of the carrier concentration

Figure 7.7 (b) shows the in- and out-scattering transfer rates in dependence of the 2D charge carrier concentrations $n_{e/h}^{2D}$ in the inorganic constituent. When going towards high carrier concentrations, more and more carriers are available as scattering partners at energies that fulfill the energy conservation, thus increasing the in-scattering rate per molecule. For low carrier concentrations, only electronic states close to the Γ point are occupied, whereas higher energy and momentum states are not populated, cf. Fig. 7.8 (c) and (d). Therefore, the transfer rate shows an initial non-linear increase until the momentum- and energy-allowed interaction channels are saturated. Then it enters a period of linear growth at $n_{e/h}^{2D} \approx 1.8 \times 10^{13} \text{ cm}^{-2}$

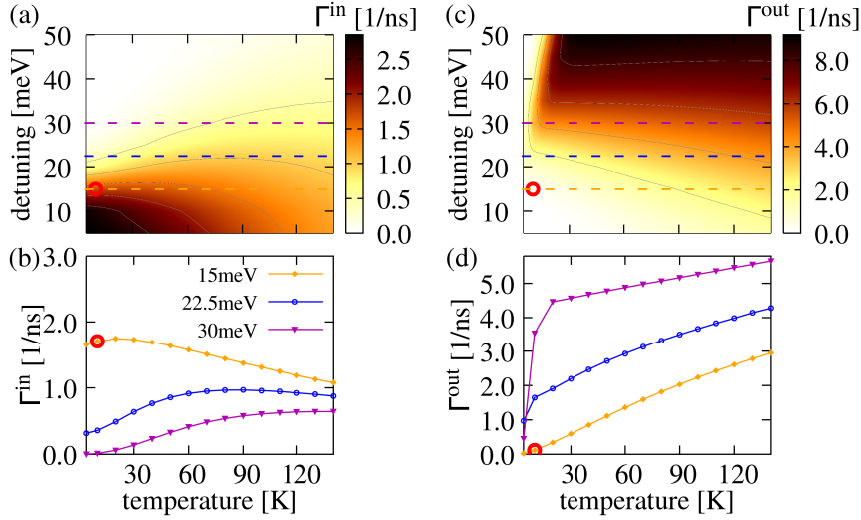


Figure 7.9: Total in-scattering (a) and out-scattering (c) rates depending on the charge carrier temperature $T_{e/h}$ and energetic detuning Δ_0 . The thin gray contour lines serve as guide to the eye. The lower panels (b) and (d) represent horizontal cuts through the 2D plots (a) and (c) (indicated by the dashed lines) at fixed detunings $\Delta_0 = 15$ meV (orange curves), 22.5 meV (blue curves), and 30 meV (purple curves). The red circles mark the standard values of Tab. 7.1 used throughout this work. [Spe18]

marked by the dashed gray line in Fig. 7.7 (b). This linear growing regime is dictated simply by the constant growth of the carrier density.

Surprisingly, up to $n_{e/h}^{2D} = 0.7 \times 10^{13} \text{ cm}^{-2}$, also the out-scattering rate increases before decreasing again. The unexpected initial growth of the out-scattering rate is explained as follows: For very low carrier densities, only few scattering channels are available in the absence of higher energy and momentum states. The possible transfer processes are therefore restricted to a small energy and momentum window, thus reducing both the in- and out-scattering excitation transfer efficiency. The higher the carrier concentrations become, the more electron-hole continuum states are occupied and contribute to the transfer. However, at a certain carrier concentration, Pauli blocking is reached in the semiconductor substrate and starts to suppress back-scattering into the ZnO QW until this process becomes negligibly small.

Variation of the carrier temperature

In this section, the interplay between the resonance energy detuning Δ_0 and the charge carrier temperatures $T_{e/h}$ is discussed by calculating 2D maps for the in-scattering (Fig. 7.9 (a)) and out-scattering rates (Fig. 7.9 (c)) depending on the temperature (depicted along the x axis) and the detuning (varied in y direction). To better resolve the different regimes, Fig. 7.9 (b) and (d) show horizontal cuts through the 2D maps (a) and (c), respectively, at fixed detunings $\Delta_0 = 15$ meV (orange curve), 22.5 meV (blue curve), and 30 meV (purple curve). The positions of the cuts are marked by the dashed lines in the corresponding 2D maps.

In the region of higher temperatures > 90 K, the in- and out-scattering rates are less sensitive to changes in the resonance energy detuning and temperature. Here, the population of higher electronic band states in the semiconductor substrate is increased, such that the energy conservation condition is more easily fulfilled. As expected, the back-scattering rate shows a monotonous growth with increasing temperature independent of the detuning, cf. Fig. 7.9 (c) and (d).

However, the in-scattering rate depicted in the left column of Fig. 7.9 shows a rather unintuitive behavior: At large detunings $\Delta_0 > 25$ meV (upper region in the 2D map of Fig. 7.9

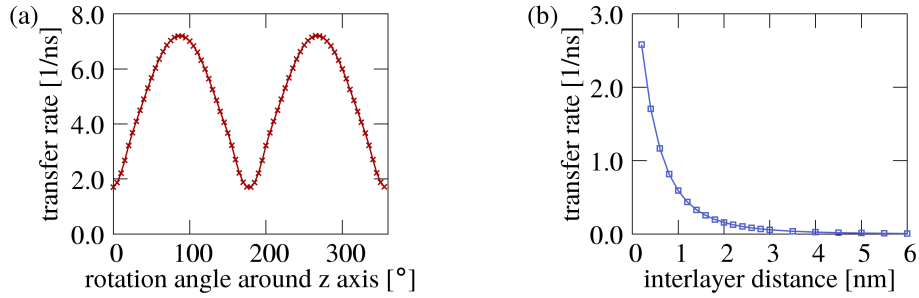


Figure 7.10: (a) Total in-scattering rate as a function of the rotational angle of the molecules within the QW plane around the z axis. (b) Total in-scattering rate as function of the interlayer separation between the ZnO QW and the molecular layer. [Spe18]

(a) and purple curve in the graph of Fig. 7.9 (b)), the in-scattering rate increases monotonously with increasing temperature, as one would expect for the same reasons as stated above in the case of the back-scattering rate (increased population filling of energy-conserving states). In contrast, for lower detunings $\Delta_0 < 25$ meV (lower region in the 2D map of Fig. 7.9 (a) and blue and orange curves in the graph of Fig. 7.9 (b)), the transfer rate exhibits initially a slight increase, but then drops down again for higher temperatures. This is explained as follows: Small detunings require a close energetic match between the semiconductor band states and the molecular gap. This condition is only fulfilled by low-energy states close to the Γ point. However, when increasing the temperature, the electron-hole continuum population is shifted from low energy states close to the Γ point at $\mathbf{k} = 0$ towards high energy states (cf. Fig. 7.8). Therefore, combining high temperatures and small resonance energy detunings is negative for the transfer efficiency.

In contrast, the back-scattering rate in Fig. 7.9 (c) increases monotonously for increasing detunings for temperatures above 30 K. Below that, the out-scattering drops down again when going to higher detunings > 30 meV, which is consistent with the non-monotonous shape of the out-scattering curve in Fig. 7.6 (b) for $T = 10$ K. Here, the large energetic detuning between the inorganic and organic part counteracts the fact that at low temperatures only low energy band states are populated [Spe18].

7.8.4 Variation of the orientation and distance of the molecular film

As detailed in Sec. 7.3, the validity of the partial charge technique exceeds the common dipole-dipole approximation. Nevertheless, effective dipole moments can be assigned to the two constituents by summing over the respective partial charges and their atomic positions according to Eqs. (7.29) and (7.30). Therefore, it is expected that the transfer efficiency changes for varying orientations of the molecules on top of the semiconductor surface. In the geometry found by DFT calculations, the effective dipole moments of the organic and inorganic component are oriented almost perpendicular to each other within the QW xy plane. Therefore, it should be instructive to rotate the molecules within their plane around the vertical z axis in order to bring the effective dipole moments to coincidence. Figure 7.10 (a) depicts the transfer rate into the molecular layer as a function of the rotational angle of the molecules around the z axis. The rate shows a \cos^2 -like behavior with maxima at roughly 85° and 265° , where the effective dipole moments are approximately parallel. This is completely in line with the expectation, since the squared absolute value of the interlayer Förster coupling element enters the rate (cf. Eq. (7.70)). Besides the simple \cos^2 dependence of the interlayer Förster coupling element, also other parameters are affected when rotating the molecules, since also the molecular band dispersion and therefore the energy matching condition change due to the

altered intermolecular coupling. Moreover, the rate does not drop to zero for perpendicular effective dipole moments as one would expect in the case of a pure dipole interaction, since there is always a substantial remaining coupling strength due to the spatial distribution of the partial charges. At perpendicular dipole moments, the rate still is around 24% of the maximum value at parallel dipoles.

In Fig. 7.10 (b), the transfer rate into the molecular layer is depicted depending on the interlayer distance Δz between the semiconductor surface and the molecular film. Different separations between the QW and the adsorbed organic layer can be realized experimentally, e.g., by inserting a spacer layer of variable thickness [Blu06]. As expected, the transfer efficiency exhibits a strong decrease for increasing interlayer separations, since the interlayer Förster coupling strength gets weaker for increasing distances [Spe18].

7.9 Summary

In this chapter, a microscopic theory for deriving the excitation transfer rate from electron-hole continuum states in an electrically pumped semiconductor substrate to excitonic states in a molecular adlayer was developed using a density-matrix equation technique. Both electrostatic shifts and Förster-type excitation transfer within the organic film as well as between the two constituents were incorporated in the calculations. A partial charge technique for the molecules and the semiconductor substrate was used to model the microscopic coupling elements beyond the common dipole-dipole treatment, where the microscopic input parameters were taken from DFT calculations of the electrostatic potential. The numerical evaluation revealed that the excitation transfer rate strongly depends (sometimes in an unintuitive way) on multiple, but tunable parameters such as the resonance energy detuning, the molecular coverage density, the charge carrier temperature and concentration in the ZnO substrate, the spatial orientation of the flat-lying molecules, and the interlayer separation. The calculations suggest that the coupling efficiency can be improved substantially by altering the geometric arrangement of the hybrid system and by varying the pumping strength. The effect of Förster coupling between the two constituents is governed by the mutual orientation of the effective dipole moments and the microscopic momentum and energy selection rules, making HIOS highly versatile building blocks for semiconductor device application.

In conclusion, the following guidelines are recommended for optimized device performance: (i) Using short distances between the constituents is advantageous for exploiting near-field effects and the effective dipoles of molecules and semiconductor should be aligned. (ii) A densely packed molecular film on top of the semiconductor substrate is beneficial for the transfer efficiency, and even further layers of molecules with smaller band gaps should be added to act as a cascade and suppress back-scattering into the substrate. (iii) A high carrier concentration must be ensured such that in-scattering outweighs out-scattering at the operating point and the resonance energy of the molecular layer and the semiconductor band gap should be aligned accordingly.

Of course, the model system treated in this chapter is idealized by assuming a perfect crystalline structure of the ZnO QW as well as a highly ordered molecular layer. However, in real systems, the inorganic film exhibits well width fluctuations which may lead to the formation of semiconductor excitons localized by disorder. In addition, in many cases the molecules will form a disordered film on top of the substrate. For these systems, a Bloch basis description as applied in this chapter is not practical and a treatment of disorder in position space becomes necessary. Such a theoretical treatment is developed in the next chapter.

8

Coupling of Wannier excitons in a disordered quantum well to Frenkel excitons in an organic film

8.1 Introduction

Excitonic effects dominate the optical and electronic properties of dielectric nanomaterials due to the strong confinement. Two types of excitons are distinguished: In organic materials with small relative permittivity such as weakly bound molecular layers, Frenkel excitons [Fre31] form with a high exciton binding energy of up to 1 eV. They are located on a small spatial scale, since both electron and hole reside within one molecule. In semiconductor nanostructures, the binding energy is usually much lower (typically between 1 and 10 meV) due to the enhanced dielectric screening, and the relative wave function of the exciton can extend over hundreds of unit cells (UCs). These types of excitons interacting on a large spatial scale and giving rise to a variety of long-range many-particle effects are referred to as Wannier excitons [Wan37].

Even very advanced growth techniques such as molecular beam epitaxy are not able to provide atomically smooth semiconductor interfaces and the quantum well (QW) width can fluctuate over a few monolayers [Zim97b, Zim97a], cf. Fig. 8.1 (a). Therefore, the disorder-induced localization of excitons due to interface roughness and alloy fluctuations is a typical phenomenon observed in many (multi-)QW structures [Sum72, Wei81, Din92, Tak94, Lef98]. With regard to possible optoelectronic applications of semiconductor nanostructures, it is essential to study the disorder-induced carrier localization dynamics. The spatial variations in the confinement potential determine the spectral position and inhomogeneous broadening of the exciton resonances [Heg85, Zim03, Sin17].

Compared to the highly ordered model considered in Chap. 7, a more elaborate theoretical approach including structural disorder in both the inorganic and organic component is developed in this chapter to describe the hybrid system. The analysis of the last chapter yielded a fundamental understanding of exciton transfer mechanisms in hybrid inorganic/organic systems (HIOS) and their dependence on material parameters and therefore served as a starting point towards the description of more realistic (and thus, theoretically more complex) hybrid structures. The new theoretical framework developed in the course of this chapter includes the treatment of disorder, radiative dephasing, and exciton-phonon scattering processes in both the organic and inorganic part.

This chapter is organized as follows: First, the inorganic semiconductor substrate is treated in Sec. 8.2. An excitonic basis in terms of disorder eigenstates is introduced in Sec. 8.2.1 and the electron-phonon (Sec. 8.2.2) and electron-photon Hamiltonians (Sec. 8.2.3) are deduced in this new eigenbasis, resulting in the total Hamiltonian of Sec. 8.2.4. Equations of motion (EOM) for the ZnO excitons are derived in density matrix formalism in Sec. 8.2.5. Finally, the incoherent optical pumping of the substrate is included phenomenologically in a Lindblad approach, cf. Sec. 8.2.6. In the next Sec. 8.3, the organic part is treated. The intermolecular Förster interaction causes that the local molecular basis states introduced in Sec. 8.3.1 are hybridized into delocalized molecular exciton states, cf. Sec. 8.3.2. The coupling to vibrational

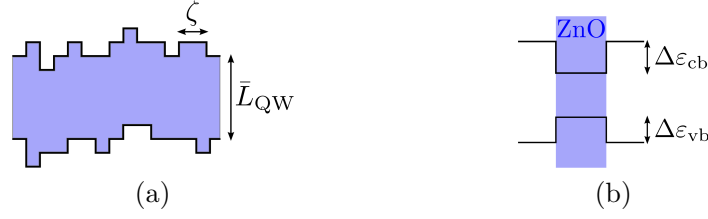


Figure 8.1: (a) Schematic of a semiconductor **QW** with disorder due to well width fluctuations of average size (correlation length) ζ . (b) Simplified level scheme of a **QW** embedded in a surrounding material with valence and conduction band offsets $\Delta\varepsilon_{vb}$ and $\Delta\varepsilon_{cb}$, respectively.

modes in the molecular layer is treated in Sec. 8.3.3. Finally, Sec. 8.4 contains the full treatment of the hybrid system, containing electrostatic and Förster-type Coulomb coupling between the inorganic and organic constituent (cf. Sec. 8.4.1). For the subsequent perturbative treatment in density-matrix formalism, the Hamiltonian is translated into a Liouville propagator in Sec. 8.4.2. With that, the amplitudes for transitions of the system between different exciton densities can be derived in a perturbative approach in Sec. 8.4.3 and a cumulant expansion technique is used to treat the coupling to the phonon bath in the organic layer, cf. Sec. 8.4.4. Finally, time-independent transition rates are derived in Sec. 8.4.5 that enter the **EOM** for the molecular and semiconductor exciton dynamics, as demonstrated in Sec. 8.4.6. A summary and outlook is given in Sec. 8.5.

8.2 Inorganic part: Wannier excitons including interface roughness, acoustic phonon scattering, and radiative recombination

This section introduces a theoretical framework for treating **QW** excitons localized by disorder due to well width fluctuations. The used microscopic model incorporates exciton-phonon scattering, radiative dephasing, and incoherent optical pumping. The theoretical approach is based on works of R. Zimmermann et al. [Zim97b, Zim97a, Zim03]. First, the exciton wave functions are derived as disorder eigenstates in Sec. 8.2.1.

8.2.1 Exciton states in disordered quantum wells

First, an orthonormal two-particle basis is introduced, given as

$$|\mathbf{k}_1, \mathbf{k}_2\rangle = \hat{a}_{c, \mathbf{k}_1}^\dagger \hat{a}_{v, \mathbf{k}_2} |\phi_0^s\rangle. \quad (8.1)$$

Here, the annihilation (creation) operator $\hat{a}_{\lambda, \mathbf{k}}^{(\dagger)}$ for an electron with wave vector \mathbf{k} in band $\lambda = c, v$ has been introduced. $|\phi_0^s\rangle$ denotes the electronic ground state of the semiconductor **QW**, where the valence bands are fully occupied. The transition to position space is possible through a Fourier series:

$$|\mathbf{r}_e, \mathbf{r}_h\rangle = \frac{1}{V_s} \sum_{\mathbf{k}_1, \mathbf{k}_2} e^{i(\mathbf{k}_1 \cdot \mathbf{r}_e - \mathbf{k}_2 \cdot \mathbf{r}_h)} |\mathbf{k}_1, \mathbf{k}_2\rangle, \quad (8.2)$$

where V_s denotes the sample volume. The wave function for exciton state α is defined as $\Psi_\alpha^s(\mathbf{r}_e, \mathbf{r}_h) \equiv \langle \mathbf{r}_e, \mathbf{r}_h | X_\alpha^s \rangle$.

Provided that the exciton binding energy is much larger than the disorder induced broadening, but small compared to the energetic subband separation, the total exciton wave function

$\Psi_\alpha^s(\mathbf{r}_e, \mathbf{r}_h)$ can be factorized into the envelope functions $\xi_e(z_e)$ and $\xi_h(z_h)$ in the growth (z) direction perpendicular to the QW plane and the in-plane part $\Psi_\alpha^s(\boldsymbol{\rho}_e, \boldsymbol{\rho}_h)$ in the QW xy plane [Zim97b, May99]:

$$\Psi_\alpha^s(\mathbf{r}_e, \mathbf{r}_h) = \xi_e(z_e)\xi_h(z_h)\Psi_\alpha^s(\boldsymbol{\rho}_e, \boldsymbol{\rho}_h), \quad (8.3)$$

where $\mathbf{r}_i = (x_i, y_i, z_i)$ denotes the electron ($i = e$) and hole ($i = h$) coordinates and $\boldsymbol{\rho}_i \equiv (x_i, y_i)$ the corresponding two-dimensional (2D) coordinates in the QW xy plane. The envelope functions obey the Schrödinger equation for the confinement potential $U_i(z_i)$ in z direction:

$$\left(-\frac{\hbar^2}{2m_i}\frac{\partial^2}{\partial z_i^2} + U_i(z_i)\right)\xi_i(z_i) = E_{z_i}\xi_i(z_i) \quad \text{with } i = e, h. \quad (8.4)$$

In the considered system, $U_i(z_i)$ can be modeled as finite potential well of width $\bar{L}_{\text{QW}} = 4.5$ nm and solved numerically. Only excitons with electrons in the lowest and holes in the highest subbands are considered. The depth of the potential well is given by the band offsets for the valence and conduction band, i.e., the energetic band edge difference between the well and barrier material, cf. Fig. 8.1 (b).¹ For a two-band model in effective mass approximation, the stationary Schrödinger equation for the 2D exciton wave function reads

$$\left(-\frac{\hbar^2}{2m_e}\nabla_{\boldsymbol{\rho}_e}^2 - \frac{\hbar^2}{2m_h}\nabla_{\boldsymbol{\rho}_h}^2 + V_{e-h}(\boldsymbol{\rho}_e - \boldsymbol{\rho}_h) + V_e(\boldsymbol{\rho}_e) + V_h(\boldsymbol{\rho}_h)\right)\Psi_\alpha^s(\boldsymbol{\rho}_e, \boldsymbol{\rho}_h) = E_\alpha^s\Psi_\alpha^s(\boldsymbol{\rho}_e, \boldsymbol{\rho}_h). \quad (8.5)$$

Here, $E_\alpha^s = E_{\alpha,3D}^s - \sum_i E_{z_i}$ denotes the exciton energy, ϵ_r the relative permittivity, m_i the effective mass, and $\nabla_{\boldsymbol{\rho}_i}^2$ the Laplace operator for the position of the electron ($i = e$) and hole ($i = h$). $V_e(\boldsymbol{\rho}_e)$ and $V_h(\boldsymbol{\rho}_h)$ are the disorder potentials responsible for the single-particle localization. $V_{e-h}(\boldsymbol{\rho}_e - \boldsymbol{\rho}_h)$ represents the attractive Coulomb interaction between the electron and the hole and is given as an effective in-plane potential incorporating the envelope functions:

$$V_{e-h}(\boldsymbol{\rho}_e - \boldsymbol{\rho}_h) = -\frac{e^2}{4\pi\epsilon_0\epsilon_r} \int dz_e \int dz_h \frac{|\xi_e(z_e)|^2 |\xi_h(z_h)|^2}{\sqrt{(\boldsymbol{\rho}_e - \boldsymbol{\rho}_h)^2 + (z_e - z_h)^2}}. \quad (8.6)$$

The disorder potentials $V_e(\boldsymbol{\rho}_e)$ and $V_h(\boldsymbol{\rho}_h)$ account for the spatial variation in the QW width

$$h(\boldsymbol{\rho}_i) = \bar{L}_{\text{QW}} + \Delta h(\boldsymbol{\rho}_i), \quad (8.7)$$

where $\Delta h(\boldsymbol{\rho}_i)$ is the deviation from the mean film thickness \bar{L}_{QW} . The spatially dependent width $h(\boldsymbol{\rho}_i)$ is normally distributed around \bar{L}_{QW} with standard deviation $\Delta L_{\text{QW}} \sim 0.1$ nm, which is chosen in a way that it suits the inhomogeneous broadening of the sample [Sin17]. The thickness fluctuation characterized by the mean deviation ΔL_{QW} can be attributed to a change in the energy of an infinite potential well, thus giving a reasonable estimate of the mean disorder energy $\Delta E(\Delta L_{\text{QW}})$ corresponding to the considered thickness fluctuation:

$$\Delta E(\Delta L_{\text{QW}}) = \left| \frac{dE_{\text{gs}}}{d\bar{L}_{\text{QW}}} \right| \Delta L_{\text{QW}} = \frac{\hbar^2\pi^2}{\mu\bar{L}_{\text{QW}}^3} \Delta L_{\text{QW}}. \quad (8.8)$$

Here, E_{gs} denotes the analytic solution for the ground state energy of a particle in an infinite potential well and $\mu \equiv 1/(\frac{1}{m_e} + \frac{1}{m_h}) = m_e m_h / (m_e + m_h)$ the exciton reduced mass. The lateral extent of the well width fluctuations is determined by the so-called correlation length $\zeta \sim 30$ nm representing the average diameter of the disorder islands [Zim97a]:

$$\langle h(\boldsymbol{\rho})h(\boldsymbol{\rho}') \rangle = c^2 \exp\left[-\frac{|\boldsymbol{\rho} - \boldsymbol{\rho}'|^2}{2\zeta^2}\right] \quad (8.9)$$

¹ In a $\text{Zn}_{0.9}\text{Mg}_{0.1}\text{O}/\text{ZnO}$ heterostructure, band offsets $\Delta\epsilon_{\text{vb}} = 0.06$ eV and $\Delta\epsilon_{\text{cb}} = 0.09$ eV have been measured by photoelectron spectroscopy [Zha13].

with c being an arbitrary constant. The subband energies E_{gs}^e and E_{gs}^h for the electron and hole are approximated as lowest energy solutions for an infinite potential well of variable width $h(\boldsymbol{\rho}_i)$ (cf. Ref. [Sin17]):

$$E_{\text{gs}}^i(h(\boldsymbol{\rho}_i)) = \frac{\hbar^2 \pi^2}{2m_i h^2(\boldsymbol{\rho}_i)} \approx \frac{\hbar^2 \pi^2}{2m_i \bar{L}_{\text{QW}}^2} - \frac{\hbar^2 \pi^2}{m_i \bar{L}_{\text{QW}}^3} \Delta h(\boldsymbol{\rho}_i). \quad (8.10)$$

Assuming small well width variations, these subband energies have been expanded in a Taylor series up to first order around the average thickness \bar{L}_{QW} with $\Delta h(\boldsymbol{\rho}_i) \equiv h(\boldsymbol{\rho}_i) - \bar{L}_{\text{QW}}$ in the last step of Eq. (8.10). The first-order contribution is identified as the disorder potential $V_i(\boldsymbol{\rho}_i)$:

$$V_e(\boldsymbol{\rho}_e) = \frac{\hbar^2 \pi^2}{m_e \bar{L}_{\text{QW}}^3} \Delta h(\boldsymbol{\rho}_e), \quad V_h(\boldsymbol{\rho}_h) = \frac{\hbar^2 \pi^2}{m_h \bar{L}_{\text{QW}}^3} \Delta h(\boldsymbol{\rho}_h), \quad (8.11)$$

such that the disorder potential is directly proportional to the spatially dependent variation in the **QW** width: $V_i(\boldsymbol{\rho}_i) \propto \Delta h(\boldsymbol{\rho}_i)$. The final numerical results are obtained by averaging over multiple random realizations of the disorder potential.

In the limit of weak localization (where the internal motion is hardly affected), the relative and center-of-mass (COM) motion can be separated via a coordinate transform and a factorization ansatz is made in order to reduce the complexity of the 4-dimensional partial differential equation for $\Psi_\alpha^s(\boldsymbol{\rho}_e, \boldsymbol{\rho}_h)$ given in Eq. (8.5):

$$\Psi_\alpha^s(\boldsymbol{\rho}_e, \boldsymbol{\rho}_h) = \phi_{1s}^s(\mathbf{r}) \psi_\alpha^s(\mathbf{R}) \quad (8.12)$$

with the relative coordinate $\mathbf{r} \equiv \boldsymbol{\rho}_e - \boldsymbol{\rho}_h$ and the **COM** coordinate $\mathbf{R} \equiv (m_e \boldsymbol{\rho}_e + m_h \boldsymbol{\rho}_h)/M$. $M \equiv m_e + m_h$ is the total mass. The relative motion satisfies the Wannier equation:

$$\left(-\frac{\hbar^2}{2\mu} \nabla_{\mathbf{r}}^2 + V_{e-h}(\mathbf{r}) \right) \phi_{1s}^s(\mathbf{r}) = E_{\text{rel}}^s \phi_{1s}^s(\mathbf{r}), \quad (8.13)$$

where E_{rel}^s the binding energy of the exciton in the ideal **QW** (without disorder). The theoretical treatment focuses on the lowest bound $1s$ exciton states, since higher states are assumed to be energetically well separated and therefore do not play a major role in the considered dynamics.

The **COM** Schrödinger equation is obtained by inserting the separation ansatz Eq. (8.12) into Eq. (8.5), multiplying with $\phi_{1s}^s(\mathbf{r})$ and integrating over the relative coordinate \mathbf{r} :

$$\left(-\frac{\hbar^2}{2M} \nabla_{\mathbf{R}}^2 + V_{\text{COM}}(\mathbf{R}) \right) \psi_\alpha^s(\mathbf{R}) = E_{\alpha, \text{COM}}^s \psi_\alpha^s(\mathbf{R}) \quad (8.14)$$

with the localization energy $E_{\alpha, \text{COM}}^s = E_\alpha^s - E_{\text{rel}}^s$ and the effective disorder potential of the **COM** motion given as:

$$V_{\text{COM}}(\mathbf{R}) = \int d^2 r |\phi_{1s}^s(\mathbf{r})|^2 \left(V_e\left(\mathbf{R} + \frac{m_h}{M} \mathbf{r}\right) + V_h\left(\mathbf{R} + \frac{m_e}{M} \mathbf{r}\right) \right). \quad (8.15)$$

The **COM** wave functions are normalized according to $\int_{A_{\text{QW}}} d^2 R \psi_\alpha^{s*}(\mathbf{R}) \psi_\beta^s(\mathbf{R}) = \delta_{\alpha, \beta}$. In a numerical evaluation, typically a few thousand of the lowest **COM** exciton states have to be calculated, such that a sufficient number of bright and dark **COM** eigenstates is included in order to account for the exciton-phonon coupling [Sin17]. A treatment in the basis of disorder eigenstates has the advantage that it avoids off-diagonal contributions due to disorder scattering [Zim03].

8.2.2 Electron–phonon interaction

Since the system dynamics at temperatures up to room temperature are of interest, the interaction with lattice vibrations will play an important role for the system dynamics. Usually, three types of electron–phonon interactions are distinguished in a semiconductor: the polar coupling to optical phonons, the piezoelectric coupling to acoustic phonons, and the deformation-potential coupling to acoustic phonons. The latter coupling type describes a periodic longitudinal displacement of the ions in the crystal in the form of compressions and expansions. The corresponding change in the band edge energy δE_λ is determined by the volume deformation potential D_λ for band $\lambda = c, v$ (or $D_{e/h}$ with $D_e = D_c$ and $D_h = -D_v$):²

$$\delta E_\lambda = D_\lambda \frac{\delta V}{V}. \quad (8.16)$$

In fact, longitudinal-acoustic (LA) phonon scattering via deformation-potential coupling makes the dominant contribution to the dephasing of the exciton dynamics in a disordered QW, whereas optical phonon scattering has no notable influence for near band-gap excitations [Tak85, Sia01, Zim03]. Starting from the general electron–phonon Hamiltonian derived in Sec. 2.2.2, the limit of long wavelengths is considered with $\mathbf{q} \approx \mathbf{0}$, where Umklapp processes with $\mathbf{G}_s \neq \mathbf{0}$ are neglected. As a consequence, the matrix elements for transverse phonon coupling vanish in the case of normal processes with $\mathbf{G}_s = \mathbf{0}$ due to $\mathbf{q} \cdot \mathbf{e}_{j,\mathbf{q}} = 0$ for transverse polarization (cf. Eq. (2.50)). Instead, only longitudinal phonons contribute with $\mathbf{e}_{j,\mathbf{q}} \rightarrow \hat{\mathbf{q}}$ (in the case of non-degenerate bands) [Mah00]. Furthermore, it is assumed that all interactions with the lattice vibrations where a phonon is absorbed or emitted are diagonal with respect to the involved electronic states: $\lambda = \lambda'$ in Eq. (2.49). This is reasonable since the electronic structure is described as two-band model where only the lowest conduction subband and highest valence subband are considered. The corresponding large energy gap is unlikely to be overcome by acoustic phonons. For simplicity, a plane-wave representation is chosen (i.e., the free bulk solution) where $\hat{\rho}(\mathbf{q}) = \sum_{\lambda,\mathbf{k}} \hat{a}_{\lambda,\mathbf{k}+\mathbf{q}}^\dagger \hat{a}_{\lambda,\mathbf{k}}$:

$$\hat{H}_{\text{el-ph, LA}}^s = \sum_{\lambda,\mathbf{k}} \sum_{j,\mathbf{q}} g_{j,\mathbf{q}}^\lambda (\hat{b}_{j,\mathbf{q}} + \hat{b}_{j,-\mathbf{q}}^\dagger) \hat{a}_{\lambda,\mathbf{k}+\mathbf{q}}^\dagger \hat{a}_{\lambda,\mathbf{k}} \quad (8.17)$$

with the matrix element for the deformation-potential coupling to LA phonons [Tak85, Mah00]:

$$g_{j,\mathbf{q}}^\lambda \equiv \sqrt{\frac{\hbar \omega_{j,\mathbf{q}}}{2\rho_s V_s u_j^2}} D_\lambda \quad (8.18)$$

with sound velocity $u_j = \omega_{j,\mathbf{q}}/q$ (assuming a linear dispersion of the acoustic phonons).³

Now, the electron–phonon coupling Hamiltonian in Eq. (8.17) is reformulated in terms of the exciton basis introduced in Sec. 8.2.1:

$$\hat{H}_{\text{el-ph, LA}}^s = \int d^3 r_e \int d^3 r_h \sum_{\alpha,\beta} |X_\alpha^s\rangle \langle X_\alpha^s| \hat{H}_{\text{el-ph, LA}}^s |\mathbf{r}_e, \mathbf{r}_h\rangle \underbrace{\langle \mathbf{r}_e, \mathbf{r}_h | X_\beta^s \rangle \langle X_\beta^s|}_{=\Psi_\beta^s(\mathbf{r}_e, \mathbf{r}_h)} \quad (8.19)$$

$$= \sum_\alpha \sum_j (\hat{b}_{j,\mathbf{0}} + \hat{b}_{j,\mathbf{0}}^\dagger) g_{j,\mathbf{0}}^\alpha |X_\alpha^s\rangle \langle X_\alpha^s| + \sum_{\alpha,\beta} \sum_{j,\mathbf{q}} g_{j,\mathbf{q}}^{\alpha\beta} (\hat{b}_{j,-\mathbf{q}} + \hat{b}_{j,\mathbf{q}}^\dagger) |X_\alpha^s\rangle \langle X_\beta^s|. \quad (8.20)$$

² First-principles calculations yield deformation potentials $D_v = -0.6$ eV and $D_c = -2.3$ eV for ZnO [Jan07].

³ A mass density of $\rho_s = 5.676$ g/cm³ and average speeds of sound of 6090 m/s (longitudinal) and 2760 m/s (transverse) have been found for ZnO [Bat62].

The matrix element $g_{j,\mathbf{q}}^{\alpha\beta}$ for deformation-potential scattering with disorder eigenstates is expressed by [Zim97b]:

$$g_{j,\mathbf{q}}^{\alpha\beta} = \sqrt{\frac{\hbar\omega_{j,\mathbf{q}}}{2\rho_s V_s u_j^2}} \left(D_c K_e(q_z) \chi\left(\frac{m_h}{M} \mathbf{q}_{\parallel}\right) - D_v K_h(q_z) \chi\left(\frac{m_e}{M} \mathbf{q}_{\parallel}\right) \right) \int d^2R \psi_{\alpha}^{s*}(\mathbf{R}) e^{i\mathbf{q}_{\parallel} \cdot \mathbf{R}} \psi_{\beta}^s(\mathbf{R}), \quad (8.21)$$

with K_i and χ being the Fourier transforms of the squared confinement and relative exciton wave functions ξ_i and ϕ_{1s}^s , respectively:

$$K_i(q_z) \equiv \int dz_i |\xi_i(z_i)|^2 e^{iq_z z_i} \quad \text{and} \quad \chi\left(\frac{m_i}{M} \mathbf{q}_{\parallel}\right) \equiv \int d^2r |\phi_{1s}^s(\mathbf{r})|^2 e^{i\frac{m_i}{M} \mathbf{q}_{\parallel} \cdot \mathbf{r}}. \quad (8.22)$$

Here, the factorization $\Psi_{\alpha}^s(\mathbf{r}_e, \mathbf{r}_h) = \xi_e(z_e) \xi_h(z_h) \phi_{1s}^s(\mathbf{r}) \psi_{\alpha}^s(\mathbf{R})$ discussed in Sec. 8.2.1 has been used. The first term of Eq. (8.20) is omitted in the following, since it only causes a constant phonon-induced shift in the system energy.

8.2.3 Electron–photon interaction

The quantized interband electron-photon interaction derived in Sec. 2.2.1 is given by

$$\hat{H}_{\text{el-pt}}^s = \sum_{l,\mathbf{q}} \sum_{\mathbf{k},\mathbf{k}'} \left\{ (M_{l,\mathbf{q}}^{\text{cv},\mathbf{k}\mathbf{k}'} \hat{c}_{l,\mathbf{q}} + M_{l,\mathbf{q}}^{\text{vc},\mathbf{k}\mathbf{k}'*} \hat{c}_{l,\mathbf{q}}^{\dagger}) \hat{a}_{c,\mathbf{k}}^{\dagger} \hat{a}_{v,\mathbf{k}'} + (M_{l,\mathbf{q}}^{\text{vc},\mathbf{k}\mathbf{k}'} \hat{c}_{l,\mathbf{q}} + M_{l,\mathbf{q}}^{\text{cv},\mathbf{k}\mathbf{k}'*} \hat{c}_{l,\mathbf{q}}^{\dagger}) \hat{a}_{v,\mathbf{k}}^{\dagger} \hat{a}_{c,\mathbf{k}'} \right\}. \quad (8.23)$$

Two polarization modes $l = \text{TE}, \text{TM}$ of the electric field are distinguished: the transverse electric (TE, electric field in the QW xy plane) and transverse magnetic (TM, electric field in the plane of incidence) mode. The respective optical matrix elements are given by [Zim03]

$$M_{\text{TE},\mathbf{q}}^{\lambda\lambda',\mathbf{k}\mathbf{k}'} \equiv M_{\text{TE},\mathbf{q}}^{\lambda\lambda'} \delta_{\mathbf{k},\mathbf{k}'} = i \sqrt{\frac{\hbar\omega_{\mathbf{q}}}{2\epsilon_0 \epsilon_r V}} d_{\lambda\lambda'} \delta_{\mathbf{k},\mathbf{k}'}, \quad (8.24)$$

$$M_{\text{TM},\mathbf{q}}^{\lambda\lambda',\mathbf{k}\mathbf{k}'} \equiv M_{\text{TM},\mathbf{q}}^{\lambda\lambda'} \delta_{\mathbf{k},\mathbf{k}'} = i \sqrt{\frac{\hbar\omega_{\mathbf{q}}}{2\epsilon_0 \epsilon_r V}} \frac{q_z}{q} d_{\lambda\lambda'} \delta_{\mathbf{k},\mathbf{k}'}, \quad (8.25)$$

where $d_{\lambda\lambda'}$ denotes the microscopic interband dipole moment at $\mathbf{k} \approx \mathbf{0}$. Note that $M_{l,\mathbf{q}}^{\lambda\lambda'*} = -M_{l,\mathbf{q}}^{\lambda'\lambda}$. Rewriting the Hamiltonian in the exciton basis defined by the disorder eigenstates $|X_{\alpha}^s\rangle$ as in the previous Sec. 8.2.2 leads to

$$\hat{H}_{\text{el-pt}}^s = \sum_{\alpha} \sum_{l,\mathbf{q}} (M_{l,\mathbf{q}}^{\alpha} \hat{c}_{l,\mathbf{q}}^{\dagger} |\phi_0^s\rangle \langle X_{\alpha}^s| + M_{l,\mathbf{q}}^{\alpha*} \hat{c}_{l,\mathbf{q}} |X_{\alpha}^s\rangle \langle \phi_0^s|) \quad (8.26)$$

with the redefined optical matrix element in excitonic basis

$$M_{l,\mathbf{q}}^{\alpha} \equiv M_{l,\mathbf{q}}^{\text{vc}} \phi_{1s}^s(\mathbf{0}) O_{\text{eh}} \int d^2R \psi_{\alpha}^s(\mathbf{R}) \quad (8.27)$$

and the confinement overlap $O_{\text{eh}} = \int dz \xi_e(z) \xi_h(z)$ (defined as in Ref. [Zim03]).⁴ The optical matrix element contains the integrals over the excitonic wave functions with equal electron and hole coordinates $\mathbf{r}_e = \mathbf{r}_h$, i.e., it is determined by the probability of finding an exciton with electron and hole at the same position (optically bright exciton).

⁴ Note that in the upper Eq. (8.26), terms that violate energy conservation (e.g., by describing the creation of an exciton under photon emission) and describe the creation of more than one exciton have been neglected.

8.2.4 Total Hamiltonian for disordered quantum wells in exciton basis

All in all, the total Hamiltonian for the **QW** substrate including disorder, acoustic phonon scattering, and radiative recombination in the excitonic basis reads:

$$\begin{aligned} \hat{H}^s = & \sum_{\alpha} E_{\alpha}^s |X_{\alpha}^s\rangle\langle X_{\alpha}^s| + \sum_{j,\mathbf{q}} \hbar\omega_{j,\mathbf{q}} \hat{b}_{j,\mathbf{q}}^{\dagger} \hat{b}_{j,\mathbf{q}} + \sum_{l,\mathbf{q}} \hbar\omega_{l,\mathbf{q}} \hat{c}_{l,\mathbf{q}}^{\dagger} \hat{c}_{l,\mathbf{q}} + \sum_{\alpha,\beta} \sum_{j,\mathbf{q}} g_{j,\mathbf{q}}^{\alpha\beta} (\hat{b}_{j,-\mathbf{q}} + \hat{b}_{j,\mathbf{q}}^{\dagger}) |X_{\alpha}^s\rangle\langle X_{\beta}^s| \\ & + \sum_{\alpha} \sum_{l,\mathbf{q}} (M_{l,\mathbf{q}}^{\alpha} \hat{c}_{l,\mathbf{q}}^{\dagger} |\phi_0^s\rangle\langle X_{\alpha}^s| + M_{l,\mathbf{q}}^{\alpha*} \hat{c}_{l,\mathbf{q}} |X_{\alpha}^s\rangle\langle\phi_0^s|). \end{aligned} \quad (8.28)$$

Note that the ground state energy E_0^s has been set to zero.

8.2.5 Equations of motion in density matrix formalism

According to the above Hamiltonian for the disordered **QW** of Eq. (8.28), the excitons do not form a closed system, but they couple to phonons and photons acting as an environment in thermal equilibrium that is often referred to as bath or reservoir. The reduced system density operator $\hat{\rho}_S \equiv \text{tr}_B[\hat{\rho}]$ is derived by taking the trace of the combined system and bath density operator $\hat{\rho}$ over the reservoir states [Car99, Bre02]. The quantities of interest for the further study are the expectation values of the exciton density matrix elements. These are on the one hand the exciton densities

$$\rho_{\alpha\beta}^s \equiv \langle |X_{\alpha}^s\rangle\langle X_{\beta}^s| \rangle = \text{tr}_S[|X_{\alpha}^s\rangle\langle X_{\beta}^s| \text{tr}_B[\hat{\rho}]] = \langle X_{\beta}^s | \hat{\rho}_S | X_{\alpha}^s \rangle = \text{tr}_B[\langle X_{\beta}^s | \hat{\rho} | X_{\alpha}^s \rangle] \quad (8.29)$$

describing the population of exciton state X_{α}^s for $\alpha = \beta$ or the amplitude for a transition from X_{β}^s to X_{α}^s for $\alpha \neq \beta$. Accordingly, the polarization between an exciton state X_{α}^s and the electronic ground state ϕ_0^s is given by

$$\rho_{\alpha 0}^s \equiv \langle |X_{\alpha}^s\rangle\langle\phi_0^s| \rangle = \text{tr}_B[\langle\phi_0^s| \hat{\rho} | X_{\alpha}^s \rangle]. \quad (8.30)$$

The ground state population is calculated as

$$\rho_{00}^s \equiv \langle |\phi_0^s\rangle\langle\phi_0^s| \rangle = \text{tr}_B[\langle\phi_0^s| \hat{\rho} | \phi_0^s \rangle]. \quad (8.31)$$

The von Neumann equation $i\hbar\partial_t\hat{\rho}_S = [\hat{H}^s, \hat{\rho}_S]$ yields the following **EOM** for the exciton densities and polarizations and the ground state population:

$$\frac{\partial}{\partial t}\rho_{\alpha\alpha}^s = -2R_{\alpha}^s\rho_{\alpha\alpha}^s + \sum_{\beta} \gamma_{\alpha\leftarrow\beta}^s\rho_{\beta\beta}^s, \quad (8.32)$$

$$\frac{\partial}{\partial t}\rho_{\alpha\beta}^s = \left(\frac{i}{\hbar}(E_{\alpha}^s - E_{\beta}^s) - (R_{\alpha}^s + R_{\beta}^s)\right)\rho_{\alpha\beta}^s + \delta_{\alpha\beta} \sum_{\zeta} \gamma_{\alpha\leftarrow\zeta}^s\rho_{\zeta\zeta}^s, \quad (8.33)$$

$$\frac{\partial}{\partial t}\rho_{\alpha 0}^s = \left(\frac{i}{\hbar}E_{\alpha}^s - R_{\alpha}^s\right)\rho_{\alpha 0}^s, \quad (8.34)$$

$$\frac{\partial}{\partial t}\rho_{00}^s = \sum_{\alpha} r_{\alpha}\rho_{\alpha\alpha}^s. \quad (8.35)$$

A detailed derivation including Markovian solutions of phonon- and photon-assisted density matrices is given in App. C.1. R_{α}^s denotes the total out-scattering rate

$$R_{\alpha}^s \equiv \frac{1}{2}\left(r_{\alpha} + \sum_{\beta} \gamma_{\beta\leftarrow\alpha}^s\right) \quad (8.36)$$

composed of the spontaneous radiative decay rate

$$r_\alpha \equiv \frac{2\pi}{\hbar} \sum_{l,\mathbf{q}} |M_{l,\mathbf{q}}^\alpha|^2 \delta(E_\alpha^s - \hbar\omega_{\mathbf{q}}) \quad (8.37)$$

and the phonon scattering rate

$$\gamma_{\beta \leftarrow \alpha}^s \equiv \frac{2\pi}{\hbar} \sum_{j,\mathbf{q}} |g_{j,\mathbf{q}}^{\beta\alpha}|^2 \left\{ (n_{j,\mathbf{q}} + 1) \delta(E_\beta^s - E_\alpha^s + \hbar\omega_{j,\mathbf{q}}) + n_{j,\mathbf{q}} \delta(E_\beta^s - E_\alpha^s - \hbar\omega_{j,\mathbf{q}}) \right\}. \quad (8.38)$$

These two rates are further evaluated in App. C.1.1. Two different processes can be distinguished: The second term in Eq. (8.38) describes the transition to an energetically higher state via phonon absorption. As a prerequisite, thermal energy is necessary to generate phonons, such that this term is purely temperature dependent. The transition to an energetically lower state under phonon emission is described by the first term. This process is either spontaneous or stimulated due to thermal energy.

The system of EOM Eqs. (8.32), (8.33), (8.34), and (8.35) shows that only the exciton population $\rho_{\alpha\alpha}^s$ is refilled by other populations via phonon scattering. Therefore, it is long-lived compared to the fast decaying polarizations $\rho_{\alpha\beta}^s$ ($\alpha \neq \beta$). The EOM for the exciton density Eq. (8.32) does not incorporate off-diagonal polarizations and is therefore only suited to describe the long-time dynamics after the initially relevant polarizations have decayed. The exciton number is conserved with the exception of radiative decay processes into the ground state [Zim03]. The EOM for the exciton polarization $\rho_{\alpha 0}^s$ of Eq. (8.34) is easily solved by $\rho_{\alpha 0}^s(t) = \exp[(\frac{i}{\hbar}E_\alpha^s - R_\alpha^s)t]$. It decays with the rate R_α^s due to phonon scattering and radiative recombination. It follows that also Eq. (8.33) is analytically solved by factorizing $\rho_{\alpha\beta}^s(t) = \rho_{\alpha 0}^s(t)\rho_{\beta 0}^{s*}(t)$ for $\alpha \neq \beta$. Thus, only the EOM for the diagonal exciton density Eq. (8.32) is left to be solved numerically.

8.2.6 Phenomenological Lindblad approach

So far, the external optical pumping of the semiconductor substrate has not been encountered in the EOM derived in Sec. 8.2.5. In many spectroscopic experiments, the laser excitation takes place at energies far above the band gap given by the lowest bound exciton of the system. However, the available computational memory restricts the number of calculated excitonic states to a very limited energy range above the band gap (even if several thousand lowest eigenstates are calculated). In order to phenomenologically include the incoherent optical pumping, a Lindblad approach is chosen [Car99, Bre02]. Therefore, the Lindblad dissipator \mathcal{D} is introduced that modifies the von Neumann equation in the following way:

$$\frac{\partial}{\partial t} \hat{\rho}_S = -\frac{i}{\hbar} [\hat{H}^s, \hat{\rho}_S] + \mathcal{D} \hat{\rho}_S \quad (8.39)$$

with

$$\mathcal{D} \hat{\rho}_S \equiv \sum_k \frac{\gamma_k}{2} (2\hat{A}_k \hat{\rho}_S \hat{A}_k^\dagger - \hat{A}_k^\dagger \hat{A}_k \hat{\rho}_S - \hat{\rho}_S \hat{A}_k^\dagger \hat{A}_k). \quad (8.40)$$

Here, the Lindblad operators $\hat{A}_k^{(\dagger)}$ describe processes that occur at a rate γ_k in the system.

In a phenomenological approach similar to [Cas17], a probability ensemble of high-energy states in the semiconductor substrate is introduced. They are assumed to form a quasi-continuous band of high energetic states labeled \tilde{h} . At a given initial time, a short laser pulse excites charge carriers from the ground state into the ensemble of high-energy band states at a rate γ^{exc} . The probability ensemble \tilde{h} itself can interact with the low-energy exciton states X_α^s in two ways: First, states of the high-energy band \tilde{h} can decay into the states X_α^s under phonon

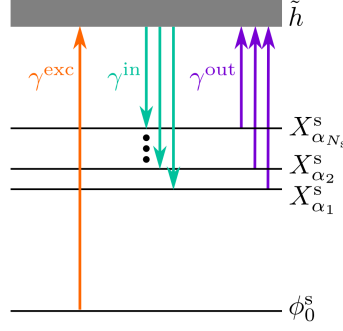


Figure 8.2: Schematic of the Lindblad processes involving the high-energy band \tilde{h} .

emission at a rate $\gamma_\alpha^{\text{in}}$ and second, the states X_α^s can be excited into the high-energy band states \tilde{h} by absorbing a phonon at rate $\gamma_\alpha^{\text{out}}$. All rates are assumed to be mean values and therefore independent of the specific auxiliary state within the high-energy band \tilde{h} , since nothing is known about these states. The three processes, namely the optical pumping from the crystal ground state into the high-energy band and the in- and out-scattering between the high-energy states and the N_s numerically calculated lowest-energy excitons X_α^s are schematically depicted in Fig. 8.2. They are described by the operators

$$\hat{A}_{\tilde{h}}^{\text{exc}} = |\tilde{h}\rangle\langle\phi_0^s|, \quad \hat{A}_{\tilde{h}}^{\text{exc}\dagger} = |\phi_0^s\rangle\langle\tilde{h}|, \quad (8.41)$$

$$\hat{A}_{\alpha\tilde{h}}^{\text{in}} = \hat{A}_{\tilde{h}\alpha}^{\text{out}\dagger} = |X_\alpha^s\rangle\langle\tilde{h}|, \quad \hat{A}_{\alpha\tilde{h}}^{\text{in}\dagger} = \hat{A}_{\tilde{h}\alpha}^{\text{out}} = |\tilde{h}\rangle\langle X_\alpha^s|. \quad (8.42)$$

With that, the three Lindblad contributions are given by

$$\mathcal{D}\hat{\rho}_S = (\mathcal{D}^{\text{exc}} + \mathcal{D}^{\text{in}} + \mathcal{D}^{\text{out}})\hat{\rho}_S \quad (8.43)$$

$$\begin{aligned} &= \frac{\gamma^{\text{exc}}}{2} (2\rho_{00}^s|\tilde{h}\rangle\langle\tilde{h}| - |\phi_0^s\rangle\langle\phi_0^s|\hat{\rho}_S - \hat{\rho}_S|\phi_0^s\rangle\langle\phi_0^s|) \\ &+ \sum_\zeta \frac{\gamma_\zeta^{\text{in}}}{2} (2\rho_{\tilde{h}\tilde{h}}^s|X_\zeta^s\rangle\langle X_\zeta^s| - |\tilde{h}\rangle\langle\tilde{h}|\hat{\rho}_S - \hat{\rho}_S|\tilde{h}\rangle\langle\tilde{h}|) \\ &+ \sum_\zeta \frac{\gamma_\zeta^{\text{out}}}{2} (2\rho_{\zeta\zeta}^s|\tilde{h}\rangle\langle\tilde{h}| - |X_\zeta^s\rangle\langle X_\zeta^s|\hat{\rho}_S - \hat{\rho}_S|X_\zeta^s\rangle\langle X_\zeta^s|). \end{aligned} \quad (8.44)$$

Recalling that $\rho_{\alpha\beta}^s = \langle X_\beta^s|\hat{\rho}_S|X_\alpha^s\rangle$, the Lindblad contributions to the **EOM** for the semiconductor exciton densities and polarizations can be determined:

$$\langle X_\alpha^s|\mathcal{D}\hat{\rho}_S|X_\alpha^s\rangle = \gamma_\alpha^{\text{in}}\rho_{\tilde{h}\tilde{h}}^s - \gamma_\alpha^{\text{out}}\rho_{\alpha\alpha}^s, \quad (8.45)$$

$$\langle X_\beta^s|\mathcal{D}\hat{\rho}_S|X_\alpha^s\rangle = \gamma_\alpha^{\text{in}}\rho_{\tilde{h}\tilde{h}}^s\delta_{\alpha,\beta} - \left(\frac{\gamma_\beta^{\text{out}}}{2} + \frac{\gamma_\alpha^{\text{out}}}{2}\right)\rho_{\alpha\beta}^s, \quad (8.46)$$

$$\langle\phi_0^s|\mathcal{D}\hat{\rho}_S|X_\alpha^s\rangle = -\left(\frac{\gamma^{\text{exc}}}{2} + \frac{\gamma_\alpha^{\text{out}}}{2}\right)\rho_{\alpha 0}^s, \quad (8.47)$$

$$\langle\phi_0^s|\mathcal{D}\hat{\rho}_S|\phi_0^s\rangle = -\gamma^{\text{exc}}\rho_{00}^s. \quad (8.48)$$

Equations (8.45) and (8.46) reveal that the exciton populations $\rho_{\alpha\alpha}^s$ and coherences $\rho_{\alpha\beta}^s$ couple to the high-energy density $\rho_{\tilde{h}\tilde{h}}^s$, whose **EOM** is given by

$$\frac{\partial}{\partial t}\rho_{\tilde{h}\tilde{h}}^s = \gamma^{\text{exc}}\rho_{00}^s - \sum_\zeta \gamma_\zeta^{\text{in}}\rho_{\tilde{h}\tilde{h}}^s + \sum_\zeta \gamma_\zeta^{\text{out}}\rho_{\zeta\zeta}^s. \quad (8.49)$$

In photoluminescence (PL) experiments, the system is usually excited with a short laser pulse of tens to hundreds of fs duration centered around the initial time t_0 .⁵ Therefore, the time-dependent pulse intensity γ^{exc} is assumed have a Gaussian shape with pulse duration τ and peak intensity I_0 : $\gamma^{\text{exc}} = I_0 \exp[-(t - t_0)^2/\tau^2]$.

Next, an expression for the phonon-assisted in- and out-scattering rates between the high-energy quasi-continuum states and the calculated lower-energy states has to be found. Treating the exciton relaxation via acoustic phonon scattering similar to Sec. 8.2.4 is not possible since the energies and wave functions of the high-energy continuum states are unknown. Therefore, the in-scattering rate is assumed to follow a Gaussian distribution around the mean energy E_h^{s} of the high-energy band: $\gamma_{\alpha}^{\text{in}} = \gamma_0^{\text{LA}} \exp[-(E_{\alpha}^{\text{s}} - E_h^{\text{s}})^2/\sigma_h^2]$. The width σ_h is expected to be rather small, but it must be large enough that at least the energetically highest calculated exciton state at energy $E_{\alpha_{N_s}}^{\text{s}}$ is significantly filled from the high-energy band. The quantities E_h^{s} and σ_h characterizing the high-energy band are modeled depending on the energy coverage $E_{\alpha_{N_s}}^{\text{s}} - E_{\alpha_1}^{\text{s}}$ [Cas17]:

$$E_h^{\text{s}} = E_{\alpha_{N_s}}^{\text{s}} + A \left(E_{\alpha_{N_s}}^{\text{s}} - E_{\alpha_1}^{\text{s}} \right) \quad \text{with} \quad 0 < A < 1, \quad (8.50)$$

$$\sigma_h = BA \left(E_{\alpha_{N_s}}^{\text{s}} - E_{\alpha_1}^{\text{s}} \right) \quad \text{with} \quad 0 < B < 1, \quad (8.51)$$

where $E_{\alpha_1}^{\text{s}}$ denotes the energetically lowest calculated exciton state. The parameter A defines the energetic distance between the high-energy band and the highest calculated exciton state. The factor B in turn determines the width of the in-scattering rate depending on the distance of E_h^{s} from the energy edge of the calculated exciton states.

For the out-scattering rate, a detailed-balance expression is chosen: $\gamma_{\alpha}^{\text{out}} = \gamma_{\alpha}^{\text{in}} \exp[E_{\alpha}^{\text{s}} - E_h^{\text{s}}/(k_{\text{B}}T)]$.

8.3 Organic part: Frenkel excitons in a disordered molecular monolayer including intermolecular Coulomb coupling and coupling to vibrational modes

8.3.1 Local molecular basis states

In this chapter, the condition of a periodically arranged molecular layer imposed in the previous chapter Chap. 7 is dropped and the treatment of the organic site is extended to disorder in the molecular layer. Therefore, the theoretical framework for the organic component will be set in position space. A molecular basis is constructed describing an excitation of the ν -th molecule:

$$|\nu\rangle \equiv \hat{a}_{\text{L},\nu}^{\dagger} \hat{a}_{\text{H},\nu} |\phi_0^{\text{m}}\rangle. \quad (8.52)$$

Here, $\hat{a}_{A,\nu}^{(\dagger)}$ denotes the annihilation (creation) operator of molecular orbital $A \in \{\text{H}, \text{L}\}$ in the ν -th molecule, as introduced in Sec. 7.2.

8.3.2 Diagonalization of the electronic Hamiltonian

The interaction-free electronic part of the Hamiltonian for the organic layer is given by

$$\hat{H}_{0,\text{e}}^{\text{m}} = \sum_{A,\nu} \varepsilon_{A,\nu} \hat{a}_{A,\nu}^{\dagger} \hat{a}_{A,\nu}. \quad (8.53)$$

⁵ For example, a femtosecond Ti:sapphire laser is used [Sch15] with a pulse duration of 150 fs.

The molecules in the organic film are assumed to be identical with $\varepsilon_{A,\nu} \equiv \varepsilon_A$ and an optical gap $\varepsilon_{\text{gap}}^{\text{m}} = \varepsilon_{\text{L}} - \varepsilon_{\text{H}}$. To describe the Coulomb coupling between the electrons in the molecular layer, the Hamiltonian in partial charge approximation derived in Secs. 7.2 and 7.3 is used:

$$\hat{H}_{\text{C}}^{\text{m-m}} = \frac{1}{2} \sum_{A,B} \sum_{\substack{\nu_a, \nu_b \\ \nu_a \neq \nu_b}} V_{A, \nu_a}^{A, \nu_a} V_{B, \nu_b}^{B, \nu_b} \hat{a}_{A, \nu_a}^\dagger \hat{a}_{B, \nu_b}^\dagger \hat{a}_{B, \nu_b} \hat{a}_{A, \nu_a} + \sum_{\substack{\nu_a, \nu_b \\ \nu_a \neq \nu_b}} V_{\text{L}, \nu_a}^{\text{H}, \nu_a} V_{\text{H}, \nu_b}^{\text{L}, \nu_b} \hat{a}_{\text{H}, \nu_a}^\dagger \hat{a}_{\text{L}, \nu_b}^\dagger \hat{a}_{\text{H}, \nu_b} \hat{a}_{\text{L}, \nu_a} \quad (8.54)$$

with the coupling element (cf. Eq. (7.17))

$$V_{A', \nu_a}^{A, \nu_a} V_{B', \nu_b}^{B, \nu_b} = \sum_{I, J} G^{\text{m-m}}(\mathbf{R}_{\nu_a} + \mathbf{r}_{I, \nu_a}, \mathbf{R}_{\nu_b} + \mathbf{r}_{J, \nu_b}) q_I^{AA'} q_J^{BB'} \quad (8.55)$$

containing the Green's function for Coulomb interaction in the organic film defined in Eq. (B.4). \mathbf{R}_ν denotes the position of the ν -th molecule in the organic film and $\mathbf{r}_{I, \nu}$ describes the relative positions of the partial charges labeled I within this molecule. In contrast to the previous Chap. 7, this time they depend on the molecular index ν , since here a non-uniform orientation of the molecules in the organic layer is considered. The first term in Eq. (8.54) is the monopole-monopole part leading to a ground and excited state renormalization, whereas the second term describes Förster excitation transfer between different molecules. The latter is responsible for an off-diagonal coupling between different molecules. Therefore, the local molecular basis states $|\nu\rangle$ are not eigenstates of the purely electronic Hamiltonian $\hat{H}_{\text{e}}^{\text{m}} = \hat{H}_0^{\text{m}} + \hat{H}_{\text{C}}^{\text{m-m}}$ for the organic layer. Analogous to Sec. 7.5, the electronic Hamiltonian is diagonalized, yielding new, delocalized exciton states $|X_\alpha^{\text{m}}\rangle$ given as linear combinations of the local basis states with coefficients c_ν^α and eigenenergies E_α^{m} :

$$|X_\alpha^{\text{m}}\rangle = \sum_\nu c_\nu^\alpha |\nu\rangle \quad \text{with} \quad \hat{H}_{\text{e}}^{\text{m}} |X_\alpha^{\text{m}}\rangle = (E_0^{\text{m}} + E_\alpha^{\text{m}}) |X_\alpha^{\text{m}}\rangle. \quad (8.56)$$

Here, the ground state energy was defined as

$$E_0^{\text{m}} \equiv \langle \phi_0^{\text{m}} | \hat{H}_{\text{e}}^{\text{m}} | \phi_0^{\text{m}} \rangle = N_{\text{m}} \varepsilon_{\text{H}} + \frac{1}{2} \sum_{\substack{\nu_a, \nu_b \\ \nu_a \neq \nu_b}} V_{\text{H}, \nu_a}^{\text{H}, \nu_a} V_{\text{H}, \nu_b}^{\text{H}, \nu_b}. \quad (8.57)$$

Evaluating the matrix element $\langle \nu | \hat{H}_{\text{e}}^{\text{m}} | X_\alpha^{\text{m}} \rangle = (E_0^{\text{m}} + E_\alpha^{\text{m}}) c_\nu^\alpha$ yields the eigenproblem for the coefficients c_ν^α and eigenvalues E_α^{m} in matrix form:

$$E_\alpha^{\text{m}} \begin{pmatrix} c_1^\alpha \\ c_2^\alpha \\ \vdots \\ c_{N_{\text{m}}}^\alpha \end{pmatrix} = \begin{pmatrix} d(1) & a(1, 2) & \cdots & a(1, N_{\text{m}}) \\ a(2, 1) & d(2) & \cdots & a(2, N_{\text{m}}) \\ \vdots & \vdots & \ddots & \vdots \\ a(N_{\text{m}}, 1) & a(N_{\text{m}}, 2) & \cdots & d(N_{\text{m}}, N_{\text{m}}) \end{pmatrix} \begin{pmatrix} c_1^\alpha \\ c_2^\alpha \\ \vdots \\ c_{N_{\text{m}}}^\alpha \end{pmatrix} \quad (8.58)$$

with diagonal and off-diagonal entries

$$d(\nu) = \varepsilon_{\text{gap}}^{\text{m}} - \frac{1}{2} \sum_{\substack{\nu' \\ \nu' \neq \nu}} V_{\text{H}, \nu}^{\text{H}, \nu} V_{\text{H}, \nu'}^{\text{H}, \nu'} + \sum_{\substack{\nu' \\ \nu' \neq \nu}} V_{\text{H}, \nu'}^{\text{H}, \nu'} V_{\text{L}, \nu}^{\text{L}, \nu} \quad \text{and} \quad a(\nu, \nu') = V_{\text{L}, \nu}^{\text{H}, \nu} V_{\text{H}, \nu'}^{\text{L}, \nu'}. \quad (8.59)$$

This eigenproblem for the molecular excitons has in general the dimension $N_{\text{m}} \times N_{\text{m}}$ with N_{m} being the number of molecules in the organic layer. Disorder in the molecular layer is included here, such that no lattice periodicity can be exploited as in Chap. 7. To make the diagonalization of this matrix numerically tractable, a quadratic supercell is defined containing a large number of flat-lying, non-overlapping molecules with a random spatial distribution

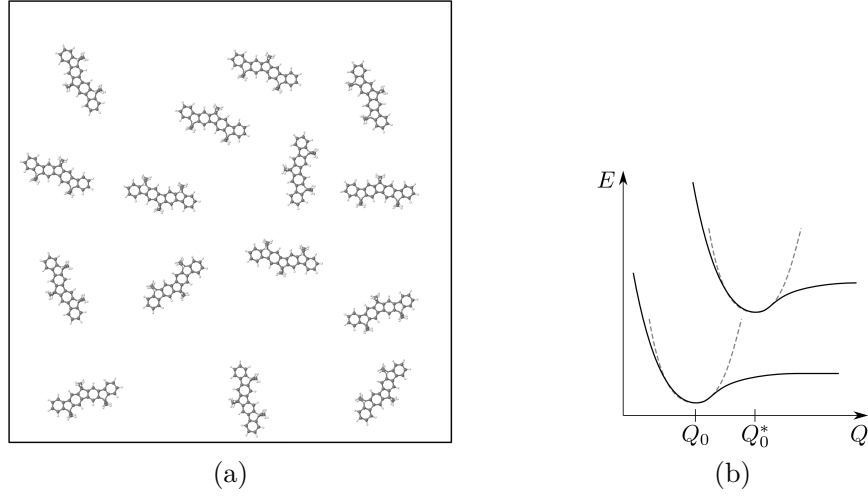


Figure 8.3: (a) Example for a small molecular supercell of dimension $10 \text{ nm} \times 10 \text{ nm}$ filled by 15 randomly arranged flat-lying L4P molecules. Note that the supercell dimensions for the numerical implementation have to be considerably larger. (b) Graphical illustration of two different PES with coordinate Q . Q_0 (Q_0^*) denotes the equilibrium position of the ground state (excited state) PES.

and orientation. This supercell is repeated periodically in the x and y directions building an extended disordered molecular layer. The supercell size is chosen large enough that (i) this periodicity does not have a physical relevance and (ii) the Coulomb interaction strength of a molecule in the center of the supercell with the surrounding molecules has sufficiently decreased at the borders of the supercell. This way, the eigenvalue problem of Eq. (8.58) gets blockdiagonal with respect to one supercell, thus reducing the dimension of the matrix to the number of molecules per supercell. Figure 8.3 (a) illustrates such a supercell.

8.3.3 Electron–phonon interaction

For lack of translational invariance, the vibrational modes in molecules (often called “vibrons”) are rather localized compared to phonons in semiconductor structures. The Hamilton operator for the interaction-free electron and phonon part as well as the electron–phonon coupling in the molecular layer is given in the electron picture by

$$\hat{H}_{0,e}^m + \hat{H}_{0,ph}^m + \hat{H}_{el-ph}^m = \sum_{A,\nu} \varepsilon_{A,\nu} \hat{a}_{A,\nu}^\dagger \hat{a}_{A,\nu} + \sum_j \hbar \omega_j \hat{b}_j^\dagger \hat{b}_j + \sum_{A,\nu} \sum_j \hbar (g_j^{A,\nu} \hat{b}_j + g_j^{A,\nu*} \hat{b}_j^\dagger) \hat{a}_{A,\nu}^\dagger \hat{a}_{A,\nu} \quad (8.60)$$

with vibrational modes j . Note that only electron–phonon coupling processes that are diagonal in the electronic states are considered. The upper representation of the Hamiltonian (Eq. (8.60)) entails the following problem related to the initial system state: The phonon dynamics is already driven at the initial time t_0 before the onset of electronic excitations in the system. The Hamiltonian includes fluctuations in the phonon number and thus in the system energy at the initial time t_0 , since phonons are created and annihilated also when applying the Hamiltonian to the electronic ground state where all highest occupied molecular orbitals (HOMOs) are occupied and all lowest unoccupied molecular orbitals (LUMOs) are empty: $\hat{H}_{el-ph}^m |\phi_0^m\rangle = \sum_\nu \sum_j \hbar (g_j^{H,\nu} \hat{b}_j + g_j^{H,\nu*} \hat{b}_j^\dagger) |\phi_0^m\rangle$. However, these phonon-induced fluctuations contradict the conventional definition of the ground state as initial dynamics-free equilibrium state without exciton-phonon coupling as stated by the Born-Oppenheimer approximation. To

solve this problem and restore the initial equilibrium state, the phonon operators are replaced by new, effective phonon operators that are defined relative to the equilibrium position

$$\hat{b}_j^g = \hat{b}_j + \frac{1}{\omega_j} \sum_{\nu} g_j^{H,\nu*} \mathbb{1}, \quad \hat{b}_j^{g\dagger} = \hat{b}_j^{\dagger} + \frac{1}{\omega_j} \sum_{\nu} g_j^{H,\nu} \mathbb{1} \quad (8.61)$$

This is called a Weyl transformation [Wey25].

Plugging this transformation into the Hamiltonian of Eq. (8.60), one obtains:

$$\begin{aligned} \hat{H}_{0,e}^{g,m} + \hat{H}_{0,ph}^{g,m} + \hat{H}_{el-ph}^{g,m} &= \sum_{A,\nu} \varepsilon_{A,\nu}^g \hat{a}_{A,\nu}^{\dagger} \hat{a}_{A,\nu} + \sum_j \hbar \omega_j \hat{b}_j^{g\dagger} \hat{b}_j^g \\ &+ \sum_{\nu} \sum_j \left(\hbar (g_j^{L,\nu} - g_j^{H,\nu}) \hat{b}_j^g + \hbar (g_j^{L,\nu*} - g_j^{H,\nu*}) \hat{b}_j^{g\dagger} \right) \hat{a}_{L,\nu}^{\dagger} \hat{a}_{L,\nu} \\ &+ \sum_j \frac{1}{\hbar \omega_j} \left(\sum_{\nu} \hbar g_j^{H,\nu} \right) \left(\sum_{\nu'} \hbar g_j^{H,\nu'*} \right) \mathbb{1}. \end{aligned} \quad (8.62)$$

Through the transformation, the modified Hamiltonian contains the following terms:

1. Free electron part with renormalized energy

$$\varepsilon_{A,\nu}^g \equiv \varepsilon_{A,\nu} - 2 \sum_j \operatorname{Re} \left[\frac{g_j^{A,\nu}}{\omega_j} \sum_{\nu'} \hbar g_j^{H,\nu'*} \right] \quad (8.63)$$

shifted by the so-called polaron (or Stokes) shift. This constant shift does not play a role for the dynamics, since only energy differences will enter the **EOM**.

2. Free phonon part with transformed phonon operators (effective phonon modes).
3. Electron–phonon interaction that only gives a contribution when applied to the exciton states and not to the phonon-assisted ground state.
4. Constant shift (renormalization): The last term of Eq. (8.62) is removed by gauge transformation in the following since it does not influence the system dynamics.

As intended, applying the transformed electron–phonon Hamilton operator to the molecular ground state yields 0: $\hat{H}_{el-ph}^{g,m} |\phi_0^m\rangle = 0$. If it operates on the molecular exciton state $|X_{\alpha}^m\rangle = \sum_{\nu} c_{\nu}^{\alpha} |\nu\rangle$, one obtains

$$\hat{H}_{el-ph}^{g,m} |X_{\alpha}^m\rangle = \sum_{\beta} \sum_{\nu} c_{\nu}^{\alpha} c_{\nu}^{\beta*} \sum_j \left(\hbar (g_j^{L,\nu} - g_j^{H,\nu}) \hat{b}_j^g + \hbar (g_j^{L,\nu*} - g_j^{H,\nu*}) \hat{b}_j^{g\dagger} \right) |X_{\beta}^m\rangle. \quad (8.64)$$

Due to the overlap of the coefficients $c_{\nu}^{\alpha} c_{\nu}^{\beta*}$ entering the expression, the contribution for $\alpha = \beta$ will dominate. The electron–phonon coupling terms with $\alpha \neq \beta$ are non-diagonal in the exciton states. They describe an electron–phonon relaxation between different disorder eigenstates in the molecular layer. With that, the free phonon and electron–phonon Hamilton operators for the system being initially in the electronic ground state is expressed in the molecular exciton basis as:

$$\hat{H}_{0,ph}^{g,m} = \sum_j \hbar \omega_j \hat{b}_j^{g\dagger} \hat{b}_j^g (|\phi_0^m\rangle \langle \phi_0^m| + \sum_{\alpha} |X_{\alpha}^m\rangle \langle X_{\alpha}^m|), \quad (8.65)$$

$$\hat{H}_{el-ph}^{g,m} = \sum_{\alpha,\beta} \sum_j \hbar (g_j^{\alpha\beta} \hat{b}_j^g + g_j^{\beta\alpha*} \hat{b}_j^{g\dagger}) |X_{\beta}^m\rangle \langle X_{\alpha}^m| \quad (8.66)$$

with the effective electron–phonon coupling element in the delocalized exciton basis

$$g_j^{\alpha\beta} \equiv \sum_{\nu} c_{\nu}^{\alpha} c_{\nu}^{\beta*} (g_j^{L,\nu} - g_j^{H,\nu}). \quad (8.67)$$

The Hamiltonian $\hat{H}_{\text{el-ph}}^{g,\text{m}}$ of Eq. (8.66) is valid if the molecular system is initially in the electronic ground state. If it is in an excited electronic state α at the initial time t_0 , the electron–phonon Hamiltonian has to be transformed in a way that it gives no contribution when acting on $|X_{\alpha}^{\text{m}}\rangle$, since this higher PES acts as new equilibrium state. Therefore, the phonon operators are transformed as follows:

$$\hat{b}_j^{\alpha} = \hat{b}_j + \frac{1}{\omega_j} \left(g_j^{\alpha\alpha*} \mathbb{1} + \sum_{\nu} g_j^{H,\nu*} \mathbb{1} \right), \quad \hat{b}_j^{\alpha\dagger} = \hat{b}_j^{\dagger} + \frac{1}{\omega_j} \left(g_j^{\alpha\alpha} \mathbb{1} + \sum_{\nu} g_j^{H,\nu} \mathbb{1} \right) \quad (8.68)$$

Applying this transformation to the phonon operators in Eq. (8.60) yields:

$$\begin{aligned} \hat{H}_{0,\text{e}}^{\alpha,\text{m}} + \hat{H}_{0,\text{ph}}^{\alpha,\text{m}} + \hat{H}_{\text{el-ph}}^{\alpha,\text{m}} &= \sum_{A,\nu} \varepsilon_{A,\nu}^{\alpha} \hat{a}_{A,\nu}^{\dagger} \hat{a}_{A,\nu} + \sum_j \hbar \omega_j \hat{b}_j^{\alpha\dagger} \hat{b}_j^{\alpha} \\ &+ \sum_{\nu} \sum_j \left(\hbar (g_j^{L,\nu} - g_j^{H,\nu}) \hat{b}_j^{\alpha} + \hbar (g_j^{L,\nu*} - g_j^{H,\nu*}) \hat{b}_j^{\alpha\dagger} \right) \hat{a}_{L,\nu}^{\dagger} \hat{a}_{L,\nu} - \sum_j \hbar (g_j^{\alpha\alpha} \hat{b}_j^{\alpha} + g_j^{\alpha\alpha*} \hat{b}_j^{\alpha\dagger}) \\ &+ \sum_j \frac{1}{\hbar \omega_j} \left(\hbar g_j^{\alpha\alpha} + \sum_{\nu} \hbar g_j^{H,\nu} \right) \left(\hbar g_j^{\alpha\alpha*} + \sum_{\nu'} \hbar g_j^{H,\nu'*} \right) \mathbb{1} \end{aligned} \quad (8.69)$$

with the renormalized energy

$$\varepsilon_{A,\nu}^{\alpha} \equiv \varepsilon_{A,\nu} - 2 \sum_j \text{Re} \left[\frac{g_j^{A,\nu}}{\omega_j} \left(\hbar g_j^{\alpha\alpha*} + \sum_{\nu'} \hbar g_j^{H,\nu'*} \right) \right]. \quad (8.70)$$

The last term constitutes the polaron or Stokes shift. It describes the displacement of the minimum of the PES of the excited state $|X_{\alpha}^{\text{m}}\rangle$ with respect to the electronic ground state configuration. As a consequence, the fluorescence spectrum is redshifted relative to the linear absorption spectrum by the Stokes shift. As before, the last term is ignored since it constitutes a constant shift that is of no importance for the system dynamics. In the exciton basis, the transformed phonon Hamiltonian for a system that is initially in the excited state $|X_{\alpha}^{\text{m}}\rangle$ is given as:

$$\hat{H}_{0,\text{ph}}^{\alpha,\text{m}} = \sum_j \hbar \omega_j \hat{b}_j^{\alpha\dagger} \hat{b}_j^{\alpha} (|\phi_0^{\text{m}}\rangle \langle \phi_0^{\text{m}}| + \sum_{\beta} |X_{\beta}^{\text{m}}\rangle \langle X_{\beta}^{\text{m}}|), \quad (8.71)$$

$$\begin{aligned} \hat{H}_{\text{el-ph}}^{\alpha,\text{m}} &= - \sum_j \hbar (g_j^{\alpha\alpha} \hat{b}_j^{\alpha} + g_j^{\alpha\alpha*} \hat{b}_j^{\alpha\dagger}) (|\phi_0^{\text{m}}\rangle \langle \phi_0^{\text{m}}| + \sum_{\beta} |X_{\beta}^{\text{m}}\rangle \langle X_{\beta}^{\text{m}}|) \\ &+ \sum_{\beta,\zeta} \sum_j \hbar (g_j^{\beta\zeta} \hat{b}_j^{\alpha} + g_j^{\zeta\beta*} \hat{b}_j^{\alpha\dagger}) |X_{\zeta}^{\text{m}}\rangle \langle X_{\beta}^{\text{m}}|. \end{aligned} \quad (8.72)$$

As required, the electron–phonon Hamiltonian of Eq. (8.72) has no contribution when acting on the excited state $|X_{\alpha}^{\text{m}}\rangle$ that was chosen as the new equilibrium state. Figure 8.3 (b) illustrates the concept of transferring the equilibrium position to the respective PES via Weyl transformation.

8.4 Exciton dynamics in the hybrid system

8.4.1 Molecule–semiconductor Coulomb coupling

This section deals with the composite system, i.e., the semiconductor substrate with the weakly bound molecular adlayer on top, both treated separately in Secs. 8.2 and 8.3. The treatment is restricted to single excitations in the hybrid systems. First, a common ground state $|\phi_0\rangle = |\phi_0^s\rangle \otimes |\phi_0^m\rangle$ is defined, designating the state where all valence bands in the QW substrate and all HOMOs in the organic layer are occupied. The local basis states introduced in Eqs. (8.1) and (8.52) are redefined with respect to the common ground state: $|\mathbf{k}_1, \mathbf{k}_2\rangle = \hat{a}_{c, \mathbf{k}_1}^\dagger \hat{a}_{v, \mathbf{k}_2} |\phi_0\rangle$ and $|\nu\rangle \equiv \hat{a}_{L, \nu}^\dagger \hat{a}_{H, \nu} |\phi_0\rangle$.

The Hamiltonian for the interlayer Coulomb coupling is derived in partial charge approximation according to Secs. 7.2 and 7.3:

$$\begin{aligned} \hat{H}_C^{m-s} = & \sum_{\lambda, \mathbf{k}, \mathbf{k}'} \sum_{A, \nu} V_{\lambda, \mathbf{k}'}^{\lambda, \mathbf{k}} V_{A, \nu}^{A, \nu} \hat{a}_{\lambda, \mathbf{k}}^\dagger \hat{a}_{A, \nu}^\dagger \hat{a}_{A, \nu} \hat{a}_{\lambda, \mathbf{k}'} \\ & + \sum_{\mathbf{k}, \mathbf{k}'} \sum_{\nu} \left(V_{v, \mathbf{k}'}^{c, \mathbf{k}} V_{L, \nu}^{H, \nu} \hat{a}_{c, \mathbf{k}}^\dagger \hat{a}_{H, \nu}^\dagger \hat{a}_{L, \nu} \hat{a}_{v, \mathbf{k}'} + \underbrace{V_{c, \mathbf{k}'}^{v, \mathbf{k}} V_{H, \nu}^{L, \nu} \hat{a}_{v, \mathbf{k}}^\dagger \hat{a}_{L, \nu}^\dagger \hat{a}_{H, \nu} \hat{a}_{c, \mathbf{k}'}}_{h.c.} \right). \end{aligned} \quad (8.73)$$

The first term constitutes the electrostatic shifts and the last term in brackets describes Förster excitation transfer between the inorganic and organic component. The molecule–substrate coupling element in partial charge approximation is given as (cf. Eq. (7.26)):⁶

$$V_{\lambda', \mathbf{k}'}^{\lambda, \mathbf{k}} V_{B, \nu}^{A, \nu} = \frac{1}{N_{uc}} \sum_{i=1}^{N_{uc}} e^{i(\mathbf{k}' - \mathbf{k}) \cdot \mathbf{R}_i} \sum_{I, J} G^{m-s}(\mathbf{R}_i + \mathbf{r}_I, \mathbf{R}_\nu + \mathbf{r}_{J_\nu}) q_I^{\lambda \lambda'} q_J^{AB} \quad (8.74)$$

with the Green's function defined in Eq. (B.6). \mathbf{R}_ν denotes the position of the ν -th molecule in the organic film and \mathbf{R}_i the position of the i -th UC in the QW substrate. The atomic partial charges are located at \mathbf{r}_I within one semiconductor UC and \mathbf{r}_{J_ν} within the ν -th molecule, respectively. Note that, compared to Chap. 7, this time the semiconductor wave vectors \mathbf{k}, \mathbf{k}' are three-dimensional. The coupling elements in partial charge approximation are transformed into position space according to

$$V_{\lambda', i}^{\lambda, i} V_{B, \nu}^{A, \nu} \equiv \sum_{I, J} G^{m-s}(\mathbf{R}_i + \mathbf{r}_I, \mathbf{R}_\nu + \mathbf{r}_{J_\nu}) q_I^{\lambda \lambda'} q_J^{AB}. \quad (8.75)$$

The Hamiltonian is rewritten in the excitonic basis of the hybrid system:

$$\begin{aligned} \hat{H}_C^{m-s} = & E_0^{m-s} (|\phi_0\rangle \langle \phi_0| + \sum_{\alpha} |X_{\alpha}^m\rangle \langle X_{\alpha}^m| + \sum_{\alpha} |X_{\alpha}^s\rangle \langle X_{\alpha}^s|) + \sum_{\alpha} V_{H-L}^{m-s}(X_{\alpha}^m) |X_{\alpha}^m\rangle \langle X_{\alpha}^m| \\ & + \sum_{\alpha} V_{v-c}^{m-s}(X_{\alpha}^s) |X_{\alpha}^s\rangle \langle X_{\alpha}^s| + \sum_{\alpha, \beta} (V_F^{m-s}(X_{\alpha}^m, X_{\beta}^s) |X_{\alpha}^m\rangle \langle X_{\beta}^s| + V_F^{m-s*}(X_{\alpha}^m, X_{\beta}^s) |X_{\beta}^s\rangle \langle X_{\alpha}^m|) \end{aligned} \quad (8.76)$$

with

$$E_0^{m-s} = \sum_{\nu=1}^{N_m} \sum_{i=1}^{N_{uc}} V_{v, i}^{v, i} V_{H, \nu}^{H, \nu}, \quad (8.77)$$

⁶ In principle, approximating the Coulomb potential by partial charges is only valid in the case of an ideal QW without disorder. However, the well width fluctuations considered in this chapter occur on a very large spatial scale compared to the UC size for which the electrostatic potential is approximated by partial charges. Therefore, the partial charge technique is also suited for the case of disordered QWs.

$$V_{\text{H-L}}^{\text{m-s}}(X_\alpha^{\text{m}}) = \sum_{\nu=1}^{N_{\text{m}}} |c_\nu^\alpha|^2 \sum_{i=1}^{N_{\text{uc}}} \left(V_{\nu,i}^{\nu,i \text{ L},\nu} - V_{\nu,i}^{\nu,i \text{ H},\nu} \right), \quad (8.78)$$

$$V_{\text{v-c}}^{\text{m-s}}(X_\alpha^{\text{s}}) = \frac{V_{\text{s}}}{N_{\text{uc}}} \sum_{\nu=1}^{N_{\text{m}}} \sum_{i=1}^{N_{\text{uc}}} \left(\int d^3 r_{\text{h}} |\Psi_\alpha^{\text{s}}(\mathbf{R}_i, \mathbf{r}_{\text{h}})|^2 V_{\text{c},i}^{\nu,i \text{ H},\nu} - \int d^3 r_{\text{e}} |\Psi_\alpha^{\text{s}}(\mathbf{r}_{\text{e}}, \mathbf{R}_i)|^2 V_{\nu,i}^{\nu,i \text{ H},\nu} \right), \quad (8.79)$$

$$V_{\text{F}}^{\text{m-s}}(X_\alpha^{\text{m}}, X_\beta^{\text{s}}) = \frac{V_{\text{s}}}{N_{\text{uc}}} \sum_{\nu=1}^{N_{\text{m}}} \sum_{i=1}^{N_{\text{uc}}} c_\nu^{\alpha*} \Psi_\beta^{\text{s}}(\mathbf{R}_i, \mathbf{R}_i) V_{\text{c},i}^{\nu,i \text{ L},\nu}, \quad (8.80)$$

where only the dominant contributions to the monopole-monopole shifts were kept that are diagonal in the exciton basis by setting $c_\nu^{\alpha*} c_\nu^\beta \approx |c_\nu^\alpha|^2 \delta_{\alpha\beta}$ and $\Psi_\alpha^{\text{s}*}(\mathbf{r}_{\text{e}}, \mathbf{r}_{\text{h}}) \Psi_\beta^{\text{s}}(\mathbf{r}_{\text{e}}, \mathbf{r}_{\text{h}}) \approx |\Psi_\alpha^{\text{s}}(\mathbf{r}_{\text{e}}, \mathbf{r}_{\text{h}})|^2 \delta_{\alpha\beta}$. Note that the interlayer Förster coupling element of Eq. (8.80) has only a contribution for $\mathbf{r}_{\text{e}} = \mathbf{r}_{\text{h}} \equiv \mathbf{R}_i$, indicating that the electron and hole in the semiconductor exciton have to be located at the same position in order to couple via dipole-dipole interaction to an exciton in the molecular layer.

8.4.2 Hamiltonian and Liouville propagator

The total Hamiltonian for the interaction between the inorganic and organic layer including vibrational coupling in the molecular layer can be split into a diagonal part and an off-diagonal part with respect to the exciton basis: $\hat{H}^{g/\alpha} = \hat{H}_{\text{diag}}^{g/\alpha} + \hat{H}_{\text{off-diag}}^{g/\alpha}$. It has two representations: Depending on whether the molecular system is initially in the ground state or the excited state $|X_\alpha^{\text{m}}\rangle$, the phonon operators are transformed into the respective equilibrium state, cf. Sec. 8.3.3. The diagonal Hamiltonian for the two equilibrium situations reads:

$$\begin{aligned} \hat{H}_{\text{diag}}^g &= \hat{H}_{0,\text{e}}^{g,\text{m}} + \hat{H}_{0,\text{ph}}^{g,\text{m}} + \hat{H}_{\text{el-ph}}^{g,\text{m}} + \hat{H}_{\text{C,mono}}^{\text{m-s}} \\ &= \left(E_0^{g,\text{m}} + \sum_j \hbar\omega_j \hat{b}_j^{g\dagger} \hat{b}_j^g + E_0^{\text{m-s}} \right) |\phi_0\rangle \langle \phi_0| \\ &\quad + \sum_\beta \left(E_0^{g,\text{m}} + E_{\beta,3\text{D}}^{\text{s}} + \sum_j \hbar\omega_j \hat{b}_j^{g\dagger} \hat{b}_j^g + E_0^{\text{m-s}} + V_{\text{v-c}}^{\text{m-s}}(X_\beta^{\text{s}}) \right) |X_\beta^{\text{s}}\rangle \langle X_\beta^{\text{s}}| \\ &\quad + \sum_\beta \left(E_0^{g,\text{m}} + E_\beta^{\text{m}} + \sum_j \hbar\omega_j \hat{b}_j^{g\dagger} \hat{b}_j^g + E_0^{\text{m-s}} + V_{\text{H-L}}^{\text{m-s}}(X_\beta^{\text{m}}) \right. \\ &\quad \left. + \sum_j \hbar(g_j^{\beta\beta} \hat{b}_j^g + g_j^{\beta\beta*} \hat{b}_j^{g\dagger}) \right) |X_\beta^{\text{m}}\rangle \langle X_\beta^{\text{m}}|, \end{aligned} \quad (8.81)$$

$$\begin{aligned} \hat{H}_{\text{diag}}^\alpha &= \left(E_0^{\alpha,\text{m}} + \sum_j \hbar\omega_j \hat{b}_j^{\alpha\dagger} \hat{b}_j^\alpha + E_0^{\text{m-s}} - \sum_j \hbar(g_j^{\alpha\alpha} \hat{b}_j^\alpha + g_j^{\alpha\alpha*} \hat{b}_j^{\alpha\dagger}) \right) |\phi_0\rangle \langle \phi_0| \\ &\quad + \sum_\beta \left(E_0^{\alpha,\text{m}} + E_{\beta,3\text{D}}^{\text{s}} + \sum_j \hbar\omega_j \hat{b}_j^{\alpha\dagger} \hat{b}_j^\alpha + E_0^{\text{m-s}} \right. \\ &\quad \left. - \sum_j \hbar(g_j^{\alpha\alpha} \hat{b}_j^\alpha + g_j^{\alpha\alpha*} \hat{b}_j^{\alpha\dagger}) + V_{\text{v-c}}^{\text{m-s}}(X_\beta^{\text{s}}) \right) |X_\beta^{\text{s}}\rangle \langle X_\beta^{\text{s}}| \\ &\quad + \sum_\beta \left\{ E_0^{\alpha,\text{m}} + E_\beta^{\text{m}} + \sum_j \hbar\omega_j \hat{b}_j^{\alpha\dagger} \hat{b}_j^\alpha + E_0^{\text{m-s}} + V_{\text{H-L}}^{\text{m-s}}(X_\beta^{\text{m}}) \right. \\ &\quad \left. + \sum_j \hbar \left((g_j^{\beta\beta} - g_j^{\alpha\alpha}) \hat{b}_j^\alpha + (g_j^{\beta\beta*} - g_j^{\alpha\alpha*}) \hat{b}_j^{\alpha\dagger} \right) \right\} |X_\beta^{\text{m}}\rangle \langle X_\beta^{\text{m}}| \end{aligned} \quad (8.82)$$

with

$$E_0^{g/\alpha, m} = N_m \varepsilon_H^{g/\alpha} + \frac{1}{2} \sum_{\substack{\nu_a, \nu_b \\ \nu_a \neq \nu_b}} V_{H, \nu_a}^{H, \nu_a} V_{H, \nu_b}^{H, \nu_b}. \quad (8.83)$$

$\varepsilon_H^{g/\alpha}$ are the renormalized free-particle energies defined in Eqs. (8.63) and (8.70). The last term of Eq. (8.82) describing the electron–phonon interaction vanishes if $\beta = \alpha$, thus fulfilling the requirement that the Hamiltonian $\hat{H}_{\text{diag}}^\alpha$ does not contribute when it is applied to the excited state $|X_\alpha^m\rangle$ that acts as equilibrium state.

The non-diagonal Hamiltonian contains the Förster part of the molecule–semiconductor Coulomb Hamiltonian and the off-diagonal part of the exciton-phonon Hamiltonian. It is treated perturbatively in the following, assuming a weak coupling compared to the system energies:

$$\begin{aligned} \hat{H}_{\text{off-diag}}^{g/\alpha} = \hat{H}_F^{m-s} + \hat{H}_{\text{el-ph}}^{g/\alpha} \Big|_{\text{off-diag}} &= \sum_{\beta, \zeta} (V_F^{m-s}(X_\beta^m, X_\zeta^s) |X_\beta^m\rangle \langle X_\zeta^s| + V_F^{m-s*}(X_\beta^m, X_\zeta^s) |X_\zeta^s\rangle \langle X_\beta^m|) \\ &+ \sum_{\substack{\beta, \zeta \\ \beta \neq \zeta}} \sum_j \hbar (g_j^{\beta\zeta} \hat{b}_j^{g/\alpha} + g_j^{\zeta\beta*} \hat{b}_j^{g/\alpha\dagger}) |X_\zeta^m\rangle \langle X_\beta^m|. \end{aligned} \quad (8.84)$$

The Liouville operator is split in the same way:

$$\mathcal{L}^{g/\alpha} = \mathcal{L}_{\text{diag}}^{g/\alpha} + \mathcal{L}_{\text{off-diag}}^{g/\alpha} \quad \text{with} \quad \mathcal{L}_{\text{diag}}^{g/\alpha} \hat{O} = [\hat{H}_{\text{diag}}^{g/\alpha}, \hat{O}]_- \quad \text{and} \quad \mathcal{L}_{\text{off-diag}}^{g/\alpha} \hat{O} = [\hat{H}_{\text{off-diag}}^{m-s}, \hat{O}]_-. \quad (8.85)$$

The Liouville propagator is defined as:

$$\mathcal{U}^{g/\alpha}(t, t_0) = \exp_{\leftarrow} \left[-\frac{i}{\hbar} \int_{t_0}^t d\tau \mathcal{L}^{g/\alpha}(\tau) \right] = \exp_{\leftarrow} \left[-\frac{i}{\hbar} \int_{t_0}^t d\tau (\mathcal{L}_{\text{diag}}^{g/\alpha}(\tau) + \mathcal{L}_{\text{off-diag}}^{g/\alpha}(\tau)) \right]. \quad (8.86)$$

It is rewritten using the Feynman disentanglement theorem [Fey51] (cf. Sec. 2.5):

$$\mathcal{U}^{g/\alpha}(t, t_0) = \underbrace{\exp_{\leftarrow} \left[-\frac{i}{\hbar} \int_{t_0}^t d\tau \mathcal{L}_{\text{diag}}^{g/\alpha}(\tau) \right]}_{\equiv \mathcal{U}_{\text{diag}}^{g/\alpha}(t, t_0)} \underbrace{\exp_{\leftarrow} \left[-\frac{i}{\hbar} \int_{t_0}^t d\tau \mathcal{U}_{\text{diag}}^{g/\alpha}(t_0, \tau) \mathcal{L}_{\text{off-diag}}^{g/\alpha}(\tau) \mathcal{U}_{\text{diag}}^{g/\alpha}(\tau, t_0) \right]}_{\equiv \mathcal{U}_I^{g/\alpha}(t, t_0)}. \quad (8.87)$$

The interaction part $\mathcal{U}_I^{g/\alpha}(t, t_0)$ is now expanded perturbatively up to second order:

$$\begin{aligned} \mathcal{U}_I^{g/\alpha}(t, t_0) &\approx 1 - \frac{i}{\hbar} \int_{t_0}^t d\tau \mathcal{U}_{\text{diag}}^{g/\alpha}(t_0, \tau) \mathcal{L}_{\text{off-diag}}^{g/\alpha}(\tau) \mathcal{U}_{\text{diag}}^{g/\alpha}(\tau, t_0) \\ &- \frac{1}{\hbar^2} \int_{t_0}^t d\tau \int_{t_0}^\tau d\tau' \mathcal{U}_{\text{diag}}^{g/\alpha}(t_0, \tau) \mathcal{L}_{\text{off-diag}}^{g/\alpha}(\tau) \underbrace{\mathcal{U}_{\text{diag}}^{g/\alpha}(\tau, t_0) \mathcal{U}_{\text{diag}}^{g/\alpha}(t_0, \tau')}_{\equiv \mathcal{U}_{\text{diag}}^{g/\alpha}(\tau, \tau')} \mathcal{L}_{\text{off-diag}}^{g/\alpha}(\tau') \mathcal{U}_{\text{diag}}^{g/\alpha}(\tau', t_0). \end{aligned} \quad (8.88)$$

The full propagator then reads:

$$\begin{aligned} \mathcal{U}^{g/\alpha}(t, t_0) &\approx \mathcal{U}_{\text{diag}}^{g/\alpha}(t, t_0) - \frac{i}{\hbar} \int_{t_0}^t d\tau \mathcal{U}_{\text{diag}}^{g/\alpha}(t, \tau) \mathcal{L}_{\text{off-diag}}^{g/\alpha}(\tau) \mathcal{U}_{\text{diag}}^{g/\alpha}(\tau, t_0) \\ &- \frac{1}{\hbar^2} \int_{t_0}^t d\tau \int_{t_0}^\tau d\tau' \mathcal{U}_{\text{diag}}^{g/\alpha}(t, \tau) \mathcal{L}_{\text{off-diag}}^{g/\alpha}(\tau) \mathcal{U}_{\text{diag}}^{g/\alpha}(\tau, \tau') \mathcal{L}_{\text{off-diag}}^{g/\alpha}(\tau') \mathcal{U}_{\text{diag}}^{g/\alpha}(\tau', t_0). \end{aligned} \quad (8.89)$$

8.4.3 Transition amplitudes

For calculating the dynamics, the amplitude for a transition of the system from the density $\rho_{\alpha\alpha}^s \equiv |X_\alpha^s\rangle\langle X_\alpha^s|$ (exciton in the semiconductor substrate excited) to the density $\rho_{\beta\beta}^m \equiv |X_\beta^m\rangle\langle X_\beta^m|$ (exciton in the molecular layer excited) is of interest. Therefore, the matrix element of the Liouville propagator is calculated:

$$t_{\rho_{\beta\beta}^m \leftarrow \rho_{\alpha\alpha}^s}(t, t_0) \equiv \text{tr} [|X_\beta^m\rangle\langle X_\beta^m| \mathcal{U}^g(t, t_0) |X_\alpha^s\rangle\langle X_\alpha^s| \hat{\rho}_B^g], \quad (8.90)$$

where $\hat{\rho}_B^g$ denotes the density operator of the phonon bath corresponding to the case where the molecular ground state acts as equilibrium state (as marked by the superscript g). It is assumed that the phononic bath and the electronic system factorize: $\hat{\rho}^g = \hat{\rho}_S \otimes \hat{\rho}_B^g$. Approximating the Liouville propagator by the expansion of Eq. (8.89), it is clear that only the last term (second order in the interaction) will survive, since here the off-diagonal Liouvillian $\mathcal{L}_{\text{off-diag}}^g$ acts twice and is thus capable of transforming the semiconductor density $\rho_{\alpha\alpha}^s$ into the molecular density $\rho_{\beta\beta}^m$ through Förster interaction. Therefore, the term to evaluate is given by

$$t_{\rho_{\beta\beta}^m \leftarrow \rho_{\alpha\alpha}^s}(t, t_0) = \text{tr} \left[|X_\beta^m\rangle\langle X_\beta^m| \left\{ -\frac{1}{\hbar^2} \int_{t_0}^t d\tau \int_{t_0}^\tau d\tau' \right. \right. \\ \left. \left. \times \mathcal{U}_{\text{diag}}^g(t, \tau) \mathcal{L}_{\text{off-diag}}^g(\tau) \mathcal{U}_{\text{diag}}^g(\tau, \tau') \mathcal{L}_{\text{off-diag}}^g(\tau') \mathcal{U}_{\text{diag}}^g(\tau', t_0) |X_\alpha^s\rangle\langle X_\alpha^s| \hat{\rho}_B^g \right\} \right]. \quad (8.91)$$

This expression is evaluated in detail in App. C.2 using the Feynman disentangling theorem [Fey51] introduced in Sec. 2.5 and assuming that the phonon bath is in thermal equilibrium, such that the mean number of vibrational quanta in a given mode, $\bar{n}(\omega_j) = \langle \hat{b}_j^\dagger \hat{b}_j \rangle_B$ is described by a Bose distribution. This yields the amplitude for the transition from the semiconductor density $\rho_{\alpha\alpha}^s$ to the molecular density $\rho_{\beta\beta}^m$ in second order:

$$t_{\rho_{\beta\beta}^m \leftarrow \rho_{\alpha\alpha}^s}(t, t_0) = \frac{1}{\hbar^2} |V_{\text{F}}^{\text{m-s}}(X_\beta^m, X_\alpha^s)|^2 \int_{t_0}^t d\tau \int_{t_0}^\tau d\tau' \left\{ e^{+\frac{i}{\hbar} E_{\text{el}}^{\text{m-s}}(X_\beta^m, X_\alpha^s)(\tau-\tau')} \text{tr}_B [U_{\text{I,ph}}^{g,\beta\dagger}(\tau, \tau') \hat{\rho}_B^g] \right. \\ \left. + e^{-\frac{i}{\hbar} E_{\text{el}}^{\text{m-s}}(X_\beta^m, X_\alpha^s)(\tau-\tau')} \text{tr}_B [U_{\text{I,ph}}^{g,\beta}(\tau, \tau') \hat{\rho}_B^g] \right\} \quad (8.92)$$

with

$$E_{\text{el}}^{\text{m-s}}(X_\beta^m, X_\alpha^s) \equiv E_\beta^m - E_{\alpha,3\text{D}}^s + V_{\text{H-L}}^{\text{m-s}}(X_\beta^m) - V_{\text{v-c}}^{\text{m-s}}(X_\alpha^s), \quad (8.93)$$

$$U_{\text{I,ph}}^{g,\beta\dagger}(\tau, \tau') = \exp_{\leftarrow} \left[-\frac{i}{\hbar} \int_0^{\tau'-\tau} d\tau'' \sum_j \hbar (g_j^{\beta\beta} \hat{b}_j^g e^{-i\omega_j \tau''} + g_j^{\beta\beta*} \hat{b}_j^{g\dagger} e^{+i\omega_j \tau''}) \right]. \quad (8.94)$$

The transition amplitude for the inverse process (transition from $\rho_{\alpha\alpha}^m$ to $\rho_{\beta\beta}^s$) is calculated using the phonon operators $\hat{b}_j^{\alpha(\dagger)}$ obtained via Weyl transformation into the excited molecular state $|X_\alpha^m\rangle$ (cf. Sec. 8.3.3):

$$t_{\rho_{\beta\beta}^s \leftarrow \rho_{\alpha\alpha}^m}(t, t_0) \equiv \text{tr} [|X_\beta^s\rangle\langle X_\beta^s| \mathcal{U}^\alpha(t, t_0) |X_\alpha^m\rangle\langle X_\alpha^m| \hat{\rho}_B^\alpha] \quad (8.95)$$

$$\approx \frac{1}{\hbar^2} |V_{\text{F}}^{\text{m-s}}(X_\alpha^m, X_\beta^s)|^2 \int_{t_0}^t d\tau \int_{t_0}^\tau d\tau' \left\{ e^{-\frac{i}{\hbar} E_{\text{el}}^{\text{m-s}}(X_\alpha^m, X_\beta^s)(\tau-\tau')} \text{tr}_B [U_{\text{I,ph}}^{\alpha\dagger}(\tau, \tau') \hat{\rho}_B^\alpha] \right. \\ \left. + e^{+\frac{i}{\hbar} E_{\text{el}}^{\text{m-s}}(X_\alpha^m, X_\beta^s)(\tau-\tau')} \text{tr}_B [U_{\text{I,ph}}^\alpha(\tau, \tau') \hat{\rho}_B^\alpha] \right\} \quad (8.96)$$

with

$$U_{\text{I,ph}}^{\alpha\dagger}(\tau, \tau') = \exp_{\leftarrow} \left[+\frac{i}{\hbar} \int_0^{\tau'-\tau} d\tau'' \sum_j \hbar (g_j^{\alpha\alpha} \hat{b}_j^\alpha e^{-i\omega_j \tau''} + g_j^{\alpha\alpha*} \hat{b}_j^{\alpha\dagger} e^{+i\omega_j \tau''}) \right]. \quad (8.97)$$

Finally, the amplitude for the transition from one molecular density denoted $\rho_{\alpha\alpha}^{\text{m}}$ to the other given by $\rho_{\beta\beta}^{\text{m}}$ (with $\alpha \neq \beta$) is deduced, describing the phonon-induced relaxation between different molecular excitons:

$$t_{\rho_{\beta\beta}^{\text{m}} \leftarrow \rho_{\alpha\alpha}^{\text{m}}}(t, t_0) \equiv \text{tr} [|X_\beta^{\text{m}}\rangle \langle X_\beta^{\text{m}} | \mathcal{U}^\alpha(t, t_0) | X_\alpha^{\text{m}}\rangle \langle X_\alpha^{\text{m}} | \hat{\rho}_{\text{B}}^\alpha]. \quad (8.98)$$

The evaluation shown in App. C.3 yields the following expression:

$$\begin{aligned} t_{\rho_{\beta\beta}^{\text{m}} \leftarrow \rho_{\alpha\alpha}^{\text{m}}}(t, t_0) &= \frac{1}{\hbar^2} \int_{t_0}^t d\tau \int_{t_0}^\tau d\tau' \left\{ e^{+\frac{i}{\hbar} E_{\text{el}}^{\text{m}}(X_\beta^{\text{m}}, X_\alpha^{\text{m}})(\tau-\tau')} \text{tr}_{\text{B}} \left[\sum_j \hbar (g_j^{\beta\alpha} \hat{b}_j^\alpha e^{-i\omega_j(\tau'-\tau)} \right. \right. \\ &\quad \left. \left. + g_j^{\alpha\beta*} \hat{b}_j^{\alpha\dagger} e^{+i\omega_j(\tau'-\tau)}) U_{\text{I,ph}}^{\alpha, \beta\dagger}(\tau, \tau') \sum_{j'} \hbar (g_{j'}^{\alpha\beta} \hat{b}_{j'}^\alpha + g_{j'}^{\beta\alpha*} \hat{b}_{j'}^{\alpha\dagger}) \hat{\rho}_{\text{B}}^\alpha \right] \right. \\ &\quad \left. + e^{-\frac{i}{\hbar} E_{\text{el}}^{\text{m}}(X_\beta^{\text{m}}, X_\alpha^{\text{m}})(\tau-\tau')} \text{tr}_{\text{B}} \left[\sum_{j'} \hbar (g_{j'}^{\beta\alpha} \hat{b}_{j'}^\alpha + g_{j'}^{\alpha\beta*} \hat{b}_{j'}^{\alpha\dagger}) U_{\text{I,ph}}^{\alpha, \beta}(\tau, \tau') \right. \right. \\ &\quad \left. \left. \times \sum_j \hbar (g_j^{\alpha\beta} \hat{b}_j^\alpha e^{-i\omega_j(\tau'-\tau)} + g_j^{\beta\alpha*} \hat{b}_j^{\alpha\dagger} e^{+i\omega_j(\tau'-\tau)}) \hat{\rho}_{\text{B}}^\alpha \right] \right\} \end{aligned} \quad (8.99)$$

with

$$\begin{aligned} E_{\text{el}}^{\text{m}}(X_\eta^{\text{m}}, X_\zeta^{\text{m}}) &\equiv E_\eta^{\text{m}} - E_\zeta^{\text{m}} + V_{\text{H-L}}^{\text{m-s}}(X_\eta^{\text{m}}) - V_{\text{H-L}}^{\text{m-s}}(X_\zeta^{\text{m}}), \quad (8.100) \\ U_{\text{I,ph}}^{\alpha, \beta\dagger}(\tau, \tau') &= \exp_{\leftarrow} \left[-\frac{i}{\hbar} \int_0^{\tau'-\tau} d\tau'' \sum_j \hbar ((g_j^{\beta\beta} - g_j^{\alpha\alpha}) \hat{b}_j^\alpha e^{-i\omega_j \tau''} + (g_j^{\beta\beta*} - g_j^{\alpha\alpha*}) \hat{b}_j^{\alpha\dagger} e^{+i\omega_j \tau''}) \right]. \quad (8.101) \end{aligned}$$

8.4.4 Cumulant expansion

In order to describe the coupling of the electronic hybrid system to the phonon bath in the molecular layer, a cumulant expansion technique is employed. Note that the electron–phonon coupling in the semiconductor substrate is already included in the phonon scattering rates (derived in App. C.1.1) entering the EOM for the semiconductor density. Its impact on the excitation transfer dynamics across the hybrid interface is negligible, since there the coupling to the vibrational modes of the molecules comes into play and dominates the dynamics. The phonon bath in the molecular layer is assumed to be in thermal equilibrium, such that cumulants of an order higher than two vanish as a consequence of Wick’s theorem [Abr75, Muk95].

Interlayer coupling

The term

$$J^{g, \beta}(\tau' - \tau) \equiv \text{tr}_{\text{B}} [U_{\text{I,ph}}^{g, \beta\dagger}(\tau, \tau') \hat{\rho}_{\text{B}}^g] = \text{tr}_{\text{B}} \left[\exp_{\leftarrow} \left[-\frac{i}{\hbar} \int_0^{\tau'-\tau} d\tau'' \hat{H}_{\text{I,ph}}^{g, \beta}(\tau'') \right] \hat{\rho}_{\text{B}}^g \right] \quad (8.102)$$

with

$$\hat{H}_{\text{I,ph}}^{g, \beta}(\tau'') \equiv \sum_j \hbar (g_j^{\beta\beta} \hat{b}_j^g e^{-i\omega_j \tau''} + g_j^{\beta\beta*} \hat{b}_j^{g\dagger} e^{+i\omega_j \tau''}) \quad (8.103)$$

occurring on the right-hand side of Eq. (8.92) is evaluated using the cumulant expansion technique. Expanding Eq. (8.102) in orders of $\hat{H}_{\text{I,ph}}^{g,\beta}(\tau'')$ yields

$$J^{g,\beta}(\tau' - \tau) = \text{tr}_{\text{B}} \left[1 - \frac{i}{\hbar} \int_0^{\tau' - \tau} d\tau'' \hat{H}_{\text{I,ph}}^{g,\beta}(\tau'') \hat{\rho}_{\text{B}}^g \right. \\ \left. - \frac{1}{\hbar^2} \int_0^{\tau' - \tau} d\tau'' \int_0^{\tau''} d\tau''' \hat{H}_{\text{I,ph}}^{g,\beta}(\tau'') \hat{H}_{\text{I,ph}}^{g,\beta}(\tau''') \hat{\rho}_{\text{B}}^g + \dots \right]. \quad (8.104)$$

The first order contribution vanishes due to $\langle \hat{b}_j^g \rangle_{\text{B}} = \langle \hat{b}_j^{g\dagger} \rangle_{\text{B}} = 0$. The cumulant expansion is derived by making the ansatz [Muk95]

$$J^{g,\beta}(\tau' - \tau) = e^{-\mathcal{F}^{g,\beta}(\tau' - \tau)}, \quad (8.105)$$

where $\mathcal{F}^{g,\beta}(\tau' - \tau)$ is expanded in powers of $\hat{H}_{\text{I,ph}}^{g,\beta}$:

$$\mathcal{F}^{g,\beta}(\tau' - \tau) = \mathcal{F}_1^{g,\beta}(\tau' - \tau) + \mathcal{F}_2^{g,\beta}(\tau' - \tau) + \dots \quad (8.106)$$

Plugging this into Eq. (8.105), expanding $J^{g,\beta}(\tau' - \tau)$ in a Taylor series, collecting terms of the same order in $\hat{H}_{\text{I,ph}}^{g,\beta}$, and comparing it to Eq. (8.104) yields

$$\mathcal{F}_1^{g,\beta}(\tau' - \tau) = 0, \quad (8.107)$$

$$\mathcal{F}_2^{g,\beta}(\tau' - \tau) = \text{tr}_{\text{B}} \left[\frac{1}{\hbar^2} \int_0^{\tau' - \tau} d\tau'' \int_0^{\tau''} d\tau''' \hat{H}_{\text{I,ph}}^{g,\beta}(\tau''') \hat{H}_{\text{I,ph}}^{g,\beta}(0) \hat{\rho}_{\text{B}}^g \right]. \quad (8.108)$$

Here, it has been used that $\langle \hat{b}_j^{g\dagger} \hat{b}_j^g \rangle_{\text{B}} = \delta_{j,j'} \langle \hat{b}_j^{g\dagger} \hat{b}_j^g \rangle_{\text{B}} = \delta_{j,j'} \bar{n}(\omega_j)$, $\langle \hat{b}_j^{g\dagger} \hat{b}_{j'}^{g\dagger} \rangle_{\text{B}} = \langle \hat{b}_j^g \hat{b}_{j'}^g \rangle_{\text{B}} = 0$. Truncating the expansion Eq. (8.106) after the second order leads to

$$J^{g,\beta}(\tau' - \tau) = \exp \left[-\frac{1}{\hbar^2} \int_0^{\tau' - \tau} d\tau'' \int_0^{\tau''} d\tau''' \left\langle \hat{H}_{\text{I,ph}}^{g,\beta}(\tau''') \hat{H}_{\text{I,ph}}^{g,\beta}(0) \right\rangle_{\text{B}} \right]. \quad (8.109)$$

The exponent is further evaluated using the definition of $\hat{H}_{\text{I,ph}}^{g,\beta}$ (cf. Eq. (8.102)) and performing the time integrals:

$$J^{g,\beta}(\tau' - \tau) = \exp \left[\sum_j |g_j^{\beta\beta}|^2 \frac{1}{\omega_j^2} \left\{ (1 + \bar{n}(\omega_j)) e^{-i\omega_j(\tau' - \tau)} + \bar{n}(\omega_j) e^{+i\omega_j(\tau' - \tau)} \right. \right. \\ \left. \left. - 2\bar{n}(\omega_j) - 1 + i\omega_j(\tau' - \tau) \right\} \right]. \quad (8.110)$$

The same calculation is performed for the amplitude of the reverse process. This way, the transition amplitudes become:

$$t_{\rho_{\beta\beta}^{\text{m}} \leftarrow \rho_{\alpha\alpha}^{\text{s}}}(t, t_0) = \frac{1}{\hbar^2} |V_{\text{F}}^{\text{m-s}}(X_{\beta}^{\text{m}}, X_{\alpha}^{\text{s}})|^2 \int_{t_0}^t d\tau \int_{t_0}^{\tau} d\tau' \left\{ e^{+\frac{i}{\hbar} E_{\text{el}}^{\text{m-s}}(X_{\beta}^{\text{m}}, X_{\alpha}^{\text{s}})(\tau - \tau')} e^{-g^{g,\beta}(\tau' - \tau)} \right. \\ \left. + e^{-\frac{i}{\hbar} E_{\text{el}}^{\text{m-s}}(X_{\beta}^{\text{m}}, X_{\alpha}^{\text{s}})(\tau - \tau')} e^{-g^{g,\beta*}(\tau' - \tau)} \right\}, \quad (8.111)$$

$$t_{\rho_{\beta\beta}^{\text{s}} \leftarrow \rho_{\alpha\alpha}^{\text{m}}}(t, t_0) = \frac{1}{\hbar^2} |V_{\text{F}}^{\text{m-s}}(X_{\alpha}^{\text{m}}, X_{\beta}^{\text{s}})|^2 \int_{t_0}^t d\tau \int_{t_0}^{\tau} d\tau' \left\{ e^{-\frac{i}{\hbar} E_{\text{el}}^{\text{m-s}}(X_{\alpha}^{\text{m}}, X_{\beta}^{\text{s}})(\tau - \tau')} e^{-g^{g,\alpha}(\tau' - \tau)} \right. \\ \left. + e^{+\frac{i}{\hbar} E_{\text{el}}^{\text{m-s}}(X_{\alpha}^{\text{m}}, X_{\beta}^{\text{s}})(\tau - \tau')} e^{-g^{g,\alpha*}(\tau' - \tau)} \right\} \quad (8.112)$$

with

$$g^{g,\beta}(\tau' - \tau) = - \sum_j \left| g_j^{\beta\beta} \right|^2 \frac{1}{\omega_j^2} \left\{ (1 + \bar{n}(\omega_j)) e^{-i\omega_j(\tau' - \tau)} + \bar{n}(\omega_j) e^{+i\omega_j(\tau' - \tau)} - 2\bar{n}(\omega_j) - 1 + i\omega_j(\tau' - \tau) \right\} \quad (8.113)$$

$$= \int_0^{\tau' - \tau} d\tau'' \int_0^{\tau''} d\tau''' C^{g,\beta}(\tau'''). \quad (8.114)$$

$C^{g,\beta}(\tau''')$ denotes the two-time correlation function:

$$C^{g,\beta}(\tau''') \equiv \frac{1}{\hbar^2} \left\langle \hat{H}_{\text{I,ph}}^{g,\beta}(\tau''') \hat{H}_{\text{I,ph}}^{g,\beta}(0) \right\rangle_{\text{B}} = \sum_j \left| g_j^{\beta\beta} \right|^2 \left\{ (1 + \bar{n}(\omega_j)) e^{-i\omega_j\tau'''} + \bar{n}(\omega_j) e^{+i\omega_j\tau'''} \right\} \quad (8.115)$$

$$= \sum_j \sum_{\nu} |c_{\nu}^{\beta}|^4 \left| g_j^{\text{L},\nu} - g_j^{\text{H},\nu} \right|^2 \left\{ (1 + \bar{n}(\omega_j)) e^{-i\omega_j\tau'''} + \bar{n}(\omega_j) e^{+i\omega_j\tau'''} \right\}. \quad (8.116)$$

In the last step, the definition of the effective coupling element in exciton basis Eq. (8.67) has been inserted and it was assumed that different molecules couple to different phonon modes due to the spatial separation.

At this point, the *spectral density* $J_{\nu}(\omega)$ of the ν -th molecule is introduced to describe the interaction of the phonon bath with the system states. It represents the density of vibrational modes in the molecular layer weighted with the reservoir–system coupling strength [Muk95, May00, Ren02]:

$$J_{\nu}(\omega) \equiv \sum_j \underbrace{\frac{|g_j^{\text{L},\nu} - g_j^{\text{H},\nu}|^2}{\omega_j^2}}_{\equiv S_{j,\nu}} \delta(\omega - \omega_j) = \sum_j S_{j,\nu} \delta(\omega - \omega_j). \quad (8.117)$$

$S_{j,\nu}$ denotes the dimensionless Huang-Rhys factor. It can be directly determined in fluorescence and absorption measurements [Muk95]. In the following, it is assumed that each molecule exhibits its own set of vibrational modes. Therefore, the sum over all modes j is reduced to a sum over the modes belonging to the ν -th molecule (since all other modes belonging to other molecules show no coupling to the ν -th molecule). Furthermore, it is assumed that the set of vibrational modes assigned to molecule ν is identical for all molecules in the organic layer. Therefore, the spectral density and Huang-Rhys factor are identical for all molecules and the molecule index ν can be removed (provided that the sum over j is reduced to the modes belonging to one molecule). With that, the two-time correlation function becomes:

$$C^{g,\beta}(\tau''') = \sum_{\nu} |c_{\nu}^{\beta}|^4 \int_0^{\infty} d\omega J(\omega) \omega^2 \left\{ (1 + \bar{n}(\omega)) e^{-i\omega\tau'''} + \bar{n}(\omega) e^{+i\omega\tau'''} \right\} \quad (8.118)$$

and Eq. (8.113) takes the form

$$g^{g,\beta}(\tau' - \tau) = - \sum_{\nu} |c_{\nu}^{\beta}|^4 \int_0^{\infty} d\omega J(\omega) \left\{ (1 + \bar{n}(\omega)) e^{-i\omega(\tau' - \tau)} + \bar{n}(\omega) e^{+i\omega(\tau' - \tau)} - 2\bar{n}(\omega) - 1 + i\omega(\tau' - \tau) \right\}. \quad (8.119)$$

Intermolecular coupling

The same procedure is applied to the intermolecular transition amplitude $t_{\rho_{\beta\beta}^m \leftarrow \rho_{\alpha\alpha}^m}(t, t_0)$ of Eq. (8.99) by defining

$$J^{\alpha,\beta}(\tau' - \tau) \equiv \text{tr}_B \left[\sum_j \hbar (g_j^{\beta\alpha} \hat{b}_j^\alpha e^{-i\omega_j(\tau' - \tau)} + g_j^{\alpha\beta*} \hat{b}_j^{\alpha\dagger} e^{+i\omega_j(\tau' - \tau)}) \right. \\ \left. \times \exp_{\leftarrow} \left[-\frac{i}{\hbar} \int_0^{\tau' - \tau} d\tau'' \hat{H}_{\text{I,ph}}^{\alpha,\beta}(\tau'') \right] \sum_{j'} \hbar (g_{j'}^{\alpha\beta} \hat{b}_{j'}^\alpha + g_{j'}^{\beta\alpha*} \hat{b}_{j'}^{\alpha\dagger}) \hat{\rho}_B^\alpha \right] \quad (8.120)$$

with

$$\hat{H}_{\text{I,ph}}^{\alpha,\beta}(\tau'') \equiv \sum_j \hbar ((g_j^{\beta\beta} - g_j^{\alpha\alpha}) \hat{b}_j^\alpha e^{-i\omega_j \tau''} + (g_j^{\beta\beta*} - g_j^{\alpha\alpha*}) \hat{b}_j^{\alpha\dagger} e^{+i\omega_j \tau''}). \quad (8.121)$$

Expanding the time-ordered exponential up to second order yields

$$U_{\text{I,ph}}^{\alpha,\beta\dagger}(\tau, \tau') = \exp_{\leftarrow} \left[-\frac{i}{\hbar} \int_0^{\tau' - \tau} d\tau'' \hat{H}_{\text{I,ph}}^{\alpha,\beta}(\tau'') \right] \quad (8.122) \\ \approx 1 - \frac{i}{\hbar} \int_0^{\tau' - \tau} d\tau'' \hat{H}_{\text{I,ph}}^{\alpha,\beta}(\tau'') - \frac{1}{\hbar^2} \int_0^{\tau' - \tau} d\tau'' \int_0^{\tau''} d\tau''' \hat{H}_{\text{I,ph}}^{\alpha,\beta}(\tau'') \hat{H}_{\text{I,ph}}^{\alpha,\beta}(\tau'''). \quad (8.123)$$

This expansion is plugged into Eq. (8.120) and the trace over the phonon bath is performed. It is used that in thermal equilibrium (i) the expectation value of an odd number of phonon operators vanishes, (ii) the expectation value of an even number of phonon operators is only non-vanishing if it contains an equal number of creation and annihilation operators, and (iii) normally ordered four-operator expectation values factorize according to

$$\langle \hat{b}_i^{\alpha\dagger} \hat{b}_j^{\alpha\dagger} \hat{b}_k^\alpha \hat{b}_l^\alpha \rangle = \langle \hat{b}_i^{\alpha\dagger} \hat{b}_l^\alpha \rangle \langle \hat{b}_j^{\alpha\dagger} \hat{b}_k^\alpha \rangle + \langle \hat{b}_i^{\alpha\dagger} \hat{b}_k^\alpha \rangle \langle \hat{b}_j^{\alpha\dagger} \hat{b}_l^\alpha \rangle = (\delta_{i,l} \delta_{j,k} + \delta_{i,k} \delta_{j,l}) \bar{n}_i \bar{n}_j. \quad (8.124)$$

It follows immediately that the first order in the expansion vanishes since it only contains three-operator expectation values. After some calculation, Eq. (8.120) becomes

$$J^{\alpha,\beta}(\tau' - \tau) = \sum_j \hbar^2 \{ |g_j^{\beta\alpha}|^2 (1 + \bar{n}(\omega_j)) e^{-i\omega_j(\tau' - \tau)} + |g_j^{\alpha\beta}|^2 \bar{n}(\omega_j) e^{+i\omega_j(\tau' - \tau)} \} \\ \times \left\{ 1 - \text{tr}_B \left[\frac{1}{\hbar^2} \int_0^{\tau' - \tau} d\tau'' \int_0^{\tau''} d\tau''' \hat{H}_{\text{I,ph}}^{\alpha,\beta}(\tau''') \hat{H}_{\text{I,ph}}^{\alpha,\beta}(0) \hat{\rho}_B^\alpha \right] \right\} \\ - \frac{1}{\hbar^2} \int_0^{\tau' - \tau} d\tau'' \sum_j \hbar^2 \{ g_j^{\alpha\beta*} (g_j^{\beta\beta} - g_j^{\alpha\alpha}) \bar{n}(\omega_j) e^{+i\omega_j \tau''} \\ + g_j^{\beta\alpha} (g_j^{\beta\beta*} - g_j^{\alpha\alpha*}) (1 + \bar{n}(\omega_j)) e^{-i\omega_j \tau''} \} \\ \times \int_0^{\tau' - \tau} d\tau''' \sum_{j'} \hbar^2 \{ g_{j'}^{\alpha\beta} (g_{j'}^{\beta\beta*} - g_{j'}^{\alpha\alpha*}) \bar{n}(\omega_{j'}) e^{+i\omega_{j'} \tau'''} \\ + g_{j'}^{\beta\alpha*} (g_{j'}^{\beta\beta} - g_{j'}^{\alpha\alpha}) (1 + \bar{n}(\omega_{j'})) e^{-i\omega_{j'} \tau'''} \}. \quad (8.125)$$

The last term is omitted in the following, since coupling processes that are diagonal in the excitonic states are assumed to involve different phonon modes than off-diagonal couplings. This means, a local bath is assumed for each molecule. Moreover, the applied treatment aims at

a realistic lineshape, which is already contained in the first term. For the cumulant expansion, the ansatz

$$J^{\alpha,\beta}(\tau' - \tau) = \hbar^2 \mathcal{A}^{\alpha,\beta}(\tau' - \tau) e^{-\mathcal{F}^{\alpha,\beta}(\tau' - \tau)} \quad (8.126)$$

is made with

$$\mathcal{A}^{\alpha,\beta}(\tau' - \tau) \equiv \sum_{\nu} |c_{\nu}^{\alpha}|^2 |c_{\nu}^{\beta}|^2 \int_0^{\infty} d\omega J(\omega) \omega^2 \{ (1 + \bar{n}(\omega)) e^{-i\omega(\tau' - \tau)} + \bar{n}(\omega) e^{+i\omega(\tau' - \tau)} \}. \quad (8.127)$$

Here, the spectral density of Eq. (8.117) has been inserted. Note that the form of $\mathcal{A}^{\alpha,\beta}$ resembles the two-time correlation function $C^{g,\beta}$ given in Eq. (8.118) with the difference that here a phonon-mediated transition between two different molecular exciton states is described.

Following the same procedure as before by expanding $\mathcal{F}^{\alpha,\beta}(\tau' - \tau)$ in powers of $\hat{H}_{1,\text{ph}}^{\alpha,\beta}$ and comparing it to Eq. (8.125) yields:

$$J^{\alpha,\beta}(\tau' - \tau) = \mathcal{A}^{\alpha,\beta}(\tau' - \tau) \exp \left[\sum_{j'} |g_{j'}^{\beta\beta} - g_{j'}^{\alpha\alpha}|^2 \frac{1}{\omega_{j'}^2} \left\{ (1 + \bar{n}(\omega_{j'})) e^{-i\omega_{j'}(\tau' - \tau)} + \bar{n}(\omega_{j'}) e^{+i\omega_{j'}(\tau' - \tau)} - 2\bar{n}(\omega_{j'}) - 1 + i\omega_{j'}(\tau' - \tau) \right\} \right]. \quad (8.128)$$

With that, the intermolecular transition amplitude becomes

$$t_{\rho_{\beta\beta}^m \leftarrow \rho_{\alpha\alpha}^m}(t, t_0) = \int_{t_0}^t d\tau \int_{t_0}^{\tau} d\tau' \left\{ e^{+\frac{i}{\hbar} E_{\text{el}}^m(X_{\beta}^m, X_{\alpha}^m)(\tau - \tau')} \mathcal{A}^{\alpha,\beta}(\tau' - \tau) e^{-g^{\alpha,\beta}(\tau' - \tau)} + e^{-\frac{i}{\hbar} E_{\text{el}}^m(X_{\beta}^m, X_{\alpha}^m)(\tau - \tau')} \mathcal{A}^{\alpha,\beta*}(\tau' - \tau) e^{-g^{\alpha,\beta*}(\tau' - \tau)} \right\} \quad (8.129)$$

with

$$g^{\alpha,\beta}(\tau' - \tau) = - \sum_{\nu} \left(|c_{\nu}^{\beta}|^2 - |c_{\nu}^{\alpha}|^2 \right)^2 \int_0^{\infty} d\omega J(\omega) \left\{ (1 + \bar{n}(\omega)) e^{-i\omega(\tau' - \tau)} + \bar{n}(\omega) e^{+i\omega(\tau' - \tau)} - 2\bar{n}(\omega) - 1 + i\omega(\tau' - \tau) \right\} \quad (8.130)$$

$$= \int_0^{\tau' - \tau} d\tau'' \int_0^{\tau''} d\tau''' C^{\alpha,\beta}(\tau'''), \quad (8.131)$$

where the two-time correlation function has been introduced:

$$C^{\alpha,\beta}(\tau''') \equiv \sum_{\nu} \left(|c_{\nu}^{\beta}|^2 - |c_{\nu}^{\alpha}|^2 \right)^2 \int_0^{\infty} d\omega J(\omega) \omega^2 \{ (1 + \bar{n}(\omega)) e^{-i\omega\tau'''} + \bar{n}(\omega) e^{+i\omega\tau'''} \}. \quad (8.132)$$

Multimode Brownian oscillator model

Usually, the vibrational modes are modeled as a set of independent harmonic oscillators in a multimode Brownian oscillator model using a Spin-Boson Hamiltonian. The correlation function is decomposed into [Muk95]

$$C(t) = \sum_j \xi_j^2 (C_j'(t) + C_j''(t)) \quad \text{with} \quad \xi_j \equiv \frac{m_j \omega_j^2 d_j}{\hbar}. \quad (8.133)$$

Here, d_j represents the polaron shift, i.e., the displacement of the equilibrium PES of the j -th mode. In order to introduce a damping of the oscillations, the nuclear motion itself is coupled

to a set of harmonic bath oscillators labeled n with coupling strength c_{nj} . In the case of a strongly overdamped harmonic oscillator, the relaxation rate

$$\gamma_j(\omega) \equiv \pi \sum_n \frac{c_{nj}^2}{2m_n \omega_n^2} (\delta(\omega - \omega_n) + \delta(\omega + \omega_n)) \quad (8.134)$$

is large compared to the characteristic frequencies, $\gamma_j \gg 2\omega_j$, and one obtains [Muk95]

$$C'_j(t) = \lambda'_j \Lambda_j \coth(\beta \hbar \Lambda_j / 2) e^{-\Lambda_j t} + \frac{4\Lambda_j \lambda'_j}{\hbar \beta} \sum_{n=1}^{\infty} \frac{\nu_n e^{-\nu_n t}}{\nu_n^2 - \Lambda_j^2}, \quad (8.135)$$

$$C''_j(t) = -i \lambda'_j \Lambda_j e^{-\Lambda_j t} \quad (8.136)$$

with the Matsubara frequencies $\nu_n \equiv \frac{2\pi}{\hbar \beta} n$ and

$$\Lambda_j \equiv \frac{\omega_j^2}{\gamma_j}, \quad \lambda'_j \equiv \frac{\hbar}{2m_j \omega_j^2}. \quad (8.137)$$

8.4.5 Transition rates

The goal is to translate the transition amplitudes calculated in the previous chapters into time-independent transition rates entering the EOM for the molecular and semiconductor exciton densities. The treatment applies a secular approximation, where the dynamics of the densities are assumed to decouple from the polarizations. As a first step, the time derivatives of the transition amplitudes are taken, yielding time-dependent transfer rates:

$$r_{\rho_{\beta\beta}^m \leftarrow \rho_{\alpha\alpha}^s}(t) = \frac{1}{\hbar^2} |V_F^{m-s}(X_\beta^m, X_\alpha^s)|^2 \int_0^t d\tau' \left\{ e^{+\frac{i}{\hbar} E_{el}^{m-s}(X_\beta^m, X_\alpha^s)(t-\tau')} e^{-g^{g,\beta}(\tau'-t)} + e^{-\frac{i}{\hbar} E_{el}^{m-s}(X_\beta^m, X_\alpha^s)(t-\tau')} e^{-g^{g,\beta*}(\tau'-t)} \right\}, \quad (8.138)$$

$$r_{\rho_{\beta\beta}^s \leftarrow \rho_{\alpha\alpha}^m}(t) = \frac{1}{\hbar^2} |V_F^{m-s}(X_\alpha^m, X_\beta^s)|^2 \int_0^t d\tau' \left\{ e^{-\frac{i}{\hbar} E_{el}^{m-s}(X_\alpha^m, X_\beta^s)(t-\tau')} e^{-g^{g,\alpha}(\tau'-t)} + e^{+\frac{i}{\hbar} E_{el}^{m-s}(X_\alpha^m, X_\beta^s)(t-\tau')} e^{-g^{g,\alpha*}(\tau'-t)} \right\}, \quad (8.139)$$

$$r_{\rho_{\beta\beta}^m \leftarrow \rho_{\alpha\alpha}^m}(t) = \int_0^t d\tau' \left\{ e^{+\frac{i}{\hbar} E_{el}^{m-m}(X_\beta^m, X_\alpha^m)(t-\tau')} \mathcal{A}^{\alpha,\beta}(\tau'-t) e^{-g^{\alpha,\beta}(\tau'-t)} + e^{-\frac{i}{\hbar} E_{el}^{m-m}(X_\beta^m, X_\alpha^m)(t-\tau')} \mathcal{A}^{\alpha,\beta*}(\tau'-t) e^{-g^{\alpha,\beta*}(\tau'-t)} \right\}. \quad (8.140)$$

Here, $t_0 = 0$ was chosen as initial time. With that, the rate equations can be written as

$$\begin{aligned} \frac{\partial}{\partial t} \rho_{\alpha\alpha}^m(t) = & - \left(\sum_{\beta} r_{\rho_{\beta\beta}^s \leftarrow \rho_{\alpha\alpha}^m}(t) + \sum_{\substack{\beta \\ \beta \neq \alpha}} r_{\rho_{\beta\beta}^m \leftarrow \rho_{\alpha\alpha}^m}(t) \right) \rho_{\alpha\alpha}^m(t) \\ & + \left(\sum_{\beta} r_{\rho_{\alpha\alpha}^m \leftarrow \rho_{\beta\beta}^s}(t) \rho_{\beta\beta}^s(t) + \sum_{\substack{\beta \\ \beta \neq \alpha}} r_{\rho_{\alpha\alpha}^m \leftarrow \rho_{\beta\beta}^m}(t) \rho_{\beta\beta}^m(t) \right) \end{aligned} \quad (8.141)$$

for the molecular exciton density and

$$\frac{\partial}{\partial t} \rho_{\alpha\alpha}^s(t) = - \sum_{\beta} r_{\rho_{\beta\beta}^m \leftarrow \rho_{\alpha\alpha}^s}(t) \rho_{\alpha\alpha}^s(t) + \sum_{\beta} r_{\rho_{\alpha\alpha}^s \leftarrow \rho_{\beta\beta}^m}(t) \rho_{\beta\beta}^m(t) \quad (8.142)$$

for the exciton density in the semiconductor substrate. In both equations, the first term represents the out-scattering processes and the second term describes in-scattering into the exciton state.

The $e^{-g^{g/\alpha, \beta(*)}}$ terms stemming from the cumulant expansion treatment in terms of the spectral density describe the line broadening through exciton-phonon relaxation. If they are replaced by a Lorentzian dephasing describing the complex lineshape, the form of Eqs. (8.141) and (8.142) resembles the Born-Markov Redfield master equation discussed in Sec. 2.1.3 in secular approximation (i.e., only densities are considered) for the density matrix elements

$$\rho_{\alpha\alpha}^{m/s} \equiv \langle |X_{\alpha}^{m/s}\rangle \langle X_{\alpha}^{m/s}| \rangle = \text{tr}_B [\langle X_{\alpha}^{m/s} | \hat{\rho}_S \otimes \hat{\rho}_B | X_{\alpha}^{m/s} \rangle] = \langle X_{\alpha}^{m/s} | \hat{\rho}_S | X_{\alpha}^{m/s} \rangle \quad (8.143)$$

and the interaction picture Hamiltonian

$$\begin{aligned} \hat{H}_I^{g/\alpha}(t) = & \sum_{\zeta, \eta} (V_F^{m-s}(X_{\zeta}^m, X_{\eta}^s) e^{-\frac{i}{\hbar} E_{\text{el}}^{m-s}(X_{\zeta}^m, X_{\eta}^s)t} |X_{\zeta}^m\rangle \langle X_{\eta}^s| \\ & + V_F^{m-s*}(X_{\zeta}^m, X_{\eta}^s) e^{+\frac{i}{\hbar} E_{\text{el}}^{m-s}(X_{\zeta}^m, X_{\eta}^s)t} |X_{\eta}^s\rangle \langle X_{\zeta}^m|) \\ & + \sum_{\substack{\zeta, \eta \\ \zeta \neq \eta}} \sum_j \hbar (g_j^{\zeta\eta} \hat{b}_j^{g/\alpha} e^{-i\omega_j t} e^{-\frac{i}{\hbar} E_{\text{el}}^m(X_{\zeta}^m, X_{\eta}^m)t} \\ & + g_j^{\eta\zeta*} \hat{b}_j^{g/\alpha\dagger} e^{+i\omega_j t} e^{-\frac{i}{\hbar} E_{\text{el}}^m(X_{\eta}^m, X_{\zeta}^m)t}) |X_{\eta}^m\rangle \langle X_{\zeta}^m|. \end{aligned} \quad (8.144)$$

Therefore, in complete analogy to the master equation, a Markovian treatment is applied to the EOM of Eqs. (8.141) and (8.142). This is valid since the discrete exciton states are very dense. τ' is substituted by $t - \tau'$ (leaving the limits of the integral unchanged) and the upper integration boundary is extended to $t \rightarrow \infty$, which is possible if the integrands vanish sufficiently fast for $\tau' \gg \tau_B$ (with the characteristic time τ_B for the decay of bath correlations) [Bre02]:

$$r_{\rho_{\beta\beta}^m \leftarrow \rho_{\alpha\alpha}^s} = \frac{1}{\hbar^2} |V_F^{m-s}(X_{\beta}^m, X_{\alpha}^s)|^2 \int_0^{\infty} d\tau' \left\{ e^{+\frac{i}{\hbar} E_{\text{el}}^{m-s}(X_{\beta}^m, X_{\alpha}^s)\tau'} e^{-g^{g, \beta}(-\tau')} \right. \\ \left. + e^{-\frac{i}{\hbar} E_{\text{el}}^{m-s}(X_{\beta}^m, X_{\alpha}^s)\tau'} e^{-g^{g, \beta*}(-\tau')} \right\}, \quad (8.145)$$

$$r_{\rho_{\beta\beta}^s \leftarrow \rho_{\alpha\alpha}^m} = \frac{1}{\hbar^2} |V_F^{m-s}(X_{\alpha}^m, X_{\beta}^s)|^2 \int_0^{\infty} d\tau' \left\{ e^{-\frac{i}{\hbar} E_{\text{el}}^{m-s}(X_{\alpha}^m, X_{\beta}^s)\tau'} e^{-g^{g, \alpha}(-\tau')} \right. \\ \left. + e^{+\frac{i}{\hbar} E_{\text{el}}^{m-s}(X_{\alpha}^m, X_{\beta}^s)\tau'} e^{-g^{g, \alpha*}(-\tau')} \right\}, \quad (8.146)$$

$$r_{\rho_{\beta\beta}^m \leftarrow \rho_{\alpha\alpha}^m} = \int_0^{\infty} d\tau' \left\{ e^{+\frac{i}{\hbar} E_{\text{el}}^m(X_{\beta}^m, X_{\alpha}^m)\tau'} \mathcal{A}^{\alpha, \beta}(-\tau') e^{-g^{\alpha, \beta}(-\tau')} \right. \\ \left. + e^{-\frac{i}{\hbar} E_{\text{el}}^m(X_{\beta}^m, X_{\alpha}^m)\tau'} \mathcal{A}^{\alpha, \beta*}(-\tau') e^{-g^{\alpha, \beta*}(-\tau')} \right\}, \quad (8.147)$$

where $J_{\nu}(\omega)$, $g^{g, \beta}(-\tau')$, $g^{\alpha, \beta}(-\tau')$, and $\mathcal{A}^{\alpha, \beta}(-\tau')$ have been defined in Eqs. (8.117), (8.119), (8.127), and (8.130), respectively. A Fourier representation of $G^{g, \beta}(-\tau') \equiv e^{-g^{g, \beta}(-\tau')}$ is introduced:

$$G^{g, \beta}(-\tau') = \int_{-\infty}^{\infty} d\tilde{\omega} \tilde{G}^{g, \beta}(\tilde{\omega}) e^{+i\tilde{\omega}\tau'}. \quad (8.148)$$

The τ' integration is transformed into a δ function (where the principal values of the two terms cancel each other out) and the $\tilde{\omega}$ integration is eliminated by evaluating the δ function:

$$r_{\rho_{\beta\beta}^m \leftarrow \rho_{\alpha\alpha}^s} = \frac{\pi}{\hbar^2} |V_F^{m-s}(X_{\beta}^m, X_{\alpha}^s)|^2 \left\{ \tilde{G}^{g, \beta}(-E_{\text{el}}^{m-s}(X_{\beta}^m, X_{\alpha}^s)/\hbar) + \tilde{G}^{g, \beta*}(-E_{\text{el}}^{m-s}(X_{\beta}^m, X_{\alpha}^s)/\hbar) \right\}, \quad (8.149)$$

$$r_{\rho_{\beta\beta}^s \leftarrow \rho_{\alpha\alpha}^m} = \frac{\pi}{\hbar^2} |V_{\text{F}}^{\text{m-s}}(X_\alpha^{\text{m}}, X_\beta^{\text{s}})|^2 \left\{ \tilde{G}^{g,\alpha}(E_{\text{el}}^{\text{m-s}}(X_\alpha^{\text{m}}, X_\beta^{\text{s}})/\hbar) + \tilde{G}^{g,\beta*}(E_{\text{el}}^{\text{m-s}}(X_\alpha^{\text{m}}, X_\beta^{\text{s}})/\hbar) \right\} \quad (8.150)$$

with

$$\tilde{G}^{g,\alpha}(\tilde{\omega}) \equiv \frac{1}{2\pi} \int_{-\infty}^{\infty} d\tau' G^{g,\alpha}(-\tau') e^{-i\tilde{\omega}\tau'} = \frac{1}{2\pi} \int_{-\infty}^{\infty} d\tau' e^{-g^{g,\alpha}(-\tau') - i\tilde{\omega}\tau'}. \quad (8.151)$$

The last expression is evaluated numerically and inserted into the rates of Eqs. (8.149) and (8.150).

8.4.6 System of equations for the population dynamics

The contributions to the population dynamics of the hybrid system derived in the last sections are now summarized. This leads to a system of $N_s + N_m + 2$ coupled equations of motion containing the $N_s + N_m$ calculated exciton eigenstates in the inorganic and organic component, the ground state, and the phenomenological high-energy excited state continuum $\rho_{\hbar\hbar}^s$ of the semiconductor substrate (introduced in Sec. 8.2.6). It includes disorder due to interface roughness, phonon scattering, radiative recombination, and incoherent pumping in the **QW** substrate as well as Coulomb interaction and coupling to vibrational modes in the molecular layer and interlayer Förster coupling. Only populations, i.e., diagonal density matrix elements are considered. Defining the vector

$$\mathbf{P} \equiv (\rho_{00}, \rho_{\alpha_1\alpha_1}^{\text{m}}, \rho_{\alpha_2\alpha_2}^{\text{m}}, \dots, \rho_{\alpha_{N_m}\alpha_{N_m}}^{\text{m}}, \rho_{\beta_1\beta_1}^{\text{s}}, \rho_{\beta_2\beta_2}^{\text{s}}, \dots, \rho_{\beta_{N_s}\beta_{N_s}}^{\text{s}}, \rho_{\hbar\hbar}^{\text{s}})^T, \quad (8.152)$$

the system of equations is given by

$$\frac{\partial}{\partial t} \mathbf{P} = \hat{A} \cdot \mathbf{P}. \quad (8.153)$$

\hat{A} is given in Eq. (8.155).

In order to access the population dynamics in the system, the derived system of equations of motion for the exciton densities can be solved numerically, e.g., using a time-stepping Runge-Kutta solver contained in the PETSc library [Bal15b, Bal15a]. This can in turn be used to calculate observables that are probed in spectroscopic experiments such as the time- and frequency-resolved detection signal for incoherent emission of a semiconductor **QW** coupled to a molecular layer [Zim03]:

$$I_{l,\mathbf{q}}^{\text{inc}}(\omega, t) = \sum_{\alpha} |M_{l,\mathbf{q}}^{\alpha}|^2 (\rho_{\alpha\alpha}^{\text{s}}(t) - |\rho_{\alpha 0}^{\text{s}}(t)|^2) \frac{R_{\alpha}^{\text{s}} + \Delta_{\text{S}}}{(\omega - E_{\alpha}^{\text{s}}/\hbar)^2 + (R_{\alpha}^{\text{s}} + \Delta_{\text{S}})^2} \quad (8.154)$$

with spectrometer resolution Δ_{S} .

8.5 Summary and outlook

In this chapter, the simple model system of a highly ordered molecular layer adsorbed on an atomically smooth ZnO substrate developed in Chap. 7 was extended towards treating structural disorder, radiative dephasing, and exciton-phonon scattering processes. Therefore, the interlayer Förster-type interaction as well as the electron-phonon couplings that are off-diagonal in the excitonic eigenstates were treated in second-order perturbation theory and a cumulant expansion technique was used to model the coupling to vibrational modes in the organic layer.

$$\hat{A} \equiv \begin{pmatrix} -\gamma^{\text{exc}}(t) & 0 & \dots & r_{\beta_1} & r_{\beta_2} & \dots & r_{\beta N_s} & 0 \\ 0 & -\Gamma_{\alpha_1}^m & \dots & r_{\alpha_1 \alpha_1}^m \leftarrow \rho_{\alpha_1}^m & r_{\alpha_1 \alpha_1}^m \leftarrow \rho_{\beta_1 \beta_1}^s & \dots & r_{\alpha_1 \alpha_1}^m \leftarrow \rho_{\beta N_s}^s & 0 \\ 0 & r_{\alpha_2 \alpha_2}^m \leftarrow \rho_{\alpha_1 \alpha_1}^m & \dots & r_{\alpha_2 \alpha_2}^m \leftarrow \rho_{\beta_1 \beta_1}^s & r_{\alpha_2 \alpha_2}^m \leftarrow \rho_{\beta_2 \beta_2}^s & \dots & r_{\alpha_2 \alpha_2}^m \leftarrow \rho_{\beta N_s}^s & 0 \\ \vdots & \vdots & \ddots & \vdots & \vdots & \ddots & \vdots & \vdots \\ 0 & r_{\alpha N_m}^m \leftarrow \rho_{\alpha_1 \alpha_1}^m & \dots & r_{\alpha N_m}^m \leftarrow \rho_{\beta_1 \beta_1}^s & r_{\alpha N_m}^m \leftarrow \rho_{\beta_2 \beta_2}^s & \dots & r_{\alpha N_m}^m \leftarrow \rho_{\beta N_s}^s & 0 \\ 0 & r_{\beta_1 \beta_1}^s \leftarrow \rho_{\alpha_1 \alpha_1}^m & \dots & -\Gamma_{\beta_1}^s & \gamma_{\beta_1}^s \leftarrow \beta_2 & \dots & \gamma_{\beta_1}^s \leftarrow \beta N_s & \gamma_{\beta_1}^{\text{in}} \\ 0 & r_{\beta_2 \beta_2}^s \leftarrow \rho_{\alpha_1 \alpha_1}^m & \dots & \gamma_{\beta_2}^s \leftarrow \beta_1 & -\Gamma_{\beta_2}^s & \dots & \gamma_{\beta_2}^s \leftarrow \beta N_s & \gamma_{\beta_2}^{\text{in}} \\ \vdots & \vdots & \ddots & \vdots & \vdots & \ddots & \vdots & \vdots \\ 0 & r_{\beta N_s}^s \leftarrow \rho_{\alpha_1 \alpha_1}^m & \dots & \gamma_{\beta N_s}^s \leftarrow \beta_1 & \gamma_{\beta N_s}^s \leftarrow \beta_2 & \dots & -\Gamma_{\beta N_s}^s & \gamma_{\beta N_s}^{\text{in}} \\ \gamma^{\text{exc}}(t) & 0 & \dots & \gamma_{\beta_1}^{\text{out}} & \gamma_{\beta_2}^{\text{out}} & \dots & \gamma_{\beta N_s}^{\text{out}} & -\sum_{\beta} \gamma_{\beta}^{\text{in}} \end{pmatrix} \quad (8.155)$$

The abbreviations

$$\Gamma_{\alpha}^m \equiv \sum_{\beta} r_{\beta \beta}^s \leftarrow \rho_{\alpha \alpha}^m + \sum_{\substack{\beta \\ \beta \neq \alpha}} r_{\beta \beta}^m \leftarrow \rho_{\alpha \alpha}^m, \quad (8.156)$$

$$\Gamma_{\beta}^s \equiv 2R_{\beta}^s + \sum_{\zeta} r_{\zeta \zeta}^m \leftarrow \rho_{\beta \beta}^s + \gamma_{\beta}^{\text{out}} \quad (8.157)$$

have been used.

As a next step, the derived equations are going to be implemented numerically and evaluated in order to calculate spectroscopic observables such as the incoherent **PL** signal in time and frequency domain accessible in optical experiments. This is not contained in the scope of this work. The above-mentioned effects are expected to significantly alter the lifetimes and thus the **PL** decay transient of the **QW** substrate. In particular, Förster coupling to the organic layer constitutes an additional decay channel for the **QW** excitons, thus decreasing the **PL** decay transient compared to the isolated inorganic ZnO **QW**, as observed in previous experimental works [Blu06, Sch15].

The developed theoretical framework thus paves the way for a large variety of further theoretical studies investigating different parameter regimes that characterize the hybrid structure. E.g., limiting cases of the semiconductor dynamics can be investigated: On the one hand, the regime where disorder constitutes the main broadening mechanism in the semiconductor substrate due to strong well width fluctuations can be studied, where phonon couplings are expected to be strongly suppressed. On the other hand, the regime of dominant phonon coupling where long-range lattice vibrations take place in the case of moderate disorder can be considered. The disorder parameters are expected to be critical for the observed phonon frequencies and coupling strengths.

In summary, the presented theoretical treatment aims at a systematic investigation of the exciton dynamics including excitation transfer and vibrational couplings in realistic (i.e., non-perfect) hybrid systems of variable geometry. It thus enables to explore different parameter regimes for optimized device performance in future studies.

9

Conclusion and outlook

In summary, this thesis comprises a theoretical treatment of nonlinear two-dimensional spectroscopy and excitation transfer processes in different (hybrid) nanostructures ranging from coupled quantum dots and monolayer transition-metal dichalcogenides to hybrid inorganic/organic systems. Thus, it contributes to a microscopic understanding of Coulomb-mediated couplings in nanoscaled systems.

Four-wave mixing experiments probing the third-order nonlinear response of semiconductor nanostructures have evolved as a versatile and valuable toolbox to examine not only the energies and oscillator strengths of the system under study, but to provide also unique access to the coherent couplings between higher-order bound states. This can be used to resolve the internal structure of excitonic wave functions. This was demonstrated in Chap. 4, where reconstruction protocols have been derived for dissecting the spin-dependent single- and two-exciton wave functions of coupled, spin-degenerate two-level quantum emitters into contributions from the local (uncoupled) basis states. Therefore, two-dimensional double quantum coherence spectroscopy was combined with polarization-resolved nanooptical fields in order to selectively excite a specific emitter. A comparison of the reconstruction results with the wave function coefficients extracted from the numerically calculated eigenstates yielded a good overall agreement even for non-ideal field distributions. This enabled a close inspection of the microscopic spin- and polarization-dependent coupling mechanisms that are not available in far-field experiments and without the proposed data postprocessing.

As a future research project, a reconstruction algorithm could be developed for systems with pronounced spin-orbit splitting, which is however difficult since (i) this alters the optical selection rules, (ii) the different spin states cannot be selectively addressed using localized excitation for lack of spatial separation and (iii) a substantial spectral overlap between the fine-structure split resonance peaks is expected, which is detrimental for the reconstruction protocol. The latter can possibly be reduced by establishing a spectral filtering method to eliminate selected resonances similar to Refs. [Ric12, Sch13].

Monolayer transition-metal dichalcogenides are known to exhibit strongly correlated many-body states that can be probed using polarization-resolved, two-dimensional coherent photon echo spectroscopy. In Chap. 5, the formation of charged and uncharged intervalley biexcitons was studied and a comparison to experiment allowed to infer the corresponding quasi-particle binding energies for exciton-exciton, exciton-trion, and even trion-trion complexes that agree well with previous theoretical predictions. The present work helps to guide efforts characterizing higher-order bound states in this novel two-dimensional semiconducting material class.

In Chap. 6, simulations of rephasing and photon echo signals of individual quantum dots and a quantum dot molecule were performed including electrostatic and Förster-type Coulomb coupling, fine-structure splitting, and linearly polarized excitation at a defined angle relative to the quantum dot axis. This allowed to ascertain the spectral signatures observed in a two-beam experiment and to trace back the coherent coupling mechanisms and strengths as well as the optical selection rules of the quantum dot system. It was found that the coupling between the

quantum dots is governed by the electrostatic biexciton shift rather than Förster coupling. The suggested methodology provides an important step towards the systematic description of electronic couplings and charge transfer in deterministically defined quantum dot molecules [Sti06, Ard16].

In the third part of this work, a theoretical model for describing Förster-type excitation transfer across the interface of hybrid inorganic/organic systems was developed. A first theoretical approach (Chap. 7) focused on the coupling between electron-hole continuum states in an electrically pumped semiconductor substrate and Frenkel excitons in a periodically arranged molecular layer. The presented parameter studies allow to find the ideal operating regime by adjusting the geometry of the organic layer and the charge carrier reservoir in the inorganic quantum well substrate: The coupling efficiency can be substantially enhanced by aligning the dipole moments and the resonance energy detunings of the two constituents, minimizing the interlayer distance, and preparing a dense molecular coverage as well as a high carrier concentration. This way, in-scattering into the molecular layer outweighs the back-scattering into the substrate, yielding a high performance of hybrid light-emitting devices.

This simple model is extended in the last Chap. 8 to a more extensive theoretical framework taking into account structural disorder, radiative dephasing, and exciton–phonon scattering processes. It uses a perturbative approach to treat the interlayer Förster interaction as well as the off-diagonal electron–phonon coupling and a cumulant expansion technique to model the coupling to vibrational modes in the organic layer. In future studies, this derived theoretical framework will be implemented numerically and evaluated in order to calculate spectroscopic observables such as the incoherent photoluminescence signal in time and frequency domain accessible in optical experiments. The photoluminescence decay transient of the quantum well excitons is expected to decrease when a molecular film is adsorbed on top of the substrate, indicating the opening of an extra decay channel into the organic film which shortens the lifetime of the quantum well excitons, as observed experimentally [Blu06, Sch15]. Also, different limiting cases of the semiconductor dynamics are going to be studied, namely (i) the regime of dominant disorder-induced broadenings due to strong fluctuations in the quantum well thickness (thus suppressing phonon coupling) and (ii) the regime where phonon coupling constitutes the main broadening mechanism in the case of moderate disorder (making long-range lattice vibrations possible). It is expected that the disorder parameters are crucial for the observed phonon frequencies and coupling strengths.

Appendices

A

Calculation of the rephasing photon echo signal

The response functions of the excited state emission (ESE), ground state bleaching (GSB), and excited state absorption (ESA) pathways contributing to the photon echo (PE) signal can be directly read out from the corresponding Feynman diagram of Fig. 5.1. This way, the third-order response of Eq. (3.4) is given by the sum-over-states expressions [Abr09]:

$$\begin{aligned} (R_{\text{ESE}}^{(3)})_{\alpha\beta\gamma\delta}(t_3, t_2, t_1) = & + \left(\frac{i}{\hbar}\right)^3 \theta(t_1)\theta(t_2)\theta(t_3) \sum_{e,e'} (\mathbf{d}_{ge'})_{\alpha} (\mathbf{d}_{eg})_{\beta} (\mathbf{d}_{e'g})_{\gamma} (\mathbf{d}_{ge})_{\delta} \\ & \times e^{-i\xi_{e'g}t_3 - i\xi_{e'e}t_2 - i\xi_{ge}t_1}, \end{aligned} \quad (\text{A.1})$$

$$\begin{aligned} (R_{\text{GSB}}^{(3)})_{\alpha\beta\gamma\delta}(t_3, t_2, t_1) = & + \left(\frac{i}{\hbar}\right)^3 \theta(t_1)\theta(t_2)\theta(t_3) \sum_{e,e'} (\mathbf{d}_{ge'})_{\alpha} (\mathbf{d}_{e'g})_{\beta} (\mathbf{d}_{eg})_{\gamma} (\mathbf{d}_{ge})_{\delta} \\ & \times e^{-i\xi_{e'g}t_3 - i\xi_{ge}t_1} \end{aligned} \quad (\text{A.2})$$

$$\begin{aligned} (R_{\text{ESA}}^{(3)})_{\alpha\beta\gamma\delta}(t_3, t_2, t_1) = & - \left(\frac{i}{\hbar}\right)^3 \theta(t_1)\theta(t_2)\theta(t_3) \sum_{e,e',f} (\mathbf{d}_{ef})_{\alpha} (\mathbf{d}_{fe'})_{\beta} (\mathbf{d}_{e'g})_{\gamma} (\mathbf{d}_{ge})_{\delta} \\ & \times e^{-i\xi_{fe}t_3 - i\xi_{e'e}t_2 - i\xi_{ge}t_1}. \end{aligned} \quad (\text{A.3})$$

The sums over e, e', f run over all states belonging to the same excited state manifold. The complex frequencies $\xi_{ab} \equiv \omega_{ab} - i\gamma_{ab}$ contain the resonances ω_{ab} and the dephasing constants γ_{ab} . The Heaviside step functions ensure the right time ordering of the interactions. Substituting the pulse times τ_j by the intervals between two pulses, $T_1 = \tau_2 - \tau_1$, $T_2 = \tau_3 - \tau_2$, and $T_3 = \tau_s - \tau_3$, and plugging the ESE response function of Eq. (A.1) into the polarization Eq. (3.10) with $(u_1, u_2, u_3) = (-1, +1, +1)$, and inserting the result into the heterodyne detected signal function of Eq. (3.2) provides the ESE signal

$$\begin{aligned} S_{\text{ESE}}^{(3)}(T_3, T_2, T_1) = & \int_{-\infty}^{\infty} dt \int_0^{\infty} dt_3 \int_0^{\infty} dt_2 \int_0^{\infty} dt_1 \sum_{\alpha,\beta,\gamma,\delta=1}^3 \left(\frac{i}{\hbar}\right)^3 \mathcal{E}_{s\alpha}^*(t - \tau_s) e^{i\omega_s(t - \tau_s)} \\ & \times e^{-i(-\omega_1 + \omega_2 + \omega_3)(t - \tau_s + T_3) - i(\omega_2 - \omega_1)T_2 + i\omega_1 T_1} e^{i(-\omega_1 + \omega_2 + \omega_3)t_3 + i(\omega_2 - \omega_1)t_2 - i\omega_1 t_1} \\ & \times \mathcal{E}_{3\beta}(t - t_3 - \tau_s + T_3) \mathcal{E}_{2\gamma}(t - t_3 - t_2 - \tau_s + T_3 + T_2) \\ & \times \mathcal{E}_{1\delta}^*(t - t_3 - t_2 - t_1 - \tau_s + T_3 + T_2 + T_1) \theta(t_1)\theta(t_2)\theta(t_3) \\ & \times \sum_{e,e'} (\mathbf{d}_{ge'})_{\alpha} (\mathbf{d}_{eg})_{\beta} (\mathbf{d}_{e'g})_{\gamma} (\mathbf{d}_{ge})_{\delta} e^{-i\xi_{e'g}t_3 - i\xi_{e'e}t_2 - i\xi_{ge}t_1}. \end{aligned} \quad (\text{A.4})$$

The intervals t_1, t_2 , and t_3 between two interactions with the radiation field are now substituted by the times $\tilde{\tau}_1 = \tilde{\tau}_2 - t_1$, $\tilde{\tau}_2 = \tilde{\tau}_3 - t_2$, $\tilde{\tau}_3 = t - t_3$, and t where the interactions

take place (cf. Fig. 3.2 (a)). Collecting terms with the same ω_j , Eq. (A.4) takes the form:

$$\begin{aligned}
S_{\text{ESE}}^{(3)}(T_3, T_2, T_1) &= \int_{-\infty}^{\infty} dt \int_{-\infty}^t d\tilde{\tau}_3 \int_{-\infty}^{\tilde{\tau}_3} d\tilde{\tau}_2 \int_{-\infty}^{\tilde{\tau}_2} d\tilde{\tau}_1 \sum_{\alpha, \beta, \gamma, \delta=1}^3 \left(\frac{i}{\hbar}\right)^3 \mathcal{E}_{s_\alpha}^*(t - \tau_s) e^{i\omega_s(t - \tau_s)} \\
&\quad \times \mathcal{E}_{3_\beta}(\tilde{\tau}_3 - \tau_s + T_3) e^{-i\omega_3(\tilde{\tau}_3 - \tau_s + T_3)} \mathcal{E}_{2_\gamma}(\tilde{\tau}_2 - \tau_s + T_3 + T_2) e^{-i\omega_2(\tilde{\tau}_2 - \tau_s + T_3 + T_2)} \\
&\quad \times \mathcal{E}_{1_\delta}^*(\tilde{\tau}_1 - \tau_s + T_3 + T_2 + T_1) e^{+i\omega_1(\tilde{\tau}_1 - \tau_s + T_3 + T_2 + T_1)} \\
&\quad \times \theta(\tilde{\tau}_2 - \tilde{\tau}_1) \theta(\tilde{\tau}_3 - \tilde{\tau}_2) \theta(t - \tilde{\tau}_3) \sum_{e, e'} (\mathbf{d}_{ge'})_\alpha (\mathbf{d}_{eg})_\beta (\mathbf{d}_{e'g})_\gamma (\mathbf{d}_{ge})_\delta \\
&\quad \times e^{-i\xi_{e'g}(t - \tilde{\tau}_3)} e^{-i\xi_{e'e}(\tilde{\tau}_3 - \tilde{\tau}_2)} e^{-i\xi_{ge}(\tilde{\tau}_2 - \tilde{\tau}_1)}.
\end{aligned} \tag{A.5}$$

The substitution of the integration boundaries already expresses the time ordering of the interactions: $t_0 \geq \tilde{\tau}_1 \geq \tilde{\tau}_2 \geq \tilde{\tau}_3 \geq t$. This condition is ensured by the Heaviside step functions in Eq. (A.5). The initial time is $t_0 \rightarrow -\infty$.

Furthermore, it is assumed that the dephasing constants γ_{ab} (and thus the linewidths) are small compared to the resonance frequencies ω_{ab} and the intervals between the pulses are approximately the same as the intervals between the light-field interactions $t_j \approx T_j$, such that the factors $\gamma_{ab}(t_j - T_j)$ are negligible. Assuming that the pulses are temporally well separated, the upper integration bounds Eq. (A.5) are extended to ∞ . The pulse envelopes $\mathcal{E}_j(t)$ are Fourier transformed:

$$\mathcal{E}_j(t) = \int_{-\infty}^{\infty} d\tilde{\omega}_j \mathcal{E}_j(\tilde{\omega}_j) e^{-i\tilde{\omega}_j t}. \tag{A.6}$$

With that, Eq. (A.5) becomes

$$\begin{aligned}
S_{\text{ESE}}^{(3)}(T_3, T_2, T_1) &= \int_{-\infty}^{\infty} dt \int_{-\infty}^{\infty} d\tilde{\tau}_3 \int_{-\infty}^{\infty} d\tilde{\tau}_2 \int_{-\infty}^{\infty} d\tilde{\tau}_1 \sum_{\alpha, \beta, \gamma, \delta=1}^3 \left(\frac{i}{\hbar}\right)^3 \\
&\quad \times \int_{-\infty}^{\infty} d\tilde{\omega}_s \int_{-\infty}^{\infty} d\tilde{\omega}_3 \int_{-\infty}^{\infty} d\tilde{\omega}_2 \int_{-\infty}^{\infty} d\tilde{\omega}_1 \theta(T_1) \theta(T_2) \theta(T_3) \\
&\quad \times \sum_{e, e'} \mathcal{E}_{s_\alpha}^*(\tilde{\omega}_s) \mathcal{E}_{3_\beta}(\tilde{\omega}_3) \mathcal{E}_{2_\gamma}(\tilde{\omega}_2) \mathcal{E}_{1_\delta}^*(\tilde{\omega}_1) (\mathbf{d}_{ge'})_\alpha (\mathbf{d}_{eg})_\beta (\mathbf{d}_{e'g})_\gamma (\mathbf{d}_{ge})_\delta \\
&\quad \times e^{it(\omega_s + \tilde{\omega}_s - \omega_{e'g})} e^{i\tau_s(-\omega_s - \tilde{\omega}_s + \omega_3 + \tilde{\omega}_3 + \omega_2 + \tilde{\omega}_2 - \omega_1 - \tilde{\omega}_1)} \\
&\quad \times e^{i\tilde{\tau}_3(-\omega_3 - \tilde{\omega}_3 + \omega_{e'g} - \omega_{e'e})} e^{iT_3(-\omega_3 - \tilde{\omega}_3 - \omega_2 - \tilde{\omega}_2 + \omega_1 + \tilde{\omega}_1 + \omega_{e'g} - \xi_{e'g})} \\
&\quad \times e^{i\tilde{\tau}_2(-\omega_2 - \tilde{\omega}_2 + \omega_{e'e} - \omega_{ge})} e^{iT_2(-\omega_2 - \tilde{\omega}_2 + \omega_1 + \tilde{\omega}_1 + \omega_{e'e} - \xi_{e'e})} \\
&\quad \times e^{i\tilde{\tau}_1(\omega_1 + \tilde{\omega}_1 + \omega_{ge})} e^{iT_1(\omega_1 + \tilde{\omega}_1 + \omega_{ge} - \xi_{ge})}.
\end{aligned} \tag{A.7}$$

Evaluating the Fourier representation of the δ function

$$\int_{-\infty}^{\infty} dt e^{i\omega t} = 2\pi \delta(\omega), \tag{A.8}$$

removes all integrals and greatly simplifies the expression:

$$\begin{aligned}
S_{\text{ESE}}^{(3)}(T_3, T_2, T_1) &= \sum_{\alpha, \beta, \gamma, \delta=1}^3 \left(\frac{i}{\hbar}\right)^3 (2\pi)^4 \sum_{e, e'} (\mathbf{d}_{ge'})_\alpha (\mathbf{d}_{eg})_\beta (\mathbf{d}_{e'g})_\gamma (\mathbf{d}_{ge})_\delta \\
&\quad \times \mathcal{E}_{s_\alpha}^*(\omega_{e'g} - \omega_s) \mathcal{E}_{3_\beta}(\omega_{eg} - \omega_3) \mathcal{E}_{2_\gamma}(\omega_{e'g} - \omega_2) \mathcal{E}_{1_\delta}^*(\omega_{eg} - \omega_1) \\
&\quad \times e^{-iT_3 \xi_{e'g}} e^{-iT_2 \xi_{e'e}} e^{-iT_1 \xi_{ge}} \theta(T_1) \theta(T_2) \theta(T_3).
\end{aligned} \tag{A.9}$$

Since multidimensional signals are often depicted in frequency space, finally a Fourier transform of the signal function is performed with respect to the first and third pulse interval (which are of interest in the case of **PE** measurements where the photon echo can be observed on the diagonal):

$$S_{\text{ESE}}^{(3)}(\Omega_3, T_2, \Omega_1) = \int_0^\infty dT_3 \int_0^\infty dT_1 S_{\text{ESE}}^{(3)}(T_3, T_2, T_1) e^{i(\Omega_3 T_3 + \Omega_1 T_1)}. \quad (\text{A.10})$$

Performing the integrations and applying the same procedure to the other space pathways leads to the signal function given in Eqs. (5.2), (5.3), and (5.4).

B

Details on the derivation and implementation of the HIOS transfer rates

B.1 Dielectric screening at the hybrid interface

Particular care has to be taken of the relative permittivity ϵ_r incorporating the impact of the core electrons [Ver13], since the organic and inorganic parts of the hybrid structure exhibit different dielectric properties. The system is treated as two half spaces with different bulk dielectrics, separated by an interface at $z = 0$: ϵ_m in the molecular layer and ϵ_s in the semiconductor substrate, depicted in Fig. B.1. Image charges are introduced in order to account for the influence of the electrostatic charges within one of the half spaces on the electrostatic potential in the other half space. A point charge q in the molecular layer at a distance d from the interface induces the image charge q' within the semiconductor substrate at the distance $-d$, such that the potential at any point P in the molecular half space ($z > 0$) expressed in cylindrical coordinates (ρ, φ, z) reads [Jac99]

$$\phi(z > 0) = \frac{1}{4\pi\epsilon_0\epsilon_m} \left(\frac{q}{\sqrt{\rho^2 + (d-z)^2}} + \frac{q'}{\sqrt{\rho^2 + (d+z)^2}} \right). \quad (\text{B.1})$$

For specifying the potential at an arbitrary point in the semiconductor half space ($z < 0$), another image charge q'' is placed at the same position as the real charge q :

$$\phi(z < 0) = \frac{1}{4\pi\epsilon_0\epsilon_s} \frac{q''}{\sqrt{\rho^2 + (d-z)^2}}. \quad (\text{B.2})$$

Evaluating the boundary conditions, the following relations between the real charge q and the image charges q' and q'' [Jac99] can be derived:

$$q' = -\frac{\epsilon_s - \epsilon_m}{\epsilon_s + \epsilon_m}q, \quad q'' = \frac{2\epsilon_s}{\epsilon_s + \epsilon_m}q. \quad (\text{B.3})$$

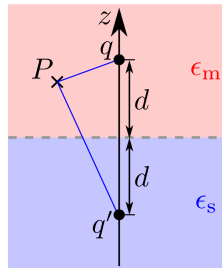


Figure B.1: Visualization of the dielectric properties at a hybrid interface between two materials with different dielectric constants (ϵ_m in the molecular layer and ϵ_s in the semiconductor substrate). A charge q within the molecular layer induces an image charge q' located in mirror symmetry to the real charge q . P denotes an arbitrary point within the molecular half space.

The Green's function $G^{\text{m-m}}(\mathbf{r}, \mathbf{r}')$ for the Coulomb interaction between two charges at \mathbf{r} and \mathbf{r}' within the molecular layer in the presence of the dielectric semiconductor substrate is given by [Jac99]

$$G^{\text{m-m}}(\mathbf{r}, \mathbf{r}') = \frac{1}{4\pi\epsilon_0\epsilon_m} \frac{1}{|\mathbf{r} - \mathbf{r}'|} - \frac{1}{4\pi\epsilon_0\epsilon_{\text{eff}}^{\text{m-m}}} \frac{1}{\sqrt{(x-x')^2 + (y-y')^2 + (z+z')^2}} \quad (\text{B.4})$$

with the effective dielectric constant

$$\epsilon_{\text{eff}}^{\text{m-m}} \equiv \epsilon_m \frac{\epsilon_s + \epsilon_m}{\epsilon_s - \epsilon_m} = \epsilon_m \frac{\frac{\epsilon_s}{\epsilon_m} + 1}{\frac{\epsilon_s}{\epsilon_m} - 1}. \quad (\text{B.5})$$

Equivalently, the Green's function $G^{\text{m-s}}(\mathbf{r}, \mathbf{r}')$ for an interaction between one charge at the organic and the other at the inorganic site takes the form [Jac99]

$$G^{\text{m-s}}(\mathbf{r}, \mathbf{r}') = \frac{1}{4\pi\epsilon_0\epsilon_s} \frac{\frac{2\epsilon_s}{\epsilon_s + \epsilon_m}}{|\mathbf{r} - \mathbf{r}'|} = \frac{1}{4\pi\epsilon_0\epsilon_{\text{eff}}^{\text{m-s}}} \frac{1}{|\mathbf{r} - \mathbf{r}'|}, \quad (\text{B.6})$$

where the effective dielectric constant $\epsilon_{\text{eff}}^{\text{m-s}}$ is the average of the intrinsic permittivities of the two constituents:

$$\epsilon_{\text{eff}}^{\text{m-s}} \equiv \frac{1}{2}(\epsilon_s + \epsilon_m). \quad (\text{B.7})$$

This way, the dielectric screening in the composite system is taken into account by introducing effective dielectric constants $\epsilon_{\text{eff}}^{\text{m-m}}$ for the intermolecular and $\epsilon_{\text{eff}}^{\text{m-s}}$ for the interlayer Coulomb matrix elements.

B.2 Quaternions

The concept of quaternions was introduced by Sir William Rowan Hamilton in 1843 as a four-dimensional extension of the complex numbers. Today, they are mainly used for simplifying the spacetime description and in computer graphics, since it is possible to express the rotation of a vector in three-dimensional vector space by a normalized quaternion in a numerically efficient and elegant way [Kui02]. The orthogonal basis of the quaternion vector space contains four elements: $1, i, j, k$. An arbitrary quaternion then has the form

$$q = s + ix + jy + kz \quad \text{or} \quad q = \left[s, \begin{pmatrix} x \\ y \\ z \end{pmatrix} \right] = [s, \mathbf{v}], \quad (\text{B.8})$$

where the latter notation reveals that quaternions are composed of a scalar (s) and a three-dimensional vector part (\mathbf{v}). As for complex numbers, the squares of the imaginary parts are -1 :

$$i^2 = j^2 = k^2 = ijk = -1. \quad (\text{B.9})$$

The addition of two quaternions is defined as:

$$q + q' = [s + s', \mathbf{v} + \mathbf{v}']. \quad (\text{B.10})$$

The multiplication is defined as:

$$qq' = [ss' - \mathbf{v} \cdot \mathbf{v}', \mathbf{v} \times \mathbf{v}' + s\mathbf{v} + s'\mathbf{v}']. \quad (\text{B.11})$$

It is not commutative: $ij = k$, $jk = i$, $ki = j$, $ji = -ij = -k$. The conjugate of a quaternion is given by

$$q^* = s - ix - jy - kz = [s, -\mathbf{v}] \quad (\text{B.12})$$

The norm is calculated as

$$\|q\| = \sqrt{qq^*} = \sqrt{q^*q} = \sqrt{s^2 + x^2 + y^2 + z^2} \quad (\text{B.13})$$

and the inverse is defined as:

$$q^{-1} = \frac{q^*}{\|q\|^2}. \quad (\text{B.14})$$

The inverse and conjugate are identical for unit quaternions with $\|q\| = 1$.

In order to describe rotations, one defines a quaternion of rotation:

$$q_R = \left[\cos\left(\frac{\theta}{2}\right), \sin\left(\frac{\theta}{2}\right) \mathbf{r} \right], \quad (\text{B.15})$$

where \mathbf{r} is the normalized axis of rotation and θ the angle of rotation. The point \mathbf{p} whose rotated coordinates are to be determined is transformed into a quaternion like $p = [0, \mathbf{p}]$. Finally, the rotated point \mathbf{p}' is obtained from the transformed quaternion p' with

$$p' = [c, \mathbf{p}'] = q_R p q_R^{-1} = q_R p q_R^*. \quad (\text{B.16})$$

There are three main reasons why expressing three-dimensional rotations as unit quaternions instead of matrices is more convenient:

1. Concatenating rotations is computationally faster and numerically more stable.
2. The use of quaternions allows for a direct rotation around the desired rotation axis and angle (without transformation to Euler angles).
3. Quaternions do not suffer from gimbal lock as Euler angles do (i.e., losing one degree of freedom due to the coincidence of two rotation axes).

B.3 Transformation to momentum representation

Introducing Bloch basis operators for the molecular electrons (given in Eq. (7.31)), the Hamilton operator of the hybrid system can be rewritten into a consistent momentum representation for both the inorganic and organic component. The free electron part transforms as

$$\begin{aligned} \hat{H}_0^m &= \sum_{A,\nu} \varepsilon_A \hat{a}_{A,\nu}^\dagger \hat{a}_{A,\nu} = \sum_A \varepsilon_A \sum_{\mathbf{l},\mathbf{l}'} \frac{1}{N_m} \sum_{\nu} \underbrace{e^{i(\mathbf{l}-\mathbf{l}') \cdot \mathbf{R}_{\nu}}}_{\approx \sum_{\mathbf{G}_m} \delta_{\mathbf{l}-\mathbf{l}', \mathbf{G}_m} = \delta_{\mathbf{l},\mathbf{l}'}} \hat{a}_{A,\mathbf{l}}^\dagger \hat{a}_{A,\mathbf{l}'} = \sum_A \varepsilon_A \sum_{\mathbf{l}} \hat{a}_{A,\mathbf{l}}^\dagger \hat{a}_{A,\mathbf{l}}. \end{aligned} \quad (\text{B.17})$$

For evaluating the Kronecker delta, it was used that the molecular wave vectors \mathbf{l} and \mathbf{l}' are restricted to the first Brillouin zone (BZ), such that the difference of two arbitrary molecular wave vectors $\mathbf{l} - \mathbf{l}'$ will never equal a reciprocal lattice vector, as illustrated in Fig. B.2.

Next, the intermolecular Coulomb Hamiltonian given in Eq. (7.8) is transformed into momentum representation:

$$\begin{aligned} \hat{H}_C^{\text{m-m}} &= \frac{1}{2} \sum_{A,B} \sum_{\nu_a \neq \nu_b} \frac{1}{N_m^2} \sum_{\substack{\mathbf{l}_1, \mathbf{l}_2, \\ \mathbf{l}_3, \mathbf{l}_4}} e^{i(\mathbf{l}_1 - \mathbf{l}_4) \cdot \mathbf{R}_{\nu_a}} e^{i(\mathbf{l}_2 - \mathbf{l}_3) \cdot \mathbf{R}_{\nu_b}} V_{A,\nu_a}^{A,\nu_a} V_{B,\nu_b}^{B,\nu_b} \hat{a}_{A,\mathbf{l}_1}^\dagger \hat{a}_{B,\mathbf{l}_2}^\dagger \hat{a}_{B,\mathbf{l}_3} \hat{a}_{A,\mathbf{l}_4} \\ &+ \sum_{\nu_a \neq \nu_b} \frac{1}{N_m^2} \sum_{\substack{\mathbf{l}_1, \mathbf{l}_2, \\ \mathbf{l}_3, \mathbf{l}_4}} e^{i(\mathbf{l}_1 - \mathbf{l}_4) \cdot \mathbf{R}_{\nu_a}} e^{i(\mathbf{l}_2 - \mathbf{l}_3) \cdot \mathbf{R}_{\nu_b}} V_{L,\nu_a}^{H,\nu_a} V_{H,\nu_b}^{L,\nu_b} \hat{a}_{H,\mathbf{l}_1}^\dagger \hat{a}_{L,\mathbf{l}_2}^\dagger \hat{a}_{H,\mathbf{l}_3} \hat{a}_{L,\mathbf{l}_4}. \end{aligned} \quad (\text{B.18})$$

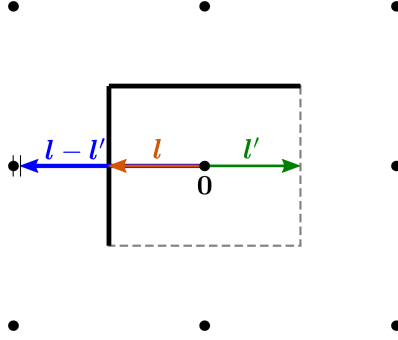


Figure B.2: Graphical illustration of the relation $\sum_{\mathbf{G}_m} \delta_{\mathbf{l}-\mathbf{l}', \mathbf{G}_m} = \delta_{\mathbf{l}, \mathbf{l}'}$ for two arbitrary lattice vectors \mathbf{l} and \mathbf{l}' that are restricted to the first BZ. The 2D reciprocal lattice shown in the figure is arbitrarily chosen to be rectangular. The rectangle marks the first BZ around the central reciprocal lattice point at $\mathbf{l} = \mathbf{0}$. Due to the periodicity condition, not all boundaries are included: The boundaries included in the first BZ are marked by thick, solid lines, whereas the boundaries represented by dashed lines are not included. Here, the extreme case of \mathbf{l} and \mathbf{l}' pointing in opposite directions and reaching the boundaries of the first BZ is depicted. Still, the vector sum $\mathbf{l} - \mathbf{l}'$ will not equal a reciprocal lattice vector \mathbf{G}_m connecting two reciprocal lattice points, since the right-hand boundary towards which \mathbf{l}' is pointing is not included.

The coupling elements in partial charge approximation derived in Eq. (7.17) are inserted and the Kronecker delta condition given in Eq. (7.32) is used to eliminate the sum over ν_a :

$$\begin{aligned} \hat{H}_C^{\mathbf{m}-\mathbf{m}} &\approx \frac{1}{N_m} \sum_{\substack{l_1, l_2, \\ l_3, l_4}} \sum_{\Delta_{\mathbf{m}-\mathbf{m}} \neq \mathbf{0}} \underbrace{\frac{1}{N_m} \sum_{\nu} e^{i(l_1 - l_4 + l_2 - l_3) \cdot \mathbf{R}_{\nu}} e^{i(l_2 - l_3) \cdot \Delta_{\mathbf{m}-\mathbf{m}}}}_{=\sum_{\mathbf{G}_m} \delta_{l_1 - l_4 + l_2 - l_3, \mathbf{G}_m}} \sum_{I, J} G^{\mathbf{m}-\mathbf{m}}(\mathbf{r}_I, \mathbf{r}_J + \Delta_{\mathbf{m}-\mathbf{m}}) \\ &\times \left(\frac{1}{2} \sum_{A, B} q_I^{AA} q_J^{BB} \hat{a}_{A, l_1}^{\dagger} \hat{a}_{B, l_2}^{\dagger} \hat{a}_{B, l_3} \hat{a}_{A, l_4} + q_I^{\text{HL}} q_J^{\text{LH}} \hat{a}_{\text{H}, l_1}^{\dagger} \hat{a}_{\text{L}, l_2}^{\dagger} \hat{a}_{\text{H}, l_3} \hat{a}_{\text{L}, l_4} \right). \end{aligned} \quad (\text{B.19})$$

Here, the substitutions $\mathbf{R}_{\nu} \equiv \mathbf{R}_{\nu_a}$ and $\Delta_{\mathbf{m}-\mathbf{m}} \equiv \mathbf{R}_{\nu_b} - \mathbf{R}_{\nu_a}$ were undertaken, and the sum over ν_b was transformed into a sum over all relative molecular positions $\Delta_{\mathbf{m}-\mathbf{m}}$ with respect to the position of molecule ν_a . This is allowed since all possible reference points $\mathbf{R}_{\nu} \equiv \mathbf{R}_{\nu_a}$ are summed up as well, such that $\Delta_{\mathbf{m}-\mathbf{m}}$ is independent of the reference point for a sufficiently extended molecular layer with translational invariance. Again, the molecular wave vectors \mathbf{l}_i are restricted to the first BZ. In contrast to Eq. (7.33), this time the vector sum $\mathbf{l}_1 - \mathbf{l}_4 + \mathbf{l}_2 - \mathbf{l}_3$ consists of four vectors, which can indeed add up to a reciprocal lattice vector. However, the sum over the reciprocal lattice vectors is restricted to vectors $\mathbf{G}_m \equiv m_1 \tilde{\mathbf{b}}_1 + m_2 \tilde{\mathbf{b}}_2$ with $m_1, m_2 \in \{0, \pm 1\}$, since only the nearest neighbored reciprocal lattice points are reached starting from the center of the first BZ (cf. Fig. B.2).

The molecule-semiconductor Hamiltonian transforms in an analogous way:

$$\begin{aligned} \hat{H}_C^{\mathbf{m}-\mathbf{s}} &= \sum_{\lambda, \mathbf{k}, \mathbf{k}'} \sum_{A, \nu} \frac{1}{N_m} \sum_{l, l'} e^{i(\mathbf{l}-\mathbf{l}') \cdot \mathbf{R}_{\nu}} V_{\lambda, \mathbf{k}'}^{\lambda, \mathbf{k}, A, \nu} \hat{a}_{\lambda, \mathbf{k}}^{\dagger} \hat{a}_{A, l}^{\dagger} \hat{a}_{A, l'} \hat{a}_{\lambda, \mathbf{k}'} \\ &+ \sum_{\mathbf{k}, \mathbf{k}'} \sum_{\nu} \frac{1}{N_m} \sum_{l, l'} e^{i(\mathbf{l}-\mathbf{l}') \cdot \mathbf{R}_{\nu}} \left(V_{\nu, \mathbf{k}'}^{\mathbf{c}, \mathbf{k}, \text{H}, \nu} \hat{a}_{\mathbf{c}, \mathbf{k}}^{\dagger} \hat{a}_{\text{H}, l}^{\dagger} \hat{a}_{\text{L}, l'} \hat{a}_{\nu, \mathbf{k}'} + V_{\mathbf{c}, \mathbf{k}'}^{\nu, \mathbf{k}, \text{L}, \nu} \hat{a}_{\nu, \mathbf{k}}^{\dagger} \hat{a}_{\text{L}, l}^{\dagger} \hat{a}_{\text{H}, l'} \hat{a}_{\mathbf{c}, \mathbf{k}'} \right) \end{aligned} \quad (\text{B.20})$$

Again, the coupling elements are expressed using the partial charge technique:

$$\begin{aligned}
\hat{H}_C^{m-s} &\approx \sum_{\mathbf{k}, \mathbf{k}'} \sum_{l, l'} \sum_{\Delta_{m-s}} \frac{1}{N_m} \sum_{\nu} \underbrace{e^{i(l-l'+\mathbf{k}'-\mathbf{k}) \cdot \mathbf{R}_{\nu}} e^{i(\mathbf{k}'-\mathbf{k}) \cdot \Delta_{m-s}}}_{=\sum_{\mathbf{G}_m} \delta_{l-l'+\mathbf{k}'-\mathbf{k}, \mathbf{G}_m}} \sum_{I, J} G^{m-s}(\mathbf{r}_I + \Delta_{m-s}, \mathbf{r}_J) \\
&\times \left(\sum_{\lambda} \sum_A q_I^{\lambda \lambda'} q_J^{AB} \hat{a}_{\lambda, \mathbf{k}}^{\dagger} \hat{a}_{A, l}^{\dagger} \hat{a}_{A, l'} \hat{a}_{\lambda, \mathbf{k}'} + q_I^{\text{cv}} q_J^{\text{HL}} \hat{a}_{c, \mathbf{k}}^{\dagger} \hat{a}_{H, l}^{\dagger} \hat{a}_{L, l'} \hat{a}_{v, \mathbf{k}'} \right. \\
&\left. + q_I^{\text{vc}} q_J^{\text{LH}} \hat{a}_{v, \mathbf{k}}^{\dagger} \hat{a}_{L, l}^{\dagger} \hat{a}_{H, l'} \hat{a}_{c, \mathbf{k}'} \right), \tag{B.21}
\end{aligned}$$

where $\Delta_{m-s} \equiv \mathbf{R}_i - \mathbf{R}_{\nu}$ was substituted.

B.4 Discrete Fourier transform

To calculate the transfer rate of Eq. (7.75), the interlayer Förster coupling element

$$\mathcal{V}_{\text{v L}}^{\text{c H}}(\mathbf{q}) = \frac{1}{4\pi\epsilon_0\epsilon_{\text{eff}}^{m-s}} \sum_{\Delta_{m-s}} e^{i\mathbf{q} \cdot \Delta_{m-s}} \sum_{I, J} \frac{q_I^{\text{cv}} q_J^{\text{HL}}}{|\mathbf{r}_J - \mathbf{r}_I - \Delta_{m-s}|}. \tag{B.22}$$

has to be evaluated for a very large number of momentum transfer vectors \mathbf{q} .

Note that the sum over the three-dimensional vector Δ_{m-s} only runs over two dimensions (x and y), since both the semiconductor and the molecular component are composed of a single layer of unit cells (UCs). Thus, all vectors Δ_{m-s} have the same (constant) z component Δ_{m-sz} defined by the interlayer separation. Without loss of generality, the x and y coordinates of the “central” UCs of both the semiconductor substrate and the molecular adlayer are chosen to be identical, such that $\Delta_{m-sx} = \Delta_{m-sy} = 0$ for the two central cells. As a result, the in-plane component $\Delta_{m-s\parallel}$ is a linear combination of integer multiples of the 2D semiconductor lattice vectors \mathbf{a}_1 and \mathbf{a}_2 : $\Delta_{m-s\parallel} = k\mathbf{a}_1 + l\mathbf{a}_2$ with integers $k, l \in \mathbb{Z}$. Here, the substrate UCs are chosen in a way that the lattice vectors coincide with the Cartesian coordinate directions: $\mathbf{a}_1 = a_1\mathbf{e}_x$, $\mathbf{a}_2 = a_2\mathbf{e}_y$. However, this is not a necessary precondition for the following deductions.

The 2D sum over Δ_{m-s} has to be evaluated in a region around 0 where the coupling elements have sufficiently dropped at the borders (which is checked using a convergence test in the program). Let this rectangular “interesting” region have the size $M\mathbf{a}_1$ in x direction and $N\mathbf{a}_2$ in y direction (cf. Fig. B.3). With that, Eq. (B.22) can be rewritten to

$$\mathcal{V}_{\text{v L}}^{\text{c H}}(\mathbf{q}) = \frac{1}{4\pi\epsilon_0\epsilon_{\text{eff}}^{m-s}} \sum_{k=-\frac{M}{2}}^{\frac{M}{2}-1} \sum_{l=-\frac{N}{2}}^{\frac{N}{2}-1} e^{i(q_x k a_1 + q_y l a_2)} \sum_{I, J} \frac{q_I^{\text{cv}} q_J^{\text{HL}}}{\left| \mathbf{r}_J - \mathbf{r}_I - \begin{pmatrix} k\mathbf{a}_1 \\ l\mathbf{a}_2 \\ \Delta_{m-sz} \end{pmatrix} \right|}. \tag{B.23}$$

This expression resembles a two-dimensional discrete Fourier transform (2D-DFT), which can be exploited for an efficient numerical calculation. To implement this numerically, the FFTW library is used [FFTW]. The forward 2D-DFT of a 2D complex array X of size $m \times n$ computes an array Y of the same size with

$$Y_{kl} = \sum_{m=0}^{M-1} \sum_{n=0}^{N-1} X_{mn} e^{-2\pi i \frac{mk}{M}} e^{-2\pi i \frac{nl}{N}} \quad \text{for } k = 0, \dots, M-1 \text{ and } l = 0, \dots, N-1. \tag{B.24}$$

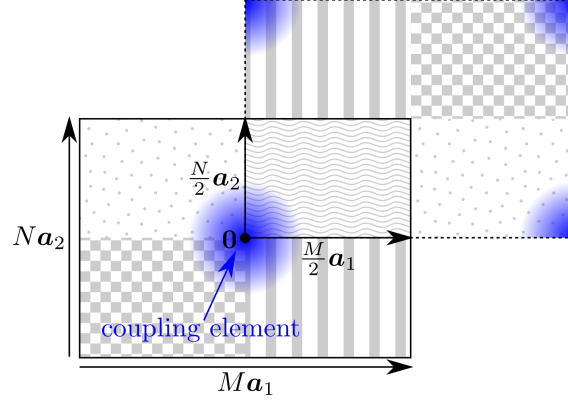


Figure B.3: Graphical illustration of the interesting region around the $\mathbf{0}$ -coordinate of $\Delta_{m-s||}$ where the Fourier coefficients of the Coulomb coupling element (marked as filled blue, fading circle) are calculated. Since the numerical computation of a discrete Fourier transform can only handle summations over positive integers, the region has to be shifted to positive values (see dashed rectangle) and the matrix element has to be continued periodically.

The backward **2D-DFT** computes:¹

$$X_{mn} = \sum_{m=0}^{M-1} \sum_{n=0}^{N-1} Y_{kl} e^{2\pi i \frac{mk}{M}} e^{2\pi i \frac{nl}{N}} \quad \text{for } m = 0, \dots, M-1 \text{ and } n = 0, \dots, N-1. \quad (\text{B.25})$$

Here we see that the sums computed numerically using the FFTW library run over positive integers, whereas the summation in Eq. (B.23) is symmetric around $\mathbf{0}$. Therefore, the summation region must be shifted to positive values and the matrix element has to be continued periodically, which is depicted in Fig. B.3. Therefore the Fourier coefficients are defined as a piecewise function:

$$Y_{kl} = \frac{1}{4\pi\epsilon_0 \epsilon_{\text{eff}}^{m-s}} \times \begin{cases} \sum_{I,J} \frac{q_I^{\text{cv}} q_J^{\text{HL}}}{\left| r_J - r_I - \begin{pmatrix} k \mathbf{a}_1 \\ l \mathbf{a}_2 \\ \Delta_{m-sz} \end{pmatrix} \right|} & \text{for } k = 0, \dots, \frac{M}{2} - 1, l = 0, \dots, \frac{N}{2} - 1 \text{ (I)} \\ \sum_{I,J} \frac{q_I^{\text{cv}} q_J^{\text{HL}}}{\left| r_J - r_I - \begin{pmatrix} k \mathbf{a}_1 \\ (l - N) \mathbf{a}_2 \\ \Delta_{m-sz} \end{pmatrix} \right|} & \text{for } k = 0, \dots, \frac{M}{2} - 1, l = \frac{N}{2}, \dots, N - 1 \text{ (II)} \\ \sum_{I,J} \frac{q_I^{\text{cv}} q_J^{\text{HL}}}{\left| r_J - r_I - \begin{pmatrix} (k - M) \mathbf{a}_1 \\ l \mathbf{a}_2 \\ \Delta_{m-sz} \end{pmatrix} \right|} & \text{for } k = \frac{M}{2}, \dots, M - 1, l = 0, \dots, \frac{N}{2} - 1 \text{ (III)} \\ \sum_{I,J} \frac{q_I^{\text{cv}} q_J^{\text{HL}}}{\left| r_J - r_I - \begin{pmatrix} (k - M) \mathbf{a}_1 \\ (l - N) \mathbf{a}_2 \\ \Delta_{m-sz} \end{pmatrix} \right|} & \text{for } k = \frac{M}{2}, \dots, M - 1, l = \frac{N}{2}, \dots, N - 1 \text{ (IV)} \end{cases} \quad (\text{B.26})$$

¹ Note that this transform is not normalized. For a proper normalization, the backward transform would have to be multiplied by a factor $\frac{1}{NM}$.

Here, (I) denotes the wavy region, (II) the stripy region, (III) the dotted region, and (IV) the checkered region of Fig. B.3. By setting up an input array with these Fourier coefficients and applying a backward **2D-DFT** using the FFTW library, an output array consisting of the following entries is obtained:

$$X_{mn} = \frac{1}{4\pi\epsilon_0\epsilon_{\text{eff}}^{m-s}} \sum_{k=-\frac{M}{2}}^{\frac{M}{2}-1} \sum_{l=-\frac{N}{2}}^{\frac{N}{2}-1} e^{2\pi i \frac{mk}{M}} e^{2\pi i \frac{nl}{N}} \sum_{I,J} \frac{q_I^{\text{cv}} q_J^{\text{HL}}}{\left| \mathbf{r}_J - \mathbf{r}_I - \begin{pmatrix} k\mathbf{a}_1 \\ l\mathbf{a}_2 \\ \Delta_{m-sz} \end{pmatrix} \right|}, \quad (\text{B.27})$$

where the summation indices have been transformed. A comparison with the Coulomb coupling element of Eq. (B.23) provides the discrete representation of the momentum transfer vector \mathbf{q} (momentum space coordinate):

$$q_x(m) = \frac{2\pi}{a_1} \frac{m}{M} \quad \text{and} \quad q_y(n) = \frac{2\pi}{a_2} \frac{n}{N}. \quad (\text{B.28})$$

The discretization

$$\Delta q_x = q_x(m) - q_x(m-1) = \frac{2\pi}{Ma_1} \quad \text{and} \quad \Delta q_y = q_y(n) - q_y(n-1) = \frac{2\pi}{Na_2} \quad (\text{B.29})$$

is determined by the discretization of Δ_{m-s} in real space (which is given by the geometry \mathbf{a}_1 and \mathbf{a}_2 of the UCs) and the spatial extent of the “interesting region” defined by M and N (cf. Fig. B.3). This means, M and N must be chosen large enough that (i) the discretization of \mathbf{q} is sufficiently fine and (ii) the value of the Fourier coefficients of the coupling elements has sufficiently dropped at the borders of the interesting region.

Note that the output array covers all \mathbf{q} values within the first **BZ** of the semiconductor substrate. Its extension is given by $\frac{2\pi}{a_1}$ in x direction and $\frac{2\pi}{a_2}$ in y direction. In conclusion, by implementing a discrete Fourier transform, one obtains a **2D** array of interlayer Förster coupling elements $\mathcal{V}_{\text{v}}^{\text{c}} \mathcal{H}_{\text{L}}^{\text{H}}(\mathbf{q})$ covering discrete equidistant \mathbf{q} values within the first semiconductor **BZ**. The value for an arbitrary \mathbf{q} vector is then obtained by bilinear interpolation.

B.5 Derivation of the eigenproblem of the molecular excitons

B.5.1 Calculation of the matrix elements in the exciton basis

The matrix elements of the electronic Hamiltonian \hat{H}^{m} in the molecular layer are derived in the new basis. The free part is given by:

$$\langle \mathbf{l}_1, \mathbf{l}_2 | \hat{H}_0^{\text{m}} | \mathbf{l}_3, \mathbf{l}_4 \rangle = \delta_{\mathbf{l}_1, \mathbf{l}_3} \delta_{\mathbf{l}_2, \mathbf{l}_4} \left((N_{\text{m}} - 1) \varepsilon_{\text{H}} + \varepsilon_{\text{L}} \right). \quad (\text{B.30})$$

The matrix element of the Coulomb interaction within the molecular layer in terms of the new basis has the form:

$$\begin{aligned} \langle \mathbf{l}_1, \mathbf{l}_2 | \hat{H}_{\text{C}}^{\text{m-m}} | \mathbf{l}_3, \mathbf{l}_4 \rangle = & \delta_{\mathbf{l}_1, \mathbf{l}_3} \delta_{\mathbf{l}_2, \mathbf{l}_4} \left[\frac{1}{2} (N_{\text{m}} - 2) \mathcal{V}_{\text{H}}^{\text{H H}}(\mathbf{0}) - \frac{1}{2} \frac{1}{N_{\text{m}}} \sum_{\mathbf{l}, \mathbf{l}'} \mathcal{V}_{\text{H}}^{\text{H H}}(\mathbf{l} - \mathbf{l}') \right. \\ & + \frac{1}{N_{\text{m}}} \sum_{\mathbf{l}} \mathcal{V}_{\text{H}}^{\text{H H}}(\mathbf{l} - \mathbf{l}_2) + \mathcal{V}_{\text{H}}^{\text{H L}}(\mathbf{0}) - \frac{1}{N_{\text{m}}} \sum_{\mathbf{l}} \mathcal{V}_{\text{L}}^{\text{H L}}(\mathbf{l} - \mathbf{l}_1) \left. \right] \\ & + \frac{1}{N_{\text{m}}} \sum_{\mathbf{G}_{\text{m}}} \delta_{\mathbf{l}_1 - \mathbf{l}_3, \mathbf{l}_2 - \mathbf{l}_4 + \mathbf{G}_{\text{m}}} \left[\mathcal{V}_{\text{L}}^{\text{H L}}(\mathbf{l}_1 - \mathbf{l}_2) - \mathcal{V}_{\text{H}}^{\text{H L}}(\mathbf{l}_2 - \mathbf{l}_4) \right] \end{aligned} \quad (\text{B.31})$$

The eigenvalue problem of Eq. (7.42) takes the form:

$$\begin{aligned}
(E_0^m + E_\alpha^m) c_{\mathbf{l}+\mathbf{q},\mathbf{l}}^\alpha &= \langle \mathbf{l} + \mathbf{q}, \mathbf{l} | \hat{H}^m | X_\alpha^m \rangle \\
&= c_{\mathbf{l}+\mathbf{q},\mathbf{l}}^\alpha \left[E_0^m + \varepsilon_{\text{gap}}^m - \mathcal{V}_{\text{H H}}^{\text{H H}}(\mathbf{0}) + \frac{1}{N_m} \sum_{\mathbf{l}'} \mathcal{V}_{\text{H H}}^{\text{H H}}(\mathbf{l}' - \mathbf{l}) + \mathcal{V}_{\text{H L}}^{\text{H L}}(\mathbf{0}) \right. \\
&\quad \left. - \frac{1}{N_m} \sum_{\mathbf{l}'} \mathcal{V}_{\text{L H}}^{\text{L H}}(\mathbf{l}' - (\mathbf{l} + \mathbf{q})) \right] + \sum_{\mathbf{l}'} c_{\mathbf{l}'+\mathbf{q},\mathbf{l}'}^\alpha \frac{1}{N_m} \left[\mathcal{V}_{\text{L H}}^{\text{L H}}(\mathbf{q}) - \mathcal{V}_{\text{H L}}^{\text{H L}}(\mathbf{l} - \mathbf{l}') \right],
\end{aligned} \tag{B.32}$$

where $\varepsilon_{\text{gap}}^m \equiv \varepsilon_{\text{L}} - \varepsilon_{\text{H}}$ denotes the highest occupied molecular orbital (HOMO)-lowest unoccupied molecular orbital (LUMO) transition energy in the molecules.

After converting the molecular wave vector sums into integrals according to Eq. (7.43), it can be used that the Coulomb coupling element in momentum space is periodic with respect to the reciprocal lattice. When integrating over all possible orientations of molecular wave vectors \mathbf{l}' within the first BZ, the reference vector \mathbf{l} of the momentum transfer vector $\mathbf{l}' - \mathbf{l}$ is arbitrary (and can be chosen as zero), since the integration over a whole period (in this case: BZ) is invariant under an arbitrary translation of the periodic function:

$$\int_{\text{1st BZ}} d^2 l' \mathcal{V}_{A' B'}^A(\mathbf{l}' - \mathbf{l}) = \int_{\text{1st BZ}} d^2 l' \mathcal{V}_{A' B'}^A(\mathbf{l}'). \tag{B.33}$$

A formal proof for a periodic one-dimensional function $f(k) = f(k + G)$ can be easily shown:

$$\begin{aligned}
\int_0^G dk f(k - a) &= \int_{-a}^{G-a} dk' f(k') = \int_{-a}^0 dk' f(k') + \int_0^G dk' f(k') - \int_{G-a}^G dk' f(k') \\
&= \int_{G-a}^G dk'' \underbrace{f(k'' - G)}_{f(k'')} + \int_0^G dk' f(k') - \int_{G-a}^G dk' f(k') = \int_0^G dk f(k).
\end{aligned} \tag{B.34}$$

The resulting expression is given in Eq. (7.44) in the main part of this thesis.

B.5.2 Normalization of the molecular exciton states in the discrete basis

The eigenvector coefficients are normalized according to

$$\begin{aligned}
\langle X_{\mathbf{q}_j, n}^m | X_{\mathbf{q}_{j'}, n'}^m \rangle &= \frac{N_m^2}{N_d^{m^2}} \sum_{i=1}^{N_d^m} \sum_{k=1}^{N_d^m} c_{\mathbf{l}_i}^{\mathbf{q}_j, n^*} c_{\mathbf{l}_k}^{\mathbf{q}_{j'}, n'} \underbrace{\langle \mathbf{l}_i + \mathbf{q}_j, \mathbf{l}_i | \mathbf{l}_k + \mathbf{q}_{j'}, \mathbf{l}_k \rangle}_{= \frac{N_d^{m^2}}{N_m^2} \delta_{i,k} \delta_{j,j'}} = \sum_{i=1}^{N_d^m} c_{\mathbf{l}_i}^{\mathbf{q}_j, n^*} c_{\mathbf{l}_i}^{\mathbf{q}_{j'}, n'} \delta_{j,j'} \\
&\stackrel{!}{=} \frac{N_d^{m^2}}{N_m^2} \delta_{j,j'} \delta_{n,n'} \Rightarrow \sum_{i=1}^{N_d^m} |c_{\mathbf{l}_i}^{\mathbf{q}_j, n}|^2 = \frac{N_d^{m^2}}{N_m^2}.
\end{aligned} \tag{B.35}$$

An orthonormal basis of eigenvectors can be found, such that

$$\frac{N_d^2}{N_d^{m^2}} \sum_{j,n=1}^{N_d^m} |X_{\mathbf{q}_j, n}^m \rangle \langle X_{\mathbf{q}_j, n}^m| = 1. \tag{B.36}$$

This is used for deriving the representation of the two-particle basis in terms of the delocalized exciton basis. Therefore, the two-particle state $|\mathbf{l}_k + \mathbf{q}_l, \mathbf{l}_k\rangle$ is multiplied from the right-hand side to the complex conjugate of Eq. (7.49):

$$\langle X_{\mathbf{q}_j, n}^m | \mathbf{l}_k + \mathbf{q}_l, \mathbf{l}_k \rangle = \frac{N_m}{N_d^m} \sum_{i=1}^{N_d^m} c_{\mathbf{l}_i}^{\mathbf{q}_j, n*} \underbrace{\langle \mathbf{l}_i + \mathbf{q}_j, \mathbf{l}_i | \mathbf{l}_k + \mathbf{q}_l, \mathbf{l}_k \rangle}_{= \frac{N_d^{m2}}{N_m^2} \delta_{i, k} \delta_{j, l}} = \frac{N_d^m}{N_m} c_{\mathbf{l}_k}^{\mathbf{q}_l, n*} \delta_{j, l}. \quad (\text{B.37})$$

$\frac{N_d^2}{N_m^2} |X_{\mathbf{q}_j, n}^m\rangle$ is finally multiplied from the left-hand side, a sum over j and n on both sides of the equation is performed and the orthonormality condition of Eq. (B.36) is used:

$$|\mathbf{l}_k + \mathbf{q}_l, \mathbf{l}_k\rangle = \frac{N_m}{N_d^m} \sum_{j, n=1}^{N_d^m} c_{\mathbf{l}_k}^{\mathbf{q}_l, n*} \delta_{j, l} |X_{\mathbf{q}_j, n}^m\rangle = \frac{N_m}{N_d^m} \sum_{n=1}^{N_d^m} c_{\mathbf{l}_k}^{\mathbf{q}_l, n*} |X_{\mathbf{q}_l, n}^m\rangle. \quad (\text{B.38})$$

B.6 Derivation of the equations of motion for the hybrid system

B.6.1 Homogeneous exciton density of the molecular system

First, in order to solve the equation of motion (EOM) for the population of the molecular exciton state $|X_{\mathbf{q}_j, n}^m\rangle$, the molecule–semiconductor Hamiltonian in momentum representation given in Eq. (7.36) is applied to the local two-particle basis state $|\mathbf{l}_1, \mathbf{l}_2\rangle$:

$$\begin{aligned} \hat{H}_C^{\text{m-s}} |\mathbf{l}_1, \mathbf{l}_2\rangle &= (\hat{H}_{C, \text{diag}}^{\text{m-s}} + \hat{H}_{C, \text{F}}^{\text{m-s}}) |\mathbf{l}_1, \mathbf{l}_2\rangle \\ &= \frac{N_m}{N_{\text{uc}}} \sum_{\mathbf{k}, \mathbf{k}'} \sum_{\mathbf{G}_m} \delta_{\mathbf{k}' - \mathbf{k}, \mathbf{G}_m} (\mathcal{V}_{\text{v}, \text{H}}^{\text{v}}(\mathbf{k}' - \mathbf{k}) \hat{a}_{\text{v}, \mathbf{k}}^\dagger \hat{a}_{\text{v}, \mathbf{k}'} + \mathcal{V}_{\text{c}, \text{H}}^{\text{c}}(\mathbf{k}' - \mathbf{k}) \hat{a}_{\text{c}, \mathbf{k}}^\dagger \hat{a}_{\text{c}, \mathbf{k}'}) |\mathbf{l}_1, \mathbf{l}_2\rangle \\ &\quad - \frac{1}{N_{\text{uc}}} \sum_{\mathbf{k}, \mathbf{k}'} (\mathcal{V}_{\text{v}, \text{H}}^{\text{v}}(\mathbf{k}' - \mathbf{k}) \hat{a}_{\text{v}, \mathbf{k}}^\dagger \hat{a}_{\text{v}, \mathbf{k}'} + \mathcal{V}_{\text{c}, \text{H}}^{\text{c}}(\mathbf{k}' - \mathbf{k}) \hat{a}_{\text{c}, \mathbf{k}}^\dagger \hat{a}_{\text{c}, \mathbf{k}'}) |\mathbf{l}_1, \mathbf{l}_2 - \mathbf{k} + \mathbf{k}'\rangle \\ &\quad + \frac{1}{N_{\text{uc}}} \sum_{\mathbf{k}, \mathbf{k}'} (\mathcal{V}_{\text{v}, \text{L}}^{\text{v}}(\mathbf{k}' - \mathbf{k}) \hat{a}_{\text{v}, \mathbf{k}}^\dagger \hat{a}_{\text{v}, \mathbf{k}'} + \mathcal{V}_{\text{c}, \text{L}}^{\text{c}}(\mathbf{k}' - \mathbf{k}) \hat{a}_{\text{c}, \mathbf{k}}^\dagger \hat{a}_{\text{c}, \mathbf{k}'}) |\mathbf{l}_1 + \mathbf{k} - \mathbf{k}', \mathbf{l}_2\rangle \\ &\quad + \frac{1}{N_{\text{uc}}} \sum_{\mathbf{k}, \mathbf{k}'} \sum_{\mathbf{G}_m} \delta_{\mathbf{l}_1 - \mathbf{l}_2, \mathbf{k}' - \mathbf{k} + \mathbf{G}_m} \mathcal{V}_{\text{v}, \text{L}}^{\text{v}}(\mathbf{k}' - \mathbf{k}) \hat{a}_{\text{c}, \mathbf{k}}^\dagger \hat{a}_{\text{v}, \mathbf{k}'} |\phi_0^{\text{m}}\rangle \\ &\quad + \frac{1}{N_{\text{uc}}} \sum_{\mathbf{k}, \mathbf{k}'} \sum_{\substack{\mathbf{l}, \mathbf{l}' \\ \mathbf{l}' \neq \mathbf{l}_1 \\ \mathbf{l} \neq \mathbf{l}_2}} \sum_{\mathbf{G}_m} \delta_{\mathbf{l}' - \mathbf{l}, \mathbf{k}' - \mathbf{k} + \mathbf{G}_m} \mathcal{V}_{\text{v}, \text{L}}^{\text{c}}(\mathbf{k}' - \mathbf{k}) \hat{a}_{\text{v}, \mathbf{k}'}^\dagger \hat{a}_{\text{c}, \mathbf{k}} |\mathbf{l}', \mathbf{l}; \mathbf{l}_1, \mathbf{l}_2\rangle. \end{aligned} \quad (\text{B.39})$$

The last term describes Förster coupling to a doubly excited molecular state $|\mathbf{l}', \mathbf{l}; \mathbf{l}_1, \mathbf{l}_2\rangle \equiv \hat{a}_{\text{L}, \mathbf{l}'}^\dagger \hat{a}_{\text{H}, \mathbf{l}} \hat{a}_{\text{L}, \mathbf{l}_1}^\dagger \hat{a}_{\text{H}, \mathbf{l}_2} |\phi_0^{\text{m}}\rangle$. In the following, only single excitations in the molecular layer will be considered, neglecting coupling to doubly (and higher) excited molecular states. Based on the upper equation, the full system Hamiltonian is applied to the excitonic state $|X_{\mathbf{q}_j, n}^m\rangle$ of the molecule in the basis set of numerically discrete wave vectors $(\mathbf{l}_i, \mathbf{q}_j)$:

$$\hat{H} |X_{\mathbf{q}_j, n}^m\rangle = \left(E_0^{\text{m}} + E_{\mathbf{q}_j, n}^{\text{m}} + \sum_{\lambda, \mathbf{k}} \varepsilon_{\lambda, \mathbf{k}} \hat{a}_{\lambda, \mathbf{k}}^\dagger \hat{a}_{\lambda, \mathbf{k}} \right) |X_{\mathbf{q}_j, n}^m\rangle + \frac{N_m}{N_d^m} \sum_{i=1}^{N_d^m} c_{\mathbf{l}_i}^{\mathbf{q}_j, n} \hat{H}_C^{\text{m-s}} |\mathbf{l}_i + \mathbf{q}_j, \mathbf{l}_i\rangle, \quad (\text{B.40})$$

where the last term was derived in Eq. (B.39).

With that, the commutator entering the EOM of the homogeneous exciton density (cf. Eq. (7.56)) can be derived:

$$\begin{aligned}
\frac{\partial}{\partial t} \langle X_{\mathbf{q}_j, n}^m | \hat{\rho} | X_{\mathbf{q}_j, n}^m \rangle &= \frac{i}{\hbar} \frac{N_m}{N_d^m} \sum_{i=1}^{N_d^m} \frac{1}{N_{\text{uc}}} \sum_{\mathbf{k}, \mathbf{k}'} \left[(\mathcal{V}_{\text{v}}^{\text{H}}(\mathbf{k}' - \mathbf{k}) \hat{a}_{\text{v}, \mathbf{k}}^\dagger \hat{a}_{\text{v}, \mathbf{k}'} + \mathcal{V}_{\text{c}}^{\text{H}}(\mathbf{k}' - \mathbf{k}) \hat{a}_{\text{c}, \mathbf{k}}^\dagger \hat{a}_{\text{c}, \mathbf{k}'}) \right. \\
&\times (-c_{l_i}^{\mathbf{q}_j, n} \langle X_{\mathbf{q}_j, n}^m | \hat{\rho} | l_i + \mathbf{q}_j, l_i - \mathbf{k} + \mathbf{k}' \rangle + c_{l_i}^{\mathbf{q}_j, n*} \langle l_i + \mathbf{q}_j, l_i - \mathbf{k}' + \mathbf{k} | \hat{\rho} | X_{\mathbf{q}_j, n}^m \rangle) \\
&+ (\mathcal{V}_{\text{v}}^{\text{L}}(\mathbf{k}' - \mathbf{k}) \hat{a}_{\text{v}, \mathbf{k}}^\dagger \hat{a}_{\text{v}, \mathbf{k}'} + \mathcal{V}_{\text{c}}^{\text{L}}(\mathbf{k}' - \mathbf{k}) \hat{a}_{\text{c}, \mathbf{k}}^\dagger \hat{a}_{\text{c}, \mathbf{k}'}) \\
&\times (c_{l_i}^{\mathbf{q}_j, n} \langle X_{\mathbf{q}_j, n}^m | \hat{\rho} | l_i + \mathbf{q}_j + \mathbf{k} - \mathbf{k}', l_i \rangle - c_{l_i}^{\mathbf{q}_j, n*} \langle l_i + \mathbf{q}_j + \mathbf{k}' - \mathbf{k}, l_i | \hat{\rho} | X_{\mathbf{q}_j, n}^m \rangle) \left. \right] \\
&+ \frac{i}{\hbar} \frac{N_m}{N_d^m} \sum_{i=1}^{N_d^m} \frac{1}{N_{\text{uc}}} \sum_{\mathbf{k}, \mathbf{k}'} \sum_{\mathbf{G}_m} \delta_{\mathbf{q}_j, \mathbf{k}' - \mathbf{k} + \mathbf{G}_m} \\
&\times (c_{l_i}^{\mathbf{q}_j, n} \mathcal{V}_{\text{v}}^{\text{c}} \mathcal{V}_{\text{L}}^{\text{H}}(\mathbf{k}' - \mathbf{k}) \hat{a}_{\text{c}, \mathbf{k}}^\dagger \hat{a}_{\text{v}, \mathbf{k}'} \langle X_{\mathbf{q}_j, n}^m | \hat{\rho} | \phi_0^m \rangle - c_{l_i}^{\mathbf{q}_j, n*} \mathcal{V}_{\text{v}}^{\text{c}} \mathcal{V}_{\text{L}}^{\text{H}*}(\mathbf{k}' - \mathbf{k}) \hat{a}_{\text{v}, \mathbf{k}'}^\dagger \hat{a}_{\text{c}, \mathbf{k}} \langle \phi_0^m | \hat{\rho} | X_{\mathbf{q}_j, n}^m \rangle). \tag{B.41}
\end{aligned}$$

Finally, a trace over the semiconductor states is performed, leading to an EOM for the population $\rho_{\mathbf{q}_j, n}^m \equiv \text{tr}_s[\langle X_{\mathbf{q}_j, n}^m | \hat{\rho} | X_{\mathbf{q}_j, n}^m \rangle]$. To further evaluate the expression, it is used that

$$\text{tr}_s[\hat{a}_{\lambda, \mathbf{k}}^\dagger \hat{a}_{\lambda', \mathbf{k}'} \langle a^m | \hat{\rho} | b^m \rangle] = \langle \hat{a}_{\lambda, \mathbf{k}}^\dagger \hat{a}_{\lambda', \mathbf{k}'} \rangle \text{tr}[[b^m] \langle a^m | \hat{\rho}]]. \tag{B.42}$$

Assuming approximative spatial homogeneity, one can set

$$\langle \hat{a}_{\lambda, \mathbf{k}}^\dagger \hat{a}_{\lambda, \mathbf{k}'} \rangle \approx \delta_{\mathbf{k}, \mathbf{k}'} \langle \hat{a}_{\lambda, \mathbf{k}}^\dagger \hat{a}_{\lambda, \mathbf{k}} \rangle. \tag{B.43}$$

This dramatically simplifies the EOM for the population of the molecular system, since all monopole-monopole coupling terms cancel out in the commutator and only the Förster coupling part remains:

$$\frac{\partial}{\partial t} \rho_{\mathbf{q}_j, n}^m = -\frac{2}{\hbar} \frac{1}{N_{\text{uc}}} \sum_{\mathbf{k}, \mathbf{k}'} \sum_{\mathbf{G}_m} \delta_{\mathbf{q}_j, \mathbf{k}' - \mathbf{k} + \mathbf{G}_m} \text{Im} \left[\frac{N_m}{N_d^m} \sum_{i=1}^{N_d^m} c_{l_i}^{\mathbf{q}_j, n} \mathcal{V}_{\text{v}}^{\text{c}} \mathcal{V}_{\text{L}}^{\text{H}}(\mathbf{k}' - \mathbf{k}) \sigma_{\mathbf{q}_j, n}^{\mathbf{k}, \mathbf{k}'} \right] \tag{B.44}$$

with the assisted molecule–semiconductor coherence $\sigma_{\mathbf{q}_j, n}^{\mathbf{k}, \mathbf{k}'} \equiv \text{tr}_s[\hat{a}_{\text{c}, \mathbf{k}}^\dagger \hat{a}_{\text{v}, \mathbf{k}'} \langle X_{\mathbf{q}_j, n}^m | \hat{\rho} | \phi_0^m \rangle]$.

B.6.2 Molecule–semiconductor coherence

In order to derive an EOM for the assisted molecule–semiconductor coherence $\sigma_{\mathbf{q}_j, n}^{\mathbf{k}, \mathbf{k}'}$, it is used that

$$\text{tr}_s[\hat{a}_{\text{c}, \mathbf{k}}^\dagger \hat{a}_{\text{v}, \mathbf{k}'} \langle X_{\mathbf{q}_j, n}^m | \hat{\rho} | \phi_0^m \rangle] = \text{tr}[\hat{a}_{\text{c}, \mathbf{k}}^\dagger \hat{a}_{\text{v}, \mathbf{k}'} \hat{\rho} | \phi_0^m \rangle \langle X_{\mathbf{q}_j, n}^m |], \tag{B.45}$$

where $\text{tr}[\dots] = \text{tr}_s[\text{tr}_m[\dots]]$ denotes the full system trace. The temporal dynamics is again calculated using the von Neumann equation:

$$\frac{\partial}{\partial t} \sigma_{\mathbf{q}_j, n}^{\mathbf{k}, \mathbf{k}'} = \frac{i}{\hbar} \text{tr} \left[[\hat{H}, \hat{a}_{\text{c}, \mathbf{k}}^\dagger \hat{a}_{\text{v}, \mathbf{k}'} | \phi_0^m \rangle \langle X_{\mathbf{q}_j, n}^m |] - \hat{\rho} \right], \tag{B.46}$$

where the invariance of the trace under cyclic permutation of its arguments was used. First, the commutator entering the EOM Eq. (B.46) for the assisted molecule–semiconductor coherence

is calculated:

$$\begin{aligned}
& [\hat{H}, \hat{a}_{c,\mathbf{k}}^\dagger \hat{a}_{v,\mathbf{k}'} | \phi_0^m \rangle \langle X_{q_j,n}^m |]_- = (-E_{q_j,n}^m + \varepsilon_{c,\mathbf{k}} - \varepsilon_{v,\mathbf{k}'}) \hat{a}_{c,\mathbf{k}}^\dagger \hat{a}_{v,\mathbf{k}'} | \phi_0^m \rangle \langle X_{q_j,n}^m | \\
& - \frac{N_m}{N_{uc}} \sum_{\mathbf{k}''} \sum_{\mathbf{G}_m} (\delta_{\mathbf{k}'-\mathbf{k}'', \mathbf{G}_m} \mathcal{V}_v^v \mathcal{H}(\mathbf{k}'' - \mathbf{k}') \hat{a}_{c,\mathbf{k}}^\dagger \hat{a}_{v,\mathbf{k}''} \\
& - \delta_{\mathbf{k}''-\mathbf{k}, \mathbf{G}_m} \mathcal{V}_c^c \mathcal{H}(\mathbf{k} - \mathbf{k}'') \hat{a}_{c,\mathbf{k}''}^\dagger \hat{a}_{v,\mathbf{k}'} | \phi_0^m \rangle \langle X_{q_j,n}^m | \\
& + \frac{N_m}{N_d^m} \sum_{i=1}^{N_d^m} c_i^{q_j,n*} \frac{1}{N_{uc}} \sum_{\mathbf{k}_1, \mathbf{k}_2} \hat{a}_{c,\mathbf{k}}^\dagger \hat{a}_{v,\mathbf{k}'} \left[(\mathcal{V}_v^v \mathcal{H}(\mathbf{k}_2 - \mathbf{k}_1) \hat{a}_{v,\mathbf{k}_1}^\dagger \hat{a}_{v,\mathbf{k}_2} + \mathcal{V}_c^c \mathcal{H}(\mathbf{k}_2 - \mathbf{k}_1) \hat{a}_{c,\mathbf{k}_1}^\dagger \hat{a}_{c,\mathbf{k}_2}) \right. \\
& \quad \times | \phi_0^m \rangle \langle \mathbf{l}_i + \mathbf{q}_j, \mathbf{l}_i - \mathbf{k}_2 + \mathbf{k}_1 | \\
& \quad - (\mathcal{V}_v^v \mathcal{L}(\mathbf{k}_2 - \mathbf{k}_1) \hat{a}_{v,\mathbf{k}_1}^\dagger \hat{a}_{v,\mathbf{k}_2} + \mathcal{V}_c^c \mathcal{L}(\mathbf{k}_2 - \mathbf{k}_1) \hat{a}_{c,\mathbf{k}_1}^\dagger \hat{a}_{c,\mathbf{k}_2}) \\
& \quad \left. \times | \phi_0^m \rangle \langle \mathbf{l}_i + \mathbf{q}_j + \mathbf{k}_2 - \mathbf{k}_1, \mathbf{l}_i | \right] \\
& + \frac{1}{N_{uc}} \sum_{\mathbf{k}_1, \mathbf{k}_2} \sum_{\mathbf{G}_m} \frac{N_m^3}{N_d^m^3} \sum_{k,l,n'=1}^{N_d^m} c_k^{q_l,n'*} \delta_{\mathbf{q}_l, \mathbf{k}_2 - \mathbf{k}_1 + \mathbf{G}_m} \\
& \quad \times \mathcal{V}_v^c \mathcal{H}^*(\mathbf{k}_2 - \mathbf{k}_1) \hat{a}_{v,\mathbf{k}_2}^\dagger \hat{a}_{c,\mathbf{k}_1} \hat{a}_{c,\mathbf{k}}^\dagger \hat{a}_{v,\mathbf{k}'} | X_{q_l,n'}^m \rangle \langle X_{q_j,n}^m | \\
& - \frac{1}{N_{uc}} \sum_{\mathbf{k}_1, \mathbf{k}_2} \sum_{\mathbf{G}_m} \frac{N_m}{N_d^m} \sum_{i=1}^{N_d^m} c_i^{q_j,n*} \delta_{\mathbf{q}_j, \mathbf{k}_2 - \mathbf{k}_1 + \mathbf{G}_m} \mathcal{V}_v^c \mathcal{H}^*(\mathbf{k}_2 - \mathbf{k}_1) \hat{a}_{c,\mathbf{k}}^\dagger \hat{a}_{v,\mathbf{k}'} \hat{a}_{v,\mathbf{k}_2}^\dagger \hat{a}_{c,\mathbf{k}_1} | \phi_0^m \rangle \langle \phi_0^m |.
\end{aligned} \tag{B.47}$$

Note that again, terms including a doubly excited molecular system have been excluded. Next step is to rearrange the quantum well (QW) operators into normal order and evaluate the trace over the commutator and the density operator in Eq. (B.46). Terms containing more than two QW operators are rewritten using Eq. (B.42). All other terms are transformed using Eq. (B.45). A Hartree-Fock factorization (cf. Sec. 2.3) is applied to expectation values of four electronic operators. Moreover, spatial homogeneity is assumed according to Eq. (B.43). The system is assumed to be in the thermodynamic quasi-equilibrium, such that the carrier populations in the respective bands are given by Fermi distribution functions $f_{e/h,\mathbf{k}}$ for the electrons (e) and holes (h) [Hau04, But04, Cho12]:

$$\rho_{v,\mathbf{k}} \equiv \langle \hat{a}_{v,\mathbf{k}}^\dagger \hat{a}_{v,\mathbf{k}} \rangle = f_{v,\mathbf{k}} = 1 - f_{h,\mathbf{k}} \quad \text{and} \quad \rho_{c,\mathbf{k}} \equiv \langle \hat{a}_{c,\mathbf{k}}^\dagger \hat{a}_{c,\mathbf{k}} \rangle = f_{c,\mathbf{k}} = f_{e,\mathbf{k}}. \tag{B.48}$$

Only \mathbf{k} states close to the Γ point are occupied, such that the sum of two \mathbf{k} vectors cannot equal a molecular reciprocal lattice vector (no Umklapp processes): $\delta_{\mathbf{k}-\mathbf{k}', \mathbf{G}_m} = \delta_{\mathbf{k},\mathbf{k}'} \delta_{\mathbf{G}_m, \mathbf{0}}$.

In order to set up a closed system of equations, only homogeneous densities of the molecular system are considered, i.e., the diagonal density matrix elements $\rho_{q_j,n}^m \equiv \text{tr}_s[\langle X_{q_j,n}^m | \hat{\rho} | X_{q_j,n}^m \rangle]$, neglecting fast decaying coherences:

$$\frac{N_m^2}{N_d^m^2} \text{tr}_s[\langle X_{q_j,n}^m | \hat{\rho} | X_{q_l,n'}^m \rangle] \approx \delta_{j,l} \delta_{n,n'} \rho_{q_j,n}^m. \tag{B.49}$$

Also, the electronic semiconductor coherences $\langle \hat{a}_{v,\mathbf{k}}^\dagger \hat{a}_{c,\mathbf{k}'} \rangle$ are assumed to decay rapidly, such that products of two coherences vanish: $\langle \hat{a}_{v,\mathbf{k}_2}^\dagger \hat{a}_{c,\mathbf{k}_1} \rangle \langle \hat{a}_{c,\mathbf{k}}^\dagger \hat{a}_{v,\mathbf{k}'} \rangle \approx 0$.

This leads to the **EOM** for the assisted molecule–semiconductor coherence:

$$\begin{aligned}
\frac{\partial}{\partial t} \sigma_{\mathbf{q}_j, n}^{\mathbf{k}, \mathbf{k}'} &= \frac{i}{\hbar} (-E_{\mathbf{q}_j, n}^m + \varepsilon_{c, \mathbf{k}} - \varepsilon_{v, \mathbf{k}'} + \mathcal{V}_{\text{mono}}^{\text{m-s}}) \sigma_{\mathbf{q}_j, n}^{\mathbf{k}, \mathbf{k}'} \\
&+ \frac{i}{\hbar} \frac{N_m}{N_d^m} \sum_{i=1}^{N_d^m} c_{l_i}^{\mathbf{q}_j, n*} \frac{1}{N_{\text{uc}}} \sum_{\mathbf{k}''} \left(f_{h, \mathbf{k}'} \mathcal{V}_v^{\text{H}}(\mathbf{k}'' - \mathbf{k}') \text{tr}_s [\hat{a}_{c, \mathbf{k}}^\dagger \hat{a}_{v, \mathbf{k}''} \langle l_i + \mathbf{q}_j, l_i - \mathbf{k}'' + \mathbf{k}' | \hat{\rho} | \phi_0^m \rangle] \right. \\
&\quad - f_{h, \mathbf{k}'} \mathcal{V}_v^{\text{L}}(\mathbf{k}'' - \mathbf{k}') \text{tr}_s [\hat{a}_{c, \mathbf{k}}^\dagger \hat{a}_{v, \mathbf{k}''} \langle l_i + \mathbf{q}_j + \mathbf{k}'' - \mathbf{k}', l_i | \hat{\rho} | \phi_0^m \rangle] \\
&\quad - f_{e, \mathbf{k}} \mathcal{V}_c^{\text{H}}(\mathbf{k} - \mathbf{k}'') \text{tr}_s [\hat{a}_{c, \mathbf{k}''}^\dagger \hat{a}_{v, \mathbf{k}'} \langle l_i + \mathbf{q}_j, l_i - \mathbf{k} + \mathbf{k}'' | \hat{\rho} | \phi_0^m \rangle] \\
&\quad \left. + f_{e, \mathbf{k}} \mathcal{V}_c^{\text{L}}(\mathbf{k} - \mathbf{k}'') \text{tr}_s [\hat{a}_{c, \mathbf{k}''}^\dagger \hat{a}_{v, \mathbf{k}'} \langle l_i + \mathbf{q}_j + \mathbf{k} - \mathbf{k}'', l_i | \hat{\rho} | \phi_0^m \rangle] \right) \\
&+ \frac{i}{\hbar} (1 - f_{h, \mathbf{k}'}) (1 - f_{e, \mathbf{k}}) \frac{1}{N_{\text{uc}}} \sum_{\mathbf{G}_m} \frac{N_m}{N_d^m} \sum_{i=1}^{N_d^m} c_{l_i}^{\mathbf{q}_j, n*} \delta_{\mathbf{q}_j, \mathbf{k}' - \mathbf{k} + \mathbf{G}_m} \mathcal{V}_v^{\text{H}*}(\mathbf{k}' - \mathbf{k}) \rho_{\mathbf{q}_j, n}^m \\
&- \frac{i}{\hbar} f_{h, \mathbf{k}'} f_{e, \mathbf{k}} \frac{1}{N_{\text{uc}}} \sum_{\mathbf{G}_m} \frac{N_m}{N_d^m} \sum_{i=1}^{N_d^m} c_{l_i}^{\mathbf{q}_j, n*} \delta_{\mathbf{q}_j, \mathbf{k}' - \mathbf{k} + \mathbf{G}_m} \mathcal{V}_v^{\text{H}*}(\mathbf{k}' - \mathbf{k}) \rho_0^m
\end{aligned} \tag{B.50}$$

with $\rho_0^m \equiv \text{tr}_s [\langle \phi_0^m | \hat{\rho} | \phi_0^m \rangle]$. $\mathcal{V}_{\text{mono}}^{\text{m-s}}$ subsumes all diagonal monopole-monopole terms, leading to a constant shift (renormalization) of the system resonance:

$$\begin{aligned}
\mathcal{V}_{\text{mono}}^{\text{m-s}} &\equiv \frac{N_m}{N_{\text{uc}}} (\mathcal{V}_c^{\text{H}}(\mathbf{0}) - \mathcal{V}_v^{\text{H}}(\mathbf{0})) + (1 - \frac{1}{2} n_{\text{h}}^{2\text{D}} A_{\text{uc}}) (\mathcal{V}_v^{\text{H}}(\mathbf{0}) - \mathcal{V}_v^{\text{L}}(\mathbf{0})) \\
&+ \frac{1}{2} n_{\text{e}}^{2\text{D}} A_{\text{uc}} (\mathcal{V}_c^{\text{H}}(\mathbf{0}) - \mathcal{V}_c^{\text{L}}(\mathbf{0})),
\end{aligned} \tag{B.51}$$

where $n_{\text{e/h}}^{2\text{D}} = N_{\text{e/h}}/A_{\text{QW}}$ denotes the **2D** carrier density for electrons (e) and holes (h).

Neglecting the inhomogeneous monopole-monopole contributions given in lines 2-5 of Eq. (B.50), one ends up with:

$$\begin{aligned}
\frac{\partial}{\partial t} \sigma_{\mathbf{q}_j, n}^{\mathbf{k}, \mathbf{k}'} &= \frac{i}{\hbar} (-E_{\mathbf{q}_j, n}^m + \varepsilon_{c, \mathbf{k}} - \varepsilon_{v, \mathbf{k}'} + \mathcal{V}_{\text{mono}}^{\text{m-s}}) \sigma_{\mathbf{q}_j, n}^{\mathbf{k}, \mathbf{k}'} + \frac{i}{\hbar} \frac{N_m}{N_d^m} \sum_{i=1}^{N_d^m} c_{l_i}^{\mathbf{q}_j, n*} \\
&\times \frac{1}{N_{\text{uc}}} \sum_{\mathbf{G}_m} \delta_{\mathbf{q}_j, \mathbf{k}' - \mathbf{k} + \mathbf{G}_m} \mathcal{V}_v^{\text{H}*}(\mathbf{k}' - \mathbf{k}) ((1 - f_{h, \mathbf{k}'}) (1 - f_{e, \mathbf{k}}) \rho_{\mathbf{q}_j, n}^m - f_{h, \mathbf{k}'} f_{e, \mathbf{k}} \rho_0^m).
\end{aligned} \tag{B.52}$$

B.7 Numerical implementation of the in-scattering rate

Starting from Eq. (7.70), first, the Kronecker delta ensuring momentum conservation during interlayer Förster transfer is evaluated, eliminating the sum over \mathbf{k} . The Kronecker delta only selects certain wave vectors \mathbf{k} within the first semiconductor **BZ** that satisfy the condition $\mathbf{k} = \mathbf{k}' - \mathbf{q}_j + \mathbf{G}_m$. Note that at the same time, the sum over \mathbf{G}_m is restricted to molecular reciprocal lattice vectors for which $\mathbf{k} = \mathbf{k}' - \mathbf{q}_j + \mathbf{G}_m$ is still within the first semiconductor **BZ**. This way, the sum over \mathbf{k} is eliminated by replacing $k_x = k'_x - q_{jx} + G_{m_x}$ and $k_y = k'_y - q_{jy} + G_{m_y}$. Assuming a spatially extended semiconductor **QW**, the remaining sum over the wave vector \mathbf{k}' can be converted into an integral over the first **BZ** of the semiconductor substrate using the relation

$$\sum_{\mathbf{k}'} \rightarrow \frac{A_{\text{QW}}}{(2\pi)^2} \int_{\text{1st BZ}} d^2 k'. \tag{B.53}$$

with the **QW** area $A_{\text{QW}} = N_s A_{\text{uc}}$. One obtains

$$\Gamma_{\mathbf{q}_j, n}^{\text{in}} = \frac{2\pi}{\hbar} \frac{1}{N_s^2} \frac{N_m^2}{N_d^{\text{m}^2}} \sum_{i=1}^{N_d^{\text{m}}} c_{\mathbf{l}_i}^{\mathbf{q}_j, n} \sum_{k=1}^{N_d^{\text{m}}} c_{\mathbf{l}_k}^{\mathbf{q}_j, n*} \frac{A_{\text{QW}}}{(2\pi)^2} \int d^2 k' \sum_{\mathbf{G}_m} \left| \mathcal{V}_{\text{vL}}^{\text{cH}}(\mathbf{q}_j - \mathbf{G}_m) \right|^2 \quad (\text{B.54})$$

$$\times f_{\text{h}, \mathbf{k}'} f_{\text{e}, \mathbf{k}' - \mathbf{q}_j + \mathbf{G}_m} \delta(\varepsilon_{\text{e}, \mathbf{k}' - \mathbf{q}_j + \mathbf{G}_m} + \varepsilon_{\text{h}, \mathbf{k}'} - \Delta_{\mathbf{q}_j, n}).$$

Finally, the Dirac delta distribution for energy conservation stemming from the Markov approximation is evaluated. Therefore, the property of a Dirac delta function composed with a smooth function $g(x)$ is used:

$$\int_{-\infty}^{\infty} dx f(x) \delta(g(x)) = \sum_i \int_{-\infty}^{\infty} dx f(x) \frac{\delta(x - x_i)}{|g'(x_i)|} = \sum_i \frac{f(x_i)}{|g'(x_i)|}, \quad (\text{B.55})$$

where the sum extends over the simple roots x_i of $g(x)$. The x -component of \mathbf{k}' , k'_x , is arbitrarily chosen to evaluate the delta condition. The argument of the Dirac delta, denoted as $g(k'_x)$, is differentiated with respect to k'_x :

$$g'(k'_x) \equiv \frac{d}{dk'_x} (\varepsilon_{\text{e}, \mathbf{k}' - \mathbf{q}_j + \mathbf{G}_m} + \varepsilon_{\text{h}, \mathbf{k}'} - \Delta_{\mathbf{q}_j, n}) = \frac{\hbar^2}{|m_{\text{v}}^*| m_{\text{c}}^*} ((|m_{\text{v}}^*| + m_{\text{c}}^*) k'_x - |m_{\text{v}}^*| (q_{jx} - G_{\text{m}x})), \quad (\text{B.56})$$

where it was used that $\varepsilon_{\text{e}, \mathbf{k}} = \frac{\hbar^2 k^2}{2m_{\text{c}}^*}$ and $\varepsilon_{\text{h}, \mathbf{k}} = \frac{\hbar^2 k^2}{2|m_{\text{v}}^*|}$. The roots of $g(k'_x)$ are:

$$k'_{x\pm} = \frac{1}{|m_{\text{v}}^*| + m_{\text{c}}^*} (|m_{\text{v}}^*| q'_{k_x} \pm \sqrt{\cdots}), \quad (\text{B.57})$$

with the abbreviation

$$\sqrt{\cdots} = \left[\frac{2}{\hbar^2} |m_{\text{v}}^*| m_{\text{c}}^* (|m_{\text{v}}^*| + m_{\text{c}}^*) \Delta_{\mathbf{q}_j, n} - (|m_{\text{v}}^*| + m_{\text{c}}^*)^2 k_y'^2 + 2|m_{\text{v}}^*| (|m_{\text{v}}^*| + m_{\text{c}}^*) k_y' (q_{jy} - G_{\text{m}y}) - |m_{\text{v}}^*| m_{\text{c}}^* (q_{jx} - G_{\text{m}x})^2 + |m_{\text{v}}^*| (|m_{\text{v}}^*| + m_{\text{c}}^*) (q_{jy} - G_{\text{m}y})^2 \right]^{1/2}. \quad (\text{B.58})$$

It follows

$$\delta(\varepsilon_{\text{e}, \mathbf{k}' - \mathbf{q}_j + \mathbf{G}_m} + \varepsilon_{\text{h}, \mathbf{k}'} - \Delta_{\mathbf{q}_j, n}) = \sum_{\gamma \in \{+, -\}} \frac{|m_{\text{v}}^*| m_{\text{c}}^*}{\hbar^2 \underbrace{(|m_{\text{v}}^*| + m_{\text{c}}^*) k'_{x\gamma} - |m_{\text{v}}^*| (q_{jx} - G_{\text{m}x})}_{= \frac{1}{|g'(k'_{x\gamma})|}}} \delta(k'_{x\gamma} - k'_{x'}) \quad (\text{B.59})$$

with $k'_{x\pm}$ given in Eq. (B.57). The expression under the square root has to be positive or zero in order to get a real solution, which will be ensured by a Heaviside step function in the transfer rate. This way, evaluating the Dirac delta distribution lifts the k'_x integration:

$$\Gamma_{\mathbf{q}_j, n}^{\text{in}} = \frac{2\pi}{\hbar} \frac{1}{N_s^2} \frac{A_{\text{QW}}}{(2\pi)^2} \frac{N_m^2}{N_d^{\text{m}^2}} \sum_{i=1}^{N_d^{\text{m}}} c_{\mathbf{l}_i}^{\mathbf{q}_j, n} \sum_{k=1}^{N_d^{\text{m}}} c_{\mathbf{l}_k}^{\mathbf{q}_j, n*} \int_{L_{\text{BZ}y}} dk'_y \sum_{\gamma \in \{+, -\}} \sum_{\mathbf{G}_m} \left| \mathcal{V}_{\text{vL}}^{\text{cH}}(\mathbf{q}_j - \mathbf{G}_m) \right|^2 \quad (\text{B.60})$$

$$\times f_{\text{h}, \mathbf{k}'_{\gamma}} f_{\text{e}, \mathbf{k}'_{\gamma} - \mathbf{q}_j + \mathbf{G}_m} \frac{|m_{\text{v}}^*| m_{\text{c}}^*}{\hbar^2 \underbrace{(|m_{\text{v}}^*| + m_{\text{c}}^*) k'_{x\gamma} - |m_{\text{v}}^*| (q_{jx} - G_{\text{m}x})}_{= \frac{1}{|g'(k'_{x\gamma})|}}} \theta(\cdots),$$

where $\mathbf{k}'_{\gamma} \equiv \begin{pmatrix} k'_{x\gamma} \\ k'_y \end{pmatrix}$ and $L_{\text{BZ}y}^{\text{s}}$ denotes the extension of the first substrate **BZ** in y direction.

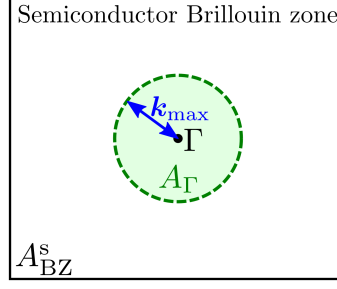


Figure B.4: Graphical illustration of the region A_Γ around the Γ point in reciprocal space. The \mathbf{k} integration over the first BZ is restricted to this area since the Fermi functions truncate any occupation outside this area.

Since the Fermi distributions contained in the semiconductor occupation density truncate high \mathbf{k} values far away from the Γ point, it is valid to restrict the evaluation to \mathbf{k} values inside a small circular region A_Γ centered around the Γ point with radius k_{\max} in the BZ: $A_\Gamma = \pi k_{\max}^2$. This is graphically illustrated in Fig. B.4. k_{\max} is determined such that the Fermi functions have sufficiently declined within A_Γ . E.g., k_{\max} is chosen such that the \mathbf{k} summation is truncated when the Fermi functions have declined below 10^{-5} :

$$f_{i,\mathbf{k}} = \frac{1}{\exp\left(\frac{\frac{\hbar^2 k^2}{2m_i} - \mu_i}{k_B T_i}\right) + 1} \geq 10^{-5} \quad \Rightarrow \quad k \leq \sqrt{\frac{2m_i}{\hbar^2} (k_B T_i \ln(99999) + \mu_i)}. \quad (\text{B.61})$$

Note that this limit is different for electrons and holes. A similar treatment can be employed for the out-scattering rate, however here not the Fermi factor is responsible for the truncation but the energy conservation condition. By now, only the one-dimensional (1D) integral over k'_y is left to be numerically discretized by converting it into a Riemann sum with a factor $\Delta k'_y = \frac{2k_{\max}}{N_{d_y}^s}$ given by the discretization step size with $N_d^s = N_{d_y}^s N_{d_x}^s$. The total in-scattering rate into the organic layer is given as the sum over all molecular exciton states enumerated by the parameter $\alpha = \mathbf{q}_j, n$:

$$\Gamma_{\text{tot}}^{\text{in}} = \frac{N_m^2}{N_d^{m^2}} \sum_{n=1}^{N_d^m} \sum_{j=1}^{N_d^m} \Gamma_{\mathbf{q}_j, n}^{\text{in}}. \quad (\text{B.62})$$

B.8 Reciprocal space analysis of the transfer rates for varying resonance energy detunings

The behavior of the in- and out-scattering transfer rates for varying resonance energy detunings is examined via a reciprocal space analysis. Therefore, the individual transfer rates $\Gamma_{\mathbf{q}_j+}^{\text{in/out}}$ which are summed up in the total rates of Fig. 7.6 (b) are studied in dependence of the molecular transfer vector \mathbf{q}_j . To support the analysis, the in- and out-scattering Fermi factors $f_{\mathbf{q}_j+}^{\text{in}}$ and $f_{\mathbf{q}_j+}^{\text{out}}$ are introduced as the sums over the products of the respective Fermi functions that obey the delta conditions for momentum and energy conservation entering the transfer rates:

$$f_{\mathbf{q}_j+}^{\text{in}} = \sum_{\mathbf{k}, \mathbf{k}'} \sum_{\mathbf{G}_m} f_{h, \mathbf{k}'} f_{e, \mathbf{k}} \delta_{\mathbf{q}_j, \mathbf{k}' - \mathbf{k} + \mathbf{G}_m} \delta\left(\varepsilon_e^{\mathbf{k}} + \varepsilon_h^{\mathbf{k}'} - \Delta_{\mathbf{q}_j}\right), \quad (\text{B.63})$$

$$f_{\mathbf{q}_j+}^{\text{out}} = \sum_{\mathbf{k}, \mathbf{k}'} \sum_{\mathbf{G}_m} (1 - f_{h, \mathbf{k}'}) (1 - f_{e, \mathbf{k}}) \delta_{\mathbf{q}_j, \mathbf{k}' - \mathbf{k} + \mathbf{G}_m} \delta\left(\varepsilon_e^{\mathbf{k}} + \varepsilon_h^{\mathbf{k}'} - \Delta_{\mathbf{q}_j}\right). \quad (\text{B.64})$$

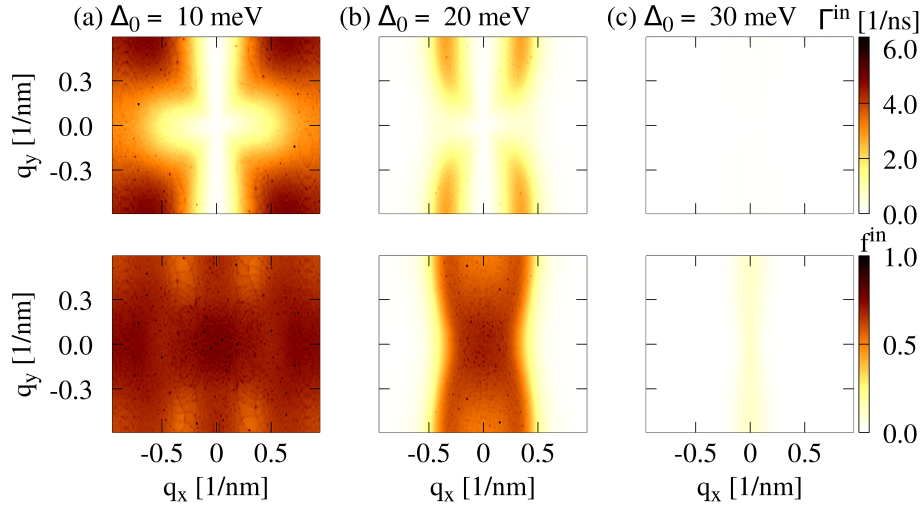


Figure B.5: In-scattering rates $\Gamma_{q_j+}^{\text{in}}$ (upper row) and Fermi factors $f_{q_j+}^{\text{in}}$ (lower row) for increasing resonance energy detuning Δ_0 of 10 meV (a), 20 meV (b), and 30 meV (c). The shown \mathbf{q} range represents the size of the first molecule **BZ** for a coverage of one molecule per 10×10 substrate **UCs**. [Spe18]

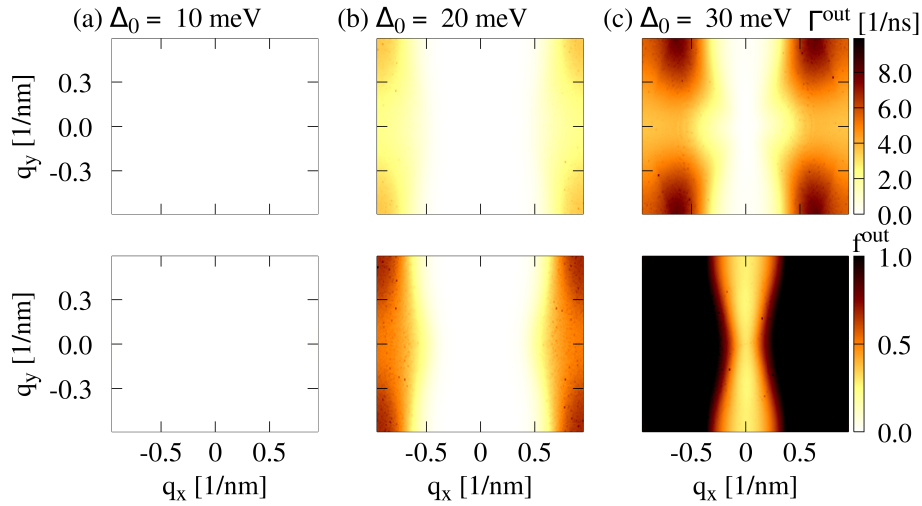


Figure B.6: Out-scattering rates $\Gamma_{q_j+}^{\text{out}}$ (upper row) and Fermi factors $f_{q_j+}^{\text{out}}$ (lower row) for increasing resonance energy detuning Δ_0 of 10 meV (a), 20 meV (b), and 30 meV (c). The shown \mathbf{q} range represents the size of the first molecule **BZ** for a coverage of one molecule per 10×10 substrate **UCs**. [Spe18]

These Fermi factors reflect the population filling resolved for the momentum transfer \mathbf{q} vectors and governed by momentum and energy conservation. Figs. B.5 and B.6 show the \mathbf{q} -dependent in- and out-scattering rates (upper row), respectively, and the corresponding Fermi factors (lower row) for increasing detuning Δ_0 of 10 meV (a), 20 meV (b), and 30 meV (c). For a small detuning $\Delta_0 = 10$ meV, the in-scattering Fermi factor depicted in the lower panel of Fig. B.5 (a) shows a constantly high value over all possible momentum transfer \mathbf{q} vectors within the first molecule **BZ**, resulting in an efficient in-scattering into the molecular film (cf. upper panel of Fig. B.5 (a)). The reason for that is the close energetic match between the resonances of the two constituents: The lower band states that fulfill energy and momentum conservation for the transfer process to the molecular system are highly occupied in the ZnO substrate (cf. left **HOMO-LUMO** system of Fig. 7.6). When the detuning is increased, the \mathbf{q} space region with a high Fermi factor that contributes to the excitation transfer shrinks significantly (lower

panel of Fig. B.5). This is due to the decreasing number of energy- and momentum-allowed scattering partners, as illustrated by the right HOMO-LUMO system in Fig. 7.6 (a).

However, this simple scheme does not explain (i) why the decrease of scattering partners occurs predominantly along the x direction and (ii) why the in-scattering rates in the upper panel of Fig. B.5 are reduced in the central region around $\mathbf{q} = 0$ for all detunings. The decrease along the x direction (i) can be understood by means of the \mathbf{q} -dependent intermolecular Förster coupling element $\mathcal{V}_{\text{L}}^{\text{H}}{}_{\text{H}}^{\text{L}}(\mathbf{q}_j)$ shown in Fig. 7.4 (a): According to the molecular dipole moment, the coupling element exhibits dumbbell-shaped maxima along the x axis at the borders of the molecular BZ, i.e., around $q_y = 0$ and $q_x = \pm \tilde{b}_1/2$ with \tilde{b}_1 being the absolute value of the molecular reciprocal lattice vector pointing in x direction. As a consequence, the molecular eigenenergy $E_{\mathbf{q}_j+}^{\text{m}} \propto \mathcal{V}_{\text{L}}^{\text{H}}{}_{\text{H}}^{\text{L}}(\mathbf{q}_j)$ entering the energy conservation shows maxima in these \mathbf{q} space regions. This further increases the energy difference $\Delta_{\mathbf{q}_j} = E_{\mathbf{q}_j+}^{\text{m}} - \mathcal{V}_{\text{mono}}^{\text{m-s}} - \varepsilon_{\text{gap}}^{\text{s}}$ and results in a reduced energy match. The reduced in-scattering at low \mathbf{q} values around $\mathbf{0}$ (ii) is caused by the interlayer Förster coupling element entering the transfer rate in Eq. (7.70). As shown in Fig. 7.4 (b), the matrix element exhibits four lobes oriented along the diagonals and is vanishing in the center, which is reflected in the transfer rate.

As expected, the opposite behavior is observed for the out-scattering rate and Fermi factor, cf. Fig. B.6. The out-scattering Fermi factor (lower row of Fig. B.6) reveals that the \mathbf{q} space regions where Pauli blocking prevents back-scattering into the substrate is decreased for increasing detunings, causing an increase in the out-scattering rate (upper row of Fig. B.6). However, the out-scattering rate decreases again for detunings larger than 30 meV. Here, the energy mismatch between the renormalized molecular gap and the semiconductor band gap is larger than the energy difference between any of the populated states in the semiconductor electron-hole continuum [Spe18].

In summary, the in-scattering efficiency decreases for large detunings as a consequence of the reduced population filling in the relevant momentum- and energy-allowed region. Note that discrete contributions are visible as sharp spots in the rather continuous in- and out-scattering rates and Fermi factors of Figs. B.5 and B.6. The appearance of these discrete points might be due to the discrete molecular positions in the periodic hybrid structure considered here, similar to the patterned observables in X-ray diffraction experiments probing the elastic scattering at crystalline structures.

C

Details on the derivation of the Wannier-Frenkel excitation transfer dynamics

C.1 Equations of motion of the exciton densities and polarizations

The **EOM** are derived following the notation of Ref. [Zim03]. First, the phonon-assisted density matrices

$$T_{j,\mathbf{q}}^{\alpha\beta} \equiv \text{tr}_B[\hat{b}_{j,\mathbf{q}}^\dagger \langle X_\beta^s | \hat{\rho} | X_\alpha^s \rangle], \quad T_{j,-\mathbf{q}}^{\beta\alpha*} \equiv \text{tr}_B[\hat{b}_{j,-\mathbf{q}} \langle X_\beta^s | \hat{\rho} | X_\alpha^s \rangle], \quad (\text{C.1})$$

$$T_{j,\mathbf{q}}^{\alpha 0} \equiv \text{tr}_B[\hat{b}_{j,\mathbf{q}}^\dagger \langle \phi_0^s | \hat{\rho} | X_\alpha^s \rangle], \quad T_{j,-\mathbf{q}}^{0\alpha*} \equiv \text{tr}_B[\hat{b}_{j,-\mathbf{q}} \langle \phi_0^s | \hat{\rho} | X_\alpha^s \rangle] \quad (\text{C.2})$$

and the photon-assisted density matrices

$$G_{l,\mathbf{q}}^{0\alpha} \equiv \text{tr}_B[\hat{c}_{l,\mathbf{q}}^\dagger \langle X_\alpha^s | \hat{\rho} | \phi_0^s \rangle], \quad G_{l,\mathbf{q}}^{0\alpha*} \equiv \text{tr}_B[\hat{c}_{l,\mathbf{q}} \langle \phi_0^s | \hat{\rho} | X_\alpha^s \rangle], \quad (\text{C.3})$$

$$G_{l,\mathbf{q}}^{\alpha\beta} \equiv \text{tr}_B[\hat{c}_{l,\mathbf{q}}^\dagger \langle X_\beta^s | \hat{\rho} | X_\alpha^s \rangle], \quad G_{l,\mathbf{q}}^{00} \equiv \text{tr}_B[\hat{c}_{l,\mathbf{q}}^\dagger \langle \phi_0^s | \hat{\rho} | \phi_0^s \rangle] \quad (\text{C.4})$$

are introduced. Plugging the Hamiltonian of Eq. (8.28) into the von Neumann equation $i\hbar\partial_t \hat{\rho}_S = [\hat{H}^s, \hat{\rho}_S]$ and making use of the orthonormality $\langle X_\alpha^s | X_\beta^s \rangle = \delta_{\alpha,\beta}$ and $\langle X_\alpha^s | \phi_0^s \rangle = 0$, the **EOM** for the exciton densities and polarizations and the ground state population can be derived:

$$\begin{aligned} \frac{\partial}{\partial t} \rho_{\alpha\beta}^s &= \frac{i}{\hbar} \left\{ (E_\alpha^s - E_\beta^s) \rho_{\alpha\beta}^s + \sum_{\zeta} \sum_{j,\mathbf{q}} \left(g_{j,\mathbf{q}}^{\zeta\alpha} (T_{j,\mathbf{q}}^{\zeta\beta} + T_{j,-\mathbf{q}}^{\beta\zeta*}) - g_{j,\mathbf{q}}^{\beta\zeta} (T_{j,\mathbf{q}}^{\alpha\zeta} + T_{j,-\mathbf{q}}^{\zeta\alpha*}) \right) \right. \\ &\quad \left. + \sum_{l,\mathbf{q}} (M_{l,\mathbf{q}}^\alpha G_{l,\mathbf{q}}^{0\beta} - M_{l,\mathbf{q}}^{\beta*} G_{l,\mathbf{q}}^{0\alpha*}) \right\}, \end{aligned} \quad (\text{C.5})$$

$$\frac{\partial}{\partial t} \rho_{\alpha 0}^s = \frac{i}{\hbar} \left\{ E_\alpha^s \rho_{\alpha 0}^s + \sum_{\beta} \sum_{j,\mathbf{q}} g_{j,\mathbf{q}}^{\beta\alpha} (T_{j,\mathbf{q}}^{\beta 0} + T_{j,-\mathbf{q}}^{0\beta*}) + \sum_{l,\mathbf{q}} (M_{l,\mathbf{q}}^\alpha G_{l,\mathbf{q}}^{00} - \sum_{\beta} M_{l,\mathbf{q}}^\beta G_{l,\mathbf{q}}^{\alpha\beta}) \right\}, \quad (\text{C.6})$$

$$\frac{\partial}{\partial t} \rho_{00}^s = \frac{i}{\hbar} \sum_{\alpha} \sum_{l,\mathbf{q}} (-M_{l,\mathbf{q}}^\alpha G_{l,\mathbf{q}}^{0\alpha} + M_{l,\mathbf{q}}^{\alpha*} G_{l,\mathbf{q}}^{0\alpha*}). \quad (\text{C.7})$$

Here it was used that the trace is invariant under cyclic permutations of bath operators. Eqs. (C.5) and (C.6) reveal that the exciton densities and polarizations couple to mixed expectation values involving both reservoir and system operators, introduced as phonon- and photon-assisted density matrices in Eqs. (C.1), (C.2), (C.3), and (C.4). These in turn couple to terms of even higher order, leading to an infinite hierarchy of assisted equations. In order to get a closed system of equations, the hierarchy is truncated by making the following approximations: First, assuming a weak interaction between the system and the reservoir, a factorization into exciton and phonon operators can be applied (second order Born approximation, cf. Sec. 2.3):

$$\text{tr}_B[\hat{b}_{j,\mathbf{q}}^\dagger \hat{b}_{j',\mathbf{q}'} \langle X_\beta^s | \hat{\rho} | X_\alpha^s \rangle] = \langle \hat{b}_{j,\mathbf{q}}^\dagger \hat{b}_{j',\mathbf{q}'} | X_\alpha^s \rangle \langle X_\beta^s | \rangle \approx \langle \hat{b}_{j,\mathbf{q}}^\dagger \hat{b}_{j',\mathbf{q}'} \rangle \text{tr}_B[\langle X_\beta^s | \hat{\rho} | X_\alpha^s \rangle] = \langle \hat{b}_{j,\mathbf{q}}^\dagger \hat{b}_{j',\mathbf{q}'} \rangle \rho_{\alpha\beta}^s. \quad (\text{C.8})$$

Second, the phonons are assumed to be in thermal equilibrium with $\langle \hat{b}_{j,\mathbf{q}}^\dagger \hat{b}_{j',\mathbf{q}'}^\dagger \rangle = \langle \hat{b}_{j,\mathbf{q}} \hat{b}_{j',\mathbf{q}'} \rangle = 0$ and are described by a Bose distribution $n_{j,\mathbf{q}}$:

$$\langle \hat{b}_{j,\mathbf{q}}^\dagger \hat{b}_{j',\mathbf{q}'} \rangle = \delta_{\mathbf{q},\mathbf{q}'} \delta_{j,j'} n_{j,\mathbf{q}} = \delta_{\mathbf{q},\mathbf{q}'} \delta_{j,j'} \frac{1}{\exp\left[\frac{\hbar\omega_{j,\mathbf{q}}}{k_B T}\right] - 1} \quad (\text{C.9})$$

The photon distribution $\langle \hat{c}_{l,\mathbf{q}}^\dagger \hat{c}_{l',\mathbf{q}'} \rangle$ is assumed to vanish since only emission into the field vacuum is considered [Zim03]. Finally, a coupling between phonons and photons is excluded by neglecting mixed expectation values of phonon and photon operators of the form $\text{tr}_B[\hat{b}_{j,\mathbf{q}}^\dagger \hat{c}_{l,\mathbf{q}'} \langle \phi_0^s | \hat{\rho} | X_\alpha^s \rangle]$.

Bringing the bath operators into normal order and applying the above mentioned approximations, one obtains the following **EOM** for the phonon-assisted quantities:

$$\frac{\partial}{\partial t} T_{j,\mathbf{q}}^{\alpha\beta} = \frac{i}{\hbar} \left\{ (E_\alpha^s - E_\beta^s + \hbar\omega_{j,\mathbf{q}}) T_{j,\mathbf{q}}^{\alpha\beta} + \sum_\zeta \left(g_{j,-\mathbf{q}}^{\zeta\alpha} (n_{j,\mathbf{q}} + 1) \rho_{\zeta\beta}^s - g_{j,-\mathbf{q}}^{\beta\zeta} n_{j,\mathbf{q}} \rho_{\alpha\zeta}^s \right) \right\}, \quad (\text{C.10})$$

$$\frac{\partial}{\partial t} T_{j,-\mathbf{q}}^{\beta\alpha*} = \frac{i}{\hbar} \left\{ (E_\alpha^s - E_\beta^s - \hbar\omega_{j,-\mathbf{q}}) T_{j,-\mathbf{q}}^{\beta\alpha*} + \sum_\zeta \left(g_{j,-\mathbf{q}}^{\zeta\alpha} n_{j,-\mathbf{q}} \rho_{\zeta\beta}^s - g_{j,-\mathbf{q}}^{\beta\zeta} (n_{j,-\mathbf{q}} + 1) \rho_{\alpha\zeta}^s \right) \right\}, \quad (\text{C.11})$$

$$\frac{\partial}{\partial t} T_{j,\mathbf{q}}^{\alpha 0} = \frac{i}{\hbar} \left\{ (E_\alpha^s + \hbar\omega_{j,\mathbf{q}}) T_{j,\mathbf{q}}^{\alpha 0} + \sum_\beta g_{j,-\mathbf{q}}^{\beta\alpha} (n_{j,\mathbf{q}} + 1) \rho_{\beta 0}^s \right\}, \quad (\text{C.12})$$

$$\frac{\partial}{\partial t} T_{j,-\mathbf{q}}^{0\alpha*} = \frac{i}{\hbar} \left\{ (E_\alpha^s - \hbar\omega_{j,-\mathbf{q}}) T_{j,-\mathbf{q}}^{0\alpha*} + \sum_\beta g_{j,-\mathbf{q}}^{\beta\alpha} n_{j,-\mathbf{q}} \rho_{\beta 0}^s \right\}, \quad (\text{C.13})$$

and for the photon-assisted matrices:

$$\frac{\partial}{\partial t} G_{l,\mathbf{q}}^{0\alpha} = \frac{i}{\hbar} \left\{ (-E_\alpha^s + \hbar\omega_q) G_{l,\mathbf{q}}^{0\alpha} + \sum_\beta M_{l,\mathbf{q}}^{\beta*} \rho_{\beta\alpha}^s \right\}, \quad (\text{C.14})$$

$$\frac{\partial}{\partial t} G_{l,\mathbf{q}}^{0\alpha*} = \frac{i}{\hbar} \left\{ (E_\alpha^s - \hbar\omega_q) G_{l,\mathbf{q}}^{0\alpha*} - \sum_\beta M_{l,\mathbf{q}}^\beta \rho_{\alpha\beta}^s \right\}, \quad (\text{C.15})$$

$$\frac{\partial}{\partial t} G_{l,\mathbf{q}}^{\alpha\beta} = \frac{i}{\hbar} (E_\alpha^s - E_\beta^s + \hbar\omega_q) G_{l,\mathbf{q}}^{\alpha\beta}, \quad (\text{C.16})$$

$$\frac{\partial}{\partial t} G_{l,\mathbf{q}}^{00} = \frac{i}{\hbar} \left\{ \hbar\omega_q G_{l,\mathbf{q}}^{00} + \sum_\alpha M_{l,\mathbf{q}}^{\alpha*} \rho_{0\alpha}^s \right\}. \quad (\text{C.17})$$

Since $G_{l,\mathbf{q}}^{\alpha\beta}$ (Eq. Eq. (C.16)) is not driven and does not change the dynamics, its contribution to the **EOM** for $\rho_{\alpha 0}^s$ (Eq. (C.6)) will be ignored.

The remaining **EOM** for the assisted quantities are solved in Markov approximation. This means, the limit $t_0 \rightarrow \infty$ is studied where the excitation pulse is assumed to be so far in the past that it is not remembered by the system at time t . The initial conditions become $T_{j,\mathbf{q}}^{\alpha\beta}(t_0) = 0$, $T_{j,\mathbf{q}}^{\alpha 0}(t_0) = 0$, and $G_{l,\mathbf{q}}^{0\alpha}(t_0) = 0$. A formal solution of the **EOM** of $T_{j,\mathbf{q}}^{\alpha\beta}$ is given by:

$$T_{j,\mathbf{q}}^{\alpha\beta}(t) = \frac{i}{\hbar} \int_0^\infty ds \sum_\zeta \left(g_{j,-\mathbf{q}}^{\zeta\alpha} (n_{j,\mathbf{q}} + 1) \rho_{\zeta\beta}^s(t-s) - g_{j,-\mathbf{q}}^{\beta\zeta} n_{j,\mathbf{q}} \rho_{\alpha\zeta}^s(t-s) \right) e^{\frac{i}{\hbar} (E_\alpha^s - E_\beta^s + \hbar\omega_{j,\mathbf{q}}) s}, \quad (\text{C.18})$$

where $s = t - t'$ has been substituted. In the absence of interactions of the excitons with the surrounding phonon and photon baths, the density matrix element $\rho_{\alpha\beta}^s(t)$ whose **EOM** is given in Eq. (C.5) would be proportional to $e^{\frac{i}{\hbar} (E_\alpha^s - E_\beta^s) t}$ (and $\rho_{\alpha 0}^s(t) \propto e^{\frac{i}{\hbar} E_\alpha^s t}$). Therefore, the term $\tilde{\rho}_{\alpha\beta}^s(t-s) \equiv e^{-\frac{i}{\hbar} (E_\alpha^s - E_\beta^s) (t-s)} \rho_{\alpha\beta}^s(t-s)$ is assumed to vary slowly in time and is taken out

of the integral in Eq. (C.18) by neglecting its memory: $\tilde{\rho}_{\alpha\beta}^s(t-s) \approx \tilde{\rho}_{\alpha\beta}^s(t)$. This treatment is often referred to as “weak-memory approach” [Zim95, Med95, Thr00, Zim03, But05]. The solution for the assisted quantity $T_{j,\mathbf{q}}^{\alpha\beta}(t)$ is now given by:

$$\begin{aligned} T_{j,\mathbf{q}}^{\alpha\beta}(t) &= \frac{i}{\hbar} \sum_{\zeta} g_{j,-\mathbf{q}}^{\zeta\alpha} (n_{j,\mathbf{q}} + 1) \rho_{\zeta\beta}^s(t) \underbrace{\int_0^{\infty} ds e^{\frac{i}{\hbar}(E_{\alpha}^s - E_{\zeta}^s + \hbar\omega_{j,\mathbf{q}})s}}_{=\pi\hbar\delta(E_{\alpha}^s - E_{\zeta}^s + \hbar\omega_{j,\mathbf{q}})} \\ &\quad - \frac{i}{\hbar} \sum_{\zeta} g_{j,-\mathbf{q}}^{\beta\zeta} n_{j,\mathbf{q}} \rho_{\alpha\zeta}^s(t) \underbrace{\int_0^{\infty} ds e^{\frac{i}{\hbar}(E_{\zeta}^s - E_{\beta}^s + \hbar\omega_{j,\mathbf{q}})s}}_{=\pi\hbar\delta(E_{\zeta}^s - E_{\beta}^s + \hbar\omega_{j,\mathbf{q}})}, \end{aligned} \quad (\text{C.19})$$

yielding the typical energy-conserving delta function that is closely related to Fermi’s Golden Rule. As usual, the principle-value terms have been neglected, since they only cause a polaron shift of the exciton energies.

The same procedure is applied to the remaining assisted quantities, yielding

$$T_{j,\mathbf{q}}^{\alpha\beta} = i\pi \sum_{\zeta} g_{j,-\mathbf{q}}^{\zeta\alpha} (n_{j,\mathbf{q}} + 1) \rho_{\zeta\beta}^s \delta(E_{\alpha}^s - E_{\zeta}^s + \hbar\omega_{j,\mathbf{q}}) - i\pi \sum_{\zeta} g_{j,-\mathbf{q}}^{\beta\zeta} n_{j,\mathbf{q}} \rho_{\alpha\zeta}^s \delta(E_{\zeta}^s - E_{\beta}^s + \hbar\omega_{j,\mathbf{q}}), \quad (\text{C.20})$$

$$\begin{aligned} T_{j,-\mathbf{q}}^{\beta\alpha*} &= i\pi \sum_{\zeta} g_{j,-\mathbf{q}}^{\zeta\alpha} n_{j,-\mathbf{q}} \rho_{\zeta\beta}^s \delta(E_{\alpha}^s - E_{\zeta}^s - \hbar\omega_{j,-\mathbf{q}}) \\ &\quad - i\pi \sum_{\zeta} g_{j,-\mathbf{q}}^{\beta\zeta} (n_{j,\mathbf{q}} + 1) \rho_{\alpha\zeta}^s \delta(E_{\zeta}^s - E_{\beta}^s - \hbar\omega_{j,-\mathbf{q}}), \end{aligned} \quad (\text{C.21})$$

$$T_{j,\mathbf{q}}^{\alpha 0} = i\pi \sum_{\beta} g_{j,-\mathbf{q}}^{\beta\alpha} (n_{j,\mathbf{q}} + 1) \rho_{\beta 0}^s \delta(E_{\alpha}^s - E_{\beta}^s + \hbar\omega_{j,\mathbf{q}}), \quad (\text{C.22})$$

$$T_{j,-\mathbf{q}}^{0\alpha*} = i\pi \sum_{\beta} g_{j,-\mathbf{q}}^{\beta\alpha} n_{j,-\mathbf{q}} \rho_{\beta 0}^s \delta(E_{\alpha}^s - E_{\beta}^s - \hbar\omega_{j,-\mathbf{q}}) \quad (\text{C.23})$$

for the phonon-assisted matrices and

$$G_{l,\mathbf{q}}^{0\alpha} = i\pi \sum_{\beta} M_{l,\mathbf{q}}^{\beta*} \rho_{\beta\alpha}^s \delta(-E_{\beta}^s + \hbar\omega_{\mathbf{q}}), \quad (\text{C.24})$$

$$G_{l,\mathbf{q}}^{0\alpha*} = -i\pi \sum_{\beta} M_{l,\mathbf{q}}^{\beta} \rho_{\alpha\beta}^s \delta(E_{\beta}^s - \hbar\omega_{\mathbf{q}}), \quad (\text{C.25})$$

$$G_{l,\mathbf{q}}^{00} = i\pi \sum_{\alpha} M_{l,\mathbf{q}}^{\alpha*} \rho_{0\alpha}^s \delta(E_{\alpha}^s + \hbar\omega_{\mathbf{q}}) \quad (\text{C.26})$$

for the photon-assisted matrices. Equations (C.24), (C.25), and (C.26) are the Markovian solutions of the respective EOM Eqs. (C.14), (C.15), and (C.17), representing the fluctuations induced by the surrounding photon bath.

These Markovian solutions are inserted into Eqs. (C.5), (C.6), and (C.7). It is used that $\omega_{j,\mathbf{q}} = \omega_{j,-\mathbf{q}}$ and $g_{j,-\mathbf{q}}^{\beta\alpha} = g_{j,\mathbf{q}}^{\alpha\beta*}$. The system of solutions is reduced by taking only the dominant contributions whose leading frequencies coincide and assuming non-degenerate exciton states, such that the resonance condition $E_{\alpha}^s = E_{\eta}^s$ directly translates into $\alpha = \eta$. This approximation is of course questionable for extended systems where the energies of the disorder eigenstates are very close. However, the approximation is consolidated by factors such as $g_{j,\mathbf{q}}^{\zeta\alpha} g_{j,-\mathbf{q}}^{\eta\zeta}$ entering the equations. From Eq. (8.21) it is clear that this term only contributes if the center-of-mass (COM) wave function of exciton ζ has a significant spatial overlap with both excitons α and η .

Therefore, states α and η have to be localized in the same spatial region. This together with the energy conservation condition $E_\alpha^s = E_\eta^s$ suggests that states α and η are indeed identical due to level repulsion [Zim03].

C.1.1 Radiative and phonon scattering rates

Radiative decay rate

In this section, the radiative rate of Eq. (8.37) is further evaluated by inserting the expression for the matrix element in exciton basis of Eq. (8.27) and carrying out the l sum over the two modes (TE and TM) given in Eqs. (8.24) and (8.25):

$$r_\alpha = \frac{\pi d_{\text{vc}}^2}{\epsilon_0 \epsilon_r V} \sum_{\mathbf{q}} \omega_q \left(1 + \frac{q_z^2}{q^2}\right) |\phi_{1s}^s(\mathbf{0})|^2 |O_{\text{eh}}|^2 |\tilde{\psi}_\alpha^s(\mathbf{q}_\parallel = \mathbf{0})|^2 \delta(E_\alpha^s - \hbar\omega_q) \quad (\text{C.27})$$

with $\omega_q = \frac{cq}{\sqrt{\epsilon_r}}$ and $q = \sqrt{q_\parallel^2 + q_z^2}$. $\tilde{\psi}_\alpha^s(\mathbf{q}_\parallel) \equiv \int d^2R \psi_\alpha^s(\mathbf{R}) e^{i\mathbf{q}_\parallel \cdot \mathbf{R}}$ denotes the Fourier transform of the COM wave function. The argument $\mathbf{q}_\parallel = \mathbf{0}$ reflects the fact that the exciton is well localized [Zim03]. $\phi_{1s}^s(\mathbf{0})$ is the relative wave function with the electron and hole at the same position and O_{eh} denotes the confinement overlap, cf. Sec. 8.2.3. The sum over \mathbf{q} is converted into a 3D integral over the photon momentum $\mathbf{q} = (\mathbf{q}_\parallel, q_z)$: $\sum_{\mathbf{q}} \rightarrow \frac{V}{(2\pi)^3} \int d^2q_\parallel \int dq_z$. The delta function for energy conservation is used to eliminate the sum over q_z by using the property of the delta function composed with a smooth function (cf. Eq. (B.55)), yielding

$$\delta(E_\alpha^s - \hbar\omega_q) = \sum_{\gamma=\pm 1} \frac{K_0 \sqrt{\epsilon_r}}{\hbar c \sqrt{K_0^2 - \mathbf{q}_\parallel^2}} \theta(K_0^2 - \mathbf{q}_\parallel^2) \delta\left(q_z - \gamma \sqrt{K_0^2 - \mathbf{q}_\parallel^2}\right). \quad (\text{C.28})$$

Here, the light cone $K_0 \equiv \frac{E_\alpha^s \sqrt{\epsilon_r}}{\hbar c}$ was introduced. It is almost constant. The Heaviside step function ensures that the solutions are real and the integration gives only a contribution close to the center of the Brillouin zone. With that, the radiative rate reads

$$r_\alpha = \frac{d_{\text{vc}}^2}{2\pi^2 \epsilon_0 \epsilon_r \hbar} |\phi_{1s}^s(\mathbf{0})|^2 |O_{\text{eh}}|^2 |\tilde{\psi}_\alpha^s(\mathbf{0})|^2 \int d^2q_\parallel \theta(K_0^2 - \mathbf{q}_\parallel^2) \frac{K_0^2 - \frac{\mathbf{q}_\parallel^2}{2}}{\sqrt{K_0^2 - \mathbf{q}_\parallel^2}} \quad (\text{C.29})$$

The integration can be performed analytically by transforming \mathbf{q}_\parallel into polar coordinates, yielding:

$$r_\alpha = \frac{2d_{\text{vc}}^2}{3\pi \epsilon_0 \epsilon_r \hbar} |\phi_{1s}^s(\mathbf{0})|^2 |O_{\text{eh}}|^2 |\tilde{\psi}_\alpha^s(\mathbf{0})|^2 K_0^3. \quad (\text{C.30})$$

Phonon scattering rate

The phonon scattering rate of Eq. (8.38) is evaluated in a similar manner by inserting the expression of the phonon coupling element in the basis of disorder eigenstates, Eq. (8.21). The sum over the 3D phonon wave vectors is converted into an integral and the q_z integration is again eliminated by evaluating the energy conserving delta function:

$$\begin{aligned} \gamma_{\beta \leftarrow \alpha}^s &= \sum_j \frac{1}{8\pi^2 \rho_s u_j^2 \hbar} \int d^2q_\parallel \sum_{\gamma=\pm 1} \frac{Q_{\alpha\beta,j}^2}{\sqrt{Q_{\alpha\beta,j}^2 - \mathbf{q}_\parallel^2}} \left\{ (n_{j,\mathbf{q}} + 1) \theta(E_\alpha^s - E_\beta^s) + n_{j,\mathbf{q}} \theta(E_\beta^s - E_\alpha^s) \right\} \\ &\times \left| D_c K_e (\gamma \sqrt{Q_{\alpha\beta,j}^2 - \mathbf{q}_\parallel^2}) \chi\left(\frac{m_h}{M} \mathbf{q}_\parallel\right) - D_v K_h (\gamma \sqrt{Q_{\alpha\beta,j}^2 - \mathbf{q}_\parallel^2}) \chi\left(\frac{m_e}{M} \mathbf{q}_\parallel\right) \right|^2 \\ &\times \int d^2R \psi_\beta^{s*}(\mathbf{R}) e^{i\mathbf{q}_\parallel \cdot \mathbf{R}} \psi_\alpha^s(\mathbf{R}) \theta(Q_{\alpha\beta,j}^2 - \mathbf{q}_\parallel^2) \end{aligned} \quad (\text{C.31})$$

with $Q_{\alpha\beta,j} \equiv \frac{E_\alpha^s - E_\beta^s}{\hbar u_j}$. The Heaviside step functions ensure that the expressions under the square roots are non-negative and account for the fact that the phonon dispersion $\hbar\omega_j$ is a positive quantity.

C.2 Calculation of the semiconductor–molecule transition amplitude

The starting point is the matrix element of the Liouville propagator in second-order perturbation expansion of Eq. (8.91):

$$\begin{aligned}
t_{\rho_{\beta\beta}^m \leftarrow \rho_{\alpha\alpha}^s}(t, t_0) = & \text{tr} \left[|X_\beta^m\rangle \langle X_\beta^m| \left\{ -\frac{1}{\hbar^2} \int_{t_0}^t d\tau \int_{t_0}^\tau d\tau' \right. \right. \\
& \times \underbrace{\mathcal{U}_{\text{diag}}^g(t, \tau) \mathcal{L}_{\text{off-diag}}^g(\tau) \mathcal{U}_{\text{diag}}^g(\tau, \tau') \mathcal{L}_{\text{off-diag}}^g(\tau') \underbrace{\mathcal{U}_{\text{diag}}^g(\tau', t_0) |X_\alpha^s\rangle \langle X_\alpha^s| \hat{\rho}_{\text{B}}^g}_{\equiv \textcircled{1}}}}_{\equiv \textcircled{2}} \left. \right\} \\
& \underbrace{\hspace{15em}}_{\equiv \textcircled{3}}
\end{aligned} \tag{C.32}$$

Term $\textcircled{1}$ is evaluated first. The time-ordered exponential is replaced by an ordinary exponential function, since \hat{H}_{diag}^g is time-independent in the Schrödinger picture:

$$\begin{aligned}
\textcircled{1} &= \mathcal{U}_{\text{diag}}^g(\tau', t_0) |X_\alpha^s\rangle \langle X_\alpha^s| \hat{\rho}_{\text{B}}^g = e^{-\frac{i}{\hbar} \hat{H}_{\text{diag}}^g(\tau' - t_0)} |X_\alpha^s\rangle \langle X_\alpha^s| \hat{\rho}_{\text{B}}^g e^{+\frac{i}{\hbar} \hat{H}_{\text{diag}}^g(\tau' - t_0)} \\
&= U_{0,\text{ph}}^g(\tau', t_0) |X_\alpha^s\rangle \langle X_\alpha^s| \hat{\rho}_{\text{B}}^g U_{0,\text{ph}}^{g\dagger}(\tau', t_0)
\end{aligned} \tag{C.33}$$

with

$$U_{0,\text{ph}}^g(\tau', t_0) \equiv e^{-\frac{i}{\hbar} \sum_j \hbar\omega_j \hat{b}_j^{g\dagger} \hat{b}_j^g(\tau' - t_0)}. \tag{C.34}$$

The second term includes an interaction with the Förster Hamiltonian:

$$\begin{aligned}
\textcircled{2} &= \mathcal{U}_{\text{diag}}^g(\tau, \tau') \mathcal{L}_{\text{off-diag}}^g \mathcal{U}_{\text{diag}}^g(\tau', t_0) |X_\alpha^s\rangle \langle X_\alpha^s| \hat{\rho}_{\text{B}}^g \\
&= e^{-\frac{i}{\hbar} \hat{H}_{\text{diag}}^g(\tau - \tau')} (\hat{H}_{\text{off-diag}} \textcircled{1} - \textcircled{1} \hat{H}_{\text{off-diag}}) e^{+\frac{i}{\hbar} \hat{H}_{\text{diag}}^g(\tau - \tau')} \\
&= \sum_{\zeta} \left(V_{\text{F}}^{\text{m-s}}(X_\zeta^m, X_\alpha^s) e^{-\frac{i}{\hbar} E_{\text{el}}^{\text{m-s}}(X_\zeta^m, X_\alpha^s)(\tau - \tau')} U_{\text{ph}}^{g,\zeta}(\tau, \tau') U_{0,\text{ph}}^g(\tau', t_0) |X_\zeta^m\rangle \langle X_\alpha^s| \hat{\rho}_{\text{B}}^g U_{0,\text{ph}}^{g\dagger}(\tau, t_0) \right. \\
&\quad \left. - V_{\text{F}}^{\text{m-s}*}(X_\zeta^m, X_\alpha^s) e^{+\frac{i}{\hbar} E_{\text{el}}^{\text{m-s}}(X_\zeta^m, X_\alpha^s)(\tau - \tau')} U_{0,\text{ph}}^g(\tau, t_0) |X_\alpha^s\rangle \langle X_\zeta^m| \hat{\rho}_{\text{B}}^g U_{0,\text{ph}}^{g\dagger}(\tau', t_0) U_{\text{ph}}^{g,\zeta\dagger}(\tau, \tau') \right)
\end{aligned} \tag{C.35}$$

with

$$E_{\text{el}}^{\text{m-s}}(X_\zeta^m, X_\alpha^s) \equiv E_\zeta^m - E_{\alpha,3\text{D}}^s + V_{\text{H-L}}^{\text{m-s}}(X_\zeta^m) - V_{\text{v-c}}^{\text{m-s}}(X_\alpha^s) \tag{C.36}$$

and

$$U_{\text{ph}}^{g,\zeta}(\tau, \tau') \equiv e^{-\frac{i}{\hbar} \sum_j \hbar(\omega_j \hat{b}_j^{g\dagger} \hat{b}_j^g + g_j^{\zeta\zeta} \hat{b}_j^g + g_j^{\zeta\zeta*} \hat{b}_j^{g\dagger})(\tau - \tau')}. \tag{C.37}$$

The Feynman disentanglement theorem [Fey51] (cf. Sec. 2.5) is applied to Eq. (C.37):

$$U_{\text{ph}}^{g,\zeta\dagger}(\tau, \tau') = U_{0,\text{ph}}^{g\dagger}(\tau, \tau') \exp_{\leftarrow} \left[+\frac{i}{\hbar} \int_{\tau'}^\tau d\tau'' U_{0,\text{ph}}^{g\dagger}(\tau', \tau'') \sum_j \hbar(g_j^{\zeta\zeta} \hat{b}_j^g + g_j^{\zeta\zeta*} \hat{b}_j^{g\dagger}) U_{0,\text{ph}}^{g\dagger}(\tau'', \tau') \right]. \tag{C.38}$$

The integrand is further evaluated:

$$U_{0,\text{ph}}^{g\dagger}(\tau', \tau'') \sum_j \hbar(g_j^{\zeta\zeta} \hat{b}_j^g + g_j^{\zeta\zeta*} \hat{b}_j^{g\dagger}) U_{0,\text{ph}}^{g\dagger}(\tau'', \tau')$$

$$= e^{+\frac{i}{\hbar} \sum_{j'} \hbar \omega_{j'} \hat{b}_{j'}^{g\dagger} \hat{b}_{j'}^g (\tau' - \tau'')} \sum_j \hbar(g_j^{\zeta\zeta} \hat{b}_j^g + g_j^{\zeta\zeta*} \hat{b}_j^{g\dagger}) e^{-\frac{i}{\hbar} \sum_{j''} \hbar \omega_{j''} \hat{b}_{j''}^{g\dagger} \hat{b}_{j''}^g (\tau' - \tau'')} \quad (\text{C.39})$$

$$= \sum_j \hbar g_j^{\zeta\zeta} \left\{ \hat{b}_j^g + i(\tau' - \tau'') \underbrace{\left[\sum_{j'} \omega_{j'} \hat{b}_{j'}^{g\dagger} \hat{b}_{j'}^g, \hat{b}_j^g \right]}_{=-\omega_j \hat{b}_j^g} \right.$$

$$\left. - \frac{(\tau' - \tau'')^2}{2} \underbrace{\left[\sum_{j'} \omega_{j'} \hat{b}_{j'}^{g\dagger} \hat{b}_{j'}^g, \left[\sum_{j''} \omega_{j''} \hat{b}_{j''}^{g\dagger} \hat{b}_{j''}^g, \hat{b}_j^g \right] \right]}_{=\omega_j^2 \hat{b}_j^g} \right. + \dots \left. \right\} \quad (\text{C.40})$$

$$+ \sum_j \hbar g_j^{\zeta\zeta*} \left\{ \hat{b}_j^{g\dagger} + i(\tau' - \tau'') \underbrace{\left[\sum_{j'} \omega_{j'} \hat{b}_{j'}^{g\dagger} \hat{b}_{j'}^g, \hat{b}_j^{g\dagger} \right]}_{=\omega_j \hat{b}_j^{g\dagger}} \right.$$

$$\left. - \frac{(\tau' - \tau'')^2}{2} \underbrace{\left[\sum_{j'} \omega_{j'} \hat{b}_{j'}^{g\dagger} \hat{b}_{j'}^g, \left[\sum_{j''} \omega_{j''} \hat{b}_{j''}^{g\dagger} \hat{b}_{j''}^g, \hat{b}_j^{g\dagger} \right] \right]}_{=\omega_j^2 \hat{b}_j^{g\dagger}} \right. - \dots \left. \right\}$$

$$= \sum_j \hbar g_j^{\zeta\zeta} \hat{b}_j^g \left\{ 1 - i\omega_j(\tau' - \tau'') - \frac{1}{2}\omega_j^2(\tau' - \tau'')^2 + \dots \right\}$$

$$+ \sum_j \hbar g_j^{\zeta\zeta*} \hat{b}_j^{g\dagger} \left\{ 1 + i\omega_j(\tau' - \tau'') - \frac{1}{2}\omega_j^2(\tau' - \tau'')^2 - \dots \right\} \quad (\text{C.41})$$

$$= \sum_j \hbar(g_j^{\zeta\zeta} \hat{b}_j^g e^{-i\omega_j(\tau' - \tau'')} + g_j^{\zeta\zeta*} \hat{b}_j^{g\dagger} e^{+i\omega_j(\tau' - \tau'')}). \quad (\text{C.42})$$

This way, Eq. (C.38) is rewritten into:

$$U_{\text{ph}}^{g,\zeta\dagger}(\tau, \tau') = U_{0,\text{ph}}^{g\dagger}(\tau, \tau') U_{\text{I,ph}}^{g,\zeta\dagger}(\tau, \tau') \quad (\text{C.43})$$

with

$$U_{\text{I,ph}}^{g,\zeta\dagger}(\tau, \tau') \equiv \exp_{\leftarrow} \left[+\frac{i}{\hbar} \int_{\tau'}^{\tau} d\tau'' \sum_j \hbar(g_j^{\zeta\zeta} \hat{b}_j^g e^{-i\omega_j(\tau' - \tau'')} + g_j^{\zeta\zeta*} \hat{b}_j^{g\dagger} e^{+i\omega_j(\tau' - \tau'')}) \right]. \quad (\text{C.44})$$

In the third term, the off-diagonal Liouvillian acts on the system a second time:

$$\textcircled{3} = \mathcal{U}_{\text{diag}}^g(t, \tau) \mathcal{L}_{\text{off-diag}}^g(\tau) \mathcal{U}_{\text{diag}}^g(\tau, \tau') \mathcal{L}_{\text{off-diag}}^g(\tau') \mathcal{U}_{\text{diag}}^g(\tau', t_0) |X_\alpha^s\rangle \langle X_\alpha^s| \hat{\rho}_B^g \quad (\text{C.45})$$

$$\begin{aligned}
&= \sum_{\zeta, \eta} V_F^{m-s*}(X_\zeta^m, X_\eta^s) V_F^{m-s}(X_\zeta^m, X_\alpha^s) e^{-\frac{i}{\hbar} E_{\text{el}}^s(X_\eta^s, X_\alpha^s)(t-\tau)} e^{-\frac{i}{\hbar} E_{\text{el}}^{m-s}(X_\zeta^m, X_\alpha^s)(\tau-\tau')} \\
&\quad \times U_{0,\text{ph}}^g(t, \tau) U_{1,\text{ph}}^{g,\zeta}(\tau, \tau') U_{0,\text{ph}}^g(\tau, t_0) |X_\eta^s\rangle \langle X_\alpha^s | \hat{\rho}_B^g U_{0,\text{ph}}^{g\dagger}(t, t_0) \\
&\quad - \sum_{\zeta, \eta} V_F^{m-s}(X_\eta^m, X_\alpha^s) V_F^{m-s*}(X_\zeta^m, X_\alpha^s) e^{-\frac{i}{\hbar} E_{\text{el}}^m(X_\eta^m, X_\zeta^m)(t-\tau)} e^{+\frac{i}{\hbar} E_{\text{el}}^{m-s}(X_\zeta^m, X_\alpha^s)(\tau-\tau')} \\
&\quad \times U_{\text{ph}}^{g,\eta}(t, \tau) U_{0,\text{ph}}^g(\tau, t_0) |X_\eta^m\rangle \langle X_\zeta^m | \hat{\rho}_B^g U_{0,\text{ph}}^{g\dagger}(\tau, t_0) U_{1,\text{ph}}^{g,\zeta\dagger}(\tau, \tau') U_{\text{ph}}^{g,\zeta\dagger}(t, \tau) \\
&\quad + \sum_{\substack{\zeta, \eta \\ \zeta \neq \eta}} V_F^{m-s}(X_\zeta^m, X_\alpha^s) e^{-\frac{i}{\hbar} E_{\text{el}}^{m-s}(X_\eta^m, X_\alpha^s)(t-\tau)} e^{-\frac{i}{\hbar} E_{\text{el}}^{m-s}(X_\zeta^m, X_\alpha^s)(\tau-\tau')} U_{\text{ph}}^{g,\eta}(t, \tau) \\
&\quad \times \sum_j \hbar (g_j^{\zeta\eta} \hat{b}_j^g + g_j^{\eta\zeta*} \hat{b}_j^{g\dagger}) U_{1,\text{ph}}^{g,\zeta}(\tau, \tau') U_{0,\text{ph}}^g(\tau, t_0) |X_\eta^m\rangle \langle X_\alpha^s | \hat{\rho}_B^g U_{0,\text{ph}}^{g\dagger}(t, t_0) \\
&\quad + h.c.
\end{aligned} \tag{C.46}$$

with

$$E_{\text{el}}^m(X_\eta^m, X_\zeta^m) \equiv E_\eta^m - E_\zeta^m + V_{\text{H-L}}^{m-s}(X_\eta^m) - V_{\text{H-L}}^{m-s}(X_\zeta^m), \tag{C.47}$$

$$E_{\text{el}}^s(X_\eta^s, X_\alpha^s) \equiv E_{\eta,3\text{D}}^s - E_{\alpha,3\text{D}}^s + V_{\text{v-c}}^{m-s}(X_\eta^s) - V_{\text{v-c}}^{m-s}(X_\alpha^s). \tag{C.48}$$

Finally, in order to derive the transition amplitude of Eq. (8.91), the trace is evaluated using its invariance under cyclic permutations. In thermal equilibrium the mean number of vibrational quanta in mode j with frequency ω_j is described by a Bose distribution:

$$\bar{n}(\omega_j) = \langle \hat{b}_j^{g\dagger} \hat{b}_j^g \rangle_B = \frac{1}{e^{\beta \hbar \omega_j} - 1} \tag{C.49}$$

with $\beta = 1/(k_B T)$, and the density operator is given as harmonic ensemble of the thermal bath [Muk95]:

$$\hat{\rho}_B^g = \sum_{j, n_j} \rho_{n_j n_j} |n_j\rangle \langle n_j| \quad \text{with} \quad \rho_{n_j n_j} = \frac{\bar{n}(\omega_j)^{n_j}}{(\bar{n}(\omega_j) + 1)^{n_j+1}}. \tag{C.50}$$

Here, Fock number states have been introduced for the phonon modes. It follows that

$$U_{0,\text{ph}}^g(\tau, t_0) \hat{\rho}_B^g U_{0,\text{ph}}^{g\dagger}(\tau, t_0) = \hat{\rho}_B^g. \tag{C.51}$$

Transforming the integration variable of Eq. (C.44) according to $\tau'' \rightarrow \tau' - \tau''$ leads to the expressions of Eqs. (8.92) and (8.93).

C.3 Calculation of the intermolecular transition amplitude

In this section, the transition amplitude between different molecular densities $\rho_{\alpha\alpha}^m$ and $\rho_{\beta\beta}^m$ (with $\alpha \neq \beta$) is calculated. Again, the first order in the perturbative expansion of the Liouville propagator vanishes and the second order is evaluated:

$$\begin{aligned}
t_{\rho_{\beta\beta}^m \leftarrow \rho_{\alpha\alpha}^m}(t, t_0) &\approx \text{tr} \left[|X_\beta^m\rangle \langle X_\beta^m| \left\{ -\frac{1}{\hbar^2} \int_{t_0}^t d\tau \int_{t_0}^\tau d\tau' \mathcal{U}_{\text{diag}}^\alpha(t, \tau) \mathcal{L}_{\text{off-diag}}^\alpha(\tau) \mathcal{U}_{\text{diag}}^\alpha(\tau, \tau') \right. \right. \\
&\quad \left. \left. \times \mathcal{L}_{\text{off-diag}}^\alpha(\tau') \mathcal{U}_{\text{diag}}^\alpha(\tau', t_0) |X_\alpha^m\rangle \langle X_\alpha^m | \hat{\rho}_B^\alpha \right\} \right]
\end{aligned} \tag{C.52}$$

$$\begin{aligned}
&= \frac{1}{\hbar^2} \int_{t_0}^t d\tau \int_{t_0}^{\tau} d\tau' \left\{ e^{+\frac{i}{\hbar} E_{\text{el}}^{\text{m}}(X_{\beta}^{\text{m}}, X_{\alpha}^{\text{m}})(\tau-\tau')} \text{tr}_{\text{B}} \left[U_{0,\text{ph}}^{\alpha}(\tau, \tau') \sum_j \hbar(g_j^{\beta\alpha} \hat{b}_j^{\alpha} + g_j^{\alpha\beta*} \hat{b}_j^{\alpha\dagger}) \right. \right. \\
&\quad \times U_{\text{ph}}^{\alpha,\beta\dagger}(\tau, \tau') \sum_{j'} \hbar(g_{j'}^{\alpha\beta} \hat{b}_{j'}^{\alpha} + g_{j'}^{\beta\alpha*} \hat{b}_{j'}^{\alpha\dagger}) \hat{\rho}_{\text{B}}^{\alpha} \left. \right] \\
&\quad + e^{-\frac{i}{\hbar} E_{\text{el}}^{\text{m}}(X_{\beta}^{\text{m}}, X_{\alpha}^{\text{m}})(\tau-\tau')} \text{tr}_{\text{B}} \left[\sum_{j'} \hbar(g_{j'}^{\beta\alpha} \hat{b}_{j'}^{\alpha} + g_{j'}^{\alpha\beta*} \hat{b}_{j'}^{\alpha\dagger}) U_{\text{ph}}^{\alpha,\beta}(\tau, \tau') \right. \\
&\quad \left. \left. \times \sum_j \hbar(g_j^{\alpha\beta} \hat{b}_j^{\alpha} + g_j^{\beta\alpha*} \hat{b}_j^{\alpha\dagger}) U_{0,\text{ph}}^{\alpha\dagger}(\tau, \tau') \hat{\rho}_{\text{B}}^{\alpha} \right] \right\}, \tag{C.53}
\end{aligned}$$

where $E_{\text{el}}^{\text{m}}(X_{\eta}^{\text{m}}, X_{\zeta}^{\text{m}})$ is defined in Eq. (C.47) and

$$U_{0,\text{ph}}^{\alpha}(\tau, \tau') \equiv e^{-\frac{i}{\hbar} \sum_j \hbar \omega_j \hat{b}_j^{\alpha\dagger} \hat{b}_j^{\alpha} (\tau-\tau')}, \tag{C.54}$$

$$U_{\text{ph}}^{\alpha,\beta}(\tau, \tau') \equiv e^{-\frac{i}{\hbar} \sum_j \hbar (\omega_j \hat{b}_j^{\alpha\dagger} \hat{b}_j^{\alpha} + (g_j^{\beta\beta} - g_j^{\alpha\alpha}) \hat{b}_j^{\alpha} + (g_j^{\beta\beta*} - g_j^{\alpha\alpha*}) \hat{b}_j^{\alpha\dagger}) (\tau-\tau')}, \tag{C.55}$$

with $U_{\text{ph}}^{\alpha,\alpha}(\tau, \tau') = U_{0,\text{ph}}^{\alpha}(\tau, \tau')$. Using the Feynman disentangling theorem [Fey51] (cf. Sec. 2.5), the propagator of (C.55) can be written as:

$$U_{\text{ph}}^{\alpha,\beta\dagger}(\tau, \tau') = U_{0,\text{ph}}^{\alpha}(\tau, \tau') U_{\text{I,ph}}^{\alpha,\beta\dagger}(\tau, \tau') \tag{C.56}$$

with

$$\begin{aligned}
U_{\text{I,ph}}^{\alpha,\beta\dagger}(\tau, \tau') \equiv \exp_{\leftarrow} \left[+\frac{i}{\hbar} \int_{\tau'}^{\tau} d\tau'' \sum_j \hbar (g_j^{\beta\beta} - g_j^{\alpha\alpha}) \hat{b}_j^{\alpha} e^{-i\omega_j(\tau'-\tau'')} \right. \\
\left. + (g_j^{\beta\beta*} - g_j^{\alpha\alpha*}) \hat{b}_j^{\alpha\dagger} e^{+i\omega_j(\tau'-\tau'')} \right]. \tag{C.57}
\end{aligned}$$

Moreover, it is used that

$$U_{0,\text{ph}}^{\alpha}(\tau, \tau') \sum_j \hbar(g_j^{\beta\alpha} \hat{b}_j^{\alpha} + g_j^{\alpha\beta*} \hat{b}_j^{\alpha\dagger}) U_{0,\text{ph}}^{\alpha\dagger}(\tau, \tau') = \sum_j \hbar(g_j^{\beta\alpha} \hat{b}_j^{\alpha} e^{-i\omega_j(\tau'-\tau)} + g_j^{\alpha\beta*} \hat{b}_j^{\alpha\dagger} e^{+i\omega_j(\tau'-\tau)}). \tag{C.58}$$

Transforming the integration variable in Eq. (C.57) finally yields Eq. (8.99) in the main part of this thesis.

Publications

- **J. F. Specht**, A. Knorr, and M. Richter. *Two-dimensional spectroscopy: An approach to distinguish Förster and Dexter transfer processes in coupled nanostructures*. Phys. Rev. B **91** (15), 155313 (2015).
- **J. F. Specht** and M. Richter. *Reconstruction of exciton wave functions of coupled quantum emitters including spin with ultrafast spectroscopy using localized nanooptical fields*. Appl. Phys. B **122** (4), 97 (2016).
- K. Hao, **J. F. Specht**, P. Nagler, L. Xu, K. Tran, A. Singh, C. K. Dass, C. Schüller, T. Korn, M. Richter, A. Knorr, X. Li, and G. Moody. *Neutral and charged inter-valley biexcitons in monolayer MoSe₂*. Nat. Commun. **8**, 15552 (2017).
- V. Delmonte, **J. F. Specht**, T. Jakubczyk, S. Höfling, M. Kamp, C. Schneider, W. Langbein, G. Nogues, M. Richter, and J. Kasprzak. *Coherent coupling of individual quantum dots measured with phase-referenced two-dimensional spectroscopy: Photon echo versus double quantum coherence*. Phys. Rev. B (R) **96** (4), 041124 (2017).
- **J. F. Specht**, E. Verdenhalven, B. Bieniek, P. Rinke, A. Knorr, and M. Richter. *Theory of Excitation Transfer between Two-Dimensional Semiconductor and Molecular Layers*. Phys. Rev. Applied **9**(4), 044025 (2018).

Proceedings

- **J. F. Specht** and M. Richter. *Signatures of Förster and Dexter transfer processes in coupled nanostructures for linear and two-dimensional coherent optical spectroscopy*. Proc. SPIE **9361**, 93610A (2015).
- **J. F. Specht**, E. Verdenhalven, S. Theuerholz, A. Knorr, and M. Richter. *Theory of coupled hybrid inorganic/organic systems: Excitation transfer at semiconductor/molecule interfaces*. Proc. SPIE **9746**, 97460F (2016).

Selbständigkeitserklärung

Hiermit erkläre ich, dass ich die vorliegende Arbeit selbstständig und eigenhändig sowie ohne unerlaubte fremde Hilfe und ausschließlich unter Verwendung der aufgeführten Quellen und Hilfsmittel angefertigt habe.

Berlin, den

Judith Specht

Danksagung

Mein erster Dank gilt meinem Doktorvater Prof. Andreas Knorr, der diese Arbeit erst ermöglicht hat und meine Forschung in den zurückliegenden Jahren nach Kräften und in inspirierender Weise unterstützt und gefördert hat. In diesem Sinne danke ich ebenfalls Dr. Marten Richter für die hervorragende Betreuung meiner Arbeit, unzählige fachliche Diskussionen über konzeptionelle Fragen bis hin zu kleinen Details sowie das Vertrauen, welches er mir stets entgegengebracht hat. Sein Ideenreichtum und sein untrügliches Gespür für physikalische und numerische Lösungsansätze haben entscheidend zum Gelingen dieser Arbeit beigetragen.

Mein Dank geht außerdem an Dr. Sylke Blumstengel, die sich als Zweitgutachterin dieser Arbeit zur Verfügung gestellt hat, sowie an Prof. Birgit Kanngießer für die Übernahme des Prüfungsvorsitzes.

Ich danke der Deutschen Forschungsgemeinschaft für die Finanzierung dieser Arbeit und die Ermöglichung zahlreicher Konferenzaufenthalte. Zudem gilt mein Dank Xiaoqin (Elaine) Li, Galan Moody, Jacek Kaprzak und Sylke Blumstengel für die fruchtbare Zusammenarbeit an der spannenden Schnittstelle zwischen Experiment und Theorie, deren Ergebnisse einen wesentlichen Teil dieser Arbeit bilden. In diesem Sinne danke ich außerdem Björn Bieniek, Patrick Rinke und Eike Verdenhalven für die Zusammenarbeit.

Ein herzliches Dankeschön geht an die gesamte AG Knorr für die tolle Arbeitsatmosphäre und den vielfältigen wissenschaftlichen Austausch. An dieser Stelle sei insbesondere meinen Bürokollegen Alexander Carmele, Nicolas Naumann, Leon Droenner, Torben Winzer und Julia Kabuß gedankt – unser Büro ist ein liebenswerter, inspirierender und Süßkram-verschlingender Mikrokosmos. Für ihren fachlichen Rat danke ich insbesondere Alexander Carmele, Sandra Kuhn, Nicolas Naumann und Anke Zimmermann. Für das sorgfältige Korrekturlesen meiner Arbeit schulde ich Alexander Carmele, Sandra Kuhn, Anke Zimmermann und Franz Knuth meine tiefe Dankbarkeit. Anke und Sandra danke ich außerdem für ihren freundschaftlichen Beistand in all der Zeit und für unsere wunderbare frühe Mensagruppe.

Unseren Netzwerkadministratoren Peter Orłowski, Marten Richter und Nicolas Naumann gebührt Dank für ihre Unterstützung bei Computerproblemen aller Art. Darüber hinaus möchte ich mich bei Kristina Ludwig, Heike Klemz, Andrea Schulze und Norma Rettich für ihre Hilfe in allen administrativen Angelegenheiten bedanken.

Meinen Eltern und Geschwistern danke ich von ganzem Herzen für ihre unermüdliche Unterstützung und dafür, dass sie mich stets nach Kräften in meinem Weg bestärkt haben. Zuletzt und im Besonderen möchte ich Franz dafür danken, dass er immer für mich da war und an mich geglaubt hat und dass das Leben mit ihm so wunderbar ist.

Bibliography

- [Abr75] A. A. Abrikosov, L. P. Gorkov, and I. E. Dzyaloshinski. *Methods of Quantum Field Theory in Statistical Physics*. Dover Publications, New York (1975).
- [Abr09] D. Abramavicius, B. Palmieri, D. V. Voronine, F. Sanda, and S. Mukamel. *Coherent Multidimensional Optical Spectroscopy of Excitons in Molecular Aggregates; Quasiparticle versus Supermolecule Perspectives*. Chem. Rev. **109**, 2350 (2009).
- [Aes11] M. Aeschlimann, T. Brixner, A. Fischer, C. Kramer, P. Melchior, W. Pfeiffer, C. Schneider, C. Strüber, P. Tuchscherer, and D. V. Voronine. *Coherent Two-Dimensional Nanoscopy*. Science **333**, 1723 (2011).
- [Agr94] V. Agranovich, R. Atanasov, and F. Bassani. *Hybrid interface excitons in organic-inorganic quantum wells*. Solid State Commun. **92**, 295 (1994).
- [Agr98] V. M. Agranovich, D. M. Basko, G. C. L. Rocca, and F. Bassani. *Excitons and optical nonlinearities in hybrid organic-inorganic nanostructures*. J. Phys.: Condens Matter **10**, 9369 (1998).
- [Ako06] N. Akopian, N. H. Lindner, E. Poem, Y. Berlatzky, J. Avron, D. Gershoni, B. D. Gerardot, and P. M. Petroff. *Entangled Photon Pairs from Semiconductor Quantum Dots*. Phys. Rev. Lett. **96**, 130501 (2006).
- [Ard16] P.-L. Ardelt, K. Gawarecki, K. Müller, A. M. Waeber, A. Bechtold, K. Oberhofer, J. M. Daniels, F. Klotz, M. Bichler, T. Kuhn, H. J. Krenner, P. Machnikowski, and J. J. Finley. *Coulomb Mediated Hybridization of Excitons in Coupled Quantum Dots*. Phys. Rev. Lett. **116**, 077401 (2016).
- [Axt94] V. M. Axt and A. Stahl. *A dynamics-controlled truncation scheme for the hierarchy of density matrices in semiconductor optics*. Z. Phys. B. **93**, 195 (1994).
- [Axt04] V. M. Axt and T. Kuhn. *Femtosecond spectroscopy in semiconductors: a key to coherences, correlations and quantum kinetics*. Rep. Prog. Phys. **67**, 433 (2004).
- [Bac98] U. Bach, D. Lupo, P. Comte, J. E. Moser, F. Weissörtel, J. Salbeck, H. Spreitzer, and M. Grätzel. *Solid-state dye-sensitized mesoporous TiO₂ solar cells with high photon-to-electron conversion efficiencies*. Nature **395**, 583 (1998).
- [Bal15a] S. Balay, S. Abhyankar, M. F. Adams, J. Brown, P. Brune, K. Buschelman, L. Dalcin, V. Eijkhout, W. D. Gropp, D. Kaushik, M. G. Knepley, L. C. McInnes, K. Rupp, and Barry. *PETSc Users Manual*. Tech. Rep. ANL-95/11 - Revision 3.6, Argonne National Laboratory (2015).
- [Bal15b] S. Balay, S. Abhyankar, M. F. Adams, J. Brown, P. Brune, K. Buschelman, L. Dalcin, V. Eijkhout, W. D. Gropp, D. Kaushik, M. G. Knepley, L. C. McInnes, K. Rupp, and Barry. *PETSc Web page*. <http://www.mcs.anl.gov/petsc> (2015).
- [Ban70] W. Band and J. L. Park. *The empirical determination of quantum states*. Found. Phys. **1**, 133 (1970).

- [Bao12] W. Bao, M. Melli, N. Caselli, F. Riboli, D. S. Wiersma, M. Staffaroni, H. Choo, D. F. Ogletree, S. Aloni, J. Bokor, S. Cabrini, F. Intonti, M. B. Salmeron, E. Yablonovitch, P. J. Schuck, and A. Weber-Bargioni. *Mapping Local Charge Recombination Heterogeneity by Multidimensional Nanospectroscopic Imaging*. Science **338**, 1317 (2012).
- [Bas88] G. Bastard. *Wave mechanics applied to semiconductor heterostructures* (1988).
- [Bas99] D. Basko, G. C. La Rocca, F. Bassani, and V. M. Agranovich. *Förster energy transfer from a semiconductor quantum well to an organic material overlayer*. Eur. Phys. J. B **8**, 353 (1999).
- [Bat62] T. B. Bateman. *Elastic Moduli of Single-Crystal Zinc Oxide*. J. Appl. Phys. **33**, 3309 (1962).
- [Bay01] M. Bayer, P. Hawrylak, K. Hinzer, S. Fafard, M. Korkusinski, Z. R. Wasilewski, O. Stern, and A. Forchel. *Coupling and Entangling of Quantum States in Quantum Dot Molecules*. Science **291**, 451 (2001).
- [Ben00] O. Benson, C. Santori, M. Pelton, and Y. Yamamoto. *Regulated and Entangled Photons from a Single Quantum Dot*. Phys. Rev. Lett. **84**, 2513 (2000).
- [Ber03] D. J. Bergman and M. I. Stockman. *Surface Plasmon Amplification by Stimulated Emission of Radiation: Quantum Generation of Coherent Surface Plasmons in Nanosystems*. Phys. Rev. Lett. **90**, 027402 (2003).
- [Ber13] T. C. Berkelbach, M. S. Hybertsen, and D. R. Reichman. *Theory of neutral and charged excitons in monolayer transition metal dichalcogenides*. Phys. Rev. B **88**, 045318 (2013).
- [Ber14] G. Berghäuser and E. Malic. *Analytical approach to excitonic properties of MoS₂*. Phys. Rev. B **89**, 125309 (2014).
- [Bes05] G. Bester, A. Zunger, and J. Shumway. *Broken symmetry and quantum entanglement of an exciton in In_xGa_{1-x}As/GaAs quantum dot molecules*. Phys. Rev. B **71**, 075325 (2005).
- [Bia09] P. Biagioni, J. S. Huang, L. Duò, M. Finazzi, and B. Hecht. *Cross Resonant Optical Antenna*. Phys. Rev. Lett. **102**, 256801 (2009).
- [Bia14] F. Bianchi, S. Sadofev, R. Schlesinger, B. Kobin, S. Hecht, N. Koch, F. Henneberger, and S. Blumstengel. *Cascade energy transfer versus charge separation in ladder-type oligo(p-phenylene)/ZnO hybrid structures for light-emitting applications*. Appl. Phys. Lett. **105**, 233301 (2014).
- [Bio00] E. Biolatti, R. C. Iotti, P. Zanardi, and F. Rossi. *Quantum Information Processing with Semiconductor Macroatoms*. Phys. Rev. Lett. **85**, 5647 (2000).
- [Blu06] S. Blumstengel, S. Sadofev, C. Xu, J. Puls, and F. Henneberger. *Converting Wannier into Frenkel Excitons in an Inorganic/Organic Hybrid Semiconductor Nanostructure*. Phys. Rev. Lett. **97**, 237401 (2006).
- [Blu08a] S. Blumstengel, S. Sadofev, and F. Henneberger. *Electronic coupling of optical excitations in organic/inorganic semiconductor hybrid structures*. New J. Phys. **10**, 065010 (2008).

- [Blu08b] S. Blumstengel, S. Sadofev, C. Xu, J. Puls, R. L. Johnson, H. Glowatzki, N. Koch, and F. Henneberger. *Electronic coupling in organic-inorganic semiconductor hybrid structures with type-II energy level alignment*. Phys. Rev. B **77**, 085323 (2008).
- [Blu09] V. Blum, R. Gehrke, F. Hanke, P. Havu, V. Havu, X. Ren, K. Reuter, and M. Scheffler. *Ab initio molecular simulations with numeric atom-centered orbitals*. Comput. Phys. Commun. **180**, 2175 (2009).
- [Blu10] S. Blumstengel, H. Glowatzki, S. Sadofev, N. Koch, S. Kowarik, J. P. Rabe, and F. Henneberger. *Band-offset engineering in organic/inorganic semiconductor hybrid structures*. Phys. Chem. Chem. Phys. **12**, 11642 (2010).
- [Bon98] N. H. Bonadeo, J. Erland, D. Gammon, D. Park, D. S. Katzer, and D. G. Steel. *Coherent Optical Control of the Quantum State of a Single Quantum Dot*. Science **282**, 1473 (1998).
- [Bor01] P. Borri, W. Langbein, S. Schneider, U. Woggon, R. L. Sellin, D. Ouyang, and D. Bimberg. *Ultralong Dephasing Time in InGaAs Quantum Dots*. Phys. Rev. Lett. **87**, 157401 (2001).
- [Bre02] H.-P. Breuer and F. Petruccione. *The Theory of Open Quantum Systems*. Oxford University Press, Oxford (2002).
- [Bri05] T. Brixner, F. J. García de Abajo, J. Schneider, and W. Pfeiffer. *Nanosopic Ultrafast Space-Time-Resolved Spectroscopy*. Phys. Rev. Lett. **95**, 093901 (2005).
- [Bri08] A. D. Bristow, D. Karaiskaj, X. Dai, and S. T. Cundiff. *All-optical retrieval of the global phase for two-dimensional Fourier-transform spectroscopy*. Opt. Express **16**, 18017 (2008).
- [Bri10] D. Brinks, F. D. Stefani, F. Kulzer, R. Hildner, T. H. Taminiau, Y. Avlasevich, K. Müllen, and N. F. van Hulst. *Visualizing and controlling vibrational wave packets of single molecules*. Nature **465**, 905 (2010).
- [But04] S. Butscher. *Theory of the Non-markovian Intersubband Dynamics of Semiconductor Quantum Wells*. Diplomarbeit, Technische Universität Berlin (2004).
- [But05] S. Butscher, J. Förstner, I. Waldmüller, and A. Knorr. *Ultrafast electron-phonon interaction of intersubband transitions: Quantum kinetics from adiabatic following to Rabi-oscillations*. Phys. Rev. B **72**, 045314 (2005).
- [But13] S. Z. Butler, S. M. Hollen, L. Cao, Y. Cui, J. A. Gupta, H. R. Guti rrez, T. F. Heinz, S. S. Hong, J. Huang, A. F. Ismach, E. Johnston-Halperin, M. Kuno, V. V. Plashnitsa, R. D. Robinson, R. S. Ruoff, S. Salahuddin, J. Shan, L. Shi, M. G. Spencer, M. Terrones, W. Windl, and J. E. Goldberger. *Progress, Challenges, and Opportunities in Two-Dimensional Materials Beyond Graphene*. ACS Nano **7**, 2898 (2013).
- [Cai15] Y. Cai, S. Ikeda, K. Nakagawa, H. Kikuchi, N. Shimidzu, and T. Ishibashi. *Strong enhancement of nano-sized circularly polarized light using an aperture antenna with V-groove structures*. Opt. Lett. **40**, 1298 (2015).
- [Cam09] C. Campa a, B. Mussard, and T. K. Woo. *Electrostatic Potential Derived Atomic Charges for Periodic Systems Using a Modified Error Functional*. J. Chem. Theory Comput. **5**, 2866 (2009).

- [Cao12] T. Cao, G. Wang, W. Han, H. Ye, C. Zhu, J. Shi, Q. Niu, P. Tan, E. Wang, B. Liu, and J. Feng. *Valley-selective circular dichroism of monolayer molybdenum disulphide*. Nat. Commun. **3**, 887 (2012).
- [Car99] H. Carmichael. *Statistical Methods in Quantum Optics 1 - Master Equation and Fokker-Planck Equations*. Springer, Berlin Heidelberg New York (1999).
- [Car10] A. Carmele, F. Milde, M.-R. Dachner, M. B. Harouni, R. Roknizadeh, M. Richter, and A. Knorr. *Formation dynamics of an entangled photon pair: A temperature-dependent analysis*. Phys. Rev. B **81**, 195319 (2010).
- [Cas16] E. Cassette, J. C. Dean, and G. D. Scholes. *Two-Dimensional Visible Spectroscopy For Studying Colloidal Semiconductor Nanocrystals*. Small **12**, 2234 (2016).
- [Cas17] M. C. Castro. *Numerical simulations of the electron-phonon interaction in two-dimensional semiconductor nanostructures*. Master's thesis, Technische Universität Berlin (2017).
- [Che01] D. S. Chemla and J. Shah. *Many-body and correlation effects in semiconductors*. Nature **411**, 549 (2001).
- [Che14] A. Chernikov, T. C. Berkelbach, H. M. Hill, A. Rigosi, Y. Li, O. B. Aslan, D. R. Reichman, M. S. Hybertsen, and T. F. Heinz. *Exciton Binding Energy and Nonhydrogenic Rydberg Series in Monolayer WS₂*. Phys. Rev. Lett. **113**, 076802 (2014).
- [Cho99] W. W. Chow and S. W. Koch. *Semiconductor-Laser Fundamentals: Physics of the Gain Materials*. Springer, Berlin (1999).
- [Cho08] M. Cho. *Coherent Two-Dimensional Optical Spectroscopy*. Chem. Rev. **108**, 1331 (2008). PMID: 18363410.
- [Cho12] W. W. Chow, S. W. Koch, and M. Sargent III. *Semiconductor-Laser Physics*. Springer Science & Business Media (2012).
- [Chr10] N. Christensson, F. Milota, A. Nemeth, I. Pugliesi, E. Riedle, J. Sperling, T. Pullerits, H. F. Kauffmann, and J. Hauer. *Electronic Double-Quantum Coherences and Their Impact on Ultrafast Spectroscopy: The Example of β -Carotene*. J. Phys. Chem. Lett. **1**, 3366 (2010).
- [Coh92] C. Cohen-Tannoudji and a. G. G. Jacques Dupont-Roc. *Atom-Photon-Interactions*. John Wiley and Sons, Inc. (1992).
- [Cun94] S. T. Cundiff. *Effects of correlation between inhomogeneously broadened transitions on quantum beats in transient four-wave mixing*. Phys. Rev. A **49**, 3114 (1994).
- [Cur08] C. Curutchet, A. Franceschetti, A. Zunger, and G. D. Scholes. *Examining Förster Energy Transfer for Semiconductor Nanocrystalline Quantum Dot Donors and Acceptors*. J. Phys. Chem. C **112**, 13336 (2008).
- [Czy04] G. Czycholl. *Theoretische Festkörperphysik*. Springer, Berlin (2004).
- [Dai12] X. Dai, M. Richter, H. Li, A. D. Bristow, C. Falvo, S. Mukamel, and S. T. Cundiff. *Two-Dimensional Double-Quantum Spectra Reveal Collective Resonances in an Atomic Vapor*. Phys. Rev. Lett. **108**, 193201 (2012).

- [Dan06] J. Danckwerts, K. J. Ahn, J. Förstner, and A. Knorr. *Theory of ultrafast nonlinear optics of Coulomb-coupled semiconductor quantum dots: Rabi oscillations and pump-probe spectra*. Phys. Rev. B **73**, 165318 (2006).
- [Del17] V. Delmonte, J. F. Specht, T. Jakubczyk, S. Höfling, M. Kamp, C. Schneider, W. Langbein, G. Nogues, M. Richter, and J. Kasprzak. *Coherent coupling of individual quantum dots measured with phase-referenced two-dimensional spectroscopy: Photon echo versus double quantum coherence*. Phys. Rev. B **96**, 041124 (2017).
- [Der16] H. Dery. *Theory of intervalley Coulomb interactions in monolayer transition-metal dichalcogenides*. Phys. Rev. B **94**, 075421 (2016).
- [Din92] J. Ding, H. Jeon, T. Ishihara, M. Hagerott, A. V. Nurmikko, H. Luo, N. Samarth, and J. Furdyna. *Excitonic gain and laser emission in ZnSe-based quantum wells*. Phys. Rev. Lett. **69**, 1707 (1992).
- [Din10] F. Ding, R. Singh, J. D. Plumhof, T. Zander, V. Křápek, Y. H. Chen, M. Benyoucef, V. Zwiller, K. Dörr, G. Bester, A. Rastelli, and O. G. Schmidt. *Tuning the Exciton Binding Energies in Single Self-Assembled InGaAs/GaAs Quantum Dots by Piezoelectric-Induced Biaxial Stress*. Phys. Rev. Lett. **104**, 067405 (2010).
- [Dju06] A. B. Djurišić and Y. H. Leung. *Optical Properties of ZnO Nanostructures*. Small **2**, 944 (2006).
- [Eng07] G. S. Engel, T. R. Calhoun, E. L. Read, T.-K. Ahn, T. Mancal, Y.-C. Cheng, R. E. Blankenship, and G. R. Fleming. *Evidence for wavelike energy transfer through quantum coherence in photosynthetic systems*. Nature **446**, 782 (2007).
- [Ess01] A. Esser, R. Zimmermann, and E. Runge. *Theory of Trion Spectra in Semiconductor Nanostructures*. Phys. Stat. Sol. B **227**, 317 (2001).
- [Eye15] M. Eyer, S. Sadofev, J. Puls, and S. Blumstengel. *Charge transfer excitons at ZnMgO/P3HT heterojunctions: Relation to photovoltaic performance*. Appl. Phys. Lett. **107**, 221602 (2015).
- [Fan57] U. Fano. *Description of States in Quantum Mechanics by Density Matrix and Operator Techniques*. Rev. Mod. Phys. **29**, 74 (1957).
- [Fey51] R. P. Feynman. *An Operator Calculus Having Applications in Quantum Electrodynamics*. Phys. Rev. **84**, 108 (1951).
- [FFT] *FFTW Website*. <http://www.fftw.org/>.
- [Fic90] E. Fick and G. Sauermann. *The Quantum Statistics of Dynamic Processes*. Springer, Berlin (1990).
- [Fin12] B. P. Fingerhut, M. Richter, J.-W. Luo, A. Zunger, and S. Mukamel. *Dissecting biexciton wave functions of self-assembled quantum dots by double-quantum-coherence optical spectroscopy*. Phys. Rev. B **86**, 235303 (2012).
- [Fin13] B. P. Fingerhut, M. Richter, J.-W. Luo, A. Zunger, and S. Mukamel. *2D optical photon echo spectroscopy of a self-assembled quantum dot*. Ann. Phys. **525**, 31 (2013).
- [Fon98] L. R. C. Fonseca, J. L. Jimenez, J. P. Leburton, and R. M. Martin. *Self-consistent calculation of the electronic structure and electron-electron interaction in self-assembled InAs-GaAs quantum dot structures*. Phys. Rev. B **57**, 4017 (1998).

- [För48] T. Förster. *Zwischenmolekulare Energiewanderung und Fluoreszenz*. Annalen der Physik **437**, 55 (1948).
- [For94] B. Fornberg and D. M. Sloan. *A review of pseudospectral methods for solving partial differential equations*. Acta Numerica **3**, 203 (1994).
- [Fra16] F. Fras, Q. Mermillod, G. Nogues, C. Hoarau, C. Schneider, M. Kamp, S. Höfling, W. Langbein, and J. Kasprzak. *Multi-wave coherent control of a solid-state single emitter*. Nat. Photonics **10**, 155 (2016).
- [Fre31] J. Frenkel. *On the Transformation of light into Heat in Solids. I*. Phys. Rev. **37**, 17 (1931).
- [Fre98] M. Freyberger. *Quantum state measurements and complementarity*. Phys. Lett. A **242**, 193 (1998).
- [Fri15] S. Friede, S. Kuehn, S. Sadofev, S. Blumstengel, F. Henneberger, and T. Elsaesser. *Nanoscale transport of surface excitons at the interface between ZnO and a molecular monolayer*. Phys. Rev. B **91**, 121415 (2015).
- [Gal68] W. Gale, E. Guth, and G. T. Trammell. *Determination of the Quantum State by Measurements*. Phys. Rev. **165**, 1434 (1968).
- [Gal98] S. M. Gallagher, A. W. Albrecht, J. D. Hybl, B. L. Landin, B. Rajaram, and D. M. Jonas. *Heterodyne detection of the complete electric field of femtosecond four-wave mixing signals*. J. Opt. Soc. Am. B **15**, 2338 (1998).
- [Gaw12] K. Gawarecki and P. Machnikowski. *Phonon-assisted relaxation between hole states in quantum dot molecules*. Phys. Rev. B **85**, 041305 (2012).
- [Ger05] B. D. Gerardot, S. Strauf, M. J. A. de Dood, A. M. Bychkov, A. Badolato, K. Hennessy, E. L. Hu, D. Bouwmeester, and P. M. Petroff. *Photon Statistics from Coupled Quantum Dots*. Phys. Rev. Lett. **95**, 137403 (2005).
- [Ger10] I. Gerhardt, G. Wrigge, J. Hwang, G. Zumofen, and V. Sandoghdar. *Coherent nonlinear single-molecule microscopy*. Phys. Rev. A **82**, 063823 (2010).
- [Gla14] M. M. Glazov, T. Amand, X. Marie, D. Lagarde, L. Bouet, and B. Urbaszek. *Exciton fine structure and spin decoherence in monolayers of transition metal dichalcogenides*. Phys. Rev. B **89**, 201302 (2014).
- [Göp31] M. Göppert-Mayer. *Über Elementarakte mit zwei Quantensprüngen*. Ann. Phys. **401**, 273 (1931).
- [Gro08] A. Grodecka, P. Machnikowski, and J. Förstner. *Phonon-assisted tunneling between singlet states in two-electron quantum dot molecules*. Phys. Rev. B **78**, 085302 (2008).
- [Gue02] T. Guenther, C. Lienau, T. Elsaesser, M. Glanemann, V. M. Axt, T. Kuhn, S. Eshlaghi, and A. D. Wieck. *Coherent Nonlinear Optical Response of Single Quantum Dots Studied by Ultrafast Near-Field Spectroscopy*. Phys. Rev. Lett. **89**, 057401 (2002).
- [Hak73] H. Haken. *Quantenfeldtheorie des Festkörpers*. Teubner Verlag, Stuttgart (1973).

- [Hao16] K. Hao, L. Xu, P. Nagler, A. Singh, K. Tran, C. K. Dass, C. Schüller, T. Korn, X. Li, and G. Moody. *Coherent and Incoherent Coupling Dynamics between Neutral and Charged Excitons in Monolayer MoSe₂*. Nano Lett. **16**, 5109 (2016).
- [Hao17] K. Hao, J. F. Specht, P. Nagler, L. Xu, K. Tran, A. Singh, C. K. Dass, C. Schüller, T. Korn, M. Richter, A. Knorr, X. Li, and G. Moody. *Neutral and charged inter-valley biexcitons in monolayer MoSe₂*. Nat. Commun. **8**, 15552 (2017).
- [Har12] B. E. Hardin, H. J. Snaith, and M. D. McGehee. *The renaissance of dye-sensitized solar cells*. Nat. Photonics **6**, 162 (2012).
- [Hau04] H. Haug and S. W. Koch. *Quantum Theory of the Optical and Electronic Properties of Semiconductors*. World Scientific, Singapore (2004).
- [He14] K. He, N. Kumar, L. Zhao, Z. Wang, K. F. Mak, H. Zhao, and J. Shan. *Tightly Bound Excitons in Monolayer WSe₂*. Phys. Rev. Lett. **113**, 026803 (2014).
- [Heg85] J. Hegarty and M. D. Sturge. *Studies of exciton localization in quantum-well structures by nonlinear-optical techniques*. J. Opt. Soc. Am. B **2**, 1143 (1985).
- [Hel11] J. Helbing and P. Hamm. *Compact implementation of Fourier transform two-dimensional IR spectroscopy without phase ambiguity*. J. Opt. Soc. Am. B **28**, 171 (2011).
- [Her05] V. Hernandez, J. E. Roman, and V. Vidal. *SLEPc: A Scalable and Flexible Toolkit for the Solution of Eigenvalue Problems*. ACM Trans. Math. Software **31**, 351 (2005).
- [Hey03] J. Heyd, G. E. Scuseria, and M. Ernzerhof. *Hybrid functionals based on a screened Coulomb potential*. J. Chem. Phys. **118**, 8207 (2003).
- [Hua09] J. S. Huang, D. V. Voronine, P. Tuchscherer, T. Brixner, and B. Hecht. *Deterministic spatiotemporal control of optical fields in nanoantennas and plasmonic circuits*. Phys. Rev. B **79**, 195441 (2009).
- [Hua16] J. Huang, T. B. Hoang, and M. H. Mikkelsen. *Probing the origin of excitonic states in monolayer WSe₂*. Sci. Rep. **6**, 22414 (2016).
- [Ima09] H. Imahori, T. Umeyama, and S. Ito. *Large π -Aromatic Molecules as Potential Sensitizers for Highly Efficient Dye-Sensitized Solar Cells*. Acc. Chem. Res. **42**, 1809 (2009). PMID: 19408942.
- [Its07] G. Itskos, G. Heliotis, P. G. Lagoudakis, J. Lupton, N. P. Barradas, E. Alves, S. Pereira, I. M. Watson, M. D. Dawson, J. Feldmann, R. Murray, and D. D. C. Bradley. *Efficient dipole-dipole coupling of Mott-Wannier and Frenkel excitons in (Ga,In)N quantum well/polyfluorene semiconductor heterostructures*. Phys. Rev. B **76**, 035344 (2007).
- [Jac98] L. Jacak, P. Hawrylak, and A. Wójs. *Quantum Dots*. Springer, New York (1998).
- [Jac99] J. D. Jackson. *Classical Electrodynamics*. John Wiley & Sons, New York, edn. 3rd (1999).
- [Jak16] T. Jakubczyk, V. Delmonte, S. Fischbach, D. Wigger, D. E. Reiter, Q. Mermillod, P. Schnauber, A. Kaganskiy, J.-H. Schulze, A. Strittmatter, S. Rodt, W. Langbein, T. Kuhn, S. Reitzenstein, and J. Kasprzak. *Impact of Phonons on Dephasing of Individual Excitons in Deterministic Quantum Dot Microlenses*. ACS Photonics **3**, 2461 (2016).

- [Jan07] A. Janotti and C. G. Van de Walle. *Absolute deformation potentials and band alignment of wurtzite ZnO, MgO, and CdO*. Phys. Rev. B **75**, 121201 (2007).
- [Jon03] D. M. Jonas. *Two-Dimensional Femtosecond Spectroscopy*. Annu. Rev. Phys. Chem. **54**, 425 (2003).
- [Kar10] D. Karaiskaj, A. D. Bristow, L. Yang, X. Dai, R. P. Mirin, S. Mukamel, and S. T. Cundiff. *Two-Quantum Many-Body Coherences in Two-Dimensional Fourier-Transform Spectra of Exciton Resonances in Semiconductor Quantum Wells*. Phys. Rev. Lett. **104**, 117401 (2010).
- [Kas10] J. Kasprzak, B. Patton, V. Savona, and W. Langbein. *Coherent coupling between distant excitons revealed by two-dimensional nonlinear hyperspectral imaging*. Nat. Photonics **5**, 57 (2010).
- [Kas13] J. Kasprzak, S. Portolan, A. Rastelli, L. Wang, J. D. Plumhof, O. G. Schmidt, and W. Langbein. *Vectorial nonlinear coherent response of a strongly confined exciton-biexciton system*. New J. Phys. **15**, 055006 (2013).
- [Kez16] R. Y. Kezerashvili and S. M. Tsiklauri. *Trion and Biexciton in Monolayer Transition Metal Dichalcogenides*. Few-Body Sys. **58**, 18 (2016).
- [Kid16] D. W. Kidd, D. K. Zhang, and K. Varga. *Binding energies and structures of two-dimensional excitonic complexes in transition metal dichalcogenides*. Phys. Rev. B **93**, 125423 (2016).
- [Kin09] A. Kinkhabwala, Z. Yu, S. Fan, Y. Avlasevich, K. Mullen, and W. E. Moerner. *Large single-molecule fluorescence enhancements produced by a bowtie nanoantenna*. Nat. Photonics **3**, 654 (2009).
- [Kla15] P. Klaer, G. Razinskas, M. Lehr, K. Krewer, F. Schertz, X.-F. Wu, B. Hecht, G. Schönhense, and H. J. Elmers. *Robustness of plasmonic angular momentum confinement in cross resonant optical antennas*. Appl. Phys. Lett. **106**, 261101 (2015).
- [Klo14] A. R. Klots, A. K. M. Newaz, B. Wang, D. Prasai, H. Krzyzanowska, J. Lin, D. Caudel, N. J. Ghimire, J. Yan, B. L. Ivanov, K. A. Velizhanin, A. Burger, D. G. Mandrus, N. H. Tolk, S. T. Pantelides, and K. I. Bolotin. *Probing excitonic states in suspended two-dimensional semiconductors by photocurrent spectroscopy*. Sci. Rep. **4**, 6608 (2014).
- [Kob12] B. Kobin, L. Grubert, S. Blumstengel, F. Henneberger, and S. Hecht. *Vacuum-processable ladder-type oligophenylenes for organic-inorganic hybrid structures: synthesis, optical and electrochemical properties upon increasing planarization as well as thin film growth*. J. Mater. Chem. **22**, 4383 (2012).
- [Kom12] H.-P. Komsa and A. V. Krasheninnikov. *Effects of confinement and environment on the electronic structure and exciton binding energy of MoS₂ from first principles*. Phys. Rev. B **86**, 241201 (2012).
- [Kou04] A. V. Koudinov, I. A. Akimov, Y. G. Kusrayev, and F. Henneberger. *Optical and magnetic anisotropies of the hole states in Stranski-Krastanov quantum dots*. Phys. Rev. B **70**, 241305 (2004).

- [Kre15] M. Krecik, S. M. Hein, M. Schoth, and M. Richter. *Protocol for detection of nonsecular conversion through coherent nanooptical spectroscopy*. Phys. Rev. A **92**, 052113 (2015).
- [Kru02] B. Krummheuer, V. M. Axt, and T. Kuhn. *Theory of pure dephasing and the resulting absorption line shape in semiconductor quantum dots*. Phys. Rev. B **65**, 195313 (2002).
- [Kuh94] T. Kuhn. *Ladungsträgerdynamik in Halbleitersystemen fern vom Gleichgewicht: Elektronisches Rauschen und kohärente Prozesse*. Verlag Shaker (1994). Zgl. Stuttgart Univ. Habil.-Schr.
- [Kui02] J. B. Kuipers. *Quaternions and Rotation Sequences: A Primer with Applications to Orbits, Aerospace and Virtual Reality*. Princeton University Press (2002).
- [Kuz07] I. Kuznetsova, T. Meier, S. T. Cundiff, and P. Thomas. *Determination of homogeneous and inhomogeneous broadening in semiconductor nanostructures by two-dimensional Fourier-transform optical spectroscopy*. Phys. Rev. B **76**, 153301 (2007).
- [Kyl15] I. Kylänpää and H.-P. Komsa. *Binding energies of exciton complexes in transition metal dichalcogenide monolayers and effect of dielectric environment*. Phys. Rev. B **92**, 205418 (2015).
- [Lan04] W. Langbein, P. Borri, U. Woggon, V. Stavarache, D. Reuter, and A. D. Wieck. *Control of fine-structure splitting and biexciton binding in $\text{In}_x\text{Ga}_{1-x}\text{As}$ quantum dots by annealing*. Phys. Rev. B **69**, 161301 (2004).
- [Lan05] W. Langbein and B. Patton. *Microscopic Measurement of Photon Echo Formation in Groups of Individual Excitonic Transitions*. Phys. Rev. Lett. **95**, 017403 (2005).
- [Lan07] W. Langbein and B. Patton. *Transient coherent nonlinear spectroscopy of single quantum dots*. J. Phys.: Condens. Matter **19**, 295203 (2007).
- [Lan10] W. Langbein. *Coherent optical spectroscopy of semiconductor nanostructures*. Riv. Nuovo Cimento Soc. Ital. Fis. **33**, 255 (2010).
- [Lee16] H. S. Lee, M. S. Kim, H. Kim, and Y. H. Lee. *Identifying multiexcitons in MoS_2 monolayers at room temperature*. Phys. Rev. B **93**, 140409 (2016).
- [Lef98] P. Lefebvre, J. Allègre, B. Gil, A. Kavokine, H. Mathieu, W. Kim, A. Salvador, A. Botchkarev, and H. Morkoç. *Recombination dynamics of free and localized excitons in $\text{GaN}/\text{Ga}_{0.93}\text{Al}_{0.07}\text{N}$ quantum wells*. Phys. Rev. B **57**, R9447 (1998).
- [Len04] A. S. Lenihan, M. V. Gurudev Dutt, D. G. Steel, S. Ghosh, and P. Bhattacharya. *Biexcitonic resonance in the nonlinear optical response of an InAs quantum dot ensemble*. Phys. Rev. B **69**, 045306 (2004).
- [Lia13] T. Liang, Y. Cui, J. Yu, W. Lin, Y. Yang, and G. Qian. *Large nonlinear optical activity from hybrid inorganic–organic films with fluorinated benzene as isolation group*. Thin Solid Films **544**, 407 (2013). The 6th International Conference on Technological Advances of Thin Films & Surface Coatings.
- [Lju17] M. P. Ljungberg, O. Vänskä, P. Koval, S. W. Koch, M. Kira, and D. Sánchez-Portal. *Charge-transfer states and optical transitions at the pentacene- TiO_2 interface*. New J. Phys. **19**, 033019 (2017).

- [Los98] D. Loss and D. P. DiVincenzo. *Quantum computation with quantum dots*. Phys. Rev. A **57**, 120 (1998).
- [Lov03] B. W. Lovett, J. H. Reina, A. Nazir, and G. A. D. Briggs. *Optical schemes for quantum computation in quantum dot molecules*. Phys. Rev. B **68**, 205319 (2003).
- [Mac09] P. Machnikowski and E. Rozbicki. *Phonon-assisted excitation transfer in quantum dot molecules: from quantum kinetics to transfer rates*. Phys. Stat. Sol. B **246**, 320 (2009).
- [Mad72] O. Madelung. *Festkörpertheorie I: Elementare Anregungen*. Springer Berlin Heidelberg (1972).
- [Mad06] M. E. Madjet, A. Abdurahman, and T. Renger. *Intermolecular Coulomb Couplings from Ab Initio Electrostatic Potentials: Application to Optical Transitions of Strongly Coupled Pigments in Photosynthetic Antennae and Reaction Centers*. J. Phys. Chem. B **110**, 17268 (2006).
- [Mah00] G. D. Mahan. *Many-Particle Physics*. Kluwer Academic/Plenum Publishers, New York (2000).
- [Mai14a] C. Mai, A. Barrette, Y. Yu, Y. G. Semenov, K. W. Kim, L. Cao, and K. Gundogdu. *Many-Body Effects in Valleytronics: Direct Measurement of Valley Lifetimes in Single-Layer MoS₂*. Nano Lett. **14**, 202 (2014).
- [Mai14b] S. Maier, P. Gold, A. Forchel, N. Gregersen, J. Mørk, S. Höfing, C. Schneider, and M. Kamp. *Bright single photon source based on self-aligned quantum dot-cavity systems*. Opt. Express **22**, 8136 (2014).
- [Mak10] K. F. Mak, C. Lee, J. Hone, J. Shan, and T. F. Heinz. *Atomically Thin MoS₂: A New Direct-Gap Semiconductor*. Phys. Rev. Lett. **105**, 136805 (2010).
- [Mak12] K. F. Mak, K. He, J. Shan, and T. F. Heinz. *Control of valley polarization in monolayer MoS₂ by optical helicity*. Nat. Nanotechn. **7**, 494 (2012).
- [Mak13] K. F. Mak, K. He, C. Lee, G. H. Lee, J. Hone, T. F. Heinz, and J. Shan. *Tightly bound trions in monolayer MoS₂*. Nat. Mater. **12**, 207 (2013).
- [Mal11] E. Malic, C. Weber, M. Richter, V. Atalla, T. Klamroth, P. Saalfrank, S. Reich, and A. Knorr. *Microscopic Model of the Optical Absorption of Carbon Nanotubes Functionalized with Molecular Spiropyran Photoswitches*. Phys. Rev. Lett. **106**, 097401 (2011).
- [May99] O. Mayrock, H.-J. Wünsche, F. Henneberger, C. Riva, V. A. Schweigert, and F. M. Peeters. *Weak localization of biexcitons in quantum wells*. Phys. Rev. B **60**, 5582 (1999).
- [May00] V. May and O. Kühn. *Charge and Energy Transfer Dynamics in Molecular Systems*. Wiley-VCH Verlag, Berlin (2000).
- [May15] M. Z. Mayers, T. C. Berkelbach, M. S. Hybertsen, and D. R. Reichman. *Binding energies and spatial structures of small carrier complexes in monolayer transition-metal dichalcogenides via diffusion Monte Carlo*. Phys. Rev. B **92**, 161404 (2015).
- [Med95] V. Meden, C. Wöhler, J. Fricke, and K. Schönhammer. *Hot-electron relaxation: An exactly solvable model and improved quantum kinetic equations*. Phys. Rev. B **52**, 5624 (1995).

- [Mer08] J. Merlein, M. Kahl, A. Zuschlag, A. Sell, A. Halm, J. Boneberg, P. Leiderer, A. Leitenstorfer, and R. Bratschitsch. *Nanomechanical control of an optical antenna*. Nat. Photonics **2**, 230 (2008).
- [Mer16a] Q. Mermillod, T. Jakubczyk, V. Delmonte, A. Delga, E. Peinke, J.-M. Gérard, J. Claudon, and J. Kasprzak. *Harvesting, Coupling, and Control of Single-Exciton Coherences in Photonic Waveguide Antennas*. Phys. Rev. Lett. **116**, 163903 (2016).
- [Mer16b] Q. Mermillod, D. Wigger, V. Delmonte, D. E. Reiter, C. Schneider, M. Kamp, S. Höfling, W. Langbein, T. Kuhn, G. Nogues, and J. Kasprzak. *Dynamics of excitons in individual InAs quantum dots revealed in four-wave mixing spectroscopy*. Optica **3**, 377 (2016).
- [Mey00] S. Meyer and V. Engel. *Non-perturbative wave-packet calculations of time-resolved four-wave-mixing signals*. Appl. Phys. B **71**, 293 (2000).
- [Mic03] P. Michler. *Single Quantum Dots: Fundamentals, Applications and New Concepts*, vol. 90. Springer, Berlin Heidelberg (2003).
- [Moo13a] G. Moody, R. Singh, H. Li, I. A. Akimov, M. Bayer, D. Reuter, A. D. Wieck, A. S. Bracker, D. Gammon, and S. T. Cundiff. *Influence of confinement on biexciton binding in semiconductor quantum dot ensembles measured with two-dimensional spectroscopy*. Phys. Rev. B **87**, 041304 (2013).
- [Moo13b] G. Moody, R. Singh, H. Li, I. A. Akimov, M. Bayer, D. Reuter, A. D. Wieck, and S. T. Cundiff. *Fifth-order nonlinear optical response of excitonic states in an InAs quantum dot ensemble measured with two-dimensional spectroscopy*. Phys. Rev. B **87**, 045313 (2013).
- [Moo14] G. Moody, I. A. Akimov, H. Li, R. Singh, D. R. Yakovlev, G. Karczewski, M. Wiater, T. Wojtowicz, M. Bayer, and S. T. Cundiff. *Coherent Coupling of Excitons and Trions in a Photoexcited CdTe/CdMgTe Quantum Well*. Phys. Rev. Lett. **112**, 097401 (2014).
- [Muk95] S. Mukamel. *Principles of Nonlinear Optical Spectroscopy*. Oxford University Press, New York (1995).
- [Muk00] S. Mukamel. *Multidimensional Femtosecond Correlation Spectroscopies of Electronic and Vibrational Excitations*. Annu. Rev. Phys. Chem. **51**, 691 (2000).
- [Muk11] S. Mukamel and M. Richter. *Multidimensional phase-sensitive single-molecule spectroscopy with time-and-frequency-gated fluorescence detection*. Phys. Rev. A **83**, 013815 (2011).
- [Nar15] G. Nardin, T. M. Autry, G. Moody, R. Singh, H. Li, and S. T. Cundiff. *Multi-dimensional coherent optical spectroscopy of semiconductor nanostructures: Collinear and non-collinear approaches*. J. Appl. Phys. **117**, 112804 (2015).
- [Nev08] A. A. R. Neves, A. Camposo, R. Cingolani, and D. Pisignano. *Interaction Scheme and Temperature Behavior of Energy Transfer in a Light-Emitting Inorganic-Organic Composite System*. Adv. Funct. Mater. **18**, 751 (2008).
- [Nie00] M. A. Nielsen and I. L. Chuang. *Quantum Computation and Quantum Information*. Cambridge University Press, Cambridge (2000).

- [Nog09] M. A. Noginov, G. Zhu, A. M. Belgrave, R. Bakker, V. M. Shalaev, E. E. Narimanov, S. Stout, E. Herz, T. Suteewong, and U. Wiesner. *Demonstration of a spaser-based nanolaser*. Nature **460**, 1110 (2009).
- [Nov11] L. Novotny. *From near-field optics to optical antennas*. Physics Today **64**, 47 (2011).
- [Ost12] I. A. Ostapenko, G. Hönig, S. Rodt, A. Schliwa, A. Hoffmann, D. Bimberg, M.-R. Dachner, M. Richter, A. Knorr, S. Kako, and Y. Arakawa. *Exciton acoustic-phonon coupling in single GaN/AlN quantum dots*. Phys. Rev. B **85**, 081303 (2012).
- [Özg05] Ü. Özgür, Y. I. Alivov, C. Liu, A. Teke, M. A. Reshchikov, S. Doğan, V. Avrutin, S.-J. Cho, and H. Morkoç. *A comprehensive review of ZnO materials and devices*. J. Appl. Phys. **98**, 041301 (2005).
- [Par05] G. Parascandolo and V. Savona. *Long-range radiative interaction between semiconductor quantum dots*. Phys. Rev. B **71**, 045335 (2005).
- [Pat06] B. Patton, W. Langbein, U. Woggon, L. Maingault, and H. Mariette. *Time- and spectrally-resolved four-wave mixing in single CdTe/ZnTe quantum dots*. Phys. Rev. B **73**, 235354 (2006).
- [Pau60] L. Pauling. *The Nature of the Chemical Bond and the Structure of Molecules and Crystals: An Introduction to Modern Structural Chemistry*. Cornell University Press, Ithaca, New York, edn. 3rd (1960).
- [Pet04] B. Pettinger, B. Ren, G. Picardi, R. Schuster, and G. Ertl. *Nanoscale Probing of Adsorbed Species by Tip-Enhanced Raman Spectroscopy*. Phys. Rev. Lett. **92**, 096101 (2004).
- [Pie15] F. Piersimoni, R. Schlesinger, J. Benduhn, D. Spoltore, S. Reiter, I. Lange, N. Koch, K. Vandewal, and D. Neher. *Charge Transfer Absorption and Emission at ZnO/Organic Interfaces*. J. Phys. Chem. Lett. **6**, 500 (2015).
- [Ple15] T. Plehn, D. Ziemann, J. Megow, and V. May. *Frenkel to Wannier–Mott Exciton Transition: Calculation of FRET Rates for a Tubular Dye Aggregate Coupled to a CdSe Nanocrystal*. J. Phys. Chem. B **119**, 7467 (2015).
- [Ple16] G. Plechinger, P. Nagler, A. Arora, A. Granados del Águila, M. V. Ballottin, T. Frank, P. Steinleitner, M. Gmitra, J. Fabian, P. C. M. Christianen, R. Bratschitsch, C. Schüller, and T. Korn. *Excitonic Valley Effects in Monolayer WS₂ under High Magnetic Fields*. Nano Lett. **16**, 7899 (2016).
- [Qia15] Y. Qiao, F. Polzer, H. Kirmse, E. Steeg, S. Kühn, S. Friede, S. Kirstein, and J. P. Rabe. *Nanotubular J-Aggregates and Quantum Dots Coupled for Efficient Resonance Excitation Energy Transfer*. ACS Nano **9**, 1552 (2015).
- [Qiu13] D. Y. Qiu, F. H. da Jornada, and S. G. Louie. *Optical Spectrum of MoS₂: Many-Body Effects and Diversity of Exciton States*. Phys. Rev. Lett. **111**, 216805 (2013).
- [Ram10] A. J. Ramsay. *A review of the coherent optical control of the exciton and spin states of semiconductor quantum dots*. Semicond. Sci. Technol. **25**, 103001 (2010).
- [Ram12] A. Ramasubramaniam. *Large excitonic effects in monolayers of molybdenum and tungsten dichalcogenides*. Phys. Rev. B **86**, 115409 (2012).
- [Red57] A. G. Redfield. *On the theory of relaxation processes*. IBM J. Res. Dev. **1**, 19 (1957).

- [Ren02] T. Renger and R. A. Marcus. *On the relation of protein dynamics and exciton relaxation in pigment-protein complexes: An estimation of the spectral density and a theory for the calculation of optical spectra*. J. Chem. Phys. **116**, 9997 (2002).
- [Ric05] M. Richter. *Quantentheorie der Terahertz-Emission laserinduzierter Plasmen*. Master's thesis, Technische Universität Berlin (2005).
- [Ric06] M. Richter, K. J. Ahn, A. Knorr, A. Schliwa, D. Bimberg, M. E.-A. Madjet, and T. Renger. *Theory of excitation transfer in coupled nanostructures - from quantum dots to light harvesting complexes*. Phys. Stat. Sol. B **243**, 2302 (2006).
- [Ric07] M. Richter, T. Renger, G. Renger, and A. Knorr. *Nonperturbative theory for the optical response to strong light of the light harvesting complex II of plants: Saturation of the fluorescence quantum yield*. J. Chem. Phys. **127**, 075105 (2007).
- [Ric12] M. Richter, F. Schlosser, M. Schoth, S. Burger, F. Schmidt, A. Knorr, and S. Mukamel. *Reconstruction of the wave functions of coupled nanoscopic emitters using a coherent optical technique*. Phys. Rev. B **86**, 085308 (2012).
- [Ric13] M. Richter. *Spatially localized spectroscopy for examining the internal structure of coupled nanostructures*. Phys. Stat. Sol. B **250**, 1760 (2013).
- [Ros13] J. S. Ross, S. Wu, H. Yu, N. J. Ghimire, A. M. Jones, G. Aivazian, J. Yan, D. G. Mandrus, D. Xiao, W. Yao, and X. Xu. *Electrical control of neutral and charged excitons in a monolayer semiconductor*. Nat. Commun. **4**, 1474 (2013).
- [Sal10] C. L. Salter, R. M. Stevenson, I. Farrer, C. A. Nicoll, D. A. Ritchie, and A. J. Shields. *An entangled-light-emitting diode*. Nature **465**, 594 (2010).
- [San02] D. Sanvitto, D. M. Whittaker, A. J. Shields, M. Y. Simmons, D. A. Ritchie, and M. Pepper. *Origin of the Oscillator Strength of the Triplet State of a Trion in a Magnetic Field*. Phys. Rev. Lett. **89**, 246805 (2002).
- [Sch94] J. Schilp, T. Kuhn, and G. Mahler. *Electron-phonon quantum kinetics in pulse-excited semiconductors: Memory and renormalization effects*. Phys. Rev. B **50**, 5435 (1994).
- [Sch03] G. D. Scholes. *Long-Range Resonance Energy Transfer in Molecular Systems*. Annu. Rev. Phys. Chem. **54**, 57 (2003).
- [Sch04] G. D. Scholes. *Selection rules for probing biexcitons and electron spin transitions in isotropic quantum dot ensembles*. J. Chem. Phys. **121**, 10104 (2004).
- [Sch12] M. Schoth, M. Richter, A. Knorr, and T. Renger. *Line Narrowing of Excited-State Transitions in Nonlinear Polarization Spectroscopy: Application to Water-Soluble Chlorophyll-Binding Protein*. Phys. Rev. Lett. **108**, 178104 (2012).
- [Sch13] F. Schlosser, A. Knorr, S. Mukamel, and M. Richter. *Using localized double-quantum-coherence spectroscopy to reconstruct the two-exciton wave function of coupled quantum emitters*. New J. Phys. **15**, 025004 (2013).
- [Sch15] R. Schlesinger, F. Bianchi, S. Blumstengel, C. Christodoulou, R. Ovsyannikov, B. Kobin, K. Moudgil, S. Barlow, S. Hecht, S. Marder, et al. *Efficient light emission from inorganic and organic semiconductor hybrid structures by energy-level tuning*. Nat. Commun. **6**, 6754 (2015).

- [Seg05] R. Seguin, A. Schliwa, S. Rodt, K. Pötschke, U. W. Pohl, and D. Bimberg. *Size-Dependent Fine-Structure Splitting in Self-Organized InAs/GaAs Quantum Dots*. Phys. Rev. Lett. **95**, 257402 (2005).
- [Sei95] L. Seidner, G. Stock, and W. Domcke. *Nonperturbative approach to femtosecond spectroscopy: General theory and application to multidimensional nonadiabatic photoisomerization processes*. J. Chem. Phys. **103**, 3998 (1995).
- [Ser01] R. A. Sergeev and R. A. Suris. *Singlet and triplet states of X^+ and X^- trions in two-dimensional quantum wells*. Nanotechnology **12**, 597 (2001).
- [Sha15] J. Shang, X. Shen, C. Cong, N. Peimyoo, B. Cao, M. Eginligil, and T. Yu. *Observation of Excitonic Fine Structure in a 2D Transition-Metal Dichalcogenide Semiconductor*. ACS Nano **9**, 647 (2015).
- [Shi12] R. Shimada, B. Urban, M. Sharma, A. Singh, V. Avrutin, H. Morkoç, and A. Neogi. *Energy transfer in ZnO-anthracene hybrid structure*. Opt. Mater. Express **2**, 526 (2012).
- [Shu12] M. D. Shulman, O. E. Dial, S. P. Harvey, H. Bluhm, V. Umansky, and A. Yacoby. *Demonstration of Entanglement of Electrostatically Coupled Singlet-Triplet Qubits*. Science **336**, 202 (2012).
- [Sia01] K. Siantidis, V. M. Axt, and T. Kuhn. *Dynamics of exciton formation for near band-gap excitations*. Phys. Rev. B **65**, 035303 (2001).
- [Sie10] M. E. Siemens, G. Moody, H. Li, A. D. Bristow, and S. T. Cundiff. *Resonance lineshapes in two-dimensional Fourier transform spectroscopy*. Opt. Express **18**, 17699 (2010).
- [Sie15] E. J. Sie, A. J. Frenzel, Y.-H. Lee, J. Kong, and N. Gedik. *Intervalley biexcitons and many-body effects in monolayer MoS₂*. Phys. Rev. B **92**, 125417 (2015).
- [Sin14] A. Singh, G. Moody, S. Wu, Y. Wu, N. J. Ghimire, J. Yan, D. G. Mandrus, X. Xu, and X. Li. *Coherent Electronic Coupling in Atomically Thin MoSe₂*. Phys. Rev. Lett. **112**, 216804 (2014).
- [Sin16] A. Singh, G. Moody, K. Tran, M. E. Scott, V. Overbeck, G. Berghäuser, J. Schaibley, E. J. Seifert, D. Pleskot, N. M. Gabor, J. Yan, D. G. Mandrus, M. Richter, E. Malic, X. Xu, and X. Li. *Trion formation dynamics in monolayer transition metal dichalcogenides*. Phys. Rev. B **93**, 041401 (2016).
- [Sin17] R. Singh, M. Richter, G. Moody, M. E. Siemens, H. Li, and S. T. Cundiff. *Localization dynamics of excitons in disordered semiconductor quantum wells*. Phys. Rev. B **95**, 235307 (2017).
- [Sit12] A. Sitek and P. Machnikowski. *Vacuum-induced coherence in quantum dot systems*. Phys. Rev. B **86**, 205315 (2012).
- [Sla34] J. C. Slater. *The Electronic Structure of Metals*. Rev. Mod. Phys. **6**, 209 (1934).
- [Spe15] J. F. Specht, A. Knorr, and M. Richter. *Two-dimensional spectroscopy: An approach to distinguish Förster and Dexter transfer processes in coupled nanostructures*. Phys. Rev. B **91**, 155313 (2015).

- [Spe16a] J. Specht, E. Verdenhalven, S. Theuerholz, A. Knorr, and M. Richter. *Theory of coupled hybrid inorganic/organic systems: Excitation transfer at semiconductor/molecule interfaces*. Proc. SPIE **9746**, 97460F (2016).
- [Spe16b] J. F. Specht and M. Richter. *Reconstruction of exciton wave functions of coupled quantum emitters including spin with ultrafast spectroscopy using localized nanooptical fields*. Appl. Phys. B **122**, 97 (2016).
- [Spe18] J. F. Specht, E. Verdenhalven, B. Bieniek, P. Rinke, A. Knorr, and M. Richter. *Theory of Excitation Transfer between Two-Dimensional Semiconductor and Molecular Layers*. Phys. Rev. Applied **9**, 044025 (2018).
- [Spl10] A. Splendiani, L. Sun, Y. Zhang, T. Li, J. Kim, C.-Y. Chim, G. Galli, and F. Wang. *Emerging Photoluminescence in Monolayer MoS₂*. Nano Lett. **10**, 1271 (2010).
- [Sri15] A. Srivastava, M. Sidler, A. V. Allain, D. S. Lembke, A. Kis, and A. Imamoglu. *Valley Zeeman effect in elementary optical excitations of monolayer WSe₂*. Nat. Phys. **11**, 141 (2015).
- [Ste06] R. M. Stevenson, R. J. Young, P. Atkinson, K. Cooper, D. A. Ritchie, and A. J. Shields. *A semiconductor source of triggered entangled photon pairs*. Nature **439**, 179 (2006).
- [Ste10] F. E. S. Steinhoff and M. C. de Oliveira. *State reconstruction of finite-dimensional compound systems via local projective measurements and one-way classical communication*. Phys. Rev. A **82**, 062308 (2010).
- [Sti06] E. A. Stinaff, M. Scheibner, A. S. Bracker, I. V. Ponomarev, V. L. Korenev, M. E. Ware, M. F. Doty, T. L. Reinecke, and D. Gammon. *Optical Signatures of Coupled Quantum Dots*. Science **311**, 636 (2006).
- [Sto02] M. I. Stockman, S. V. Faleev, and D. J. Bergman. *Coherent Control of Femtosecond Energy Localization in Nanosystems*. Phys. Rev. Lett. **88**, 067402 (2002).
- [Sto09] K. W. Stone, K. Gundogdu, D. B. Turner, X. Li, S. T. Cundiff, and K. A. Nelson. *Two-Quantum 2D FT Electronic Spectroscopy of Biexcitons in GaAs Quantum Wells*. Science **324**, 1169 (2009).
- [Sto11] E. Stock, M.-R. Dachner, T. Warming, A. Schliwa, A. Lochmann, A. Hoffmann, A. I. Toropov, A. K. Bakarov, I. A. Derebezov, M. Richter, V. A. Haisler, A. Knorr, and D. Bimberg. *Acoustic and optical phonon scattering in a single In(Ga)As quantum dot*. Phys. Rev. B **83**, 041304 (2011).
- [Sum72] H. Sumi. *Exciton-Phonon Interaction in the Coherent Potential Approximation with Application to Optical Spectra*. J. Phys. Soc. Jpn. **32**, 616 (1972).
- [Szy17] M. Szymsizewski, E. Mostaani, N. D. Drummond, and V. I. Fal'ko. *Binding energies of trions and biexcitons in two-dimensional semiconductors from diffusion quantum Monte Carlo calculations*. Phys. Rev. B **95**, 081301 (2017).
- [Tak85] T. Takagahara. *Localization and energy transfer of quasi-two-dimensional excitons in GaAs-AlAs quantum-well heterostructures*. Phys. Rev. B **31**, 6552 (1985).
- [Tak94] Y. Takahashi, S. S. Kano, K. Muraki, S. Fukatsu, Y. Shiraki, and R. Ito. *Direct observation of exciton localization in a GaAs/AlGaAs quantum well*. Appl. Phys. Lett. **64**, 1845 (1994).

- [Tek04] A. Teke, Ü. Özgür, S. Doğan, X. Gu, H. Morkoç, B. Nemeth, J. Nause, and H. O. Everitt. *Excitonic fine structure and recombination dynamics in single-crystalline ZnO*. Phys. Rev. B **70**, 195207 (2004).
- [Thr00] A. Thränhardt, S. Kuckenburg, A. Knorr, T. Meier, and S. W. Koch. *Quantum theory of phonon-assisted exciton formation and luminescence in semiconductor quantum wells*. Phys. Rev. B **62**, 2706 (2000).
- [Tia03] P. Tian, D. Keusters, Y. Suzaki, and W. S. Warren. *Femtosecond Phase-Coherent Two-Dimensional Spectroscopy*. Science **300**, 1553 (2003).
- [Tka09] A. Tkatchenko and M. Scheffler. *Accurate Molecular Van Der Waals Interactions from Ground-State Electron Density and Free-Atom Reference Data*. Phys. Rev. Lett. **102**, 073005 (2009).
- [Ton12] C. Tonin, R. Hostein, V. Voliotis, R. Grousson, A. Lemaitre, and A. Martinez. *Polarization properties of excitonic qubits in single self-assembled quantum dots*. Phys. Rev. B **85**, 155303 (2012).
- [Tur10] D. B. Turner and K. A. Nelson. *Coherent measurements of high-order electronic correlations in quantum wells*. Nature **466**, 1089 (2010).
- [Uge14] M. M. Ugeda, A. J. Bradley, S.-F. Shi, F. H. da Jornada, Y. Zhang, D. Y. Qiu, W. Ruan, S.-K. Mo, Z. Hussain, Z.-X. Shen, F. Wang, S. G. Louie, and M. F. Crommie. *Giant bandgap renormalization and excitonic effects in a monolayer transition metal dichalcogenide semiconductor*. Nat. Mater. **13**, 1091 (2014).
- [Van05] L. M. K. Vandersypen and I. L. Chuang. *NMR techniques for quantum control and computation*. Rev. Mod. Phys. **76**, 1037 (2005).
- [Vas08] P. Vasa, R. Pomraenke, S. Schwieger, Y. I. Mazur, V. Kunets, P. Srinivasan, E. Johnson, J. E. Kihm, D. S. Kim, E. Runge, G. Salamo, and C. Lienau. *Coherent Exciton-Surface-Plasmon-Polariton Interaction in Hybrid Metal-Semiconductor Nanostructures*. Phys. Rev. Lett. **101**, 116801 (2008).
- [Vay12] Y. Vaynzof, A. A. Bakulin, S. Gélinas, and R. H. Friend. *Direct Observation of Photoinduced Bound Charge-Pair States at an Organic-Inorganic Semiconductor Interface*. Phys. Rev. Lett. **108**, 246605 (2012).
- [Ver13] E. Verdenhalven, R. Binder, A. Knorr, and E. Malic. *Derivation of the screened Bloch equations and application to carbon nanostructures*. Chem. Phys. **413**, 3 (2013).
- [Ver14] E. Verdenhalven, A. Knorr, M. Richter, B. Bieniek, and P. Rinke. *Theory of optical excitations in dipole-coupled hybrid molecule-semiconductor layers: Coupling of a molecular resonance to semiconductor continuum states*. Phys. Rev. B **89**, 235314 (2014).
- [vFr98] G. von Freymann, T. Schimmel, M. Wegener, B. Hanewinkel, A. Knorr, and S. W. Koch. *Computer simulations on near-field scanning optical microscopy: Can sub-wavelength resolution be obtained using uncoated optical fiber probes?* Appl. Phys. Lett. **73**, 1170 (1998).
- [Vos06] T. Voss, I. Rückmann, J. Gutowski, V. M. Axt, and T. Kuhn. *Coherent control of the exciton and exciton-biexciton transitions in the generation of nonlinear wave-mixing signals in a semiconductor quantum well*. Phys. Rev. B **73**, 115311 (2006).

- [Wal04] I. Waldmüller, J. Förstner, and A. Knorr. *Self-consistent Projection Operator Theory of Intersubband Absorbance in Semiconductor Quantum Wells*. in *Nonequilibrium Physics at Short Time Scales* (edited by K. Morawetz), pp. 251–273. Springer, Berlin (2004).
- [Wan37] G. H. Wannier. *The Structure of Electronic Excitation Levels in Insulating Crystals*. Phys. Rev. **52**, 191 (1937).
- [Wan12] Q. H. Wang, K. Kalantar-Zadeh, A. Kis, J. N. Coleman, and M. S. Strano. *Electronics and optoelectronics of two-dimensional transition metal dichalcogenides*. Nat. Nanotechnol. **7**, 699 (2012).
- [Wan14] G. Wang, L. Bouet, D. Lagarde, M. Vidal, A. Balocchi, T. Amand, X. Marie, and B. Urbaszek. *Valley dynamics probed through charged and neutral exciton emission in monolayer WSe₂*. Phys. Rev. B **90**, 075413 (2014).
- [Web08] C. Weber, M. Richter, S. Ritter, and A. Knorr. *Semiconductor Nanostructures*, chap. Theory of the Optical Response of Single and Coupled Quantum Dots, pp. 189–210. Springer, Berlin (2008).
- [Web11] A. Weber-Bargioni, A. Schwartzberg, M. Cornaglia, A. Ismach, J. J. Urban, Y. Pang, R. Gordon, J. Bokor, M. B. Salmeron, D. F. Ogletree, P. Ashby, S. Cabrini, and P. J. Schuck. *Hyperspectral Nanoscale Imaging on Dielectric Substrates with Coaxial Optical Antenna Scan Probes*. Nano Lett. **11**, 1201 (2011).
- [Wei81] C. Weisbuch, R. Dingle, A. Gossard, and W. Wiegmann. *Optical characterization of interface disorder in GaAs-Ga_{1-x}Al_xAs multi-quantum well structures*. Solid State Commun. **38**, 709 (1981).
- [Wei09] A. M. Weiner. *Ultrafast optics*. Wiley, New York (2009).
- [Wey25] H. Weyl. *Theorie der Darstellung kontinuierlicher halb-einfacher Gruppen durch lineare Transformationen. I*. Mathematische Zeitschrift **23**, 271 (1925).
- [Woo86] W. K. Wootters. *Quantum mechanics without probability amplitudes*. Found. Phys. **16**, 391 (1986).
- [Wüt03] K. Wüthrich. *NMR studies of structure and function of biological macromolecules (Nobel Lecture)*. Journal of Biomolecular NMR **27**, 13 (2003).
- [Xia12] D. Xiao, G.-B. Liu, W. Feng, X. Xu, and W. Yao. *Coupled Spin and Valley Physics in Monolayers of MoS₂ and Other Group-VI Dichalcogenides*. Phys. Rev. Lett. **108**, 196802 (2012).
- [Yan08] L. Yang and S. Mukamel. *Two-Dimensional Correlation Spectroscopy of Two-Exciton Resonances in Semiconductor Quantum Wells*. Phys. Rev. Lett. **100**, 057402 (2008).
- [Yos97] H. Yoshikawa and S. Adachi. *Optical Constants of ZnO*. Jpn. J. Appl. Phys. **36**, 6237 (1997).
- [You15] Y. You, X.-X. Zhang, T. C. Berkelbach, M. S. Hybertsen, D. R. Reichman, and T. F. Heinz. *Observation of biexcitons in monolayer WSe₂*. Nat. Phys. **11**, 477 (2015).
- [Yu05] P. Y. Yu and M. Cardona. *Fundamentals of Semiconductors*. Springer, Berlin (2005).

- [Yu14] H. Yu, G.-B. Liu, P. Gong, X. Xu, and W. Yao. *Dirac cones and Dirac saddle points of bright excitons in monolayer transition metal dichalcogenides*. Nat. Commun. **5**, 3876 (2014).
- [Zen12] H. Zeng, J. Dai, W. Yao, D. Xiao, and X. Cui. *Valley polarization in MoS₂ monolayers by optical pumping*. Nat. Nanotechnol. **7**, 490 (2012).
- [Zha09] Z. Zhang, A. Weber-Bargioni, S. W. Wu, S. Dhuey, S. Cabrini, and P. J. Schuck. *Manipulating Nanoscale Light Fields with the Asymmetric Bowtie Nano-Colorsorter*. Nano Lett. **9**, 4505 (2009).
- [Zha11] G.-X. Zhang, A. Tkatchenko, J. Paier, H. Appel, and M. Scheffler. *Van der Waals Interactions in Ionic and Semiconductor Solids*. Phys. Rev. Lett. **107**, 245501 (2011).
- [Zha13] H. H. Zhang, X. H. Pan, B. Lu, J. Y. Huang, P. Ding, W. Chen, H. P. He, J. G. Lu, S. S. Chen, and Z. Z. Ye. *Mg composition dependent band offsets of Zn_{1-x}Mg_xO/ZnO heterojunctions*. Phys. Chem. Chem. Phys. **15**, 11231 (2013).
- [Zha14] C. Zhang, H. Wang, W. Chan, C. Manolatu, and F. Rana. *Absorption of light by excitons and trions in monolayers of metal dichalcogenide MoS₂: Experiments and theory*. Phys. Rev. B **89**, 205436 (2014).
- [Zha15] D. K. Zhang, D. W. Kidd, and K. Varga. *Excited Biexcitons in Transition Metal Dichalcogenides*. Nano Lett. **15**, 7002 (2015).
- [Zhu11] Z. Y. Zhu, Y. C. Cheng, and U. Schwingenschlögl. *Giant spin-orbit-induced spin splitting in two-dimensional transition-metal dichalcogenide semiconductors*. Phys. Rev. B **84**, 153402 (2011).
- [Zim95] R. Zimmermann. *Theory of resonant rayleigh scattering of excitons in semiconductor quantum wells*. Il Nuovo Cimento D **17**, 1801 (1995).
- [Zim97a] R. Zimmermann, F. Grosse, and E. Runge. *Excitons in semiconductor nanostructures with disorder*. Pure Appl. Chem. **69**, 1179 (1997).
- [Zim97b] R. Zimmermann and E. Runge. *Excitons in Narrow Quantum Wells: Disorder Localization and Luminescence Kinetics*. Phys. Stat. Sol. A **164**, 511 (1997).
- [Zim03] R. Zimmermann, E. Runge, and V. Savona. *Theory of resonant secondary emission: Rayleigh scattering versus luminescence*. in *Quantum Coherence Correlation and Decoherence in Semiconductor Nanostructures* (edited by T. Takagahara), pp. 89–165. Elsevier Science (USA) (2003).